Mechanical behavior and thermal stability of Ti-Zr-Hf-Nb-Ta alloys

A Dissertation Presented for the

Doctor of Philosophy

Degree

The University of Tennessee, Knoxville

William Jackson Carpenter

May 2025

Acknowledgements

First and foremost, I would like to thank my advisor Easo George. Easo took me into the group at probably what would been one of the more frantic times of our lives during 2020 and kept me on through his retirement. Your advice and guidance are like finding gold. I give you a parting gift – full retirement.

Second, I must thank my other advisor, the Austrian (no kangaroos) in Australia (with kangaroos), Bernd Gludovatz. Coming up and doing the idea of going to Australia to do fracture mechanics was only possible with his and Easo's bureaucratic tenacity and technical expertise. I learned a lot and hope to return. Bernd, I'll eat any pepper coming out of the garden!

I would also like to extend my thanks to my committee members. Veerle Keppens, who generously took the responsibility of being on my committee despite becoming a provost. Claudia Rawn, who donated her time, and likely her patience, to teach me the nuances of GSAS. I would especially like to thank Ying Yang, who assisted in providing valuable thermodynamic data, which provided me with one of the few compasses to explore the compositional wilderness.

A personal thanks also goes out to the current and former technical staff at ABAD and ORNL, specifically Ian Stinson and Cody Taylor, as well as those at the MDF, Bryan Lim, Julio Ortega Rojas, and Andrés Márquesz Rossy. Additional thanks goes to Kevin Hanson who performed the arc-melting, and Carlos Rodriguez-Flores and J. Craig at the glass shop who were always helpful and fantastic at their craft.

My fellow graduate students in Easo's group, Josh Cicotte and Jeff Brookins, who were invaluable for turning the PhD from a purely academic exercise in the study of metallic behavior to a wonderful academic exercise in the study of metallic behavior *and* depraved methods of ramen and coffee synthesis. I would be amiss to not thank Emily Proehl and Sean Drewry, who, for whatever god forsaken reason, decided to study thermodynamics outside with me… during the winter... I need to mention the wonderful people that helped me at UNSW as well. To the technical staff, especially Seetha Mahadevan and Alex Chariyekkara, again both very helpful and great to talk to. My fellow graduate students over there, thank you. Moses James Paul, first and foremost, thank you for being my fracture mechanics angel and dear friend. Included in this is Michael Moschetti, Mihee Shin, Bibek Kumar Shah, Caroline, Harikrishna, and Daisy Chu. Thank you all for being great group members and friends.

Finally, to my family and partner Diāna Stamberga. Your kind nature and attention are something that I see as an endless well of inspiration.

This work was supported by the UT-ORNL Governor's Chair for Advanced Alloy Theory and Development.

Abstract

Refractory high entropy alloys (RHEAs) are interesting from both scientific and engineering viewpoints. Using group IV, V, and VI elements, the compositional space available to RHEAs grants greater freedom to obtain material properties that are often in competition with each other such as high melting temperature and room-temperature ductility. As a model system, Ti-Zr-Hf-Nb-Ta alloys show promise with their high melting temperature and ductility that allows for cold rolling. Despite over a decade since the discovery of the equiatomic alloy TiZrHfNbTa, there is still a dearth of basic composition-property data for its derivatives. This work aims to address three issues with respect to TiZrHfNbTa alloys: relationship between composition and (i) uniaxial tensile behavior, (ii) fracture toughness behavior, and (iii) thermal stability. The equiatomic alloy TiZrHfNbTa and four other alloys were investigated that represented relatively wide compositional changes within the Ti-Zr-Hf-Nb-Ta space that could be processed. With respect to tensile properties in the single-phase state, the alloys behave similarly and their yield strengths can be predicted well by an analytical theory based on edge dislocations. During fracture toughness testing, sudden crack extension is seen in TiZrHfNbTa but not the other alloys. Finally, the thermally stable phases in the four derivative alloys showed three unique microstructures: single-phase with incidental minor phases, HCP homogenously precipitated in BCC, and lamellar BCC-HCP microstructure akin to eutectoid microstructures.

Table of Contents

List of Tables

List of Supplementary Tables

List of Figures

List of Supplementary Figures

Chapter 1 Introduction to refractory high entropy alloys

A version of this chapter is being prepared for publication in *Journal of Materials Research* as an invited perspectives paper. WJ Carpenter performed the literature review and wrote the first draft. EP George, after being asked to provide a Distinguished Invited Speaker article, conceived the general outline, discussed it with WJC, and is editing the drafts.

Introduction

High-temperature materials have been a persistent challenge for materials scientists and engineers where the goal is simple to define but difficult to achieve: survive higher temperatures, bear higher loads, often in reactive environments. Nickel superalloys have historically met these needs with their useful material properties including strength and fabricability, oxidation resistance, and density [1]. However, materials that operate beyond nickel's melting temperature rarely meet these engineering criteria. Noble metals such as iridium are cost prohibitive and have volatile oxides [2] and are limited to only the most specific structural uses [3]. Refractory metals (Mo, W, and Ta) have poor oxidation resistance, are brittle, and dense [4]. While efforts through the 1950s – 1980s provided fundamental data for refractory alloys [5] such as high temperature creep [6] and oxidation behavior [7], they did not yield a satisfying engineering solution that surpassed nickel superalloys.

The early 2000s saw the emergence of high entropy alloys (HEAs) [8] and was followed by the refractory high entropy alloys (RHEAs) in 2010 [9]. The new HEA class was exciting for its large compositional space, roughly defined as 3 -5 primary elements

with 5 – 35 at% each, and single-phase microstructure [8, 10]. Much of the initial scientific interest stemmed from their single-phase microstructure, which seemed to run counter to the Gibbs phase rule and metallurgical intuition but was later found to be an issue of kinetics rather than thermodynamic stability since many face centered cubic (FCC) HEAs would form secondary phases after prolonged heat treatments [11]. RHEAs use metallic elements from groups IV, V, and VI of the periodic table [10, 12]. Originally, RHEAs were intended to be single-phase alloys but have also come to include alloys with secondary phases [12]. The discovery of metastable single-phase RHEAs presented an opportunity to reapproach high temperature alloys with more compositional freedom than previous refractory alloys.

While HEAs do have a more strict definition that depends on the entropy of mixing [10], here we will refer to alloys generically as HEAs if the alloy has at least three elements and its elemental compositions fall near HEA definitions rather than specifying each alloy as low, medium, or high entropy.

Comprehensive reviews of the field can be found in [10, 12] and [13-15]. For more detailed insights on mechanical behavior, the reader is directed to [14], [16], and [17, 18].

The high temperature properties of single-phase RHEAs

There is a relative dearth of high temperature mechanical data on RHEAs. VNbTaMoW and NbTaMoW were the first RHEAs synthesized and mechanically tested [9, 19]. The initial interest in these RHEAs stemmed from their high-temperature yield

strength. The alloys had remarkably high compressive strengths between 600 ˚C and 1600 ˚C at 10^{-3} s^{-1} ranging from 862 to 477 MPa for VNbTaMoW and 561 MPa to 405 MPa for NbTaMoW, as seen in **Figure 1.1a** where data for common nickel alloys Inconel 718 and Haynes 230 are also shown [19]. More recent work on bulk NbTaMoW showed that despite having some ductility in compression, **Figure 1.1b**, the alloy had no tensile ductility at elevated temperatures as seen by the stress-strain curves in **Figure 1.1c** [20]. Furthermore, measured fracture toughness values up to 1200 ˚C were all below 11 MPa $m^{0.5}$, and were microstructure and crack-path dependent, which was partially attributed to a nanoscale oxide layer on the grain boundaries, and to the differences between the columnar and equiaxed grain structure between specimens [20].

The more ductile TiZrHfNbTa is softer than VNbTaMoW at elevated temperatures. Two studies have been performed on the high temperature compressive yield strengths: Senkov et al. [21], whose data are shown in **Figure 1.2a**, and Yasuda et al. [22]. Both studies found an unsurprising decrease in yield strength from room temperature to 1200 ˚C, decreasing to 92 MPa at 1200 ˚C [21]. The Yasuda et al. [22] found an increase in yield strength at 600 ˚C associated with the formation of a secondary HCP phase. However, strengthening from secondary phases can be problematic. In Mills et al. [23] found that TiZrHfNbTa is embrittled under quasistatic tensile loading, 10^{-2} /s and 10^{-1}/s, at 800 ˚C due to the formation of a Nb-Ta rich BCC phase that formed on the grain boundaries.

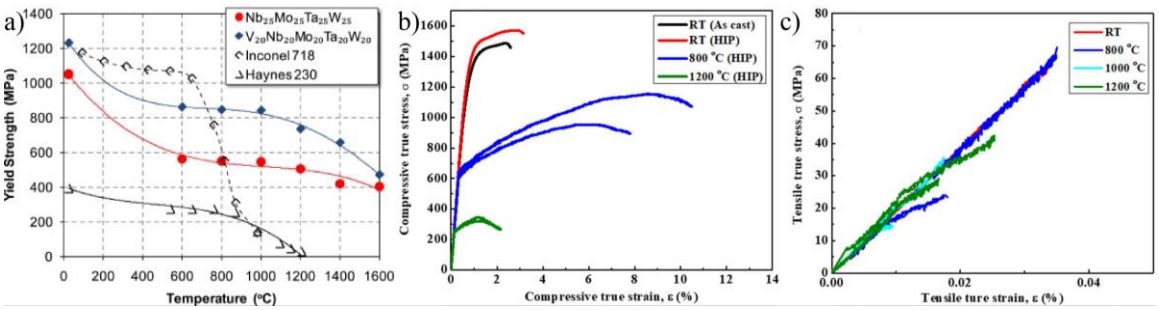

Figure 1.1: (a) Temperature dependence of yield strengths in compression for NbTaMoW and VNbTaMoW compared to Inconel 718 and Haynes 230 [19]. (b) Compressive stress-strain curves of NbTaMoW as a function of temperature in the HIPed state, showing some compressive ductility [20]. (c) Same material as in (b) tested in tension showing no plasticity [20]. (b,c) Reproduced from [20] and with permission from Elsevier.

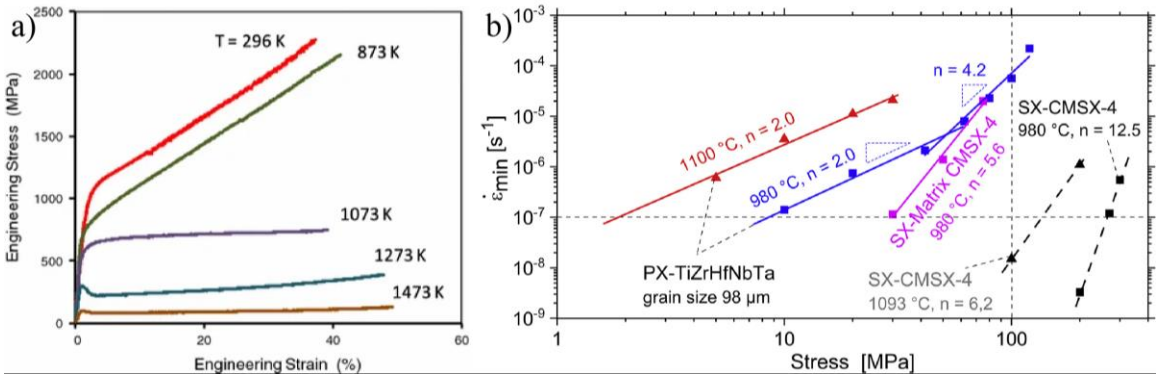

Figure 1.2: (a) Compressive stress-strain curves of TiZrHfNbTa from room temperature to 1200 ˚C [21]. (b) Norton plot (minimum creep rate vs. applied stress) of TiZrHfNbTa at 1100 ˚C (red) and 980 ˚C (blue) compared to single crystal matrix of CMSX-4 (purple) and precipitate-strengthened CMSX-4 (black) [24].

In the single-phase state, TiZrHfNbTa is ~70 times weaker in creep compared to a leading nickel-base superalloy CMSX-4, which is precipitate-strengthened (see horizontal dashed line in **Figure 1.2** [24]). Even compared to the single-phase matrix of CMSX-4, TiZrHfNbTa is a factor of three weaker at 980 ˚C, **Figure 1.2b** [24]. Liu et al. [25] obtained somewhat higher but nevertheless comparable creep exponents as above, namely, 2.5 – 2.8 between 1100 ˚C and 1250 ˚C, and activation energies of 273 ± 15 kJ mol^{-1}. The stress exponents, all being below 3.0, suggests that the main creep mechanism is solute drag [25]. It should be noted that in radioactive tracer diffusion measurements of Zr-89 in TiZrHfNbTa and TiZrHfVNbTa, measured between 850 ˚C and 1150 ˚C, Zr diffusion was abnormally fast in TiZrHfNbTa at both absolute and homologous temperatures [26]. If this diffusion result is extrapolated to the other elements, relatively fast diffusion will be a hinderance to improving the creep life in TiZrHfNbTa.

Despite TiZrHfNbTa being the most studied refractory alloy, $Nb_{45}Ta_{25}Ti_{15}Hf_{15}$ has a more complete set of high temperature mechanical properties. $Nb_{45}Ta_{25}Ti_{15}Hf_{15}$ is one of the few RHEAs whose high-temperature fracture toughness has been measured [27]. Its fracture toughness ranged from 52 MPa $m^{0.5}$ at 950 ˚C to 88 MPa $m^{0.5}$ at 1200 ˚C. In the same study, the yield strength of $Nb_{45}Ta_{25}Ti_{15}Hf_{15}$ was reported to be 596 MPa at room temperature and 140 MPa at 1200 ˚C. Monfared et al. [28] performed creep tests at 850 ˚C, 900 ˚C, and 950 ˚ to determine activation energies and the stress exponent at 900 ˚C. They found the activation energy to be 253 kJ/ mol, similar to Liu et al.'s [25] value for TiZrHfNbTa, and attributed it to vacancy diffusion based on grain growth data

from Senkov, Pilchak, and Semiatin [29]. $Nb_{45}Ta_{25}Ti_{15}Hf_{15}$ had a measured stress exponent of 4.1 at 900 ˚C in vacuum, and 1.2 and 5.7, depending on stress, in Ar atmosphere. The low creep exponents suggest diffusion mechanisms and higher values suggest dislocation climb [28]. Monfared et al. also noted that specimens tested in the Ar environment had higher O content after testing, measured by inert gas fusion, which was associated with the "open system" of the Ar environment.

The oxidation behavior of RHEAs

Oxidation is critical issue for high temperature use and it is worth briefly summarizing the oxidation behavior of RHEAs. The elemental additions that promote desirable mechanical behavior, high strength and ductility, can be at odds with its oxidation resistance and vice versa. One such example is V [30] which can be useful for hardening but results in low melting temperature oxides [31]. RHEAs still have to contend with the fundamental issues of refractory oxidation such as volatile oxides [32] and pesting [33]. The main approach to improve oxidation resistance is to add Al, Si, and Cr in sufficient quantities to form a scale [2, 34], but such additions promote secondary phases in RHEAs [35, 36]. Al additions to TiZrHfNbTa reduce mass gain in oxidation tests by scale formation below 1100 ˚C [37], but such additions embrittle the alloy [38]. More recent efforts by Anber et al. [39] focused on reducing the Al content needed to passivate, reporting the prevention of pesting with 4.8 at% Al. They also suggested a new design approach based on reducing Zr and Hf to prevent their oxides forming at the scale metal interface. Many RHEAs without the additions of strong scale formers have thick

and porous oxides after oxidation, rendering poor oxidation resistance [40]. The need for a suitable scale is also seen in VNbTaMoW and NbTaMoW [41], where a 1 min exposure at 1300 ˚C resulted in the formation of a VMo liquid oxide and consequently a porous multilayered oxide in VNbTaMoW. Careful analysis is needed when assessing mass gain experiments: many of the RHEA oxidation studies lack mass spectroscopy and thus mass loss from volatilization could reduce overall mass gain and render a false impression of performance [32, 42]. A particularly noteworthy development is the passivation by $CrTaO_4$ since it was not previously not known to be a protective oxide [42]. $CrTaO_4$ provides effective resistance to mass gain at 1000 ˚C and 1100 ˚C in SiAlTiCrNbMoTa alloys [43], adheres well and maintains low growth rates between 500 ˚C and 1500 ˚C in TaMoMoTiAl [44]. More detailed overviews of oxidation in RHEAs can found be in Gorr et al.'s review [42], and more recent work in Dehury et al.'s review [45].

The microstructure of "single-phase" RHEAs

RHEAs were originally intended to be single-phase alloys. The premise being that adding more elements stabilizes solid solutions by increasing the entropy of mixing [8]. This was not the case in the FCC HEAs [11] and is most likely the same for RHEAs but has yet to be thoroughly studied in a similar way. The basic issue in RHEA microstructures is the stability of the BCC and other phases present. The BCC stability is important since much of the intended alloy design is for a single-phase BCC structure and the other phases that form are the possible engineering opportunities to change material properties.

Between VNbTaMoW alloys and TiZrHfNbTa, TiZrHfNbTa has received more work on microstructural evolution and thus will be the main focus in this section. The multi-phase region of TiZrHfNbTa occurs, roughly, between 500 ˚C and 1000 ˚C. Thermomechanical processing by cold rolling followed by annealing at 800 ˚C for 2 h [46] and up to 256 h [29] resulted in a microstructure consisting of two BCC phases, BCC1 and BCC2, as shown in **Figure 1.3a-c**. Schuh et al. [47] annealed TiZrHfNbTa after high pressure torsion at 500 ˚C for 100 h resulting in a microstructure consisting of BCC1, BCC2, and HCP phases. Annealing for 1 h above 1000 ˚C resulted in a single-phase BCC microstructure [47]. After creep testing at 980 ˚C for 61 h, Gadelmeier et al. [24] found secondary phases forming at the grain boundaries of TiZrHfNbTa but only in the gauge section, presumably driven by the tensile stress within the creep specimen. Similarly, the embrittlement found by Mills et al. was attributed to a secondary BCC formed at 800 ˚C during preheating [23], with further annealing at 100 h confirming its presence as a thermodynamically favored phase.

There are only a few studies of compositional modifications of TiZrHfNbTa and their effects on thermal stability. Coury et al. [48] looked at three groups of RHEAs: (i) containing NbTaTi (AlNbTaTi, HfNbTaTi, WNbTaTi, MoNbTaTi, and CrNbTaTi), (ii) containing Al (AlCrMoNb, AlHfNbTi, AlHfTaTi, and AlNbTaTi), and (iii) containing Cr (CrNbTaTi, CrMoTaTi, CrMoNbTi, CrNbTiW, AlCrMoNb), several alloys, i.e. AlNbTaTi, fall into multiple groups.

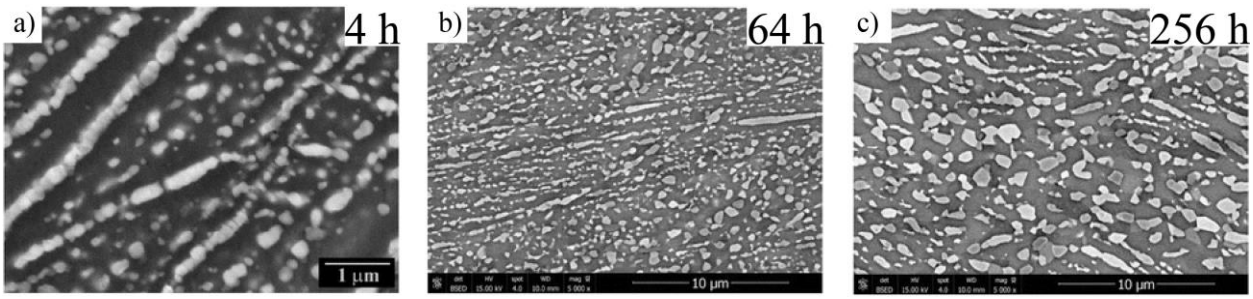

Figure 1.3: TiZrHfNbTa microstructure after annealing at 800 ˚C for (a) 4 h, (b) 64 h, and (c) 254 h [29], where the bright precipitates are secondary BCC phases. (a-c) Reproduced from [29] and with permission from Springer-Nature.

The alloys were homogenized after casting at 1400 ˚C for 35 h. Alloys with Cr tended to form BCC, C14 and C15 Laves phases, except for CrMoNbTi which remained single-phase BCC, while Al containing alloys formed A15 phases. Of particular importance is the relative stability of the BCC phase. Maiti and Struer [49] found that after annealing ZrHfNbTa at 1800 ˚C between 6 h and 192 h, Zr and Hf clustered together and formed secondary HCP phases, a temperature where the material should be single-phased BCC. Similar instabilities are observed in the presence of interstitial elements. Recently, Poulain et al. [50] examined the thermal stability of TiZrHfNbTa containing three levels of O: clean TiZrHfNbTa, ~3 at% O added by arc-melting, and O introduced by a purposeful partial pressure of O in an encapsulation. After 1000 h at 900 ˚C, the clean specimen had only a single-phase BCC structure, while the oxygen-contaminated samples had two BCC phases and one HCP phase rich in Zr-Hf, as shown in **Figure 1.4a-c**. The secondary BCC and HCP phases were located mostly at grain boundaries in the sample annealed in partial pressure of O, as opposed to the arc-melted sample containing O where the secondary phases were more homogenously distributed. Poulain et al.'s result has implications for both scientific understanding and potential applications of TiZrHfNbTa alloys. Most studies do not report their interstitial content, so it is unclear whether secondary phases are anomalous or repeatable. Further, if the presence of a common interstitial breaks down the intended microstructure, TiZrHfNbTa's use will be severely hampered in an oxidative atmosphere.

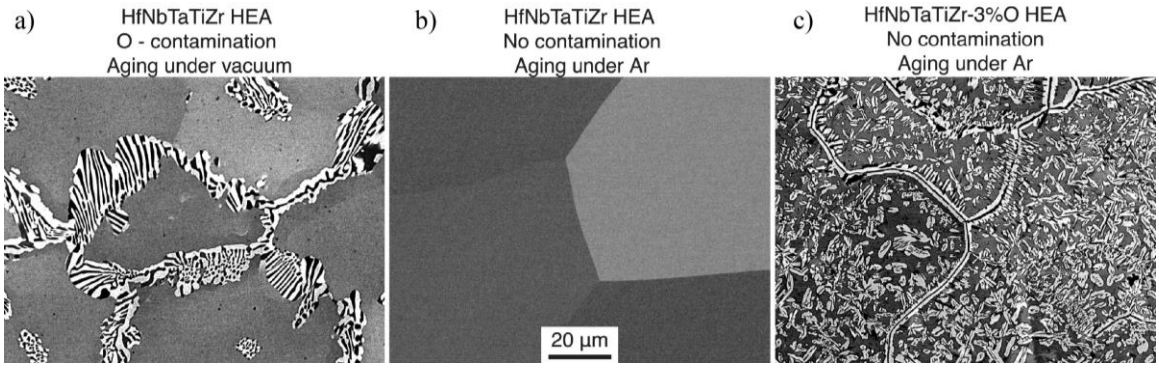

Figure 1.4: (a) Phase decomposition of O-contaminated TiZrHfNbTa occurs after a 1000-h anneal in vacuum at 900 ˚C, but does not occur in a clean sample annealed in Ar (b). The addition of oxygen by arc-melting and annealing (c) also results in pronounced phase separation [50]. (a-c) Reproduced from [50] under Creative Commons CC-BY license.

Multiphase microstructures of RHEAs

Single-phase RHEAs based on TiZrHfNbTa will likely not be usable as high temperature materials. Efforts have been made to purposefully modify the microstructures of RHEAs to improve creep properties and oxidation resistance at high temperature. A desirable high temperature microstructure consists of a matrix, ideally disordered to accommodate deformation, and an ordered intermetallic, ideally with similar lattice parameters as the disordered phase, packed tightly to hinder dislocation movement [1]. Senkov et al. [51] achieved a superalloy like microstructure in $AlMo_{0.5}NbTa_{0.5}TiZr$ where the B2 phase (an ordered BCC phase) is the matrix and the BCC phase is the precipitate, seen in

Figure 1.5. While a promising start, a topological inversion was needed to satisfy the ideal microstructure described above, that is, the likely brittle B2 matrix needed to be converted to a BCC matrix containing B2 precipitates. Such a BCC-matrix and B2 precipitate microstructure was achieved in $AlNbTa_{0.8}Ti_{1.5}V_{0.2}Zr$ by annealing the alloy at 1200 ˚C for 24 h, then annealing at 1400 ˚C for 20 minutes and quenching, followed finally by annealing at 600 ˚C for 120 h [52]. The mechanism of inversion was later determined to be driven by elastic strain [53]. The initial B2 and BCC had a low lattice misfit of ~0.9%. As the alloy is aged at 600 ˚C the B2 phase becomes enriched in Al and Zr, causing an increase in lattice parameter. Meanwhile, the BCC phase is depleted in Al and enriched in Ta, resulting in a similar lattice parameter to the initial condition.

Accordingly, the lattice misfit energy increases, favoring the B2 phase to pinch itself off and become discontinuous [53].

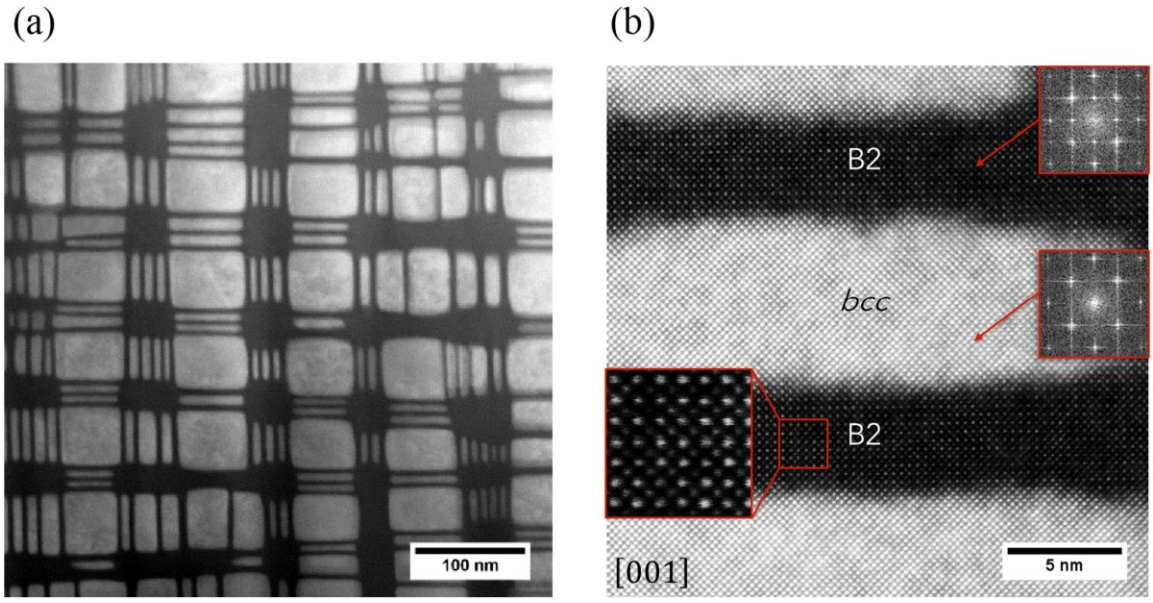

Figure 1.5: TEM micrographs showing (a) $AlMo_{0.5}NbTa_{0.5}TiZr$ after HIPing at 207 MPa at 1200 ˚C followed by 1400 ˚C for 6 h, and (b) the ordered B2 matrix and BCC precipitate at higher magnification [51]. (a, b) Reproduced from [51] and with permission from Elsevier.

This process is shown **Figure 1.6a-f**, where the initial solutionized microstructure (a) gives way to a B2 lattice (b), which breaks down over the course of annealing into BCC and B2 (c-f).

However, the next significant hurdle is the thermal stability of the B2 phase as evidenced by a rapid drop in strength in the continuous B2 microstructure of $AlNbTa_{0.8}Ti_{1.5}V_{0.2}Zr$ between 800 ˚C and 1200 ˚C [54]. Additional work using calorimetry [55] found it to be related to the low order-disorder temperature of the B2 phase, which meant that above 800 ˚C two disordered BCC phases comprise the microstructure rather than B2 plus BCC. Clearly, this is untenable because the B2 must be present and ideally ordered to provide strengthening. Losing the ordering and hence strengthening at relatively low temperatures is antagonistic to achieving high-temperature strength. Furthermore, the B2 phase is not thermally stable at relatively low temperatures. After 120 h at 800 ˚C, $Al_{0.5}Mo_{0.5}NbTa_{0.5}TiZr$ forms an ω phase (P63/mcm space group) from the B2 [56], **Figure 1.7a-b**. Similar results were found in $Al_{0.5}NbTa_{0.8}Ti_{1.5}V_{0.2}Zr$ with TEM showing secondary phases of ω Zr_5Al_4, $L1_0$, and ordered hexagonal [57]. Recent work in suppressing the ω phase modified the Zr/Al ratio where the goals are twofold [58]: (i) decrease the ω phase solvus temperature, (ii) increase the miscibility gap temperature, functionally the B2 solvus, by adding group V and VI elements.

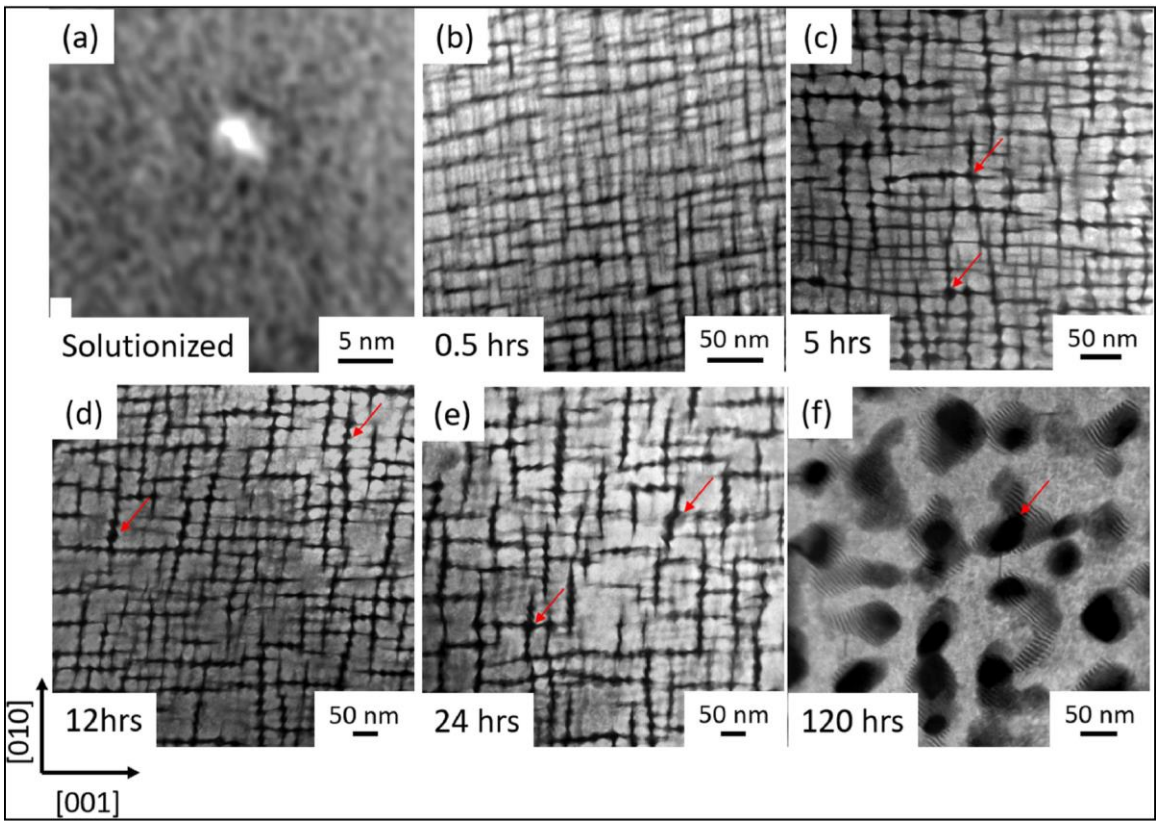

Figure 1.6: TEM micrographs (a-f) showing microstructural evolution in $Al_{0.5}NbTa_{0.8}Ti_{1.5}V_{0.2}Zr$ [53]. The initial microstructure (a) is obtained by solutionizing at 1200 ˚C for 2 h, followed by isothermal annealing at 600 °C for different times (b-f). The dark regions are the B2 phase which begin as an interconnected matrix (b), but slowly form bulges (red arrows) that eventually become coalescence sites for the disconnected B2 phase (f). (a-f) Reproduced from [53] and with permission from Elsevier.

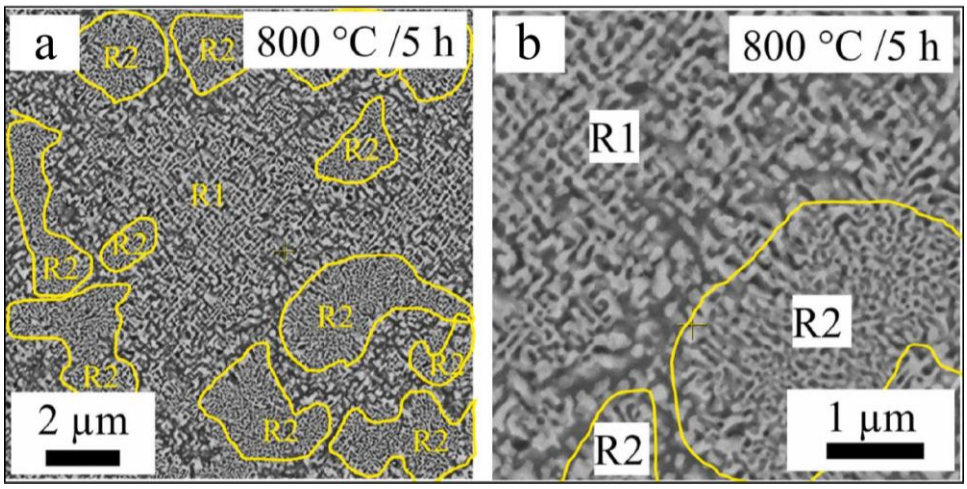

Figure 1.7: (a,b) Al0.5Mo0.5NbTa0.5TiZr after annealing for 5 h at 800 ˚C, imaged by backscattered electrons in a SEM [56]. The three phases present include the BCC (bright), B2 (grey), and ω (dark). R1 and R2 represent regions of distinct morphology. (a, b) Reproduced from [56] and with permission from Elsevier.

Since the thermal stability of Al-containing BCC-B2 RHEAs is a significant drawback and the miscibility gap is unknown, they are unlikely to be viable successors to nickel superalloys. Thus, other approaches are needed to discover suitable multiphase RHEAs. Kube et al. [59] performed computational-experimental work that took a thorough look at the possible BCC-B2 intermetallic combinations to determine feasible alloy systems. It was determined by CALPHAD that Ru will be the most useful intermetallic former since some Ru intermetallics could be solutionized but also maintained a high solvus temperature up to 1950 ˚C. Up to 200-h vacuum heat treatments at 1300 ˚C, 1600 ˚C, 1750 ˚C, and 1900 ˚C were carried out on $Al_{15}Ru_{15}(NbMo, VMo)_{70}$, $Ti_{15}Ru_{15}(Nb, NbTa, NbMo, Mo, VMo)_{70}$, Hf_{15} $Ru_{15}(Nb, NbMo)_{70}$ and $Al_{10}Ru_{10}(NbMo)_{80}$ and precipitates were observed in all of them after cooling down to room temperature [59]. This suggested that the solvus temperatures of RuTi and RuHf in various matrices was high (>1900 °C), but could not rule out whether the slow cooling rate after annealing had played a role (that is, whether the precipitates dissolved during any of the high-temperatures anneals and then re-precipitated during cool down) [59]. In later studies, the precipitation behavior and thermal stability of ZrRu [60] and HfRu [60-62] were analyzed. In an attempt to adjust the lattice misfit of the BCC matrix to ZrRu and HfRu [60], a binary Nb-V matrix was chosen since its lattice parameter can be changed between those of Nb and V while in principle not affecting the tensile ductility [7, 63].

The HfRu B2 had a higher solvus temperature than ZrRu as deduced from post-annealed microstructures and Hf additions to ZrRu containing alloys reduced the tertiary phases forming along the grain boundaries [60], seen in **Figure 1.8a-b**. Frey et al. also found that HfRu formed as cuboidal precipitates in $Nb_{52}V_{28}Hf_{11}Ru_9$, **Figure 1.8b**, lending credence to their approach of changing matrix lattice parameter to achieve a more suitable microstructure [61].

Room temperature mechanical properties

While intended for high temperature use, serviceable alloys must be resistant to brittle fracture at room temperature, such as being dropped on the floor, and ideally have enough ductility to allow thermomechanical processing. Most mechanical properties measured in RHEAs are done so at room temperature. Room temperature single-phase RHEAs have two distinct behaviors: (i) brittle failure with little plastic deformation, (ii) ductile, often nonuniform, low work hardening tensile behavior. Examples of the former include VNbTaMoW [19] and the latter TiZrHfNbTa [21, 46] as measured by uniaxial compression in the former and tension in the latter. These alloys, and their derivatives, will be the focus of discussion here since they are among the most studied RHEAs and embody the opportunities and challenges.

Measured in compression, VNbTaMow and NbTaMoW only have 1.5% and 2% ductility respectively, with fracture surfaces orientated parallel to the compression direction, indicating that tensile ductility is a limiting factor for these alloys [19].

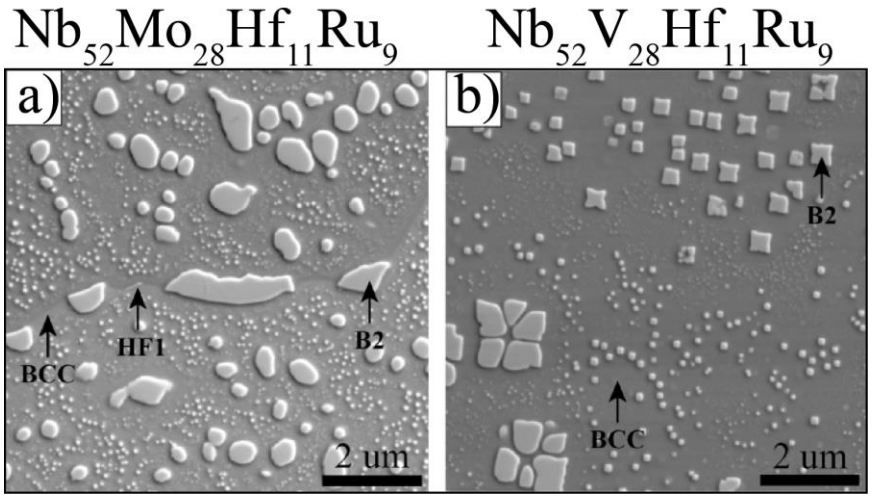

Figure 1.8: Microstructures of HfRu containing alloys in a NbMo matrix (a) and NbV matrix (b) [61], imaged by secondary SEM. The NbV matrix was specifically chosen to more closely match the lattice parameter of HfRu and change the second phase morphology from spherical to cuboidal. The HF1 is a Hf rich phase, while the B2 phase is the HfRu precipitate. Both alloys were annealed at 1750 ˚C for 10 h in vacuum. (a, b) Reproduced from [61] and with permission from Elsevier.

The recent work by Kumar et al. [20], previously mentioned in the high temperature section, provides a more complete view of the room temperature ductility issues in NbTaMoW. They performed compression, tension, and fracture toughness tests on NbTaMoW at room temperature, and in short, factors such as grain structure and oxides do change the mechanical behavior, but the alloy is brittle and functionally useless in any sort of tensile loading.

Improving the ductility of VNbTaMoW and NbTaMoW has been the focus of research on the two alloys. A first approach was to use nanosized grains from magnetron sputtering with tandem ion-beam [64] to increase ductility by increasing the amount of defects. Films of NbTaMoW made by magnetron sputtering with tandem ion-beam resulted in a thin film with 70 nm columnar grains, and a regularly sputtered film had 150 nm columnar grains, without tandem ion-beam [64]. The micropillar compression tests, with diameters ranging from 100 nm to 1 μm and aspect ratios of 2.5 – 5.0, showed an increase in strength and ductility for the tandem ion-beam sputtered material compared to normally sputtered and bulk NbTaMoW. The engendered strength and ductility were associated with heavier concentration of defects induced by the ion-beam, but which defects were responsible for the ductility is not entirely clear since the ion-beam processed film also had a smaller columnar grain diameter. Measured fracture toughness from microcantilever beam tests were only 3.3 MPa $m^{0.5}$ with intergranular failure [65]. Additional NbTaMoW microcantilever fracture toughness tests found that single crystals, 8 μm x 2 μm cross section, had fracture toughness of 1.3-2.1 MPa $m^{0.5}$, higher than the

0.2 MPa $m^{0.5}$ of bicrystals, where failure occurred at the grain boundary [66]. Atom probe tomography (APT) showed that the grain boundaries had nitrides and oxides, implying that the grain boundary weakening is the result of impurities [66]. Wang et al.'s [67] results corroborate the importance of impurities at the grain boundaries. Wang et al. doped NbTaMoW with B and C, up to 0.8 at%, and increased the ductility from 2% to 10%, measured by strain gauge during compression. The higher ductility was due to B and C displacing O at the grain boundaries (determined by APT) and favoring a more cohesive grain boundary (implied by transgranular cleavage in doped specimens as opposed to intergranular failure).

In stark contrast to VNbTaMoW, one of the most significant findings in RHEAs is the tensile ductility of TiZrHfNbTa and its ability to be cold rolled [46]. This ductility allows for more reproducible thermomechanical processing methods that avoid having to maintain a process temperature and oxygen uptake issues that would hinder reproducibility. At room temperature in tension, TiZrHfNbTa has ~1000 MPa yield strength; reported values fall between 905 MPa [68] and 1145 MPa [46]. Tensile ductilities vary from ~13% (measured by extensometer) [69] to 22% (measured by crosshead displacement) [46], though much of the ductility is nonuniform and thus size dependent on the tensile gauge geometry. The tensile deformation of TiZrHfNbTa, **Figure 1.9**, occurs in three stages [69]: (i) uniform low work hardening ending at ~1% strain, (ii) a gradual decrease in flow stress up to ~10% strain, and (iii) rapid decrease in flow stress and failure.

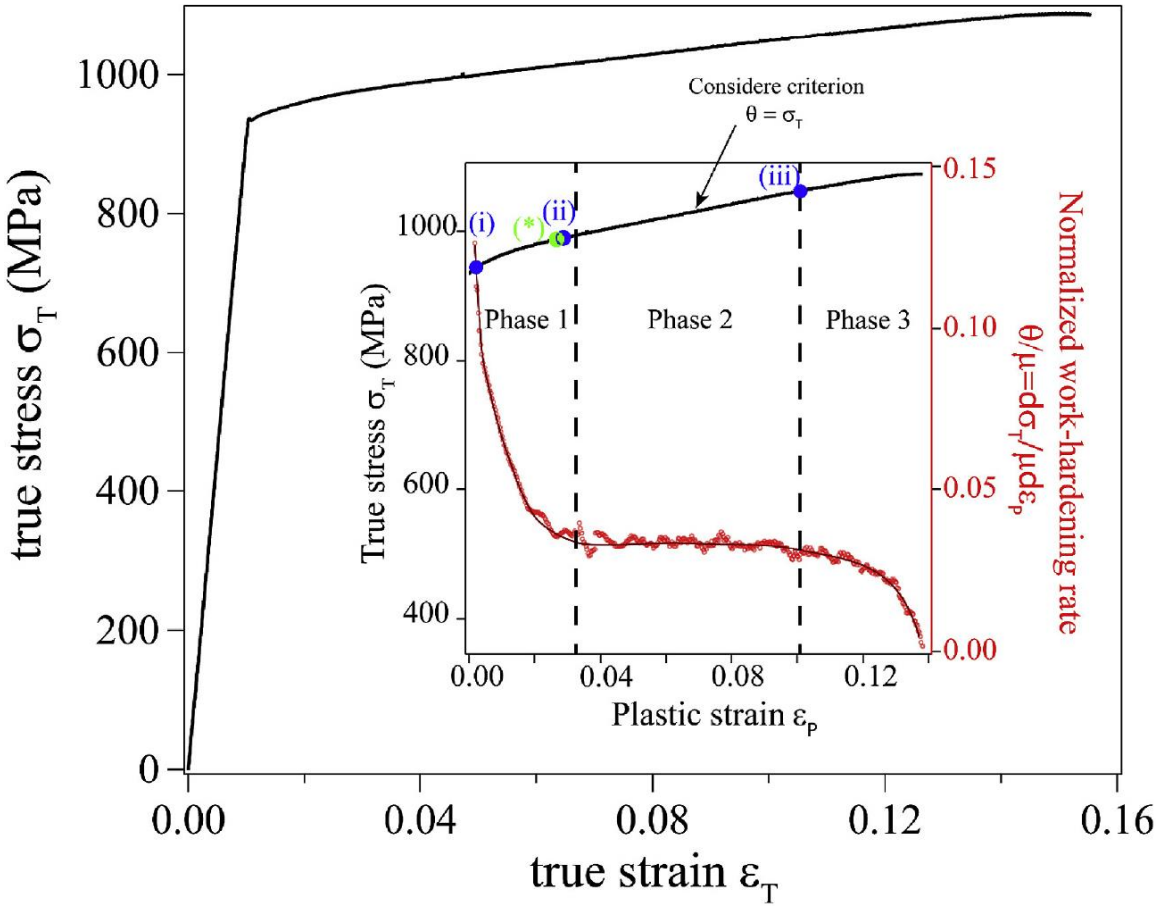

Figure 1.9: True stress-strain behavior of TiZrHfNbTa [69]. Note that despite the apparent increase in true-stress, the Considère criterion is met relatively early, shown by the intersection of the work-hardening curve and the true stress-strain curve, dotted (i) in the insert. Reproduced from [69] and with permission from Elsevier.

Tensile tests in the cold-rolled condition (>85% thickness reduction) showed strength increase between 57 MPa [46] and 324 MPa [29] compared to the recrystallized condition at the cost of ductility. Additional annealing below 1000 ˚C results in the formation of HCP and BCC phases which embrittles the alloy at room temperature [29, 46, 70]. Grain boundaries do not contribute much to room temperature strengthening, as measured by low Hall-Petch constants of 240 MPa $\mu m^{0.5}$ [71] and 270 MPa $\mu m^{0.5}$ [72].

Similar to other BCC metals, room temperature deformation in TiZrHfNbTa is controlled by the movement of a/2<111> screw dislocations, as evidenced by activation volume measurements from stress relaxation [68, 69], X-ray line profile analysis [73], and transmission electron microscopy [68, 69, 73]. Repeatedly found in the aforementioned studies is that the dislocation structures formed in dense bands with the number and dislocation density of bands increasing with plastic strain. Slip trace analyses in microcantilever specimens with atomic force microscopy [74] and high-resolution direct image correlation with electron backscatter detection (EBSD) on tensile bars [75] both corroborate that a/2<111> dislocations control plasticity but does not necessarily follow Schmid law for {110} and {112} planes macroscopically. Rather, dislocations follow the plane of maximum resolved shear stress and that cross slipping occurs to maintain movement on said plane [75].

Mechanical behavior of other RHEA alloys

Compositional variations of RHEAs are difficult to study since the alloys have high melting temperatures that makes processing to repeatable microstructures difficult.

Furthermore, ductility is not guaranteed, adding uncertainty to processing and testing. Due to the possible lack of ductility, it can be more sensible to approach such studies with compression tests to avoid issues with tensile ductility and at least measure yield strength. However, it is difficult to infer if alloys will have tensile ductility from compression since mechanical instability is only observed in extremely brittle alloys under compression. A first order approach to understanding tension and compression ductilities is that failure under compression with anything less than 30% compression ductility will likely lack tensile ductility [18].

The compositional variation studies take several different approaches. Juan et al. [76] studied Mo additions to TiZrHfNbTa by adding Mo in a systematic way. Senkov et al. used CALPHAD to analyze Al, Cr, Fe, Hf, Mo, Re, Si, Ta, V or W additions to TiZrNb. Subsequently, Senkov et al. added Cr, Re, and Ta to TiZrNb by arc-melting to validate the CALPHAD calculations and evaluate the alloys in compression [77]. Another Senkov et al. study [78] focused on alloying additions to Nb to maintain low density and cost. Of particular note is Coury et al.'s work [79] on solid solution strengthening since it was compositionally wide and revealed some of the finer details of thermal and athermal strengthening in RHEAs with compression testing. They found that the athermal stress in RHEAs corresponded with atomic size mismatch, the alloy shear modulus, and modulus mismatch – which could be inferred from rule of mixtures. However, the thermal component of strength could not be as easily deduced with rule of mixtures and required analysis based on screw dislocations.

Many of the alloys with Cr [80] and Mo [35, 76] are more brittle than their base alloy. Al and Si additions have also been studied since they can stabilize secondary B2 [51] and silicide phases [81] for strengthening and promote oxidation resistance by scale formation, but generally embrittle the alloy [38, 81]. Interestingly, Senkov et al. [54] took the BCC-B2 $Al_{0.5}NbTa_{0.8}Ti_{1.5}V_{0.2}Zr$ and tested their B2 phase and BCC phase in separate compression tests by creating melts of their respective compositions. Both the BCC and B2 phases were found to be reasonably ductile in compression with ductile deformation mechanisms in both. They attributed the behavior to the low yield stress in the BCC phase and low anti-phase boundary energy in the B2. The two-phase alloy, with a continuous B2 phase, was brittle with cracking at the grain boundaries.

There are two recent exceptions to embrittling behavior by Si and Al. Xu et al. [36] formed silicides in $TiVNbTaSi_{0.1}$ that could be made finer through hot rolling. The processed samples had tensile ductility, high room temperature strength, and added oxidation resistance. An et al. [82] demonstrated in HfNbTiV that Al additions can increase ductility. They added 5, 10, and 15 at% Al to the base HfNbTiV, and found that tensile yield strength increased from 1100 MPa to 1390 MPa in the alloy with 10 at% Al while ductility increased simultaneously from ~5% to ~18%, as measured by extensometer. Additions of 15 at% Al embrittled the alloy resulting in only ~1% ductility. An et al. [82] associated this behavior with three levels of chemical heterogeneities: atomic pairs, atomic clusters, and secondary spinodes ~9 nm x 100 nm. The atomic pairs and clusters are the result of Al forming preferred atomic bonds; the

preferred atomic bonds and clustering were observed by TEM. Concurrently, the formation of a spinodal decomposition created longer-range order. Interestingly, while uniform ductility did increase with increasing Al from 0 to 10 at%, the work hardening increment, 26 MPa, in the 10 at% Al alloy is similar to other RHEAs, as measured from the engineering stress strain curve, despite the increased opportunities for dislocation interactions to provide work hardening in the extended strain region.

The more studied derivative alloys are those of TiZrHfNbTa. Much like TiZrHfNbTa, the tensile properties of derivative alloys often have high yield strengths and low work hardening, such as TiZrHfNb [83], its non-equiatomic derivative $Ti_{30}Zr_{30}Hf_{16}Nb_{24}$ [84], $Nb_{45}Ta_{25}Ti_{15}Hf_{15}$ [27], and $Hf_{15}Nb_{40}Ta_{25}Ti_{15}Zr_5$ that can be cold rolled to ~90% of the original thickness in the as-cast state [85]. Compositional studies have focused primarily on the substitution and/or removal of one element: Hf/Ti into NbTa [86], Ta into TiZrHf [87, 88], Zr into $Ti_{(80-x)}Zr_xHf_{10}Nb_{10}$ [89] (x = 20, 30 ,40), and Zr into $Ti_{65-x}Ta_{25}Nb_{10}Zr_x$ (x = 0, 5, 10, 15, 20) [90]. One study by Yuan et al. [91] is notable because of its compositional breadth, focusing on $(TiZrHf)_{1-x}(NbTa)_x$ (x = 0, 0.2, 0.4, 0.5, 0.6, 0.8, 1) with an emphasis on tensile properties and elastic modulus for biomedical purposes, but the lack of microstructural detail makes correlating their results difficult. There are ductile RHEAs containing V, such as VNbTa that have room temperature tensile ductility [92, 93]. V is chemically similar to Nb and Ta, but it has a relatively small atomic radius compared to the other refractory elements, which makes it a potent solid solution strengthener [30].

TiZrHfNbTa derivatives with sufficient HCP content will activate other deformation mechanisms. Twinning is seen in $Ti_{80-x}Zr_xHf_{10}Nb_{10}$ (x= 20, 30, 40) [89], $TiZrHfNb_x$ (x = 0.5, 0.55, 0.6) at 77 K [94], and $Ti_{48.9}Zr_{32.0}Nb_{12.6}Ta_{6.5}$ [95]. Phase transformation induced by deformation includes: hexagonal α by decreasing Nb in HfNbxTa0.2TiZr [96], α' in $TiZrHf(VNbTa)_{0.1}$[97], α'' in $Ti_{35}Zr_{27.5}Hf_{27.5}Nb_5Ta_5$ [98] and in $TiZrHfTa_X$ (x = 0.5, 0.6, 0.8) [87]. These mechanisms increase ductility and work hardening. For example, a decrease of Ta in TaTiZrHf to $Ta_{0.4}$TiZrHf [87], increased ductility from 4% to 27%, decreased yield strength from 1356 MPa to 537 MPa and ultimate stress from 1452 MPa to 1126 MPa, as shown in **Figure 1.10**,. Twinning and phase transformations during deformation have been rationalized using the Bo-Md approach in Ti alloys [99], and TiZrHfNbTa can be thought of in a similar vein [87, 98].

In addition to the direct TiZrHfNbTa derivatives, additional derivative alloys include those containing interstitials elements like O. In TiZrHfNb, the purposeful addition of O (~2 at%) increased yield strength and ductility, at room temperature, from 750 MPa and 14.2% in TiZrHfNb to 1100 MPa and 27.7% with added oxygen [100]. The increase in strength and ductility was determined to be from ordered oxygen complexes providing additional dislocation sources and changing the slip character from planar to wavy. Similar results have been found in TiZrNb [101], where again O additions (up to 2.25% as measured by a LECO TCH600) increased strength and ductility at room temperature.

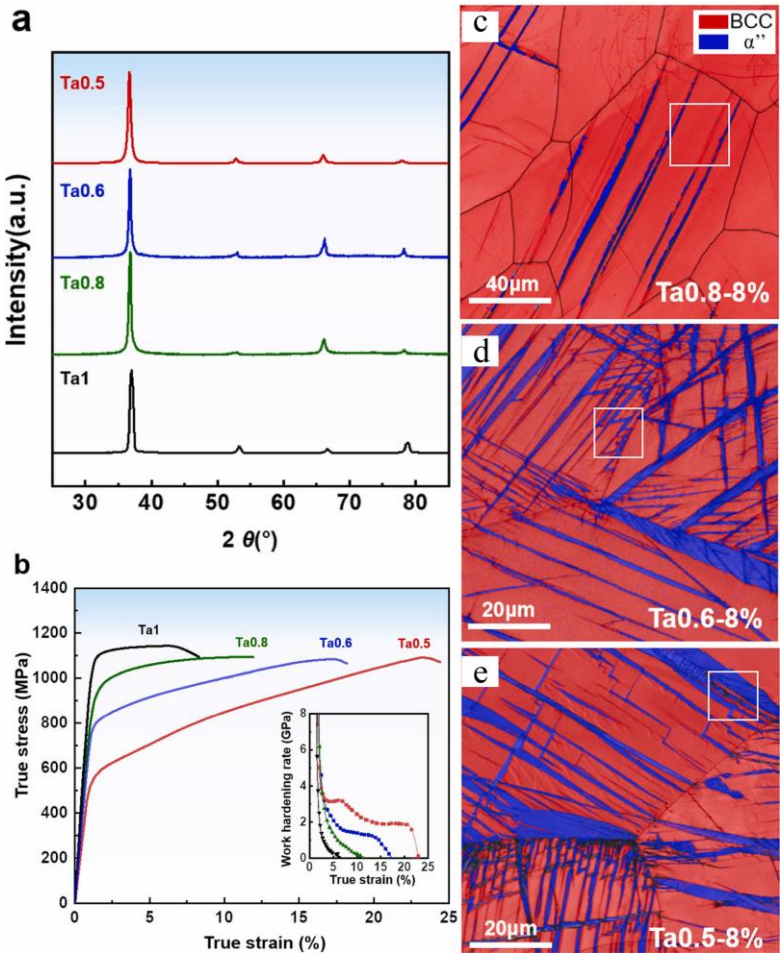

Figure 1.10: Analysis of microstructure after deformation in TiZrHfNbTa (Ta1), $TiZrHfNbTa_{0.8}$ (Ta0.8), $TiZrHfNbTa_{0.6}$ (Ta0.6), and $TiZrHfNbTa_{0.5}$ (Ta0.5) [87]. The initial microstructure begins as single-phase BCC denoted by the XRD patterns in (a). Decreasing Ta content increases work-hardening in the true tensile stress-strain curves accompanied by lowering of the yield strength (b). EBSD analyses in $TiZrHfNbTa_{0.8}$ (c), $TiZrHfNbTa_{0.6}$ (d), and $TiZrHfNbTa_{0.8}$ (e) after 8% tensile deformation show an increase in α'' martensite with decreasing Ta content. (a-e) Reproduced from [87] and with permission from Elsevier.

However, the garnered ductility from oxygen at room temperature was lost at -196 ˚C, as seen by brittle fracture in tension, whereas the base TiZrNb alloy was still ductile in tension. At high temperatures, O additions to TiZrNb increased the compressive yield strength between 600 ˚C and 1000 ˚C until being more or less the same at 1200 ˚C. Both of these studies [100, 101] added O in the form of TiO_2 during arc-melting, which is the second most stable single metal oxide of TiZrHfNbTa above 2000 ˚C, with HfO_2 being the most stable [102].

Theoretical efforts to explain the strengthening in RHEAs with dislocation theory have been successful. Fundamentally different to dilute BCC metals, where they are controlled by screw dislocations [103], RHEAs can sometimes be edge dislocation controlled [104, 105] because alloys with large normalized volume misfits are expected to be controlled by edge dislocations [106]. Analytical theories have been developed for screw [107, 108] and edge dislocations [109, 110], both of which follow the trends of experimental yield strength data reasonably well, including recent analysis of high-temperature compression tests in TiZrHfNb [105]. The analytical theories require elastic constants, which are rarely reported in RHEAs. The few exceptions include $Al_{10}Nb_{20}Ta_{15}Ti_{30}V_5Zr_{20}$ [55], TiZrHfNbTa [111], TiZrHfNb [112], and NbTaTiV [113]. Use of rule of mixtures moduli is questionable since group IV elements go through a HCP to BCC transformation at high temperature [114], thus their room temperature elastic moduli are likely erroneous since it would require applying the HCP elastic constants to a BCC structure. In a more recent and fundamental look at RHEAs [115],

TiZrHfNbTa and VNbMoTaW were compared to understand the intrinsic factors affecting ductility. Where VNbMoTaW only has BCC elements its dislocation core energy remains relatively high and its dislocation structure compact, while the HCP elements in TiZrHfNbTa spread out the dislocation core thus making it easier to move and in principle more ductile.

Summary and objectives

While much effort has gone into studying RHEAs, there is still fundamental data that are missing. The most obvious, and difficult, are high-temperature mechanical properties. A limited number of uniaxial quasi-static tests have been performed above 1300 ˚C but no creep tests. Other important missing data include the thermal stability at intermediate temperatures. Whether the microstructure is stable at temperatures such as 700 ˚C is relevant for application such as jet turbines [116] and needs to be understood. Even for the room-temperature mechanical tests, there are still relatively few tests on compositional variations and fracture toughness.

In this work, all these missing data cannot be filled. Focus is placed on obtaining room-temperature mechanical behavior since it can provide insight into compositional variation and success with cold rolling generally lends itself to success in tensile testing. Fracture toughness is a relatively riskier endeavor due to sample size requirements but provides insight into the real-world use of the alloys. Finally, thermal stability can provide basic data that inform alloy design in the future and can be obtained in tandem with other tests.

Chapter 2 Effects of HCP/BCC element ratios on the room-temperature tensile properties of Ti-Zr-Hf-Nb-Ta refractory high-entropy alloys

A version of this chapter has been submitted to *Acta Materlia* and is currently in revision. WJ Carpenter performed all the sample preparation, testing, characterization, analysis, and writing of the first draft. Kevin Hason was the technician that arc-melted. Ying Yang performed CALPHAD calculation. WA Curtin provided code for formal analys. BP Gludovatz edited the drafts. EP George conceived and supervised the study and edited the drafts.

Abstract

Equiatomic and non-equiatomic Ti-Zr-Hf-Nb-Ta refractory high-entropy alloys (RHEAs) were arc melted, homogenized, cold rolled, and recrystallized to produce single-phase, body-centered cubic (BCC), microstructures with weak texture and equiaxed grains 76-199 μm in size. The non-equiatomic alloys had either a 60:40 or 80:20 atomic ratio of hexagonal close-packed (HCP) elements (Ti+Zr+Hf) to BCC elements (Nb+Ta). Alloy compositions were measured after thermomechanical processing to determine the concentrations of the major (substitutional) and minor (interstitial) elements. We investigated how elastic constants and uniaxial tensile properties were affected by changes in the relative concentrations of the constituent elements at fixed HCP:BCC ratios. Yield strengths ranged from 801 to 922 MPa and ultimate tensile strengths from 815 to 933 MPa. Good agreement is obtained between the experimental yield strengths and those predicted by a strength theory based on edge dislocations indicating that the observed compositional effects are due to their effects on shear modulus and volume misfit. Fracture occurred by dimpled rupture with fracture

strains of 19.4% to 25.7%, but uniform strains were an order of magnitude lower at 1.1% to 3.2%, calling into question the usable ductility (prior to necking) of RHEAs considered to be ductile based on their fracture strain.

Introduction

RHEAs have garnered attention as possible new high temperature-materials [10, 12]. They predominately have the BCC crystal structure, limited room-temperature tensile ductility and work hardening, and often contain secondary phases from spinodal decomposition or precipitation [10, 12, 117]. The first reported exception to the above was the equiatomic RHEA TiZrHfNbTa, which Senkov and Semiatin [46] showed could be extensively cold rolled and then recrystallized to yield a single-phase BCC microstructure with a respectable strain to fracture at room temperature of ~8%. We refer to this equiatomic alloy henceforth as the ductile Senkov alloy. Certain derivatives of this Senkov alloy have also been shown to exhibit room-temperature tensile ductility [29, 46, 83, 96, 118, 119].

While the single-phase Senkov alloy exhibits ductility at room temperature, it is extremely weak in creep at temperatures to ~1100 ˚C when compared to advanced Ni-base superalloys [24]. Given that a main target of RHEAs is high-temperature structural applications, there is much ongoing research aimed at developing RHEAs containing suitable intermetallic precipitates that can potentially improve high-temperature strength [54, 59, 62]. However, there are no reports yet on the performance of such microstructures under tensile creep conditions nor their ductilities at room temperature.

Therefore, it remains of interest to improve understanding of the room-temperature tensile behavior of single-phase RHEAs as the addition of high volume-fractions of strengthening precipitates is likely to induce embrittlement.

The ductile Senkov alloy has a single-phase BCC microstructure after ~80% thickness reduction by cold rolling followed by annealing above 1000 ˚C [29, 46]. Annealing between 600 and 980 ˚C results in the formation of additional BCC [24, 29, 46] and HCP phases [23, 70, 120] that are detrimental to overall tensile ductility [23, 29]. In the single-phase state, different groups have reported room-temperature yield strengths of ~1 GPa with fracture strains of 10 - 20% [23, 46, 121]. A caveat is that, except in [121] where an extensometer was used, ductilities were determined from crosshead displacement and not directly from the gage sections and are, therefore, probably overestimates. Plastic deformation appears to be controlled by the movement of <111> {110} screw dislocations that undergo heavy cross slip [68, 69, 73]. Additionally, kink bands are seen during plastic deformation implying plastic anisotropy in the Senkov alloy and its derivatives [121-123].

Binary through quaternary Senkov-alloy derivatives have been chemically modified by the addition of Ti/Hf to NbTa [86], Zr to Ti-Zr-Nb [124], Ta to TiZrHf [88], Zr to non-equiatomic Ti-Zr-Hf-Nb [89], and Zr to $Ti_{65-x}Zr_xNb_{10}Ta_{15}$ [90]. Effects of similar modifications have not yet been studied in the quinary Senkov alloy and, therefore, knowledge of composition-property relationships is lacking. From what is known about the lower-order derivatives, it is difficult to infer how the quinary

derivatives might behave because the microstructures of the lower-order alloys are inconsistent, and their compositions are far from that of the ductile Senkov alloy. In a limited number of studies, effects of additional elements (beyond five) [35, 80, 97], or just one modified Senkov alloy [125, 126], have been investigated. The comparison between alloys becomes more difficult when deformation-induced phase transformations occur in compositions with high Ti, Zr, and Hf content [88, 96]. Yuan *et al.* [91] investigated $Ta_xHfZrTi$, $Nb_xHfZrTi$, and $Ta_xNb_xHfZrTi$ (where x varied from 0 to 1) but that study focused on elastic moduli and tensile properties in the as-cast condition and gave little information on its microstructure.

In this study, systematic compositional modifications were made to the ductile Senkov alloy while maintaining a single-phase BCC structure and comparable grain sizes. To provide a simple basis for the compositional modifications, the constituent elements of the ductile Senkov alloy were first separated into two categories based on their room-temperature crystal structure: HCP (Ti, Zr, and Hf) or BCC (Ta and Nb). Then the ratio of the sum of HCP to sum of BCC elements was varied. There is evidence to suggest that increasing the concentration of HCP elements favors the formation of HCP phases during deformation [96, 97, 127]; it also decreases the valence electron concentration, which has been postulated to promote intrinsic ductility in BCC alloys [128]. Recently, a combined experimental and theoretical study [115] of two model RHEAs, VNbTaMoW, whose constituents are all BCC (the brittle Senkov alloy [9, 19]) and TiZrHfNbTa (the ductile Senkov alloy), concluded that the latter's ductility is due to

its HCP elements which, among other things, extend the dislocation core and lower its energy, increase lattice distortion, and lower its shear modulus.

In light of the above, we set out to investigate how changes in the concentrations of individual elements affect mechanical properties at fixed HCP:BCC ratios. The investigated alloys are listed in **Table 2.1**. Below the composition of each alloy, the relative amounts (in at%) of HCP to BCC elements rounded to the nearest percent (60:40 or 80:20) are provided. Within a given ratio, our compositional modifications focused on altering the relative amounts of Nb and Ti to obtain alloys that were malleable (processable by rolling at room temperature).

Methods

CALPHAD calculations

Computer coupling of phase diagrams and thermo-chemistry, i.e., the CALPHAD approach [129], was used to develop thermodynamic models of phases in the Ti-Zr-Hf-Nb-Ta system. Specifically, the Gibbs energies of individual phases in this quinary system were modeled in a stepwise manner from thermodynamic models of its constituent unary, binary, and ternary systems. The Gibbs energy functions of phases for the pure elements Ti, Zr, Hf, Nb, Ta and their constituent binaries were adopted from the SGTE (Scientific Group Thermodata Europe) database compiled by Dinsdale [130]. The Gibbs energy functions of phases in the constituent ternary systems were optimized in previous works [24, 131] based on experimental data [29, 47]. The relevant calculations

were performed in Pandat [132]. The relevant calculations were performed in Pandat [132] using our database "TiZrHfNbTa.tdb".

Alloy fabrication and heat treatment

Alloys were fabricated by arc melting the constituent elements (>99.9% purity) in Ti-gettered Ar atmosphere. For each alloy investigated in this study, two master alloys were first prepared, one consisting of Ta and Zr and the other comprising Hf, Nb, and Ti. The Ta-Zr master alloys were melted and flipped four times while the Hf-Nb-Ti master alloys were melted and flipped three times. Subsequently, the master alloys were melted together to create the final alloy buttons. Each of these buttons was remelted and flipped five times to promote thorough mixing after which they were drop-cast into a 25.4 mm × 25.4 mm × 25.4 mm copper mold. The castings were cut in half parallel to the solidification direction using electrical discharge machining (EDM). The cut surfaces were ground to get rid of EDM burn and any exposed shrinkage porosity in the center of the castings. The outer surfaces that were in contact with the copper mold were wire brushed to eliminate any Cu contamination. The alloys were then cleaned with nitric acid followed by sonication in ethanol before being homogenized at 1200 ˚C for 24 h (except the $Ti_{20}Zr_{20}Hf_{20}Nb_{20}Ta_{20}$ alloy, which was annealed for 48 h). Homogenization was carried out either in quartz capsules that were evacuated and backfilled with 0.5 atm of Ar and placed in an air furnace, or without encapsulation in a vacuum furnace (chamber pressure on the order of 10^{-6} torr). After homogenization, the samples were rolled at room temperature to a final thickness of ~2 mm using 5% reduction per pass for the first 10

passes followed by 10% reduction per pass thereafter, resulting in a total thickness reduction of 79-81%. The exception was the equiatomic $Ti_{20}Zr_{20}Hf_{20}Nb_{20}Ta_{20}$ alloy because it contained more shrinkage porosity that had to be ground away before rolling and thus ended up with a smaller final thickness of 1.5 mm. Sections of the cold rolled sheets were cleaned with nitric acid and sonicated in ethanol to remove contamination. They were then sealed in evacuated quartz capsules backfilled with 0.5 atm Ar and annealed at the temperatures and times shown in **Table 2.1** followed by removal from the furnace and cooling to room temperature within the capsules. Annealing times and temperatures were chosen based on trial recrystallization runs that aimed to produce a single-phase microstructure with a grain size of ~100 μm. Target compositions of the investigated alloys and their processing parameters are provided in **Table 2.1** along with their HCP:BCC ratios (60:40 or 80:20), which will be used to refer to groups of alloys in this study.

Microstructure analysis

Alloy microstructures were analyzed with back scattered electron (BSE) scanning electron microscopy (SEM), energy-dispersive X-ray spectroscopy (EDS), and electron backscattered diffraction (EBSD) in a Zeiss AURIGA operated at 20 kV. Samples for these analyses were ground to 1200 grit and polished with colloidal silica (0.05 μm). Grain sizes were measured with the linear intercept method [133] on at least 5 fields-of-view at a magnification of 200× for each direction and 1500 intercepts total for each specimen.

Table 2.1: Target compositions and processing conditions of the studied alloys.

Alloy composition (at%) (Ti+Zr+Hf:Nb+Ta)	Homogenization temperature and time	Cold rolling reduction in thickness (%)	Recrystallization temperature and time
$Ti_{20}Zr_{20}Hf_{20}Nb_{20}Ta_{20}$ (60:40)	1200 ˚C, 48 h *	79	1100 ˚C, 1.00 h
$Ti_{20}Zr_{20}Hf_{20}Nb_{35}Ta_{5}$ (60:40)	1200 ˚C, 24 h #	81	1055 ˚C, 0.83 h
$Ti_{5}Zr_{20}Hf_{35}Nb_{20}Ta_{20}$ (60:40)	1200 ˚C, 24 h #	81	1200 ˚C, 0.50 h
$Ti_{26.7}Zr_{26.7}Hf_{26.7}Nb_{10}Ta_{10}$ (80:20)	1200 ˚C, 24 h #	79	1100 ˚C, 0.25 h
$Ti_{40}Zr_{20}Hf_{20}Nb_{10}Ta_{10}$ (80:20)	1200 ˚C, 24 h #	80	1000 ˚C, 0.25 h

* Homogenization in vacuum furnace followed by cooling in vacuum.
# Homogenization in quartz ampule followed by water quenching.

EDS and EBSD were performed with an Oxford X-Max silicon drift EDS detector and an Oxford EBSD NordlysF detector. EBSD data were analyzed using the OIM software from EDAX. For phase analyses, X-ray diffraction (XRD) with Cu Kα (0.154 nm) was performed with a Panalytical Empyrean diffractometer. XRD patterns were collected using a step size of 0.026° and at 55 s / ° from samples in two states: after recrystallization (before tensile testing), and after tensile testing.

Ultrasonic measurement of elastic moduli

Longitudinal and transverse ultrasonic waves were propagated through samples of known thickness and, by measuring their times of flight (in reflection mode), wave velocities were determined. The transducers used for time-of-flight measurements were calibrated with a known stainless-steel standard. An Archimedes method with degassed, deionized water was then used to measure the density of each alloy. From the measured velocities and densities, polycrystalline elastic constants were calculated using equations (1-3) below [134], assuming the specimens were random polycrystals based on their weak texture (shown later).

$$\nu = \frac{1 - 2\left(\frac{V_T}{V_L}\right)^2}{2 - 2\left(\frac{V_T}{V_L}\right)^2} \quad (1)$$

$$E = \frac{V_L^2 \rho(1+\nu)(1-2\nu)}{1-\nu} \quad (2)$$

$$G = V_T^2 \rho \quad (3)$$

where v is Poisson's ratio, E is Young's modulus, G is shear modulus, V_L is longitudinal wave velocity, V_T is transverse wave velocity, and ρ is density.

Tensile testing

Tensile specimens were cut with EDM from the recrystallized plates with the loading axis aligned along the rolling direction. Starting from an oversized gage width, the specimens were ground to remove any EDM damage, to final gage dimensions of 7.62 mm × 1.5 mm × 2 mm, except for $Ti_{20}Zr_{20}Hf_{20}Nb_{20}Ta_{20}$ whose final dimensions were 7.62 mm × 1.5 mm × 1.5 mm since it was thinner after rolling (as mentioned above). Tensile testing was performed with an Instron 5600 at a crosshead speed of 0.00762 mm s^{-1}, which corresponds to an engineering strain rate of 1×10^{-3} s^{-1}. Digital image correlation (DIC) was used to determine the tensile strain in the gage section using a sprayed-on speckle pattern on the specimen surface. Four specimens from all alloys were tested for reproducibility, except for $Ti_{40}Zr_{20}Hf_{20}Nb_{10}Ta_{10}$ where only three specimens were tested because one specimen was lost due to a machining error. After testing, fracture surfaces were observed with secondary electron SEM at 5 kV.

Results

Measured chemical compositions

Chemical compositions of the recrystallized alloys were measured by inductively coupled plasma optical emission spectroscopy (ICP-OES) for the major (metallic) elements and gas fusion analysis for the minor (interstitial) elements. The measured values in wt% are provided in **Table 2.2** from which the concentrations in at% shown in

Supplementary Table 2.1 were calculated. The atomic concentrations of the major elements are close to the target concentrations (**Table 2.1**), with Zr and Hf in general being slightly lower than the target values and Ti, Nb and Ta correspondingly higher. The deviations from the intended compositions correspond, roughly, to the tendency for oxide formation, namely Hf > Zr > Ti > Nb > Ta, with the notable exception that Ti has a greater oxidation tendency than Zr above ~2000 ˚C [102]. This would suggest that the reduced Zr and Hf contents are the result of oxide formation and removal from solid solution. For purposes of this paper, we assume that the measured concentrations of the major elements are close enough to the target concentrations and, therefore, use the latter in all further discussions. As for the interstitial elements, their contents here are similar to those reported in the isolated RHEA studies where interstitial contents have been measured [23, 121], with the exception of $Ti_{40}Zr_{20}Hf_{20}Nb_{10}Ta_{10}$ which has a relatively high oxygen content (0.14 wt%). The latter is of similar magnitude as those reported in a recent study of BCC Mo-Ti alloys [135] as well as in commercially pure titanium ASTM grade 4 [136] where up to 0.4 wt% O is allowed.

CALPHAD calculations

The calculated stable phases,

Figure 2.1, show similar thermodynamically predicted phases for all alloys: a high temperature BCC phase followed mostly by secondary BCC and HCP phases at lower temperatures.

Table 2.2: Analyzed compositions (wt%) of the investigated alloys measured by ICP-OES (major metallic elements) and gas fusion (minor nonmetallic interstitials).

Alloy	Ti	Zr	Hf	Nb	Ta	O	N	C
$Ti_{20}Zr_{20}Hf_{20}Nb_{20}Ta_{20}$	8.2	14.6	27.6	17.9	31.7	0.027	0.009	<0.005
$Ti_{20}Zr_{20}Hf_{20}Nb_{35}Ta_{5}$	9.1	16.5	31.6	31.2	11.5	0.043	0.022	0.009
$Ti_{5}Zr_{20}Hf_{35}Nb_{20}Ta_{20}$	1.8	12.9	42.6	14.9	27.6	0.031	0.014	0.010
$Ti_{26.67}Zr_{26.67}Hf_{26.7}Nb_{10}Ta_{10}$	11.4	20.6	39.2	10.4	18.8	0.061	0.011	0.005
$Ti_{40}Zr_{20}Hf_{20}Nb_{10}Ta_{10}$	18.6	17.4	31.7	11.1	21.1	0.14	0.011	0.008

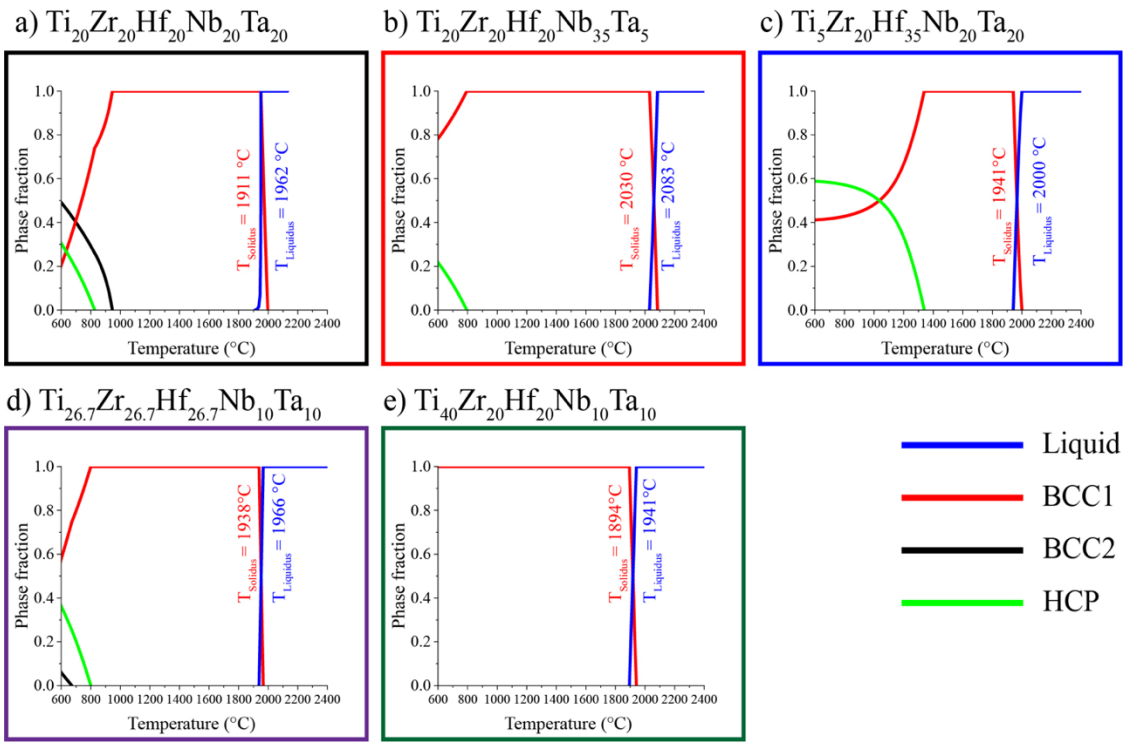

Figure 2.1: CALPHAD predictions of phases in the investigated alloys as a function of temperature. In each case, the liquidus/solidus temperatures are shown along with the thermodynamically favored phases at lower temperatures.

All alloys have similar solidus and liquidus temperatures that lie between 1894 ˚C and 2083 ˚C. The HCP phase is stable up to 800 ˚C except in $Ti_5Zr_{20}Hf_{35}Nb_{20}Ta_{20}$ where it is stable to 1325 ˚C. In the $Ti_{40}Zr_{20}Hf_{20}Nb_{10}Ta_{10}$ alloy, BCC is the only phase predicted to be thermodynamically stable in the solid state at any of the investigated temperatures.

Recrystallized microstructures

Figure 2.2 shows the microstructures after recrystallization. All alloys exhibit an equiaxed grain structure in the rolling direction (RD), transverse direction (TD), and normal direction (ND). XRD patterns, **Figure 2.3**, can be indexed as a single BCC phase. Lattice parameters calculated using the Nelson-Riley method [137, 138] and Rietveld refinement [139] (with the HighScore® software package) range from 0.340 nm to 0.344 nm. Based on EBSD analysis, it is concluded that the alloys are weakly textured, maximum of 2.9 above random in $Ti_{40}Zr_{20}Hf_{20}Nb_{10}Ta_{10}$, as shown in the EBSD inverse pole figure maps and unit triangles in **Figure 2.4**. Therefore, we assume our alloys are random polycrystals after recrystallization. Grain sizes were measured to be between 76 and 199 μm. All directions (ND, TD, and RD in **Figure 2.2**) had similar grain sizes, consistent with the visual appearance of an equiaxed grain structure in **Figure 2.2**. EDS performed on the RD plane shows the microstructures are chemically homogeneous, **Figure 2.5**.

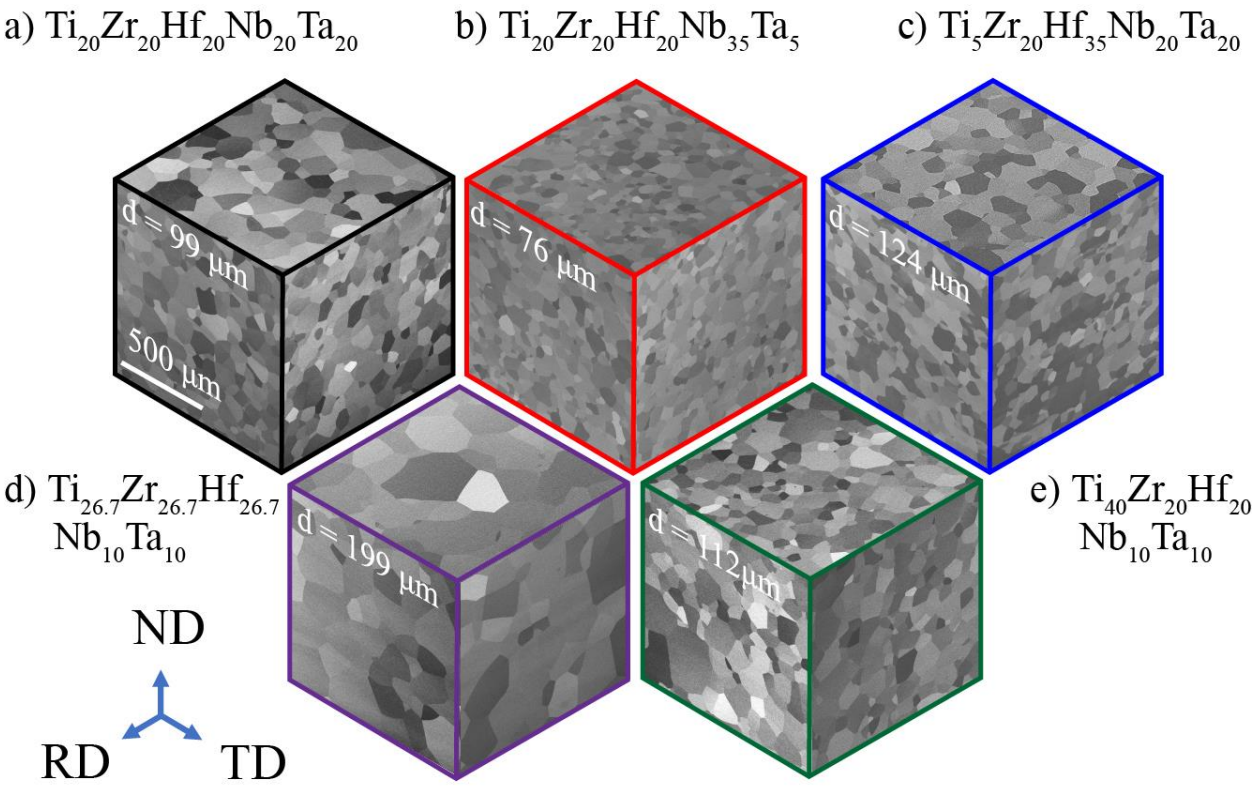

Figure 2.2: Microstructures of the investigated alloys after recrystallization showing equiaxed grains with no secondary phases. The orientations of the imaged planes are shown at the lower left where ND, RD, and TD stand for normal, rolling, and transverse directions, respectively.

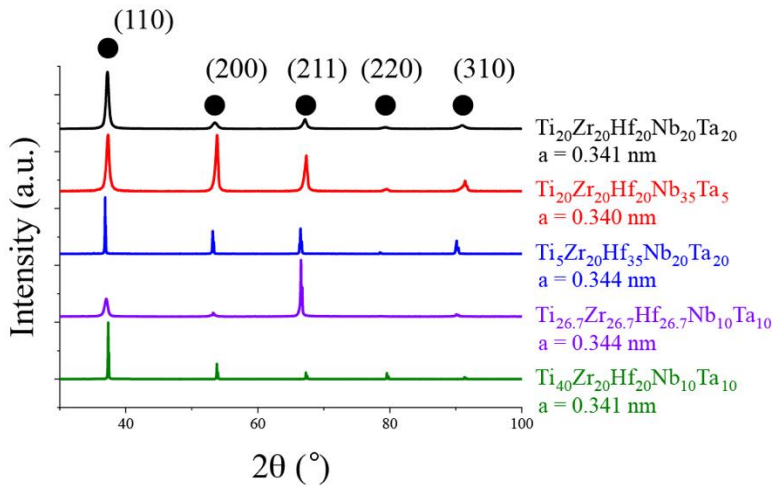

Figure 2.3: XRD patterns for each alloy after recrystallization in which all peaks can be indexed as belonging to a single BCC phase.

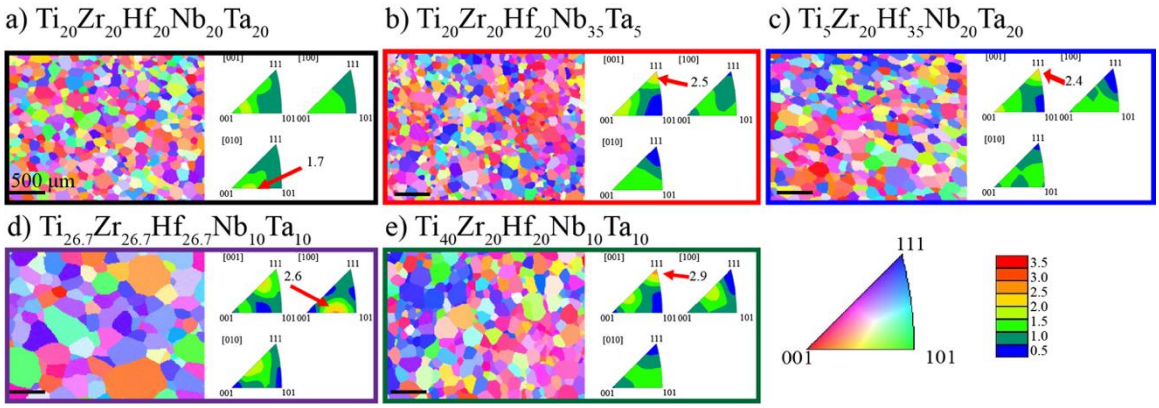

Figure 2.4: EBSD IPF maps on the normal plane of the recrystallized alloys; rolling direction (RD) is horizontal and points to the right. IPFs were determined with 5° Gaussian half width and 16 order harmonic series.

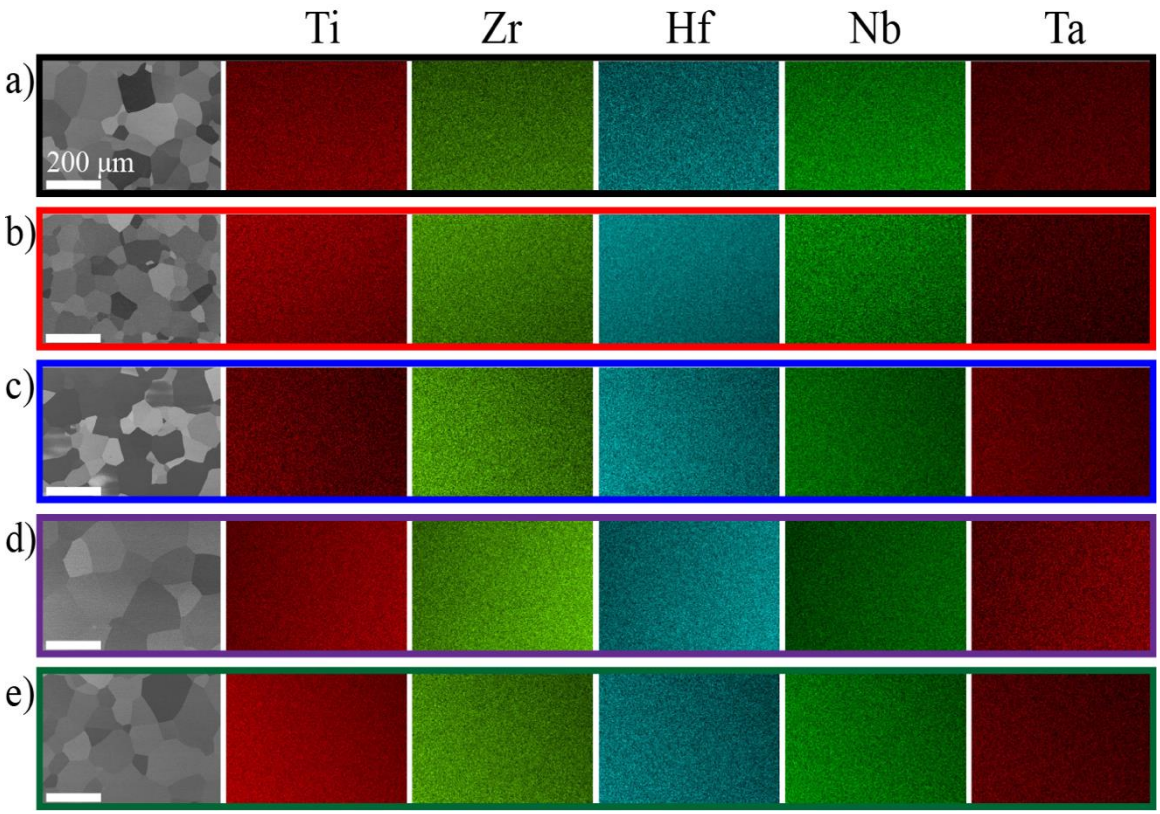

Figure 2.5: BSE images of (a) $Ti_{20}Zr_{20}Hf_{20}Nb_{20}Ta_{20}$, (b) $Ti_{20}Zr_{20}Hf_{20}Nb_{35}Ta_{5}$, (c) $Ti_{5}Zr_{20}Hf_{35}Nb_{20}Ta_{20}$, (d) $Ti_{26.7}Zr_{26.7}Hf_{26.7}Nb_{10}Ta_{10}$, and (e) $Ti_{40}Zr_{20}Hf_{20}Nb_{10}Ta_{10}$, of the recrystallized alloys on a plane normal to the rolling direction with the transverse direction (TD) horizontal. Elemental EDS maps for each alloy are shown to the right of their BSE images.

Elastic moduli

Measured densities and longitudinal and transverse wave velocities are listed in **Table 2.3**. From these values, Young's (E) and shear (G) moduli were calculated using equations 1-3. Young's moduli range from 81.9 GPa to 100 GPa, and shear moduli from 29.6 GPa to 36.7 GPa with $Ti_5Zr_{20}Hf_{35}Nb_{20}Ta_{20}$ having the highest moduli and $Ti_{26.7}Zr_{26.7}Hf_{26.7}Nb_{10}Ta_{10}$ the lowest. The largest contributor to error in the elastic modulus is the accuracy of wave velocity measurement. After multiple measurements on the same sample, we found that the last reported digit in the ultrasonic measurement is the uncertain digit, which yields an upper limit of error of ± 0.6% (i.e., 10/1800) in the velocity measurements. An additional error comes from the density measurements. Since the densities of the investigated alloys were not known, oxygen-free copper was measured beforehand and its density erred by ±0.5% relative to literature values. The reported standard deviations of the moduli in **Table 2.3** reflect the above two errors. It is assumed that the measured elastic moduli in this study are isotropic since EBSD showed weak texture.

Our measured G for $Ti_{20}Zr_{20}Hf_{20}Nb_{20}Ta_{20}$ (34.9 GPa) is similar to, but slightly lower than, a previous G measured by beam and plate resonance techniques (35.8 GPa) [111]; while our E (95.4 GPa) is ~6% larger compared to the same study (90 GPa). Additionally, E of $Ti_{26.67}Zr_{26.67}Hf_{26.7}Nb_{10}Ta_{10}$ (81.9 GPa) is comparable to its value determined by a tensile fitting technique (85 GPa) [91]. The remaining alloys do not have modulus values in the literature for comparison.

Table 2.3: Density (measured), longitudinal and transverse wave velocities (measured) and isotropic elastic constants (calculated). For details see text.

Alloy	**Density (g/cm^3)**	**Longitudinal wave velocity (m/s)**	**Transverse wave velocity (m/s)**	**Young's modulus (GPa)**	**Shear modulus (GPa)**
$Ti_{20}Zr_{20}Hf_{20}Nb_{20}Ta_{20}$	9.99 ± 0.05	4061	1870	95.4 ± 0.9	34.9 ± 0.5
$Ti_{20}Zr_{20}Hf_{20}Nb_{35}Ta_{5}$	8.90 ± 0.04	4288	2008	97.6 ± 0.9	35.9 ± 0.4
$Ti_{5}Zr_{20}Hf_{35}Nb_{20}Ta_{20}$	11.27 ± 0.06	3875	1806	100.0 ± 1.0	36.7 ± 0.5
$Ti_{26.67}Zr_{26.67}Hf_{26.7}Nb_{10}Ta_{10}$	9.13 ± 0.05	4160	1800	81.9 ± 0.8	29.6 ± 0.4
$Ti_{40}Zr_{20}Hf_{20}Nb_{10}Ta_{10}$	8.90 ± 0.04	4259	1895	88.0 ± 0.9	31.9 ± 0.4

Tensile results

Representative tensile stress-strain curves of $Ti_{20}Zr_{20}Hf_{20}Nb_{20}Ta_{20}$ and $Ti_{26.7}Zr_{26.7}Hf_{26.7}Nb_{10}Ta_{10}$ are presented in **Figure 2.6**. Curves for the remaining alloys are shown in **Supplementary Figure 2.1**. The average strengths and strains of the alloys along with their standard deviations are shown in **Table 2.4**. All the engineering stress-strain curves show negligible work hardening between the yield and ultimate tensile stress. Yield strengths range from 801 MPa to 922 MPa with the $Ti_{20}Zr_{20}Hf_{20}Nb_{35}Ta_5$ and $Ti_{20}Zr_{20}Hf_{20}Nb_{20}Ta_{20}$ alloys having the lowest and highest yield strengths respectively. Ultimate strengths follow the same trends, with minimum and maximum values of 815 MPa and 933 MPa for $Ti_{20}Zr_{20}Hf_{20}Nb_{35}Ta_5$ and $Ti_{20}Zr_{20}Hf_{20}Nb_{20}Ta_{20}$ respectively. The flow stress increment (from yield to ultimate) ranges from 5 MPa to 14 MPa with the lowest in $Ti_{40}Zr_{20}Hf_{20}Nb_{10}Ta_{10}$ and the highest in $Ti_{20}Zr_{20}Hf_{20}Nb_{35}Ta_5$. As shown in **Figure 2.6b**, with additional examples in **Supplementary Figure 2.1**, the 80:20 alloys are distinguished by a noticeable stress-drop after the ultimate stress (which occurs shortly after yielding). In contrast, the 60:40 alloys show a more gradual decrease in stress. Consequently, the 80:20 alloys have lower uniform strains (1.2% – 1.5%) than the 60:40 alloys (2.3% – 3.2%). Uniform strain is defined here as the strain corresponding to the Considère criterion for the onset of necking, **Figure 2.6c-d**. All the alloys have similar fracture strains with the 80:20 alloys having somewhat lower fracture strains (19.4% - 23.1%) than the 60:40 alloys (23.0% – 25.7%).

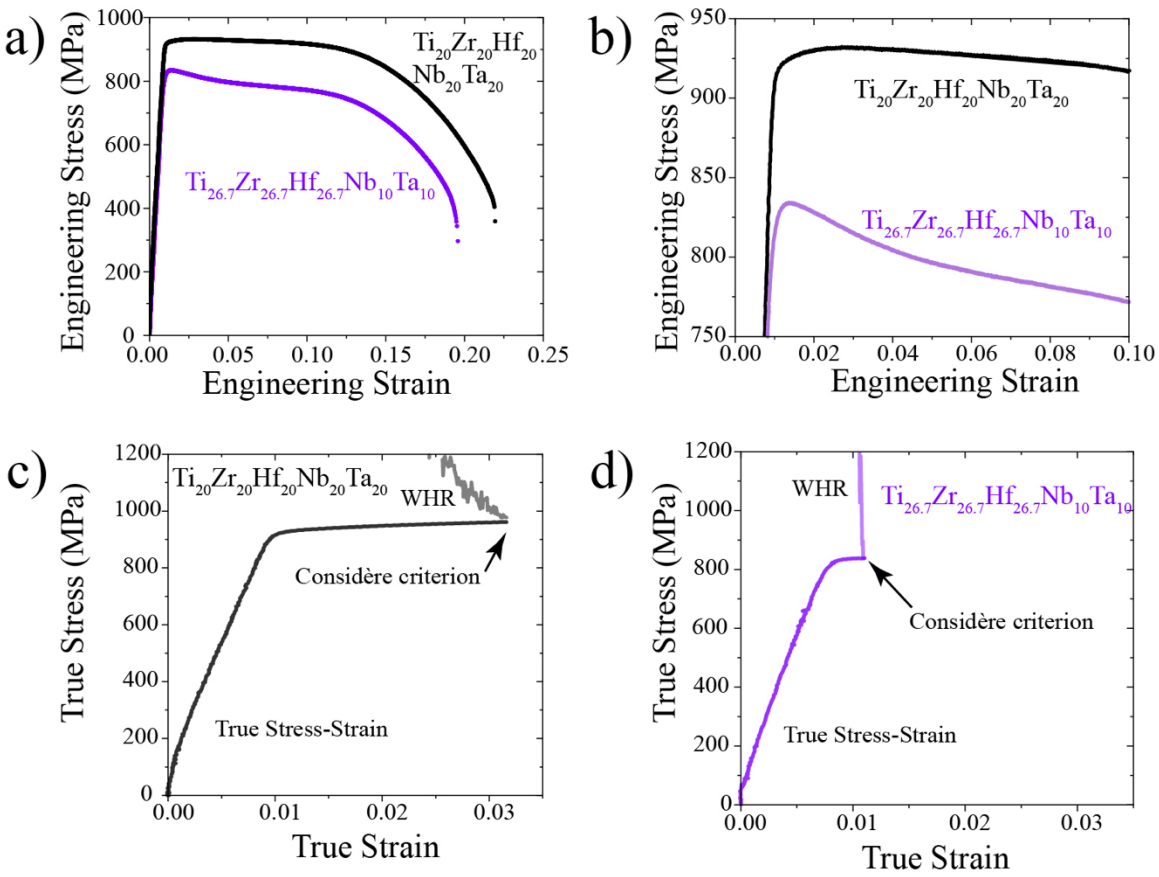

Figure 2.6: (a) Example of tensile engineering stress-strain curves for $Ti_{20}Zr_{20}Hf_{20}Nb_{20}Ta_{20}$ and $Ti_{26.7}Zr_{26.7}Hf_{26.7}Nb_{10}Ta_{10}$; curves for the remaining alloys are shown in **Supplementary Figure 2.1**. (b) Magnified views of the plots in (a) near the region of yielding. True stress-strain curves and work-hardening curves for $Ti_{20}Zr_{20}Hf_{20}Nb_{20}Ta_{20}$ (c) and $Ti_{26.7}Zr_{26.7}Hf_{26.7}Nb_{10}Ta_{10}$ (d). The point where necking occurs (Considère criterion) is marked by arrows in (c) and (d).

Table 2.4: Tensile properties of the investigated alloys: yield strength (σ_y), ultimate tensile strength (σ_{UTS}), strain at the ultimate tensile stress (ε_{UTS}), and fracture (ε_T). Note that the 60:40 alloys with a lower concentration of HCP elements have higher ε_{UTS} and ε_T values than the 80:20 alloys with more HCP indicating that HCP alloying does not promote ductility (uniform or fracture).

Alloy	**σ_y (MPa)**	**σ_{UTS} (MPa)**	**ε_{UTS} (%)**	**ε_T (%)**
$Ti_{20}Zr_{20}Hf_{20}Nb_{20}Ta_{20}$	922 ± 2	933 ± 3	3.2 ± 0.2	23.9 ± 0.3
$Ti_{20}Zr_{20}Hf_{20}Nb_{35}Ta_{5}$	801 ± 11	815 ± 6	2.9 ± 0.5	23.0 ± 3.0
$Ti_{5}Zr_{20}Hf_{35}Nb_{20}Ta_{20}$	916 ± 6	926 ± 5	2.3 ± 0.4	25.7 ± 2.0
$Ti_{26.67}Zr_{26.67}Hf_{26.7}Nb_{10}Ta_{10}$	822 ± 10	834 ± 10	1.2 ± 0.3	19.4 ± 1.2
$Ti_{40}Zr_{20}Hf_{20}Nb_{10}Ta_{10}$	872 ±10	879 ± 10	1.5 ± 0.2	23.1 ± 1.2

Since the 80:20 alloys have lower uniform and fracture strains than the 60:40 alloys, the present results do not support the hypothesis laid out in the Introduction that increasing HCP content increases the ductility of RHEAs.

Fracture strains are provided in our paper since in previous studies these are the only values typically reported (and not uniform strains). However, caution has to be exercised when attributing post-necking strain to ductility as most of the corresponding deformation is localized and dependent on the ratio of gauge area to length. In alloys where such strain is a small fraction of the fracture strain, the latter might be a reasonable proxy for ductility but in RHEAs where post-necking strain is a large fraction of the fracture strain, it is doubtful that fracture strain can be a useful indicator of whether a material is truly ductile. Additionally, engineering structures are typically designed to withstand loads. In cases where there is practically no work hardening (as in most RHEAs), rapid failure can occur if the applied stress even slightly exceeds the yield strength, leaving little margin for safety. Another way of putting it is that post-necking strain is "useless" in load-bearing conditions. This is especially relevant in the case of RHEAs where most of the fracture strain occurs after necking. Therefore, researchers would be well advised to report uniform strain rather than total fracture strain. The XRD patterns from the gauge section after tensile testing, **Supplementary Figure 2.2**, were indexed as single-phase BCC with the same BCC phase and similar peak locations as before testing, indicating the lack of any deformation-induced phase transformations at this scale.

DIC strain maps generated from the speckle-pattern image frames captured at the ultimate tensile stress of each alloy are shown on the left in **Figure 2.7**. There is a greater degree of strain localization in the 60:40 alloys than in the 80:20 alloys. The images on the right in **Figure 2.7** are DIC maps from the frame just before failure. Necking is evident in each alloy, albeit more so in the 60:40 alloys than in the 80:20 alloys. Failure subsequently occurred in the necked regions. The fracture surfaces, **Figure 2.8**, all contain large dimples and microvoids with no particles inside them. The large cavities are similar to those seen on other RHEA fracture surfaces where large cavities (hundreds of μm in size) with no secondary phases have been reported [23, 46, 83]. In contrast, cavities in FCC HEAs normally nucleate at secondary particles, such as Cr and Mn rich particles in CrMnFeCoNi [140]. The dimpled fracture surfaces observed here are consistent with "ductile" failure (void nucleation, growth, and coalescence). Thus, the alloys are indeed "ductile" in the classical sense but exhibit very low uniform strains.

Discussion

CALPHAD predicted phases and microstructure

We determined the solidus and liquidus temperatures (T_s and T_l, respectively) of the different alloys from CALPHAD calculations and found them to be roughly similar across the compositions.

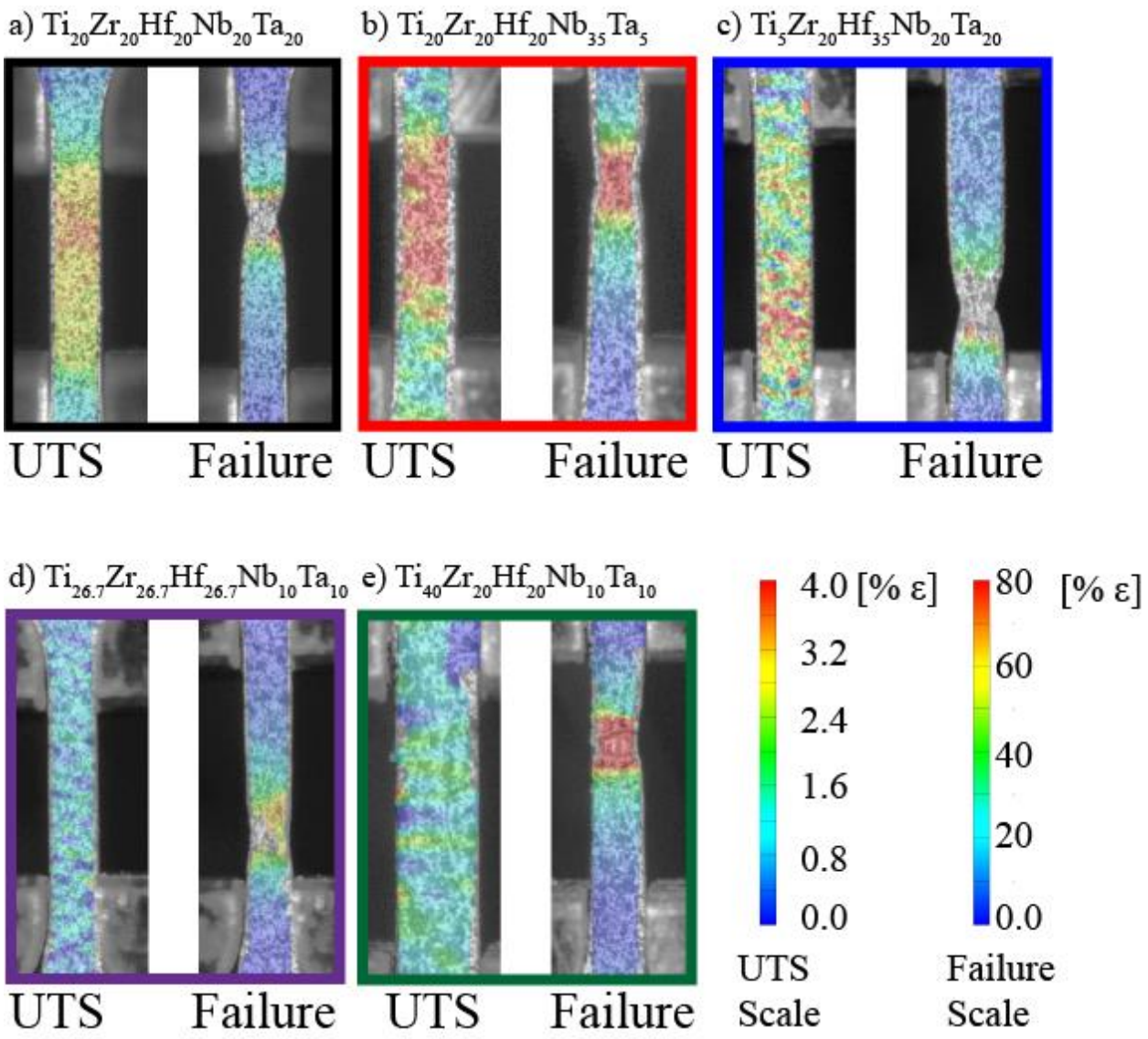

Figure 2.7: Strain maps determined by DIC for each alloy. UTS image is the frame at the maximum engineering stress, and failure image is the last frame before fracture. Color-bar scales at the bottom right represent longitudinal strain.

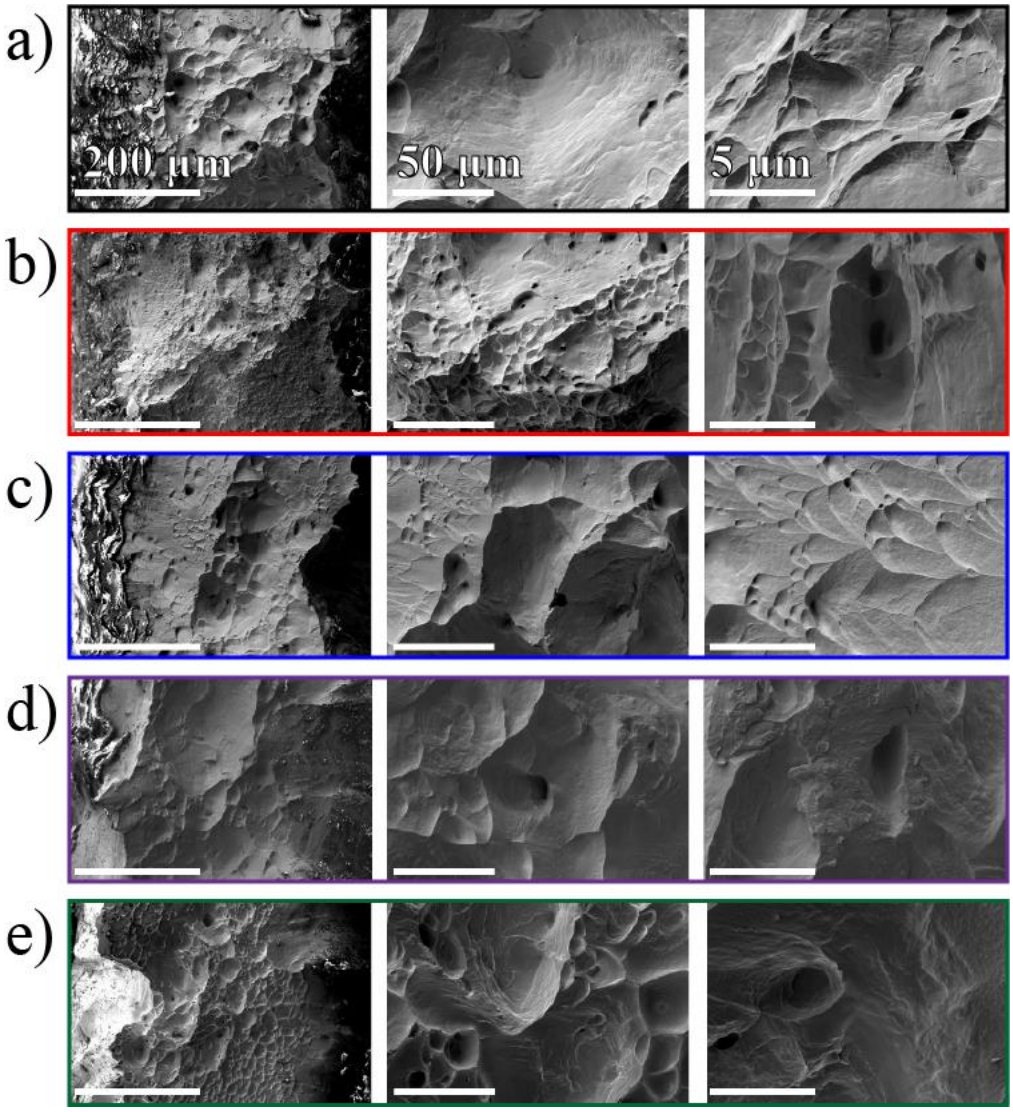

Figure 2.8: Fracture surfaces of (a) $Ti_{20}Zr_{20}Hf_{20}Nb_{20}Ta_{20}$, (b) $Ti_{20}Zr_{20}Hf_{20}Nb_{35}Ta_{5}$, (c) $Ti_{5}Zr_{20}Hf_{35}Nb_{20}Ta_{20}$, (d) $Ti_{26.7}Zr_{26.7}Hf_{26.7}Nb_{10}Ta_{10}$, and (e) $Ti_{40}Zr_{20}Hf_{20}Nb_{10}Ta_{10}$ with increasing magnification from left to right, showing large cavities (dimples) and heavy deformation, characteristic of ductile failure.

For comparison, if we use the melting temperature (T_m) of the constituent elements and weight them by their respective atomic concentrations to calculate a weighted average (i.e., rule of mixtures), the resulting values do not agree with the CALPHAD T_s or T_l values (nor do they always follow the same trends, see **Supplementary Figure 2.2**). It is well known that in alloys whose phase diagrams contain deep eutectics or high-T_m intermetallics, there are significant deviations from the rule of mixtures. Even in the absence of such discontinuities, some binary phase diagrams of the Ti-Zr-Hf-Nb-Ta system, such as Hf-Ta, Nb-Zr, Hf-Ta, and Ti-Zr, display local minimums in melting temperature in otherwise smoothly varying T_s curves [114]. Our present results suggest that the T_s of complex concentrated alloys behave similarly to some of the constituent binaries and using a rule of mixtures to estimate their solidus and liquidus temperatures can lead to erroneous results.

The pseudobinary TiZrHf-NbTa phase diagram, **Figure 2.9a**, shows that T_s and T_l remain more or less constant between 0 and 40 at% BCC content (Nb+Ta), i.e., at the HCP-rich end. The equiatomic alloy sits near the elbow of the liquidus curve: an increase in the BCC content beyond this point raises T_l but a decrease does not result in a lower T_l. The T_s and T_l values of $Ti_{40}Zr_{20}Hf_{20}Nb_{10}Ta_{10}$ and $Ti_5Zr_{20}Hf_{35}Nb_{20}Ta_{20}$ imply that certain non-equiatomic modifications are consistent with the rule of mixtures in that substitution of lower-T_m elements decreases the melting temperature.

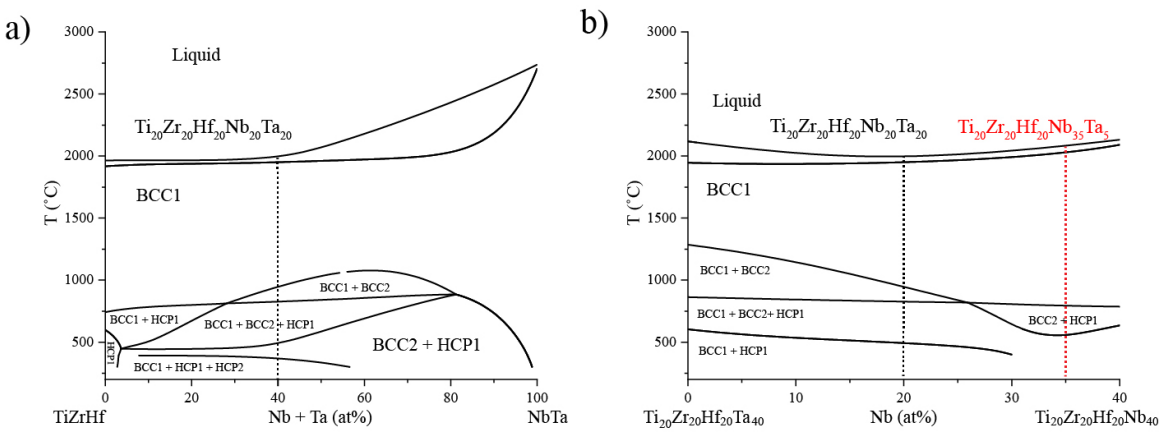

Figure 2.9: Pseudo-binary diagrams for (a) TiZrHf-NbTa, and (b) TiZrHfTa-Nb. In (a), the TiZrHf-NbTa pseudo-binary compositions from 0% NbTa to 40% NbTa have a relatively constant solidus and liquidus temperature (T_s and T_l). On the other hand, in the TiZrHfTa-TiZrHfNb pseudo-binary (b), there is a local minimum near the $Ti_{20}Zr_{20}Hf_{20}Nb_{20}Ta_{20}$ composition where an increase or decrease in Nb content raises the T_l.

In contrast, $Ti_{20}Zr_{20}Hf_{20}Nb_{35}Ta_5$ has a higher solidus temperature than the equiatomic alloy, even though the former contains significantly more Nb (T_m = 2477 ˚C) and significantly less Ta (T_m = 3017 ˚C) than the latter. The increase in T_m can be explained by considering the TiZrHfTa-TiZrHfNb pseudobinary phase diagram in **Figure 2.9b**: the $Ti_{20}Zr_{20}Hf_{20}Nb_{20}Ta_{20}$ alloy sits at 20% Nb, near a local minimum in T_l, with increases or significant decrease in Nb content causing an increase in T_l.

The predicted stable phases in the investigated alloys include BCC and HCP depending on temperature. At elevated temperatures the BCC phase is the only one that is predicted to be stable in the solid state. Secondary phases are predicted to appear at intermediate temperatures as shown in **Figure 2.9**. Experimentally, the BCC-indexed XRD patterns were all in agreement with the CALPHAD results except for one. The exception, $Ti_5Zr_{20}Hf_{35}Nb_{20}Ta_{20}$, had only a single BCC phase, as seen in SEM and XRD, contrary to the CALPHAD results which predict ~30% HCP at 1200 ˚C (the recrystallization temperature). Lower-temperature CALPHAD calculations show that this HCP phase remains at temperatures down to 25 ˚C suggesting that it should have been experimentally detected in the $Ti_5Zr_{20}Hf_{35}Nb_{20}Ta_{20}$ alloy examined at room temperature after recrystallization at 1200 ˚C followed by cooling in the quartz capsule to room temperature. The fact that it was not detected suggests that the CALPHAD database needs further refinement.

Tensile stress-strain behavior

The large changes in composition across the investigated alloys had relatively small effects on the tensile stress-strain behavior. They all showed low work-hardening, with minor differences in flow behavior, strain, and strength. The 60:40 alloys maintain a high flow stress with gradual strain softening, while the 80:20 alloys display an initial stress drop after the ultimate tensile stress followed by more gradual strain softening. This is a fortuitous result that was not anticipated and might turn out to be relevant in the future design of precipitate-strengthened RHEAs. A matrix that can accommodate large compositional changes, retain its single-phase BCC structure, and not undergo drastic changes in mechanical properties can serve as a testbed for searching for useful intermetallic formers in said matrix. Intermetallic precipitates can in some cases deplete one or more of the elements in the matrix. However, if there is a large compositional space where the matrix composition remains more or less constant, then depletion of some of its constituents to form precipitates is less of a concern.

The DIC strain maps in **Figure 2.7** show longitudinal strains up to ~80% within the neck regions before failure. Clearly, the alloys can accommodate large local strain but limited uniform strain before necking starts. In earlier work, the introduction of chemical heterogeneity [82] and activation of other deformation mechanisms such as deformation-induced phase transformation [96] have succeeded to some extent in increasing the amount of uniform strain.

Factors affecting yield strength

There are various factors that can, in principle, affect the yield strength of the present alloys. Most of them can be ruled out as follows. Strengthening due to precipitates and other dislocations can be ignored as our alloys are single-phase solid solutions in the fully recrystallized state (i.e., with presumably low dislocation density). Similarly, texture effects can be ignored as our grain orientations are close to random with weak fiber components (**Figure 2.4**), which is typical for recrystallized BCC structures [141]. Differences in their homologous temperatures are small enough (given the similarity of their solidus and liquidus temperatures, as indicated in **Supplementary Table 2.2** and **Figure 2.1**) that they are not expected to significantly affect room-temperature yield strength.

Strengthening stemming from the different grain sizes of our alloys (76-199 μm, **Figure 2.2**) can be estimated if we assume that their Hall-Petch coefficients are all the same as that of the equiatomic Senkov alloy, 270 MPa $\mu m^{0.5}$ [72]. In that case, the largest strength difference due to grain size is between $Ti_{26.7}Zr_{26.7}Hf_{26.7}Nb_{10}Ta_{10}$ (199 μm grain size) and $Ti_{20}Zr_{20}Hf_{20}Nb_{35}Ta_5$ (76 μm grain size) with the former alloy stronger by 7.9 MPa and the latter weaker by 4.0 MPa when normalized to an alloy with 100 μm grain size (i.e., a small relative difference of <1%). However, when the absolute experimental yield strength of an alloy is compared with its theory-calculated yield strength (as discussed later), there will be a discrepancy because the theoretical calculation does not take into account Hall-Petch strengthening which should contribute ~27 MPa

$\left(\frac{K}{\sqrt{d}} = \frac{270}{\sqrt{100}}\right)$ at a grain size of ~100 μm. In other words, assuming the same Hall-Petch coefficient of 270 MPa $\mu m^{0.5}$ for all alloys as stated before, the theory-calculated yield strengths will all be roughly 27 MPa lower than the experimental values (more on this later).

We neglect intrinsic lattice friction because (i) the chemical heterogeneity in RHEAs allows for spontaneous nucleation of kinks along screw dislocations, thus removing the activation barrier for double-kink nucleation and rendering lattice friction negligible [107], and (ii) the lattice friction of edge dislocations is very small. This leaves solid solution strengthening as likely the biggest contributor to the observed yield strength of these alloys. Theories have been developed to estimate the degree of solid solution strengthening in FCC [142] and BCC HEAs based on moving screw [107, 108, 143] and edge [109, 110] dislocations. Unlike dilute BCC alloys where strength is controlled by screw dislocations, experimental evidence in some RHEAs suggests that edge dislocations can contribute significantly to strengthening [104, 115]. The strengthening of edge dislocations arises from the complex energy landscape created by the collective solute-dislocation interactions. In TiZrHfNbTa specifically, screw dislocations are the dominant dislocation type seen in TEM [68, 69, 73]. However, in other alloys of this system such as TiZrHfNb, deformation may be controlled at least partially by edge dislocations [105], which are thus also worth considering. As for the non-equiatomic alloys, the relative contributions of edges and screws remains to be determined. Analysis of screw dislocations requires difficult to determine parameters

regarding the geometry of screw dislocations [107, 108, 143].Edge dislocation strengthening is considered here as it is more tractable. The calculated edge strengths represent a lower bound because some of the present alloys may be controlled by screw strengthening [109].

The edge dislocation strengthening theory determines the 0 K shear yield stress τ_{y0} (Eq. 6), the zero-stress energy barrier ΔE_b (Eq. 7) to move an edge dislocation from one local energy minimum to the next local minimum in the energy landscape along the glide plane, and the temperature- and strain-rate dependent strength τ_y (Eq. 8) is then obtained using standard thermal activation theory:

$$\tau_{y0} = 0.040\alpha^{-\frac{1}{3}} G \left(\frac{1+\nu}{1-\nu}\right)^{\frac{4}{3}} \left[\frac{\sum_n c_n \Delta V_n^2}{b^6}\right]^{\frac{2}{3}} \quad (4)$$

$$\Delta E_b = 2.00\alpha^{\frac{1}{3}} G b^3 \left(\frac{1+\nu}{1-\nu}\right)^{\frac{2}{3}} \left[\frac{\sum_n c_n \Delta V_n^2}{b^6}\right]^{\frac{1}{3}} \quad (5)$$

$$\tau_y(T, \dot{\epsilon}) = \tau_{y0} exp\left[-\frac{1}{0.55}\left(\frac{k_B T}{\Delta E_b} ln\frac{\dot{\epsilon_0}}{\dot{\epsilon}}\right)^{0.91}\right] \quad (6)$$

Analysis requires the concentrations of all alloying elements (c_n in at%), their volume misfits (ΔV_n [144, 145]) in the alloy, a line tension coefficient (α = 1/12), magnitude of $\boldsymbol{b}$ = ½a<111> the Burgers vector, isotropic alloy elastic constants G and ν, temperature T=298K, a reference strain rate ($\dot{\epsilon_0}$ = 10^4 s^{-1}), strain rate of the tensile tests ($\dot{\epsilon}$ = 10^{-3} s^{-1}), and Boltzmann's constant k_B. For the concentrations c_n, experimental values given in **Supplementary Table 2.2** are used. The calculated shear yield stresses were multiplied

by a Taylor factor *M* of 3.067 for untextured BCC plasticity controlled by edge dislocations to obtain a uniaxial yield strength $\sigma_y = M\,\tau_y$ [109]. Furthermore, as a first order approach to account for the influence of interstitial elements, O and N are incorporated into the edge theory through the misfit parameter $\sum_n c_n \Delta V_n^2$ as additional (interstitial) solutes with misfit volumes estimated using the average DFT-computed misfit volumes in Nb and Ta, 6.85 x 10^{-3} nm^3 and 6.985 x 10^{-3} nm^3 for O and N respectively [104, 146]. Carbon, unfortunately, does not have a similarly calculated volume misfit, and is incorporated by using the misfit volume of nitrogen due to its similar atomic radius; error due to this approximation is expected to be small since the concentration of C is much lower than that of O and N.

Calculations were carried out with two sets of inputs (see **Supplementary Table 2.3**). In both cases, Vegard's Law is used for the volume misfits, computed in terms of the elemental atomic volumes (C_{ij}) as $\Delta V_n = V_n - V_{avg}$ with $V_{avg} = \sum_{i=1}^{n} c_n\, V_n$. The first set of inputs then computes the Burgers vector $b = \frac{\sqrt{3}}{2}\left(2V_{avg}\right)^{\frac{1}{3}}$ [144, 145] and uses the rule-of-mixtures for the elastic constants [109] in which the single-crystal elastic constants (C_{ij}) of the alloy are computed in terms of the values (C_{ij}^n) as $C_{ij} = \sum_{i=1}^{n} c_n C_{ij}^n$ [109, 144, 145]. The isotropic shear modulus is then calculated as $G = \sqrt{C_{44}(C_{11} - C_{12})/2}$, the bulk modulus as $B = (C_{11} + 2C_{12})/3$, and the Poisson's ratio as $\nu = (3B - 2G)/\left(2(3B + G)\right)$. The second set of inputs uses *b* calculated from the measured lattice parameter *a* (**Figure 2.3**) as $b = \frac{a\sqrt{3}}{2}$ and the measured elastic constants

E and *G* (**Table 2.3**), with Poisson's ratio calculated $\nu = \frac{E}{2G} - 1$. Note that the two values for the Burgers vector are essentially identical, supporting the use of Vegard's Law for V_{avg}.

Figure 2.10 shows the calculated vs. experimental yield strengths where empty circles represent results obtained using the first set of inputs (rule of mixtures) and solid triangles the second set of inputs (experimental). The majority of the data lie between the dashed lines which represent ±15% deviation from the solid line representing perfect agreement between experiment and theory. Overall, given the various uncertainties, both in experiment and theory, there is good agreement between the two. That said, the experimental yield strengths are better-predicted with the rule of mixtures inputs. A potential drawback of using the rule of mixtures to obtain alloy moduli from those of the constituent elements is that some of the elements (Ti, Zr, Hf) are HCP at room temperature whereas the alloys are BCC. Use of experimentally measured alloy moduli eliminates this problem. The slight underestimate using the experimental moduli (**Figure 2.10)** may then be due to the fact that, as mentioned before, the edge theory offers a lower bound for yield strength. Another reason for the underestimate is the lack of a Hall-Petch contribution in the edge theory which would move the data points up by ~27 MPa and thus close to the 45° line. Accounting for interstitials in the calculations significantly improved the correlation.

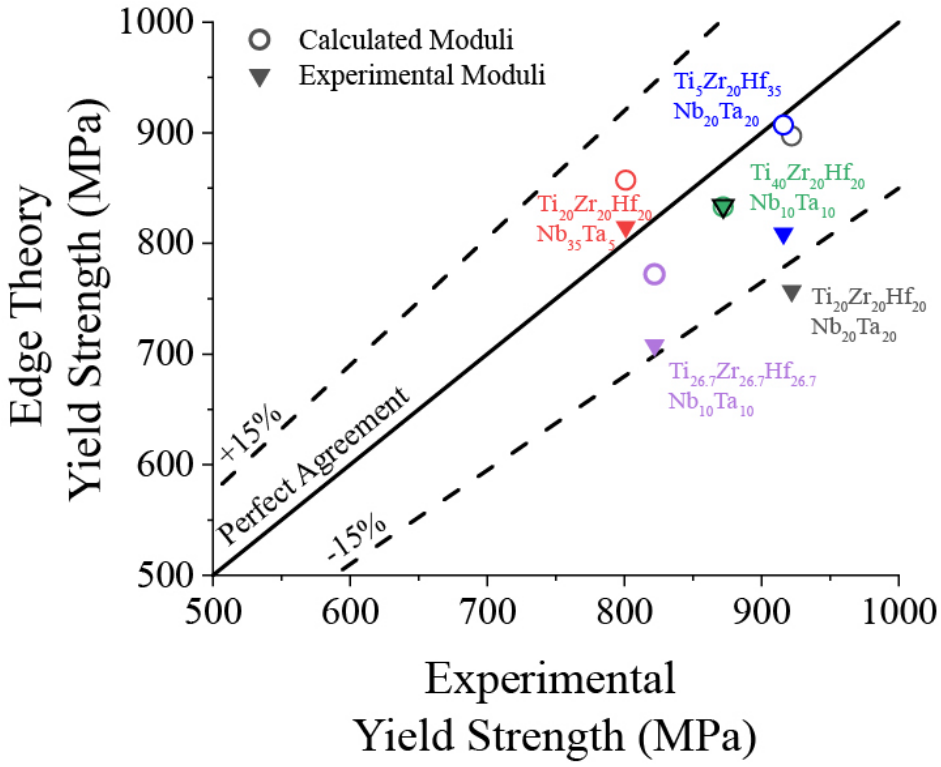

Figure 2.10: Comparison of theory-predicted and experimental yield strengths.

In $Ti_{20}Zr_{20}Hf_{20}Nb_{20}Ta_{20}$ and $Ti_{40}Zr_{20}Hf_{20}Nb_{10}Ta_{10}$, the alloys with the lowest and highest interstitial content, interstitials strengthened the alloys by 58 MPa and 143 MPa respectively, moving the predicted yield strength closer to the experimentally measured values. Overall, therefore, there is remarkably good agreement between the predictions of the edge theory and experimentally measured yield strengths.

Conclusions

Starting from the equiatomic ductile Senkov alloy TiZrHfNbTa, four derivative alloys (comprising the same five refractory elements) were synthesized by arc melting, casting, homogenization, cold rolling, and recrystallization. These five alloys, despite having different amounts of HCP and BCC elements as their constituents, all have a single-phase BCC microstructure with grain sizes ranging from 76 to 199 μm. Alloys with higher HCP-element content have higher shear-modulus-normalized yield strengths resulting from their lower shear modulus, compared to those with lower HCP-element content, suggesting that compositional changes in shear moduli do not fully account for the changes in yield strength. Predictions of an analytical theory previously developed for the yield strengths of RHEAs controlled by edge dislocations are in good agreement with the experimentally measured yield strengths indicating that both the shear modulus and volume misfit need to be taken into account to predict strength. Despite all the alloys displaying relatively large fracture strain to fracture (~20%) and characteristic features (dimples) on the fracture surfaces suggestive of “ductile” behavior, uniform strain prior to the onset of necking were an order of magnitude lower suggesting that their “useful”

ductilities may be low. Additionally, regardless of whether uniform or fracture strain is used as a measure of ductility, higher HCP-element concentrations do not make the alloys more ductile. The large single-phase BCC region characterized in this study provides a playground in which additional strengthening mechanisms, especially precipitation hardening, can be systematically explored in future studies.

Appendix – Supplementary Material

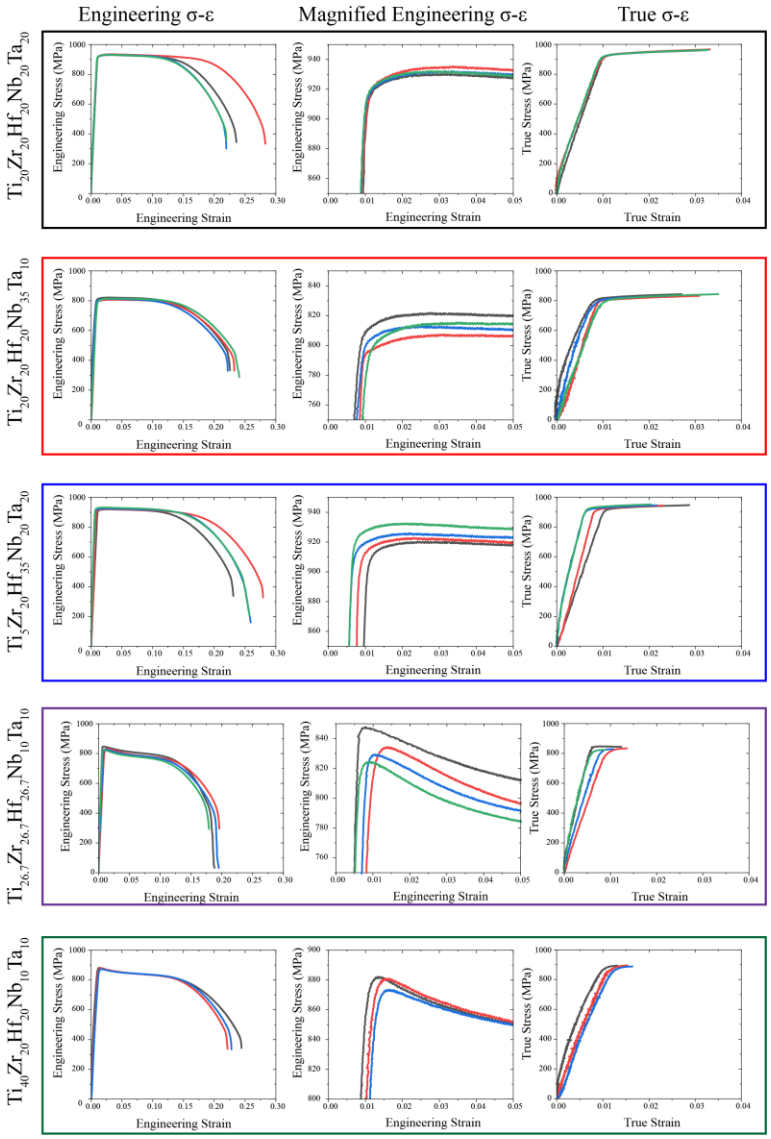

Supplementary Figure 2.1: Tensile curves for all alloys included in the study. The left column shows the measured engineering stress-strain curves. Magnified views of the engineering stress-strain curves, near the region of yielding, are presented in the middle column. True stress-strain curves, up to the UTS, are shown in the right column.

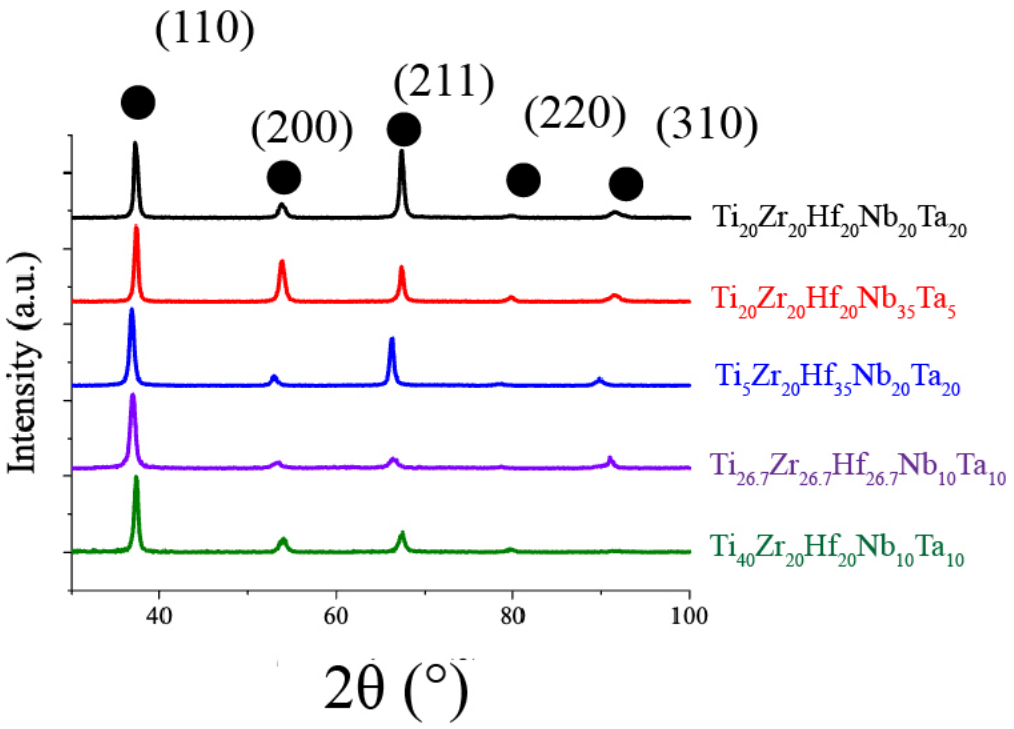

Supplementary Figure 2.2: XRD patterns from the fractured tensile specimens. All peaks were indexed as a single BCC phase, indicating no evidence of deformation-induced phase transformation (at the resolution of XRD).

Supplementary Table 2.1 Calculated compositions of the investigated alloys in at% (from **Table 2.2** of the main paper).

Alloy	**Ti**	**Zr**	**Hf**	**Nb**	**Ta**	**N**	**O**	**C**
$Ti_{20}Zr_{20}Hf_{20}Nb_{20}Ta_{20}$	20.1	18.7	18.1	22.6	20.5	0.075	0.198	<0.049
$Ti_{20}Zr_{20}Hf_{20}Nb_{35}Ta_{5}$	20.1	19.1	18.7	35.4	6.7	0.166	0.283	0.079
$Ti_{5}Zr_{20}Hf_{35}Nb_{20}Ta_{20}$	5.1	19.4	32.7	22	20.9	0.137	0.265	0.114
$Ti_{26.67}Zr_{26.67}Hf_{26.7}Nb_{10}Ta_{10}$	26.6	25.1	24.4	12.5	11.5	0.088	0.425	0.046
$Ti_{40}Zr_{20}Hf_{20}Nb_{10}Ta_{10}$	39.1	19.2	17.9	12	11.7	0.079	0.880	0.067

Supplementary Table 2.2: Melting temperatures of the constituent elements and calculated melting temperatures (T_m) of the studied alloys using rule of mixtures, and CALPHAD calculated solidus (T_s) and liquidus temperatures (T_l).

Element	Elemental T_m (K)	Alloy	Alloy T_m (K)	Alloy T_s (K)	Alloy T_l (K)
Ti	1907	$Ti_{20}Zr_{20}Hf_{20}Nb_{20}Ta_{20}$	2486*	2184	2235
Zr	2092	$Ti_{20}Zr_{20}Hf_{20}Nb_{35}Ta_{5}$	2403*	2303	2356
Hf	2468	$Ti_{5}Zr_{20}Hf_{35}Nb_{20}Ta_{20}$	2507*	2214	2273
Nb	2706	$Ti_{26.67}Zr_{26.67}Hf_{26.7}Nb_{10}Ta_{10}$	2321*	2211	2239
Ta	3257	$Ti_{40}Zr_{20}Hf_{20}Nb_{10}Ta_{10}$	2271*	2167	2214

*Calculated by rule of mixtures $T_m = \sum c_i T_{m,i}$ where c_i are the atomic concentrations of the individual elements and $T_{m,i}$ are their melting temperatures. Melting temperatures of the constituent elements were obtained from [114].

Supplementary Table 2.3: Parameters and results for the edge theory calculations: shear modulus (***G***), Young's modulus (***E***), Poisson's ratio (***v***), and Burgers vector (***b***) The calculated column (Calc.) contains the rule of mixture calculations and experimental moduli under experimental column (Exp.).

Alloy	***G (GPa)***		***E (GPa)***		***v***		***b (nm)***	
	Calc.	**Exp.**	**Calc.**	**Exp.**	**Calc.**	**Exp.**	**Calc.**	**Exp.**
$Ti_{20}Zr_{20}Hf_{20}Nb_{20}Ta_{20}$	38.1	34.9	104.8	95.4	0.376	0.367	0.294	0.295
$Ti_{20}Zr_{20}Hf_{20}Nb_{35}Ta_{5}$	35.0	35.9	96.9	97.6	0.383	0.359	0.295	0.294
$Ti_{5}Zr_{20}Hf_{35}Nb_{20}Ta_{20}$	38.7	36.7	106.4	100.0	0.373	0.362	0.298	0.298
$Ti_{26.67}Zr_{26.67}Hf_{26.7}Nb_{10}Ta_{10}$	30.9	29.6	85.7	81.9	0.388	0.383	0.297	0.298
$Ti_{40}Zr_{20}Hf_{20}Nb_{10}Ta_{10}$	30.7	31.9	85.3	88.0	0.389	0.379	0.294	0.295

Chapter 3 Fracture behavior in equi- and non-equiatomic TiZrHfNbTa alloys

A version of this study is being prepared for publication in a peer-reviewed journal. WJ Carpenter performed all the sample preparation, testing, characterization, analysis, and writing of the first draft. K Hanson performed the arc melting. MJ Paul assisted with testing and analysis. JJ Kruzic provided formal analysis. BP Gludovatz and EP George conceived and supervised the study as well as edited the drafts.

Abstract

The equiatomic TiZrHfNbTa and three derivative non-equiatomic alloys, $Ti_{20}Zr_{20}Hf_{20}Nb_{35}Ta_5$, $Ti_{26.7}Zr_{26.7}Hf_{26.7}Nb_{10}Ta_{10}$, and $Ti_{40}Zr_{20}Hf_{20}Nb_{10}Ta_{10}$ were prepared by arc-melting, homogenization, cold-rolling, and recrystallization. Their fracture toughness at room temperature was then determined using elastic-plastic fracture mechanics methods. Despite the absence of secondary phases, two distinct fracture behaviors were observed: in the equiatomic alloy, after initial blunting, sudden crack growth occurred as a combination of trans- and intergranular cleavage, whereas the non-equiatomic alloys showed predominantly crack tip blunting together with excessive tearing and intergranular cavities. While crack-tip opening displacements (CTODs) determined by profilometry ranged from 85-201 μm in TiZrHfNbTa, from which a lower-bound fracture toughness of ~105 $MPa.m^{0.5}$ can be estimated, the non-equiatomic materials showed CTODs of 207-335 μm, with $Ti_{26.7}Zr_{26.7}Hf_{26.7}Nb_{10}Ta_{10}$ having the largest CTOD and, as such, the highest fracture resistance, ~183 $MPa.m^{0.5}$. However, these values are geometry dependent. The differences in fracture behavior are associated with less-constrained specimen geometries, due to the lower yield strength and low work

hardening in the non-equiatomic alloys. Based on the present results, future fracture toughness tests should take into account nuances in specimen geometries, notably the thickness and initial ligament, since TiZrHfNbTa and its derivatives are high yield strength and low work hardening alloys. Particularly the low work hardening allows for large plastic zones that break crack tip constraint while technically being a valid test, leading to inflated fracture toughness values.

Introduction

High entropy alloys (HEAs) have received considerable interest as a possible alloy design strategy to address current alloy limitations [147]. Recent efforts to develop new alloys that surpass nickel superalloys' operating temperature and overcome brittle room temperature behavior in refractory alloys have culminated in refractory high entropy alloys (RHEAs) [9, 147]; RHEAs are typically BCC alloys that are based on group IV, V, VI elements with high melting temperatures. However, despite their promising high temperature yield strengths, many RHEAs are, like traditional refractory metals and alloys, brittle at room temperature [12, 19, 117]. An exception to such characteristics is the equiatomic TiZrHfNbTa alloy that has been reported to have 10-20% total elongation to failure with ~3% uniform strain and 950-1200 MPa yield strength in tension at room temperature [23, 46, 72, 121]. Derivatives of TiZrHfNbTa can be described, generally, as being similarly ductile [83, 84]. Most of the ductile non-equiatomic alloys avoid group VI element additions and avoid compositional extremes of TiZrHfNbTa, such as excessive amounts of Ta [14, 16, 17]. Though the effect of

compositional variation on the deformation mechanisms and strengthening has not been fully described, indications are that the derivative alloys have similar tensile behavior with 10-20% total elongation, and little work hardening.

While tensile stress-strain properties are crucial to understanding the mechanical characteristics of an alloy, such as yield strength and uniaxial plastic deformation, fracture toughness is often the limiting mechanical property in structural engineering. Previous investigations into the fracture resistance and failure characteristics of HEAs have primarily focused on the exceptionally tough FCC alloys, whose toughness values exceed 200 MPa.$m^{0.5}$ [140, 148, 149]. Compared to that, fracture toughness studies on RHEAs are limited and include non-standard specimens such as micro-cantilever beams in the case of NbMoTaW [65, 66] and notched fracture toughness tests for $(TiZrNbTa)_{100-x}Mo_x$ [150]. Fan et al. [151] performed fracture toughness tests on a single-edge notch bend specimen of the equiatomic TiZrHfNbTa alloy using the *J*-integral approach and measured a fracture toughness of 210 MPa.$m^{0.5}$. Recently, ion irradiated equiatomic TiZrHfNbTa specimens were tested with a nanocrystalline microstructure using microcantilever single edge notch beam and millimeter single edge bend configurations; a fracture toughness of 38.1 MPa $m^{0.5}$ was obtained in the unirradiated condition [152]. A notable non-equiatomic NbTaTiHf RHEA showed high fracture toughness resistance, up to 253 MPa $m^{0.5}$ at room temperature, but it did not meet specimen size requirements [27]. Interestingly, the non-equiatomic NbTaTiHf had useful cryogenic and high

temperature fracture toughness values of 86 MPa $m^{0.5}$ at cryogenic temperatures and 67-93 MPa $m^{0.5}$ at elevated temperatures.

The wide range of reported fracture toughness values raises a question of the "real" toughness of TiZrHfNbTa-based RHEAs that requires further understanding. Is the high fracture toughness specific to a few compositions or is it more general to the TiZrHfNbTa composition? To investigate this, the equiatomic TiZrHfNbTa alloy and three non-equiatomic derivative alloys ($Ti_{26.7}Zr_{26.7}Hf_{26.7}Nb_{10}Ta_{10}$, $Ti_{20}Zr_{20}Hf_{20}Nb_{35}Ta_{5}$, and $Ti_{40}Zr_{20}Hf_{20}Nb_{10}Ta_{10}$) were synthesized. The alloys were designed with two different ratios of HCP elements (Ti, Zr, Hf) to BCC elements (Nb, Ta), namely, 60:40 and 80:20 HCP:BCC. This approach is based on the notion that increasing the concentration of HCP elements spreads the dislocation core structure and promotes ductile behavior [115]. These alloys were chosen since they represent large compositional variations yet exhibit similar tensile stress-strain behavior as the equiatomic alloy. The materials were tested using the compact tension geometry, measuring crack initiation and growth resistance as described in ASTM standard E1820 [153]. The arc-melted alloys had comparable microstructures after homogenization, cold-rolling, and recrystallization. In what follows, their fracture behavior is characterized and reasons for differences in their failure characteristics are discussed in detail.

Methods

Alloy Processing

The investigated alloys had compositions of HCP to BCC elements with ratios of 60:40 and 80:20. They were chosen because of their ductile nature and ability to be deformation processed at room temperature. Alloys were prepared by arc-melting the constituent elements. The arc-melted buttons were flipped and remelted at least five times and drop-cast into a 25.4 mm × 25.4 mm × 25.4 mm mold in a titanium-gettered atmosphere. After drop casting, the hot tops were removed from the ingots using wire electrical discharge machining (WEDM) and subsequently inspected for porosity. The ingots were cleaned with nitric acid and then ethanol, followed by homogenization at 1200 °C for 24 h in a Brew vacuum furnace (previously Brew, Concord, NH, USA, currently Thermal Technology LLC, Minden, NV, USA) and furnace cooled to room temperature. The homogenized ingots were cold-rolled to ~78% thickness reduction using 5% reduction per pass to a ~5.5 mm final thickness. After cold rolling, rectangular specimens were cut from the ingot, cleaned, and encapsulated in quartz ampules filled with 0.5 atm 99.99% argon after three purge and backfill sequences. The encapsulated samples were recrystallized at 1000-1100 °C for 0.25-1 h in a Nabertherm muffle furnace (Nabertherm GmBH, Lilienthal, Germany), followed by cooling to room temperature by removing the quartz ampules from the furnace. Details of the recrystallization treatments are in **Table 3.1**.

Table 3.1: Recrystallization parameters for each composition.

Alloy	Recrystallization temperature and time
$Ti_{20}Zr_{20}Hf_{20}Nb_{20}Ta_{20}$	1100 °C, 1 h
$Ti_{20}Zr_{20}Hf_{20}Nb_{35}Ta_{5}$	1055 °C, 0.83 h
$Ti_{26.7}Zr_{26.7}Hf_{26.7}Nb_{10}Ta_{10}$	1100 °C, 0.25 h
$Ti_{40}Zr_{20}Hf_{20}Nb_{10}Ta_{10}$	1000 °C, 1 h

Chemical analyses using inductively coupled plasma atomic emission spectroscopy (ICP-AES) and LECO combustion were performed on recrystallized samples to obtain alloy compositions and interstitial chemistry. Throughout this manuscript, $Ti_{20}Zr_{20}Hf_{20}Nb_{20}Ta_{20}$ is referred to as equiatomic and all other alloys are collectively termed as non-equiatomic.

Fracture Toughness Characterization

Fracture toughness tests in accordance with ASTM standard E1820 [153] were performed using compact tension, C(T) specimens with thickness B ~5 mm and width W ~16 mm to assess the alloys' resistance to crack growth with crack extension, i.e., their crack resistance curve, R-curve behavior; the C(T) specimens were machined from the recrystallized batches of material using wire-electrical discharge machining (WEDM). Samples were ground with SiC paper from 500 through 4000 grit and polished with colloidal silica (0.05 μm) to enable measurement of the length of the precrack on the surface of the samples. Precracking and testing were done on an Instron 8872 (Instron, Norwood, MA, USA) servo-hydraulic fatigue testing system with a constant stress intensity range, ΔK, of 6-12 $MPa.m^{0.5}$, a minimum to maximum load ratio, $R = 0.1$, at a frequency, f of 30 Hz using a 5 kN dynamic load cell. Crack length, a, was monitored using unloading compliance as described in the standard [153] and, additionally, repeatedly measured with optical microscopy (OM) throughout interrupted precracking. Compliance was measured with an Epsilon clip gauge (-1/+4 mm travel; Epsilon Technology, Jackson, WY, USA) mounted onto knife edges that were machined at the

crack mouth on the front face of the samples. After precracking, with the exception of one equiatomic sample, specimens were side grooved using WEDM to ~4 mm net thickness, B_n to increase crack tip constraint during testing. Fracture toughness tests utilized a 25 kN load cell and a displacement rate of 2 mm/min; unloading cycles to 20% of the peak load were started at an initial displacement of 0.1 mm and subsequently at 0.02 mm incremental displacements. To facilitate the CTOD measurements with crack path profilometry, specimens were tested beyond the calibrated range of the clip gauge and cyclically loaded to failure at $R = 0.5$. Subsequently, the initial precrack length was measured throughout the thickness of the samples and used to correct the final *R*-curves. For the non-equiatomic alloys, two specimens were tested for each alloy to assess repeatable behavior with precracks ranging between $0.53 < a/W < 0.61$. For the equiatomic alloy, three samples with different crack lengths and geometries were tested: one side-grooved with $a/W \sim 0.63$, one without side grooves and $a/W \sim 0.62$, and one additional sample that was side-grooved with $a/W \sim 0.72$ – this sample with extended initial crack length was tested to understand the impact of ligament width and make it directly comparable to the Fan et al. study [151]. Mechanical data including yield strength, σ_y, ultimate tensile strength, σ_{UTS}, flow stress, σ_f (defined here as $\sigma_f = (\sigma_y + \sigma_{UTS}) / 2$), Young's modulus, *E*, and Poisson's ratio, ν, were obtained from Chapter 2.

Microstructure and Fractographic Analysis

X-Ray diffraction (XRD) was performed on recrystallized specimens using a Panalytical Empyrean instrument (Malvern Panalytical Ltd, Malvern, UK) with a Cu

source (λ = 0.15406 nm) on the ground surface (>2000 grit) of the recrystallized specimens. Samples for microstructure characterization were cut from both the recrystallized bar and from tested C(T) specimens, mechanically ground to 4000 grit, and polished with colloidal silica. Backscattered electron (BSE) imaging and fractography were performed with a Zeiss Auriga scanning electron microscope (SEM; Carl Zeiss Microscopy, München, Germany) and electron backscatter diffraction (EBSD) scans were performed with a JEOL 7001 SEM (Jeol, Tokyo, Japan) with an EDAX EBSD detector (EDAX, LLC, Pleasanton, CA, USA). Energy dispersive X-ray spectroscopy was performed with a Zeiss EVO15 (Carl Zeiss Microscopy, München, Germany) with Elite Super detector (EDAX, LLC, Pleasanton, CA, USA) in tandem with BSE imaging and EBSD was performed at 20 kV and fractography images taken at 5 kV. CTODs were determined through profilometry measurements using an Olympus DSX510 optical microscope (Evident Corporation, Tokyo, Japan). For the profilometry, stacks of OM images taken at ~3 μm vertical steps were stitched together up to a height of ~1300 μm to capture the lowest and highest points of each fracture surface. From the stitched images, a cavity was identified near the crack tip and the profiles of the corresponding crack paths from both fracture surfaces were aligned to determine the CTOD of the cavity using a 45°-degree right triangle as describe by Shih [154]. CTOD measurements used at least two lines averaged from different fractographic surfaces from each specimen. After the fractographic analysis, one half of a tested specimen was bisected along W for post-test microstructural and deformation analysis.

Results

Initial microstructure

EBSD scans taken from the midplane below the precrack after each alloy was tested, **Figure 3.1a-d**, show their fully recrystallized microstructures with equiaxed grains ranging from 83 μm in $Ti_{20}Zr_{20}Hf_{20}Nb_{35}Ta_5$ to 223 μm in $Ti_{26.7}Zr_{26.7}Hf_{26.7}Nb_{10}Ta_{10}$. All four alloys exhibit an overall randomly oriented grain structure with only minor texture, as seen in the inverse pole figure. Texture is most pronounced for the $Ti_{26.7}Zr_{26.7}Hf_{26.7}Nb_{10}Ta_{10}$ alloy at 4.1 above random (i.e., 4.1 times more likely for grains to be specifically orientated than their orientation being randomly distributed) and weakest for the $Ti_{20}Zr_{20}Hf_{20}Nb_{35}Ta_5$ alloy, 2.0 above random. It should be noted that the higher number indicating the minor texture in $Ti_{26.7}Zr_{26.7}Hf_{26.7}Nb_{10}Ta_{10}$ may be associated with the larger grain size and the correspondingly lower number of indexed grains. Consistent with this, preferred texture decreases qualitatively with grain size, **Figure 3.1**. BSE images, insets of **Figure 3.1a-d**, indicate no secondary phases at grain boundaries and triple points, in accordance with the XRD patterns from the recrystallized samples, **Figure 3.2**, that show only single-phase BCC peaks with lattice parameters close to those previously reported for TiZrHfNbTa RHEAs [68, 98], and in Chapter 2. ICP-AES and LECO combustion results, **Table 3.2**, show all alloys have low amounts of interstitial elements and are close to the intended composition, although with a slightly reduced Hf content; compositions in atomic% are provided in supplemental **Table 3.1**.

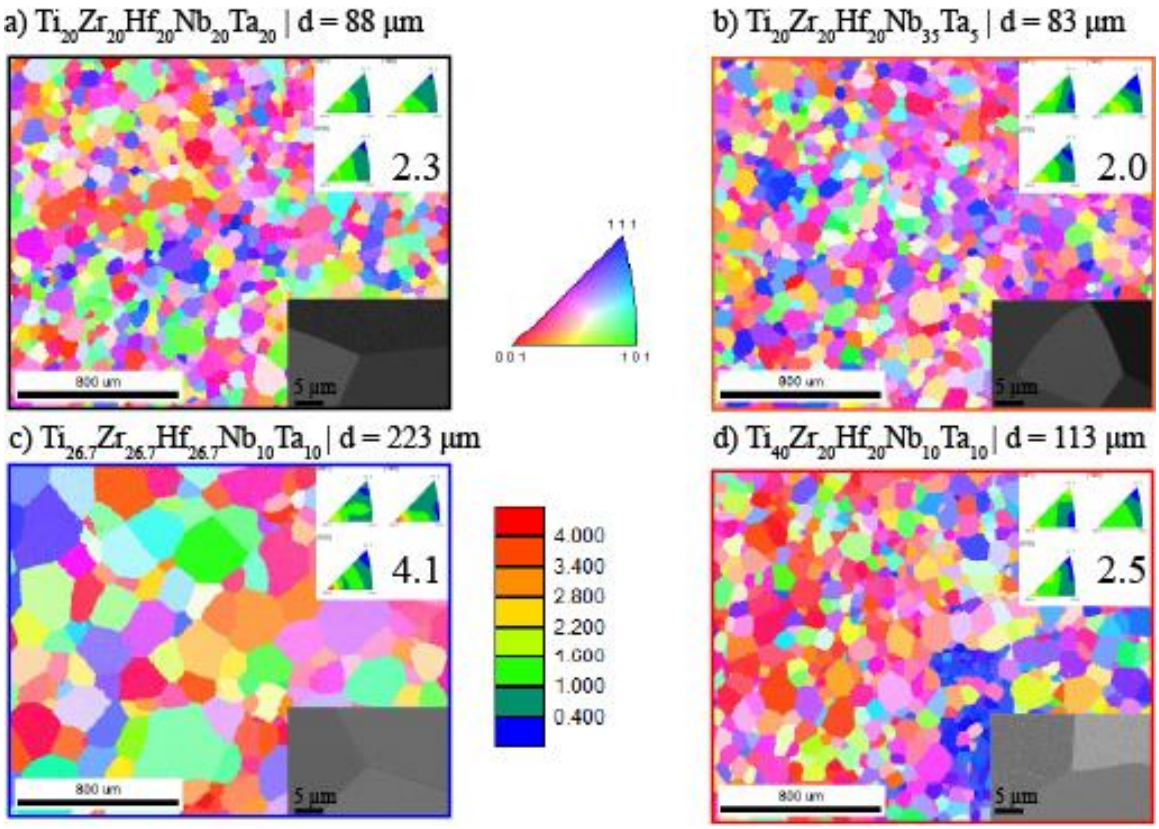

Figure 3.1: EBSD maps with corresponding grain sizes and pole figures from recrystallized microstructures of the (a) equiatomic and (b-d) non-equiatomic RHEAs; inserts display BSE images indicating grain boundaries and triple points free of secondary phases.

Table 3.2: Alloy compositions measured by ICP-AES for metallic elements and LECO combustion for interstitial elements. Metallic elements are reported in weight percent and interstitial elements are reported in parts per million by weight.

	Ti	Zr	Hf	Nb	Ta	O	N	H	C
$Ti_{20}Zr_{20}Hf_{20}Nb_{20}Ta_{20}$	9.3	15.7	24.4	18.4	31.8	360	90	20	<100
$Ti_{20}Zr_{20}Hf_{20}Nb_{35}Ta_{5}$	9.6	17.4	27.2	33.3	12.1	170	110	20	<100
$Ti_{26.7}Zr_{26.7}Hf_{26.7}Nb_{10}Ta_{10}$	20.2	18.7	28.9	9.6	21	50	20	10	<100
$Ti_{40}Zr_{20}Hf_{20}Nb_{10}Ta_{10}$	12.5	22.4	34.5	9.8	20.2	160	100	30	<100

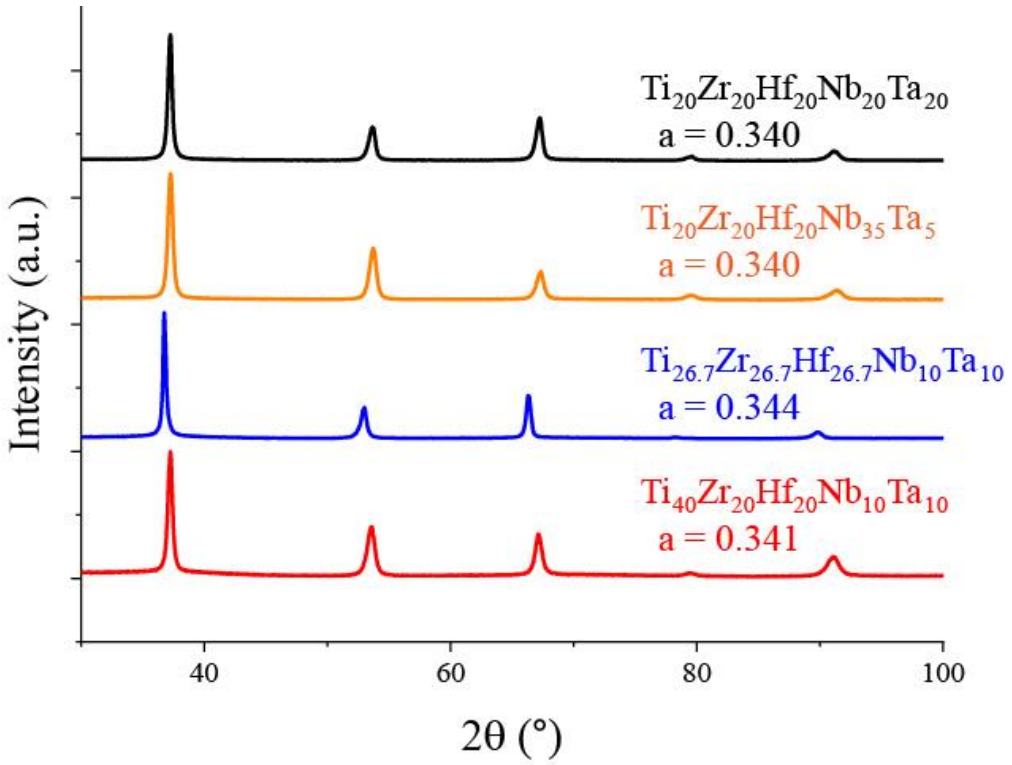

Figure 3.2: XRD patterns taken from samples with recrystallized microstructures prior to testing indicate a single-phase BCC crystal structure for all four alloys.

Chemical maps from energy dispersive X-ray spectroscopy are located in **Supplementary Figure 3.1.**

J-integral testing

Representative *R*-curves for each alloy are shown in **Figure 3.3**. R-Curves in **Figure 3.3a** are for the equiatomic specimens in three conditions: side-grooved with a/W ~0.63, and ~0.72, and not side-grooved with a/W ~0.6. **Figure 3.3b** shows R-curves from non-equiatomic alloys; samples are side-grooved samples with similar precrack lengths (a/W ~ 0.6) and thicknesses (B ~ 5 mm and B_n ~ 4 mm) and only values from the calibrated clip gauge range (-1/+4 mm) are shown. Negative crack growth was seen at the onset of testing and is likely associated with crack closure, as a result, causes a decrease in sample compliance, to cause apparent negative crack growth. To compensate, the *R*-curves were moved to the 0-mm blunting line as suggested by Seok [155]. Two types of failure were observed during testing: sudden crack extension after the initial blunting, only seen in the equiatomic alloy, and excessive blunting where the crack resistance increases linearly without substantial crack growth up to the limit of the clip gauge, that is above the *J*-limit (= $b_0 \sigma_f /7.5$) of our used sample size – this behavior was seen for the non-equiatomic alloys. The E1820 J_Q analysis cannot be used for the three non-equiatomic alloys as the data do not meet the power-law fitting requirements of the standard. J_Q for the equiatomic alloy is based on the *J*-value at sudden crack extension, i.e., ~105 kJ/m^2.

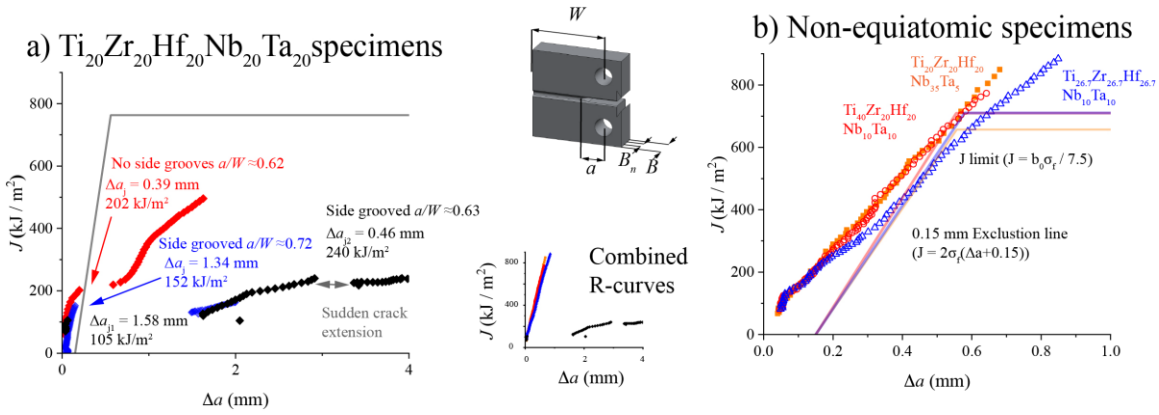

Figure 3.3: Fracture behavior of the investigated TiZrNbHfTa alloys. (a) *R*-curves for $Ti_{20}Zr_{20}Hf_{20}Nb_{20}Ta_{20}$, and (b) non-equiatomic. Solids lines are the blunting lines (diagonal) and *J*-limit lines (horizontal), which are alloy and sample dependent respectively. Middle inserts are the C(T) geometries used and a combined R-curve for comparison.

This number, however, does not meet the sample size criterion of the standard for sudden crack extension (i.e., B, $b_0 = 100\ J_Q/\sigma_f$) and the J-value, and corresponding fracture resistance in terms of stress intensity of 108 MPa.m$^{0.5}$ calculated under the assumption of predominantly plane-strain conditions, $K_Q = [E\ J_Q/(1-\nu^2)]^{1/2}$ using the mechanical properties listed in the previous chapter, should hence only be seen as a size-dependent value.

The different failure characteristics of the equiatomic alloy were further investigated by testing samples that i) had a longer precrack and therefore a shorter initial ligament, b_0, and ii) had no side grooves; both modifications result in reduced crack tip triaxiality and hence less constraint. Despite these changes in sample configuration, the modified specimens showed sudden crack extension similar to the side-grooved sample with $a/W \sim 0.63$, but with increased J_Q, 152 kJ/m^2 (i.e., $K_Q \sim 129$ MPa.m$^{0.5}$) for the specimen with increased crack length ($a/W \sim 0.72$), and 202 kJ/m^2 (i.e., $K_Q \sim 149$ MPa.m$^{0.5}$) for the specimen without side grooves ($a/W \sim 0.62$). Compared to that, first crack extension in the side-grooved $a/W \sim 0.63$ sample occurred at $J_Q \sim 105$ kJ/m^2 (i.e., $K_Q \sim 108$ MPa.m$^{0.5}$) whereas after stable crack growth to $a/W \sim 0.80$ a second sudden crack extension occurred at $J \sim 240$ kJ/m^2. The R-curves of the various samples together with the J-values at sudden crack extension, back-calculated K-values, and the crack extensions, Δa_j are shown in **Figure 3.3a**.

Crack Tip Opening Displacement

CTOD profilometry measurements from cavities near the crack tip, that form in ductile materials during crack initiation and growth, enable an alternative measure of J via $J_{CTOD} = \delta\ \sigma_y/d_n$, where δ is the CTOD value and d_n a constant dependent on work hardening and thus an alternative means to assess an alloy's fracture toughness [154]. Examples of crack path profilometry measurements taken from the mid-section at the transition of the precrack to the overload fracture region are seen in **Figure 3.4**. The fractographs of side-grooved sample with $a/W \sim 0.63$ from the equiatomic alloy, **Figure 3.5a**, and from the non-equiatomic alloys, **Figure 3.5b-d**, show the morphology of the blunting region. While the measured CTODs in TiZrHfNbTa are only ~85 µm, the CTODs in the non-equiatomic alloys range from ~207 µm in the $Ti_{40}Zr_{20}Hf_{20}Nb_{10}Ta_{10}$ alloy to ~335 µm in $Ti_{26.7}Zr_{26.7}Hf_{26.7}Nb_{10}Ta_{10}$. The corresponding J_{CTOD} in the equiatomic alloy, using $d_n = 0.78$ for a low work hardening material, is 101 kJ/m^2 and, as such, in agreement with $J_Q \sim 105$ kJ/m^2 at the first sudden crack extension. Compared to that, for the non-equiatomic alloys, J_{CTOD} range from 231-352 kJ/m^2; due to the lack of crack extension in these alloys J_Q-values according to the standard could not be determined and a direct comparison to the J_{CTOD}-numbers is hence not possible. The CTOD measurements for the various sample geometries of the TiZrHfNbTa and the non-equiatomic alloys together with the corresponding J_{CTOD}-numbers and K_{CTOD}-values are summarized in **Figure 3.4e**.

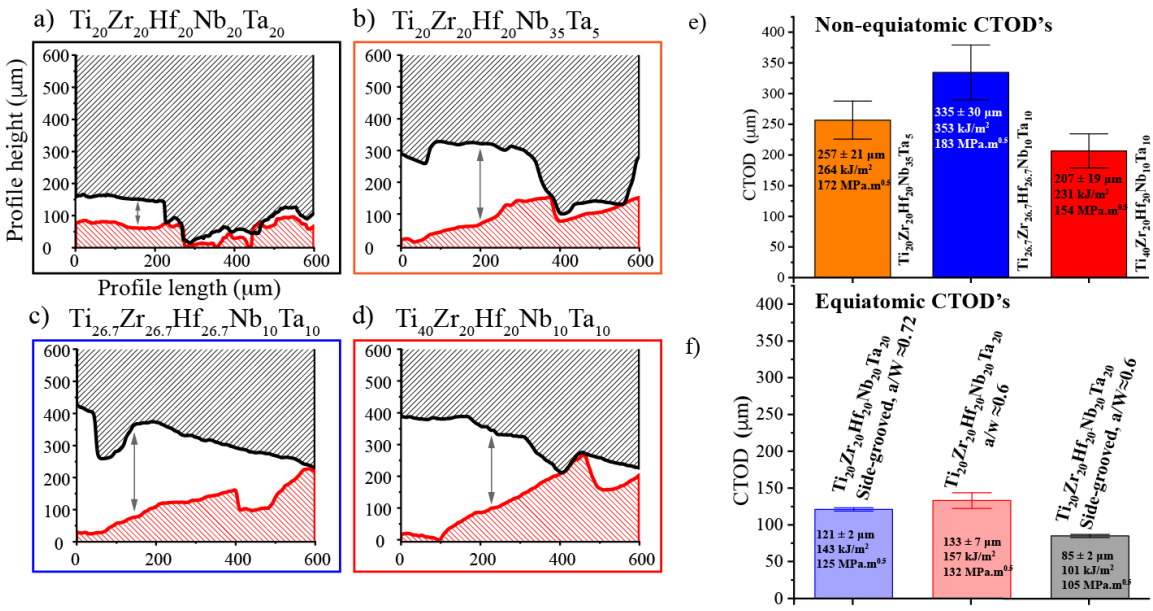

Figure 3.4: (a-d) CTOD profiles for each alloy showing location of measurements. (e) CTOD statistics for the non-equiatomic alloys and (f) the equiatomic samples, with *J* calculated using the Shih equation and K calculated using plane strain assumption.

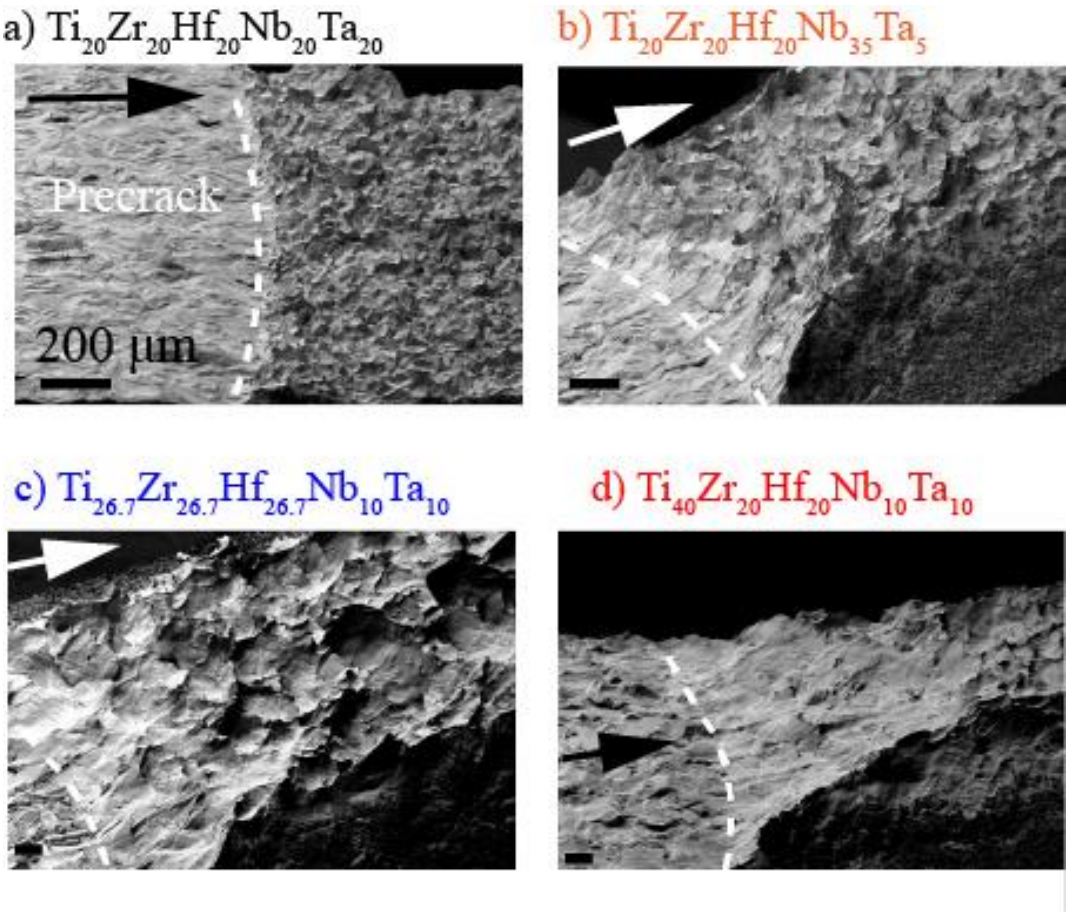

Figure 3.5: Fracture surface overviews for each alloy after testing: (a) $Ti_{20}Zr_{20}Hf_{20}Nb_{20}Ta_{20}$, (b) $Ti_{20}Zr_{20}Hf_{20}Nb_{35}Ta_{5}$, (c) $Ti_{26.7}Zr_{26.7}Hf_{26.7}Nb_{10}Ta_{10}$, and (d) $Ti_{40}Zr_{20}Hf_{20}Nb_{10}Ta_{10}$.

They clearly show the differences in fracture resistance between the equiatomic and non-equiatomic alloys, where the equiatomic samples are consistently below the non-equiatomic. Note that CTOD in the equiatomic $a/W \sim 0.72$ specimen was measured by fitting a right triangle onto the fracture surface, since both sides were preserved for EBSD analysis.

Fractography

The equiatomic alloy has an overall flat fracture surface after a relatively small stretch zone, indicating blunting at the end of the precrack, as shown in **Figure 3.5a**, and in the polished side view, **Figure 3.6a**. In stark contrast, the non-equiatomic alloys have significantly larger stretch zones that are evident in **Figure 3.5b-d**, and by the large vertical tearing seen in the side views, **Figure 3.6b-d**, followed by shear overload in the plane stress regions. Details of the fracture process in TiZrNbHfTa are indicated in **Figure 3.7**, where **Figure 3.7a** gives an overview of the fracture surface showing the extent of the tested region through the formation of the stretch zone and the overload fracture region, which contains both cleavage and dimples. The subsequent fast fracture event, that is shown as sudden crack extension in the *R*-curve in **Figure 3.3a**, is primarily governed by cleavage before the crack arrests after ~1.7 mm crack extension, shown in **Figure 3.7c**. Further crack growth occurs through sub-critical crack growth between ~1.7-3 mm crack extension, **Figure 3.7d**, after which another fast fracture event occurs, shown in the *R*-curve in **Figure 3.3a** as second 'jump' in crack extension.

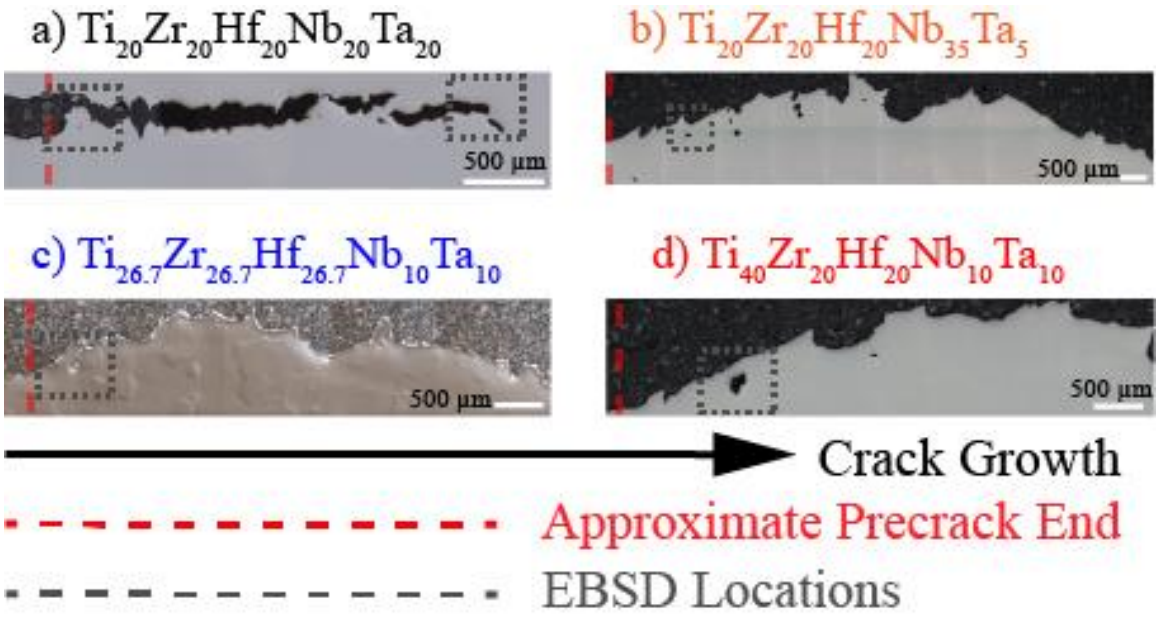

Figure 3.6: Crack paths in each alloy in OM as polished, (a) $Ti_{20}Zr_{20}Hf_{20}Nb_{20}Ta_{20}$ (b) $Ti_{20}Zr_{20}Hf_{20}Nb_{35}Ta_{5}$ (c) $Ti_{26.7}Zr_{26.7}Hf_{26.7}Nb_{10}Ta_{10}$, and (d) $Ti_{40}Zr_{20}Hf_{20}Nb_{10}Ta_{10}$. Samples are orientated the same and differences in path are solely the result of crack growth.

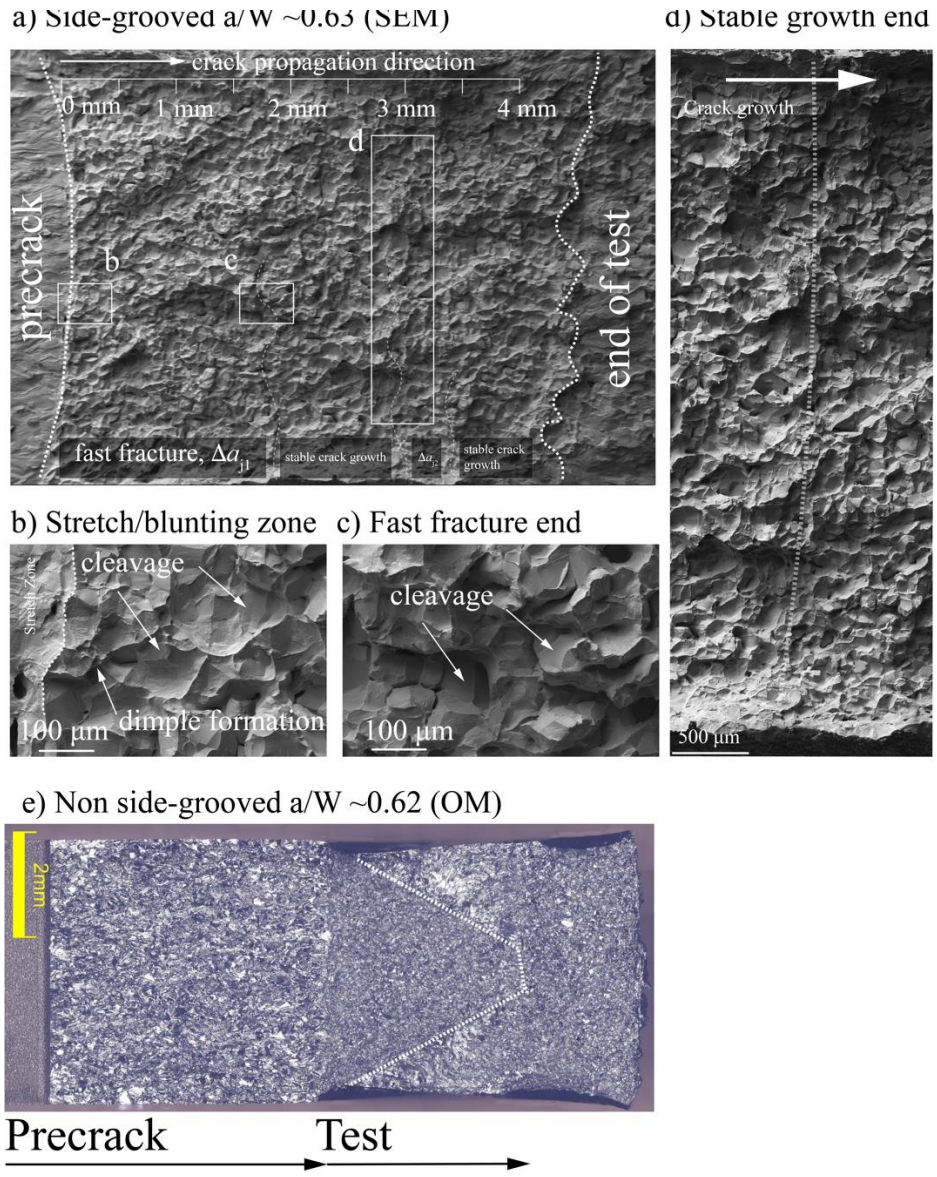

Figure 3.7: Macroscopic SEM images of the side-grooved and non-side-grooved precracked $a/W \sim 0.6$ equiatomic specimen. (a) Macroscopic image of the fracture surface with image locations overlaid. (b) Stretch/blunting region with the formation of some dimples and primarily cleavage fracture. (c) The end of sudden crack extension containing cleavage. (d) Overview of the end of sudden crack extension and beginning of a second fast fracture (roughly indicated with dotted line) showing dimpling and cleavage. Scale bars in images b-e are 100 µm. (e) OM image of non-side-grooved sample where the dotted line indicates the crack growth during testing resulting in a tunneled fracture surface.

In **Figure 3.7d**, crack tip blunting and the formation of dimples at the onset of fast fracture do not occur uniformly throughout the entire thickness of the sample but at individual locations along the crack front. For the non-side-grooved sample, the OM image in **Figure 3.7e** shows that the lack of crack-tip triaxiality throughout the sample thickness results in pronounced tunneling with significantly more crack extension in the center of the sample than closer to the surface [156].

Comparatively, the non-equiatomic alloys exhibit extensive plastic deformation during testing, as shown through the thickness contractions in the OM macroscopic views, **Figure 3.8a-c**, and the resulting pronounced stretch zones, **Figure 3.8d-f**, that lead to excessive crack tip blunting and fully ductile failure, as evident from the fracture surface overviews **Figure 3.5** and **Figure 3.6b-d**. Detailed examples of the fracture surfaces, **Figure 3.8g-i**, show that failure in these alloys occurs primarily through the formation of cavities and dimples that leads to pronounced shear offset throughout localized regions on the fracture surface and, ultimately, in tearing. As a result, crack growth occurs without clearly distinguishable inter- and transgranular features that would indicate cleavage fracture as in the equiatomic alloy. EBSD scans from bisected samples of the equiatomic alloy, **Figure 3.9a** and **Figure 3.10a**, and the non-equiatomic alloys, **Figure 3.9b-d**, show differences in the micromechanisms of the materials. Crack propagation in $Ti_{20}Zr_{20}Hf_{20}Nb_{20}Ta_{20}$ occurs primarily along the grain boundaries with only limited plastic deformation within the grains in the vicinity of the propagated crack and the formation of few kink bands along the crack path that have previously been

reported to extensively form in this alloy [151, 157]. Despite the intergranular failure, crack propagation appears to occur with the formation of voids, as evident from cavities that form at the grain boundaries, shown in **Figure 3.9a**, and ahead of the crack tip in **Figure 3.10a**. Further evidence for this mechanism, that is typical for ductile materials, can be seen in **Figure 3.10b**, where facets at a grain boundary indicate the formation of dimples. Compared to that, the non-equiatomic alloys show fully ductile failure characteristics with pronounced grain misorientations along the path of the propagated crack, grains contorted towards the tensile direction, and extensive plastic deformation throughout the sample, **Figure 3.9b-d**. While there are no signs of cleavage in the non-equiatomic alloys, there are cavities forming along grain boundaries near the crack path and a few locations of heavily distorted grain boundaries indicate decohesion and intergranular tearing. Furthermore, there is significantly more kink band formation than in the equiatomic alloy, similar to what has been reported for $Ti_{20}Zr_{20}Hf_{20}Nb_{20}Ta_{20}$ in previous studies [157].

Discussion

The fracture behavior of the equiatomic alloy is distinct from the non-equiatomic alloys. J_Q was not the same in equiatomic alloy with the changes in specimen geometry; J_{CTOD} increases to 143 kJ/m^2 with $a/W \sim 0.72$ and 157 kJ/m^2 with the removal of side grooves, indicating an issue of size constraint. J_{CTOD} for the equiatomic alloy correlate well with the *R*-curve, particularly the side grooved specimens, since J_Q is based on sudden crack extension rather than 0.2 mm regression.

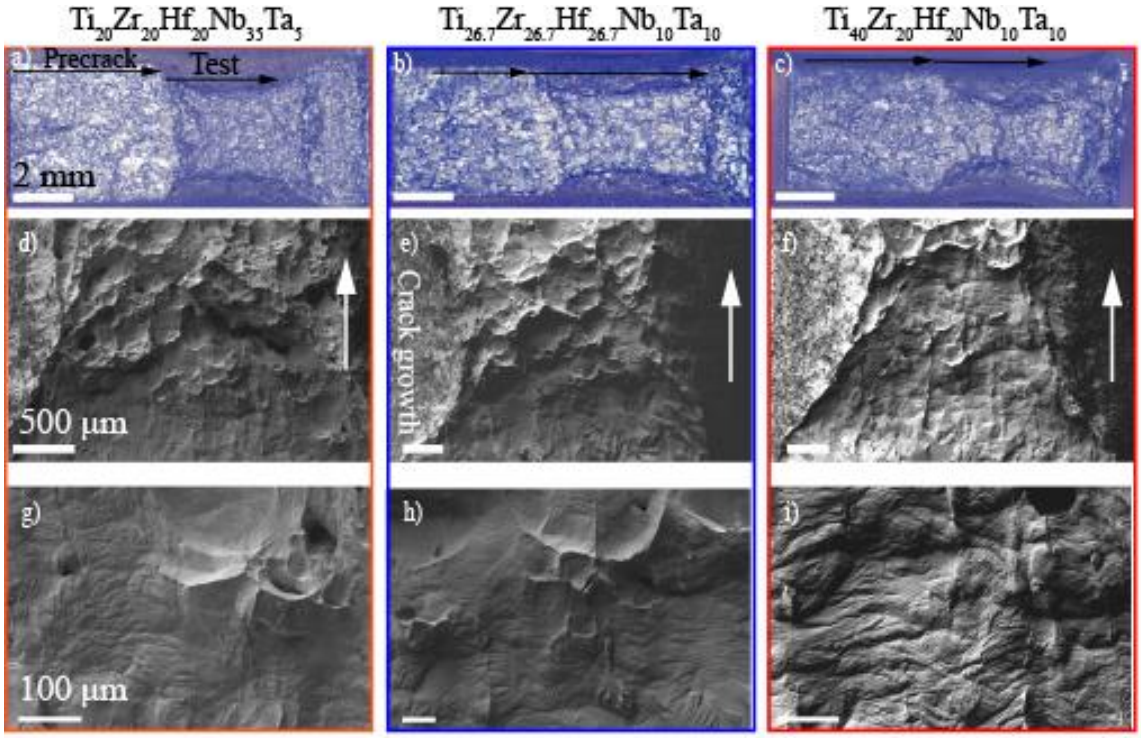

Figure 3.8: Fracture surface analysis in the non-equiatomic alloys: (a,d) $Ti_{20}Zr_{20}Hf_{20}Nb_{35}Ta_5$, (b, e) $Ti_{26.7}Zr_{26.7}Hf_{26.7}Nb_{10}Ta_{10}$, and (c, f) $Ti_{40}Zr_{20}Hf_{20}Nb_{10}Ta_{10}$. (a-c) Fracture surfaces of the tested specimens, scale bar is 2 mm. (d-f) Fracture surfaces near the precrack showing the blunted portion of the extended crack.

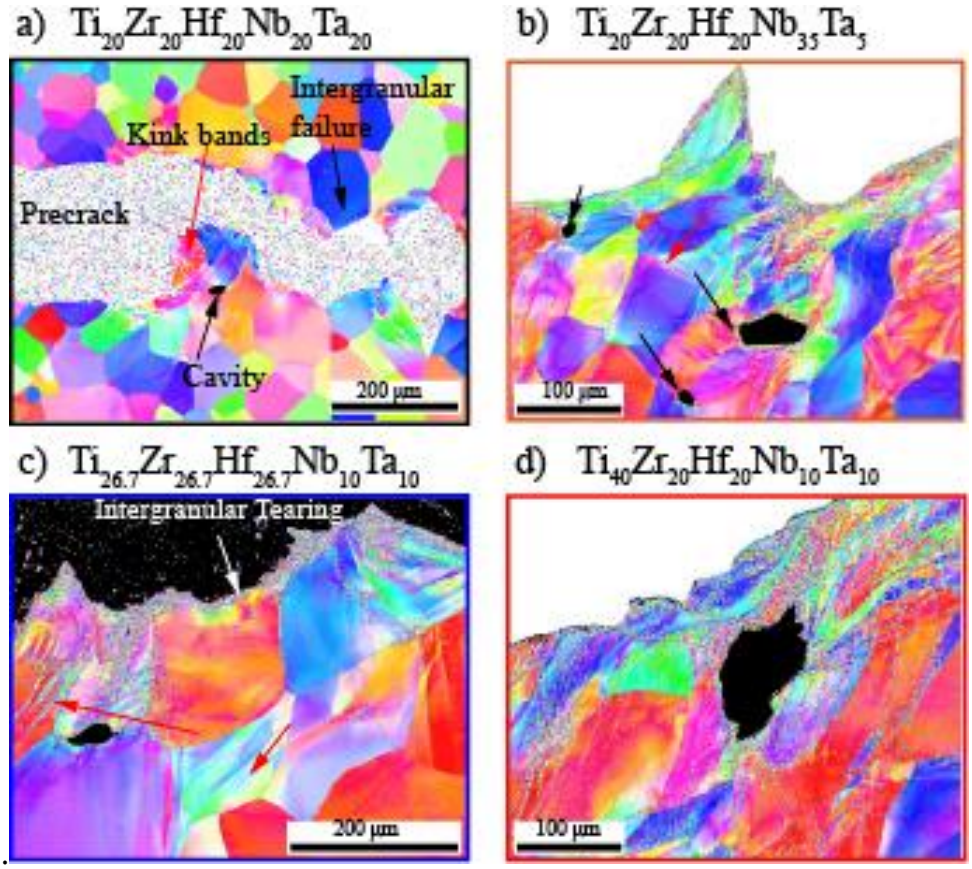

Figure 3.9: EBSD scans taken near the precrack of samples that were bisected after testing: (a) side-grooved $Ti_{20}Zr_{20}Hf_{20}Nb_{20}Ta_{20}$ with $a/W \sim 0.72$, (b) $Ti_{20}Zr_{20}Hf_{20}Nb_{35}Ta_{5}$, (c) $Ti_{26.7}Zr_{26.7}Hf_{26.7}Nb_{10}Ta_{10}$, and (d) $Ti_{40}Zr_{20}Hf_{20}Nb_{10}Ta_{10}$. Black arrows show cavities, red arrows kink bands, and white arrows intergranular failure. The cavities were manually cropped to black since they were falsely indexed during EBSD. Locations of EBSD scans are shown in Figure 3.6.

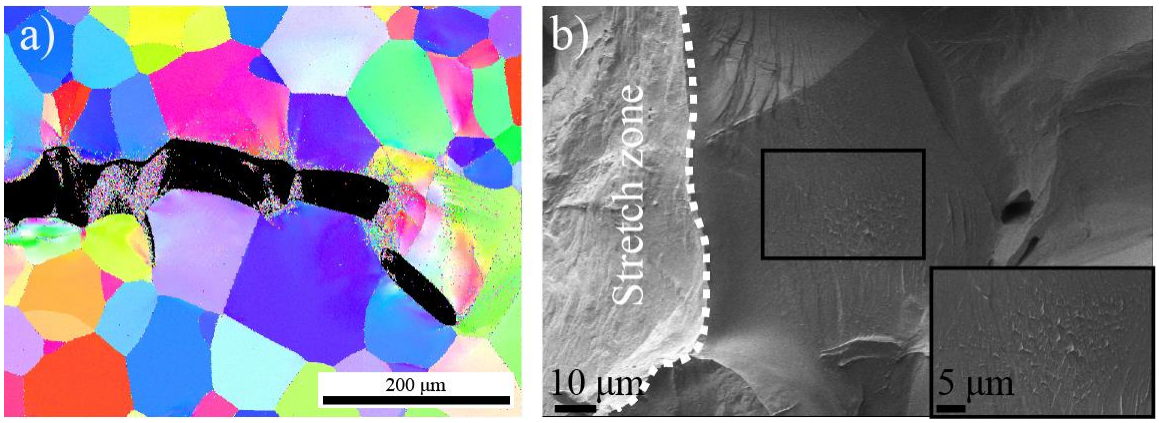

Figure 3.10 Micromechanisms occurring during crack growth in the equiatomic alloy. (a) EBSD image showing intergranular failure with a hairline fracture before a blunted intergranular void. (b) Micrograph near the precrack/blunted region showing a grain facet with small dimples, dimples magnified in insert.

Conversely, the non-equiatomic alloys - despite being side grooved - have plastic contraction, seen in the fracture surfaces **Figure 3.8a-c** by the change in thickness, resulting in poor constraint which inflate J-values. The non-equiatomic *R*-curves are abnormal in that they are almost parallel to their respective blunting lines and make their interpretation unfeasible with ASTM E1820. This behavior can be better described as the material tearing and does not display the usual power law behavior associated with meaningful crack growth. The ductile behavior of the non-equiatomic alloys can be seen in the standard deviations in the CTODs: the excessive plastic deformation caused greater variability in the measured non-equiatomic CTODs compared to the equiatomic CTODs. The profiles for CTOD measurements were not rotated, making them conservative measurements but more erroneous at higher CTOD measurements.

The cause of the equiatomic brittle fracture behavior cannot be understood through the *R*-curves alone and requires further analysis of the fracture surfaces. The initial blunting at the precrack has intermittent regions of dimpling within ~170 μm of the blunted precrack, **Figure 3.7b**. Past the blunted region, the sudden crack extension region is predominantly cleavage and intergranular failure with little to no dimpling, **Figure 3.7c** , and transitions into a blunting region with dimpling but not covering the whole thickness of the specimen, **Figure 3.7d**. It occurs at a similar distance as where the R curve indicates the end of the sudden crack extension (first gap in the black curve **Figure 3.3a**). The dimple formation in the middle of the sample is indicative of dynamic mechanical constraint where crack tip triaxiality is sufficient near the crack tip to cause

sudden crack extension but insufficient further down the ligament to continue. Lack of sufficient triaxiality is further confirmed in the non-side grooved specimen, **Figure 3.7e**, where the tunneled surface is an indication that crack tip triaxiality is insufficient to uniformly extend the crack [156]. EBSD scans in the equiatomic alloy, **Figure 3.9a** and **Figure 3.10a**, show that void and crack growth occur intergranularly. Near the blunting region, **Figure 3.10b**, initial dimples formed along the grain facet indicating that the grain boundary is the most likely site of dimple-cavity formation in the equiatomic alloy. The non-equiatomic alloys also show similar intergranular behavior. The intergranular features in **Figure 3.9b-d**, notably grain boundary cavities and kink bands that either start or end at grain boundaries, indicate that the non-equiatomic alloys, despite being very fracture resistant, are mechanistically prone to grain boundary failure. While all these alloys show roughly similar tensile behavior, as indicated in Chapter 2, the equiatomic alloy does have the highest yield strength and ultimate tensile strength.

The previous fracture toughness test performed by Fan et al. [151] on the equiatomic alloy had a J_{IC} of 384 kJ/m^2 in a three-point bend geometry where the limiting dimension was the initial ligament at 4.54 mm. Our study has a ~5 mm thickness with an initial ligament ranging from 6.4 mm to 4.48 mm. The blunting seen in the non-equiatomic alloys is similar to Fan et al.'s results, but the equiatomic alloy in the current study does not behave accordingly. The difference between Fan et al.'s study and the current study could be attributed to specimen geometry and constraint. *T*-stress, the transverse stress, has been used as a measurement of crack constraint [158, 159] and has

previously been correlated with embrittling fracture behavior in A533 steel measuring *J* and *T*-stress [160]. Using the plane-strain values from Sherry et al. [161], the C(T) geometry used in this study had a biaxiality ratio $\left(\beta = T\sqrt{\pi a}/K_I\right)$ of 0.59 and the three-point bend geometry in Fan et al.'s study had 0.46, indicating lower constraint in the three-point bend geometry. While *T*-stress is an elastic stress, *J*-*Q* finite element analysis, where *Q* is a unitless description of triaxiality, is better suited to describe triaxiality during plastic deformation [162]. Both the three-point bend [162] and the C(T) [163] geometries have similar trends in *Q* during deformation with high triaxiality at low deformation followed by constraint loss with increased *J* (deformation is normalized as $J / b\ \sigma_{ys}$) but a shorter initial ligament loses constraint at lower *J*-values. Interestingly with the side grooved equiatomic specimens, the length of sudden crack extension decreases linearly with $J / b\ \sigma_{ys}$, where *J* and *b* are *J*-value and the ligament before the sudden crack extension, **Figure 3.11**. The plot does not include the non-side grooved specimen since the constraint along the crack front is different from the side grooved specimens. The decreasing trend would indicate that the sudden crack extension is dependent on the initial crack geometry and deformation rather than the material. Increasing $J / b\ \sigma_{ys}$ results in constraint loss and would decrease the amount of material under sufficient constraint for the crack to extend suddenly. While the relationship has no physical meaning outside the first quadrant, i.e. with enough deformation the crack extends backwards, the trend indicates that with a sufficiently small ligament sudden crack extension can be avoided.

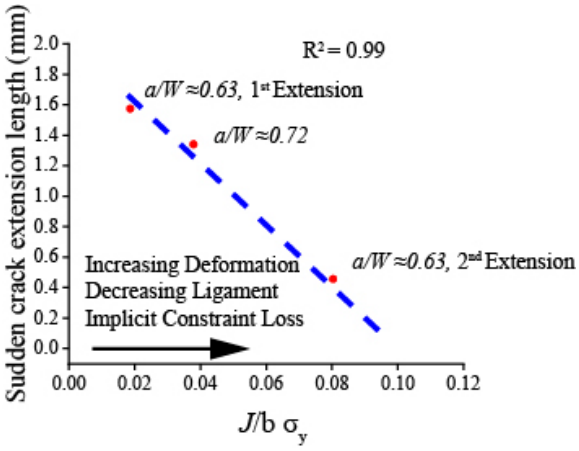

Figure 3.11 Normalized deformation ($J/b\ \sigma_y$) against the sudden crack extension length, *a/W* corresponds to the specimen in **Figure 3.3a** – not the length of crack taken at measurement.

The difference between fracture behavior in the non-equiatomic and equiatomic alloys could be attributed to the equiatomic alloy's higher yield strength resulting in a dynamic mechanical constraint [164]. Sudden crack extension has previously been investigated, referred to as pop-in [164], and is associated with heterogenous microstructures such as welds [165], and chemical segregation [166], but does occur in homogenous microstructures with yield phenomena [167] and dynamic mechanical constraint [164, 168]. The crack growth behavior in the equiatomic is consistent with similarly strong bainitic steel [168]. The bainitic steel had a homogenous microstructure of 50 μm prior austenite grains and 10 μm bainite colonies, distributed uniformly, where cleavage facets were similarly sized as the prior austinite grains and dimple size consistent with bainite colonies. The equiatomic alloy has the high strength that allows for high triaxial stress near the crack tip but insufficiently large stresses further away to maintain constraint and extend the crack throughout the whole ligament. The lack of meaningful dimple formation in the equiatomic is likely the result of no secondary phases to provide a cavity nucleation site and the high triaxial stresses at the crack tip preventing void growth. The non-equiatomic alloys, however, have sufficiently low yield strengths to prevent dynamic constraint and allow for dimple formation and tearing. The lack of secondary phases makes grain boundaries the most likely microstructural feature to accommodate voids and deformation.

The issue of crack tip constraint has been previously addressed in fracture mechanics and the issue can be summarized as "*low work hardening materials increase*

plastic zone sizes and break constraint". E813, the previous standard for *J* testing [169], used $B, b_0 > 25\ J / \sigma_y$ as the size requirement. The sample size requirement was relaxed to $B, b_0 > 10\ J / \sigma_f$ using data from DIN 22NiMoCr37 steel [170, 171]. However, TiZrHfNbTa type alloys typically exhibit little work hardening and little uniform strain [46, 72, 83] with previously reported work hardening increments ranging from 30 MPa to 120 MPa [46, 72]. Therefore, it does not require much crack growth before the plastic zone size increases to unacceptable levels and the surrounding elastic constraint is lost. A similar problem occurred in strain-softening bulk metallic glasses [172] where the elastic K_{IC} size requirements were determined to be reasonable for bulk metallic glasses but the E1820 size requirements were too lenient to measure size-independent fracture toughness. For determining the true (i.e., size-independent) fracture toughness of TiZrHfNbTa alloys, sample sizes should be increased. Increasing the sample size should not only focus on thicker specimens but also include larger initial ligaments to maintain constraint [162]. The difficulty in processing large ingots of TiZrHfNbTa alloys places practical size limitations but future tests might try to achieve E813 size requirements ($B, b_0 > 25\ J / \sigma_y$) to ensure valid fracture toughness measurements. A more practical approach for designing future experiments might use the E1820 [153] size requirements for sudden crack growth ($B, b_0 > 100\ J / \sigma_f$). This would place B and b_0 at 11 mm for sudden crack extension at $J_Q = 100$ kJ/m^2; while placing the upper valid J_Q limit on regular size requirements at ~400 kJ/m^2 using $B, b_0 > 25\ J / \sigma_y$. Using the sudden crack

extension size requirement does make sample preparation more difficult but would provide clarity to the fracture toughness behavior of TiZrHfNbTa alloys.

Conclusions

This study investigated the fracture behavior in equiatomic and compositionally modified TiZrHfNbTa alloys. Alloys were prepared by arc-melting, homogenization, cold-rolling, and recrystallization. All the alloys had a similar microstructure with a single-phase BCC microstructure with grain sizes 82 µm – 223 µm, after recrystallization as determined by XRD and SEM.

Two distinct fracture behaviors were seen in C(T) J_I tests: the equiatomic TiZrHfNbTa had sudden crack extension after an initial blunting, and the non-equiatomic alloys showed extensive blunting and tearing. CTOD measurements from profilometry show that $Ti_{26.7}Zr_{26.7}Hf_{26.7}Nb_{10}Ta_{10}$ had the highest CTOD at 335 µm and TiZrHfNbTa the lowest at 85 µm, in the most constrained sample, with respective *J*-values of 353 kJ/m^2 (183 MPa.m$^{0.5}$) and 100 kJ / m^2 (105 MPa m$^{0.5}$). Analyzed with EBSD on bisected specimens, the main crack propagation mechanism in the equiatomic alloy, after blunting, was intergranular and transgranular cleavage; while the non-equiatomic alloys had stable tearing, and intergranular cavity formation. As seen in previous studies, kink bands were near the crack path in all alloys but more prevalent in the non-equiatomic alloys.

While this study did not replicate the results in Fan et al.'s study [151] on the equiatomic alloy, similar behavior was seen in the non-equiatomic alloys, though the tests did not meet ASTM E1820 requirements making all fracture toughness values in this

study geometry dependent. Due to the low work hardening in TiZrHfNbTa alloys, it is possible that the E1820 J_{IC} size requirements could be inappropriate in analyzing the fracture behavior. Future tests should focus on achieving larger specimen sizes to determine J_{IC} so that sufficient constraint is ensured. In the context of room temperature mechanical behavior, the lower fracture toughness of 105 MPa.m$^{0.5}$ found in this study – though an overestimate – would still be a structurally functional material, akin to fracture toughness values seen in solution treated β-titanium alloys [173, 174].

Appendix – Supplementary Material

Supplementary Table 3.1: Compositions reported in **Table 3.2** converted to atomic percent for metallic elements and atomic parts per million for interstitial elements.

Alloy	Ti	Zr	Hf	Nb	Ta	N	O	C
$Ti_{20}Zr_{20}Hf_{20}Nb_{20}Ta_{20}$	21.9	19.5	15.5	22.5	19.9	729	2552	2251
$Ti_{20}Zr_{20}Hf_{20}Nb_{35}Ta_{5}$	20.6	19.6	15.6	36.8	6.9	806	1091	2037
$Ti_{26.7}Zr_{26.7}Hf_{26.7}Nb_{10}Ta_{10}$	41.6	20.2	16.0	10.1	11.5	705	987	2937
$Ti_{40}Zr_{20}Hf_{20}Nb_{10}Ta_{10}$	28.4	26.7	21.0	11.5	12.1	155	340	1079

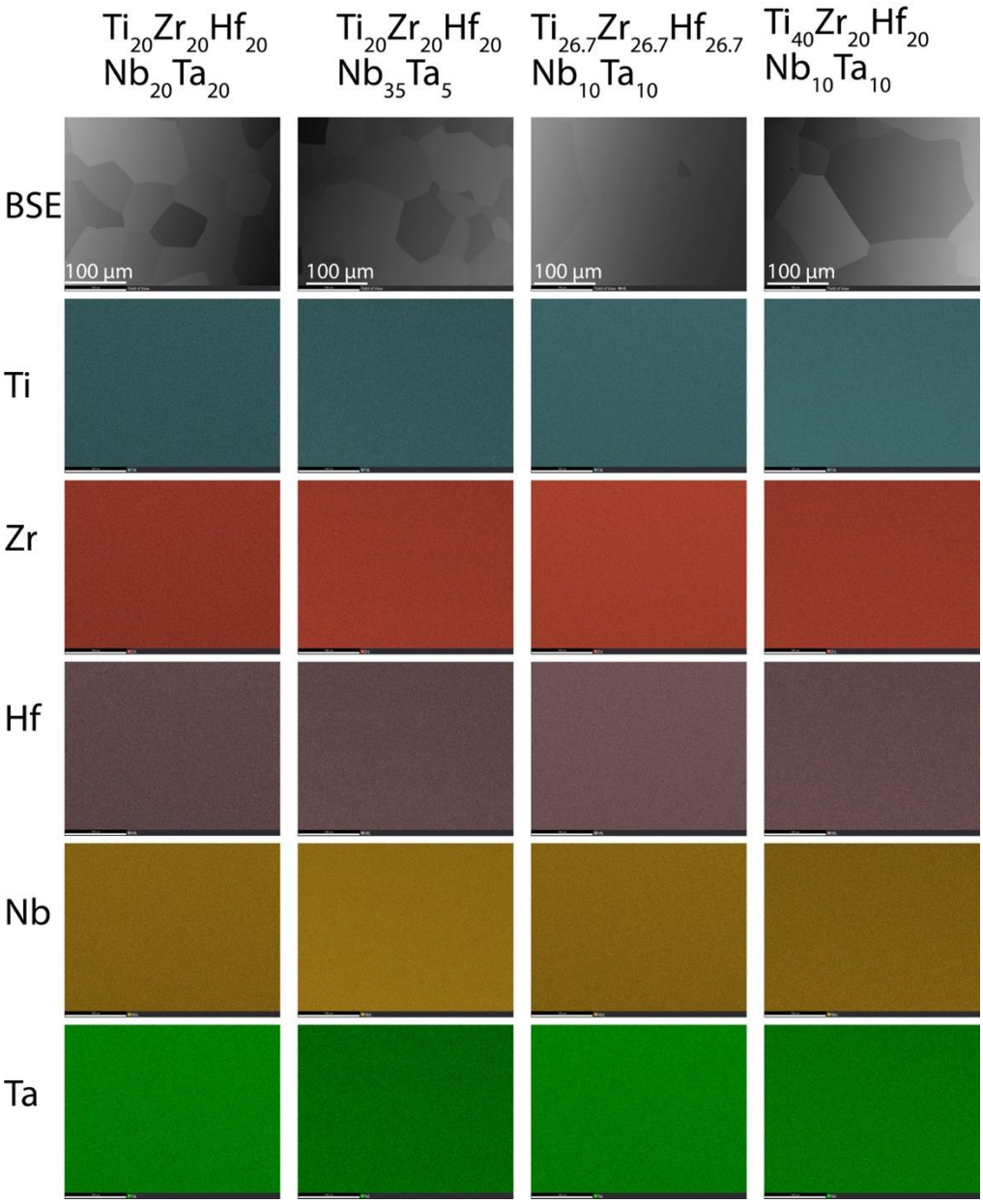

Supplementary Figure 3.1: BSE images and their complementary EDS maps. EDS was performed at 20 kV and 10 nA. The maps do not show any significant inhomogeneities in the alloys.

Chapter 4 Thermal stability in derivative Senkov alloys

This work is being prepared for publication. WJ Carpenter performed the specimen preparation, microscopy, analysis, and wrote the first draft. Y. Yang performed CALPHAD analysis. EP George conceived and supervised the study and edited the drafts.

Abstract

Derivatives of TiZrHfNbTa were annealed in vacuum for times to 4800 h at 700 ˚C and 1000 ˚C followed by water quenching to assess their thermodynamically stable microstructures. At 700 ˚C, microstructures included single-phase body centered cubic (BCC) with incidental secondary phases, homogenously precipitated secondary phases in BCC grains, and lamellar microstructures comprising hexagonal close-packed (HCP) and BCC layers. Among these, only the lamellar structure, deduced to be from a decomposition reaction rather than a eutectoid, shows substantial hardening after 48 h at 700 ˚C. After the 1000 ˚C anneals, specimens show predominately BCC grains with incidental secondary phases at the grain boundaries. Hardness tests however indicate that the 1000 ˚C heat treated specimens at 4800 h absorbed interstitial elements, which confounds the interpretation of thermal stability. Nevertheless, it is believed that the stability of the BCC phase is not due to oxygen absorption but rather because it is inherently stable at 1000 °C.

Introduction

RHEAs are being investigated for high temperature applications. Initial interest was spurred by the relatively high yield strengths of NbTaMoW and VNbTaMoW [19]

and the room temperature ductility of TiZrHfNbTa [46]. A “classic” RHEA is single-phase [12] and runs contrary to the fact that many engineering materials such as pearlitic steels, precipitation hardened Al, and *γ/γ’* Ni-base superalloys are not single-phase microstructures. TiZrHfNbTa alloys can be processed by cold rolling [46], while VNbTaMoW cannot [19], rendering TiZrHfNbTa more amendable to alloy design. Adhering to the single-phase microstructure does not provide many avenues for modifying material properties: compositions can be changed but usually requires a gross change and it is difficult to know whether useful alloys will result. If processing permits, grain size and dislocation density can be modified but are not ideal for high temperature application since smaller grains promote creep and the increased dislocation density will disappear by recovery and dynamic recrystallization, lowering the strength during service [175]. In the few creep studies done on TiZrHfNbTa alloys [24, 25, 28], TiZrHfNbTa underperforms compared to single-crystal Ni-base superalloys [24].

To have high temperature strength, RHEAs need multiphase microstructures. The secondary phases of TiZrHfNbTa appear between 500 ˚C and ~1000 ˚C [47]. Secondary BCC phases form between 500 ˚C - 900 ˚C in high pressure torsion samples [47] and at 800 ˚C in conventionally processed material [23, 29, 120]. At 980 ˚C, the BCC phase forms within the gauge section of creep specimens after 61 h [24], implying stress assisted precipitation. HCP phases emerge at 500 ˚C to 800 ˚C in high pressure torsion samples [47], as also seen in conventionally processed material [120]. Fewer studies have been performed on the thermal stabilities of derivatives of TiZrHfNbTa. HfNbTaTi

annealed at 1400 ˚C for 35 h showed a homogenized microstructure [48]. Unexpectedly, annealing of TaNbZrHf at 1800 ˚C for 192 hours results in Hf-Zr rich HCP and NbTa rich BCC phases [49]. So far, secondary phases in TiZrHfNbTa appear to be only detrimental to ductility, both at high temperature [23] and at room temperature [29, 47]. Purposeful additions of intermetallic formers to RHEAs have been used to specifically obtain desirable microstructures. Initial results by Senkov et al. on $AlMo_{0.5}NbTa_{0.5}TiZr$ showed a promising B2 + BCC microstructure that looked similar to γ/γ' superalloys [51]. While the initial issue of inverting the microstructure from a B2 matrix with BCC precipitates to a BCC matrix with B2 precipitates was solved relatively quickly [53], there remains the detrimental transformation of the B2 phase to an ω phase [56]. More recent work on finding suitable B2 formers has suggested Ru being the most suitable candidate [59]. Significant effort has been put into understanding HfRu [60-62] and HfZr [60] precipitates as well as modifying matrix compositions to suitably fit the precipitates [60].

Regardless of whether or not the Ru and Al additions will result in multi-phase alloys that have suitable creep properties, there is still a need to understand the thermal stability of single-phase RHEAs. Simply put, if a RHEA matrix is used with an intermetallic compound, the matrix by itself will still have thermal stability issues to contend with at intermediate temperatures such as cyclic heating and cooling in jet turbines during takeoff and landing [116]. There is a dearth of long-term heat treatments on TiZrHfNbTa derivatives at intermediate temperatures. At the very least such data can

be used to assist CALPHAD calculations, but more importantly, such studies can provide insight on issues and opportunities that can arise from the intermediate microstructures. In this study, the same TiZrHfNbTa derivatives as described in previous chapters were subjected to long term heat treatments up to 4800 h. Their microstructural evolution was studied with SEM and XRD.

Methods

Alloys were arc-melted and flipped five times before being dropped cast into 25.4 mm x 25.4 mm x 25.4 mm copper mold. Afterwards, the alloys were homogenized for 24 h at 1200 ˚C in quartz capsules and cold rolled to 80% reduction. From here, samples were either left in the cold rolled state to provide nucleation sites for secondary phases (at dislocations) or were recrystallized at 1200 ˚C for 1 h to obtain a lower-energy starting state. The processing flow is shown in **Figure 4.1**. Specimens were then prepared in the following order: mechanically ground, sonicated in soapy deionized (DI) water, cleaned with 2:1 water to nitric acid, rinsed with distilled water, sonicated in ethanol and dried. The cleaned samples were encapsulated in quartz under vacuum with at least three purges with high purity argon and placed in a tube furnace at 700 ˚C and 1000 ˚C for 48 h, 480 h, and 4800 h. After each of the above times, the corresponding specimens were quenched in water by breaking the quartz ampoule.

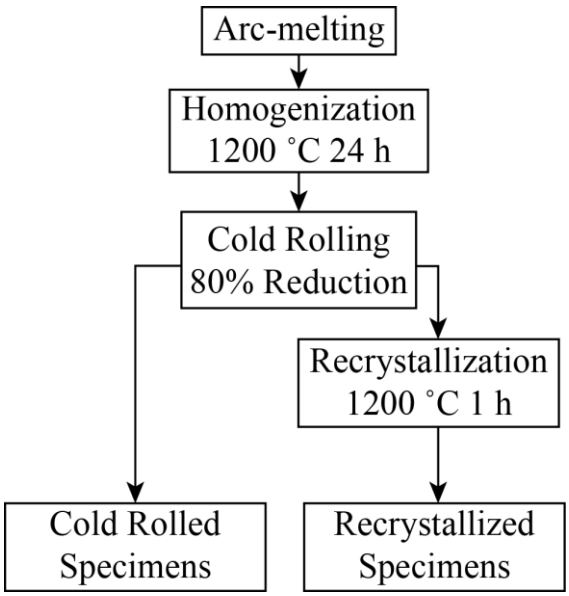

Figure 4.1: Specimen processing where the recrystallized specimens go through an additional heat treatment to obtain equiaxed microstructure.

Hardness was performed with Shimadzu Vickers HMV-G hardness tester using 0.3 kgf, with specimens at least three diagonal lengths away from surface and spaced throughout the entire sample. The reported hardness values are averages of five indents each.

Specimens were prepared for X-ray diffraction (XRD) by grinding with SiC paper to 2000 grit. X-ray diffraction was performed on Malvern Panalytical Emperyan with a Cu kα source. Microscopy specimens were mounted and polished to 2000 grit with SiC and polished with colloidal silica in vibratory polisher. Scanning electron microscopy (SEM) was performed with Zeiss Gemini at 20 kV with an Ultim Max 100 Oxford EDS detector and Bruker xFlash EDS detector. CALPHAD calculations are described under *CALPHAD Calculations* in the methods section of Chapter 2.

Results and Discussion

Summary of microstructures

A complete set of XRD patterns are provided in supplementary material under *Initial Condition XRD* and *700 ˚C and 1000 ˚C XRD*. Their indexed phases are summarized in **Table 4.1** for the convenience of the reader. In short, three distinct behaviors are seen: (i) strong BCC peaks that can have low intensity secondary phases at what appear to be HCP peak locations, (ii) BCC with a similar 2θ to the initial BCC phase with HCP peaks, (iii) BCC with high intensity HCP peaks but the BCC peaks have a smaller lattice parameter as indicated by higher 2θ angle.

Table 4.1: Summary of indexed crystal structures from the XRD patterns shown in **Supplementary Figure 4.10 - 4.12**. BCC represents single-phase BCC and U represents unknown peaks, (i) BCC+HCP represents a two-phase structure in which the BCC phase has similar 2θ as the single BCC, and (ii) BCC+HCP represents a two-phase structure where the BCC peak is at a higher angle. Minor unknown peaks are labeled in the supplementary material.

Alloy		Temperature (˚C)	Condition	48 h	480 h	4800 h
$Ti_{20}Zr_{20}Hf_{20}$	$Nb_{35}Ta_5$	1000	Cold Worked	BCC	BCC + U	BCC + U
		1000	Recrystallized	BCC	BCC	BCC + U
		700	Cold Worked	BCC + U	BCC	BCC + U
		700	Recrystallized	BCC + U	BCC	BCC
$Ti_{40}Zr_{20}Hf_{20}$	$Nb_{10}Ta_{10}$	1000	Cold Worked	BCC	BCC + U	BCC
		1000	Recrystallized	BCC	BCC + U	BCC + U
		700	Cold Worked	BCC + U	BCC + U	BCC
		700	Recrystallized	BCC + U	BCC + U	BCC
$Ti_{26.7}Zr_{26.7}Hf_{26.7}$	$Nb_{10}Ta_{10}$	1000	Cold Worked	BCC	BCC	BCC
		1000	Recrystallized	BCC	BCC	BCC
		700	Cold Worked	(i) BCC+HCP	(i) BCC+HCP	(i) BCC+HCP
		700	Recrystallized	(i) BCC+HCP	(i) BCC+HCP	(i) BCC+HCP
$Ti_5Zr_{20}Hf_{35}$	$Nb_{20}Ta_{20}$	1000	Cold Worked	BCC	BCC	BCC + U
		1000	Recrystallized	BCC	BCC	BCC
		700	Cold Worked	(ii) BCC+HCP	(ii) BCC+HCP	(ii) BCC+HCP
		700	Recrystallized	(ii) BCC+HCP	(ii) BCC+HCP	(ii) BCC+HCP

Most of the 1000 ˚C specimens, omitting $Ti_5Zr_{20}Hf_{35}Nb_{20}Ta_{20}$ at 4800 h and some of $Ti_{40}Zr_{20}Hf_{20}Nb_{10}Ta_{10}$, fall into the first category as well as $Ti_{20}Zr_{20}Hf_{20}Nb_{35}Ta_5$ and $Ti_{40}Zr_{20}Hf_{20}Nb_{10}Ta_{10}$ after heat treatment at 700 ˚C. $Ti_{26.7}Zr_{26.7}Hf_{26.7}Nb_{10}Ta_{10}$ at 700 ˚C and $Ti_5Zr_{20}Hf_{35}Nb_{20}Ta_{20}$ at 1000 ˚C for 4800 h fall into the second, and only $Ti_5Zr_{20}Hf_{35}Nb_{20}Ta_{20}$ at 700 ˚C fits into the third. Example XRDs for the 700 ˚C 4800 h samples are shown in **Figure 4.2**. The initial starting material is all single-phase as indexed by XRD. Quantification of the phase fractions is not possible because small sample sizes lead to displacement error and large grains after annealing result in textured peaks. Powder production by filing is not possible because the alloys are ductile. Furthermore, the displacement error convolutes lattice parameter measurements.

A full set of micrographs along with EDS results are provided in the supplementary material, under *Initial Condition SEM-EDS* and *700 ˚C and 1000 ˚C SEM-EDS*, ordered with respect to their initial condition, time and anneal temperature. Three distinct microstructures are seen after 700 ˚C heat treatments: (i) large BCC grains with incidental secondary phases, (ii) precipitated HCP secondary phases, and (iii) lamellar HCP-BCC. The microstructural results are summarized in **Table 4.2**. The initial starting microstructures are single-phase as seen by SEM-EDS, corroborating the XRD.

Alloy microstructures

Both $Ti_{20}Zr_{20}Hf_{20}Nb_{35}Ta_5$ and $Ti_{40}Zr_{20}Hf_{20}Nb_{10}Ta_{10}$ are predominately BCC but have secondary phases occurring at the grain boundaries at 700 ˚C an example of which is seen in **Figure 4.3** for $Ti_{20}Zr_{20}Hf_{20}Nb_{35}Ta_5$.

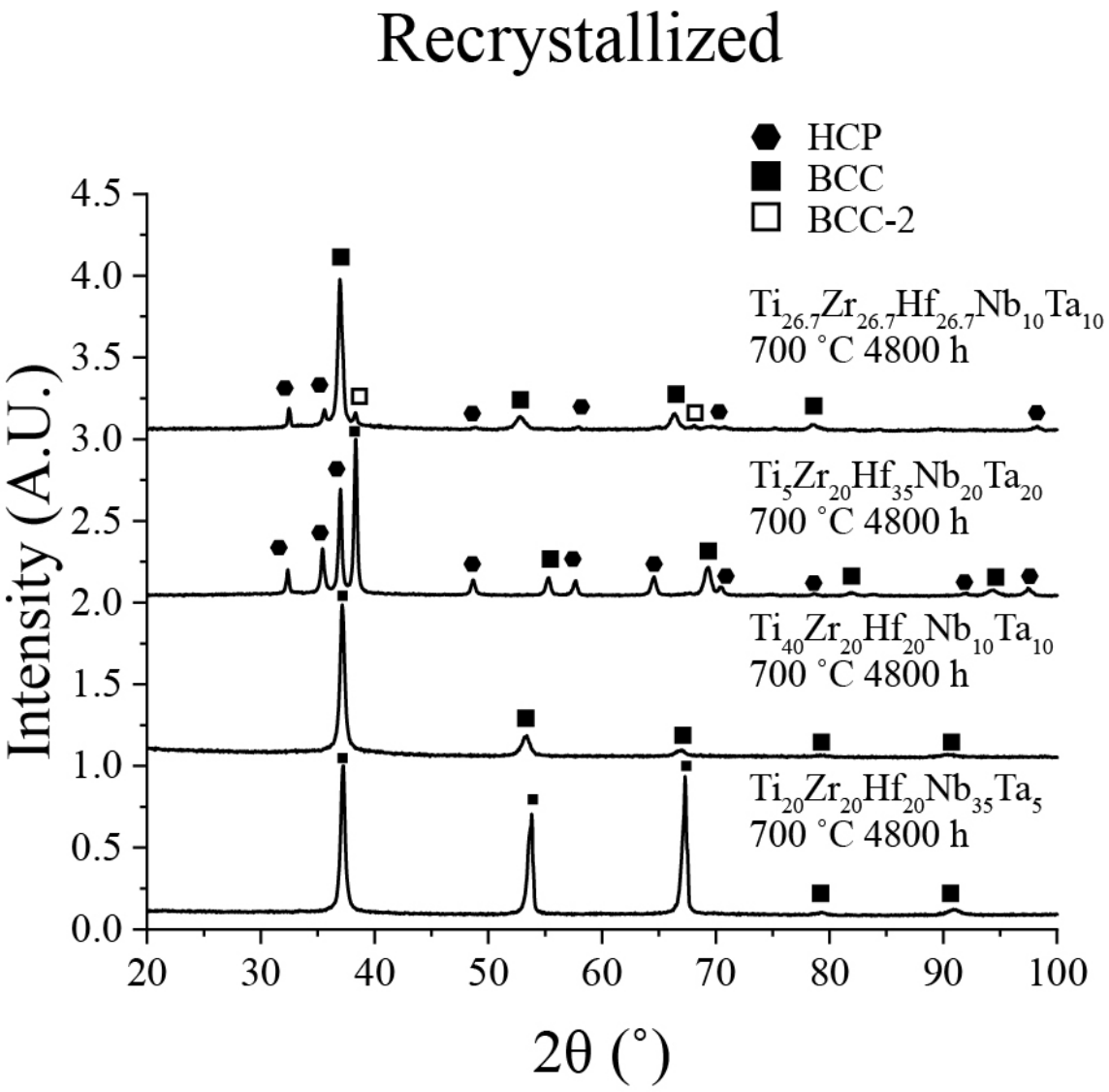

Figure 4.2: Representative XRD patterns taken after 700 ˚C heat treatment showing the indexed phases.

Table 4.2: Summary of observed phases in SEM. BCC is for predominately large grain microstructures, with incidental minor phases at grain boundaries noted as BC-GB (m), while minor phases not at grain boundaries noted as BCC-(m), and BCC-GB (l) is for larger grain boundary phases. BCC+HCP represents the more classically nucleated BCC-HCP microstructure as to the lamellar.

Alloy		Temperature (˚C)	Condition	48 h	480 h	4800 h
$Ti_{20}Zr_{20}Hf_{20}$	$Nb_{35}Ta_5$	1000	Cold Worked	BCC	BCC-GB (m)	BCC-GB (m)
		1000	Recrystallized	BCC-GB(m)	BCC-GB (m)	BCC-GB (m)
		700	Cold Worked	BCC-GB (m)	BCC-GB (m)	BCC-GB (m)
		700	Recrystallized	BCC-GB (m)	BCC-GB (m)	BCC-GB (m)
$Ti_{40}Zr_{20}Hf_{20}$	$Nb_{10}Ta_{10}$	1000	Cold Worked	BCC	BCC-(m)	BCC
		1000	Recrystallized	BCC	BCC	BCC-GB(m)
		700	Cold Worked	BCC	BCC	BCC
		700	Recrystallized	BCC-GB (m)	BCC-GB (m)	BCC-GB (m)
$Ti_{26.7}Zr_{26.7}Hf_{26.7}$	$Nb_{10}Ta_{10}$	1000	Cold Worked	BCC	BCC	BCC
		1000	Recrystallized	BCC	BCC	BCC
		700	Cold Worked	BCC+HCP	BCC+HCP	BCC+HCP
		700	Recrystallized	BCC+HCP	BCC+HCP	BCC+HCP
$Ti_5Zr_{20}Hf_{35}$	$Nb_{20}Ta_{20}$	1000	Cold Worked	BCC	BCC	BCC-GB (l)
		1000	Recrystallized	BCC	BCC-GB (l)	BCC-GB (l)
		700	Cold Worked	Lamellar	Lamellar	Lamellar
		700	Recrystallized	Lamellar	Lamellar	Lamellar

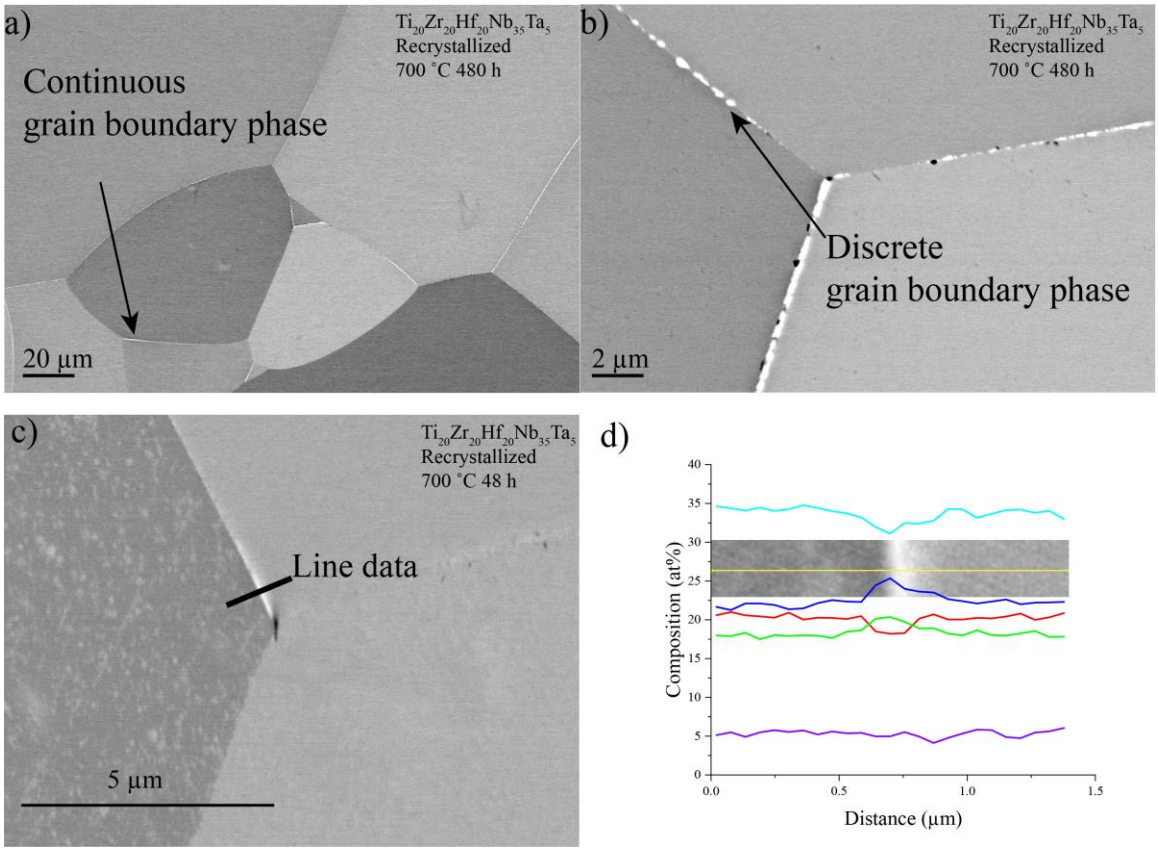

Figure 4.3: BSE images of $Ti_{20}Zr_{20}Hf_{20}Nb_{35}Ta_5$ after the indicated heat treatment showing (a) continuous and (b) discrete particles at the grain boundaries. (c) BSE image with EDS line scan. (d) Element concentrations from EDS indicating enrichment of Zr and Hf at the cost of Nb and Ta at the grain, with the x-axis acting as the scale bar. Atomic compositions were binned by four.

The secondary phases in $Ti_{20}Zr_{20}Hf_{20}Nb_{35}Ta_5$ are seen at the grain boundaries as either discrete particles or continuous phases, **Figure 4.3a-b**. EDS line scan, **Figure 4.3c**, shows a grain boundary enriched in Hf and Zr, **Figure 4.3d**. Occasionally, secondary phases are seen within the grain but are most likely not nucleating homogenously but left behind by advancing grain boundaries. **Figure 4.4** shows lined up secondary phases throughout the grains (as though they were previously at grain boundaries). This would suggest that the secondary phases nucleating in $Ti_{20}Zr_{20}Hf_{20}Nb_{35}Ta_5$ prefer to do so heterogeneously at grain boundaries, similar to what has been observed in FCC HEAs [176]. $Ti_{40}Zr_{20}Hf_{20}Nb_{10}Ta_{10}$, similarly has Hf-Zr rich phases, examples seen in **Supplementary Figure 4.31**, but also has a Zr-Ta rich phase, seen only after the 1000 ˚C heat treatments, an example seen in **Supplementary Figure 4.33**.

$Ti_{26.7}Zr_{26.7}Hf_{26.7}Nb_{10}Ta_{10}$ features more homogenous nucleation at 700 ˚C. Two phases are observed to form within the alloy, a Hf-Zr rich presumably HCP phase and Ta-rich presumably BCC phase, inferred from composition and XRD. The microstructures are shown in **Figure 4.5** and an example EDS is shown in **Figure 4.6**. The recrystallized and cold rolled microstructures are distinct from each other in that the recrystallized microstructure has needle like Hf-Zr rich phases forming at 45˚ while the cold-rolled microstructure contains roughly equiaxed Hf-Zr rich and Ta rich phases. The area fractions of the Ta rich phase and Hf-Zr rich phase are lower in the cold rolled specimens compared to the recrystallized specimens after 4800 h anneals, as seen in **Table 4.3** based on five fields of view using grid analysis.

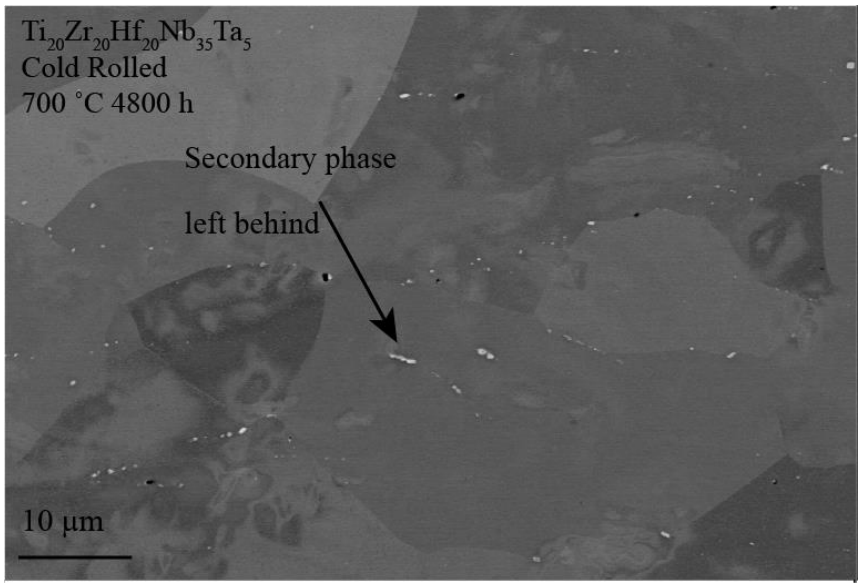

Figure 4.4: $Ti_{20}Zr_{20}Hf_{20}Nb_{35}Ta_5$ showing secondary phases in relatively straight lines apparently left behind by moving grain boundaries.

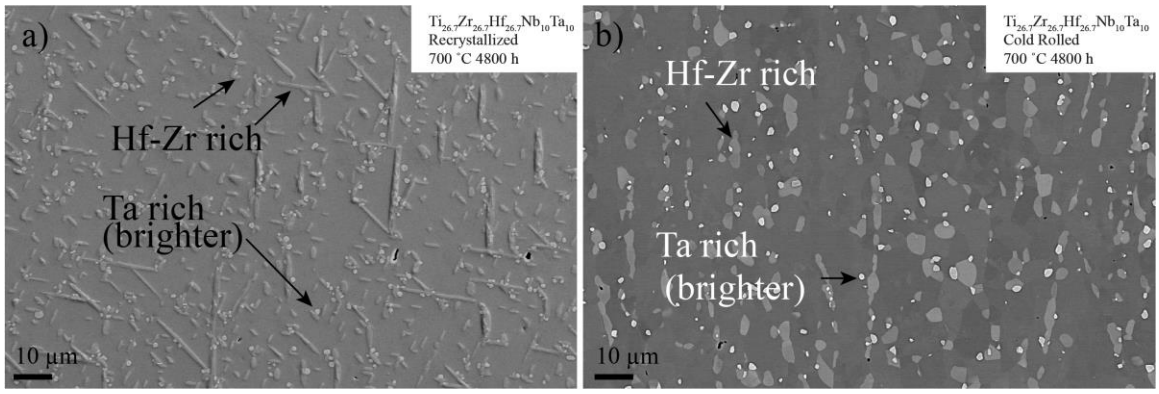

Figure 4.5: $Ti_{26.7}Zr_{26.7}Hf_{26.7}Nb_{10}Ta_{10}$ microstructure after 4800 h in the (a) recrystallized specimen and (b) cold rolled specimen, resulting in different secondary phase morphology.

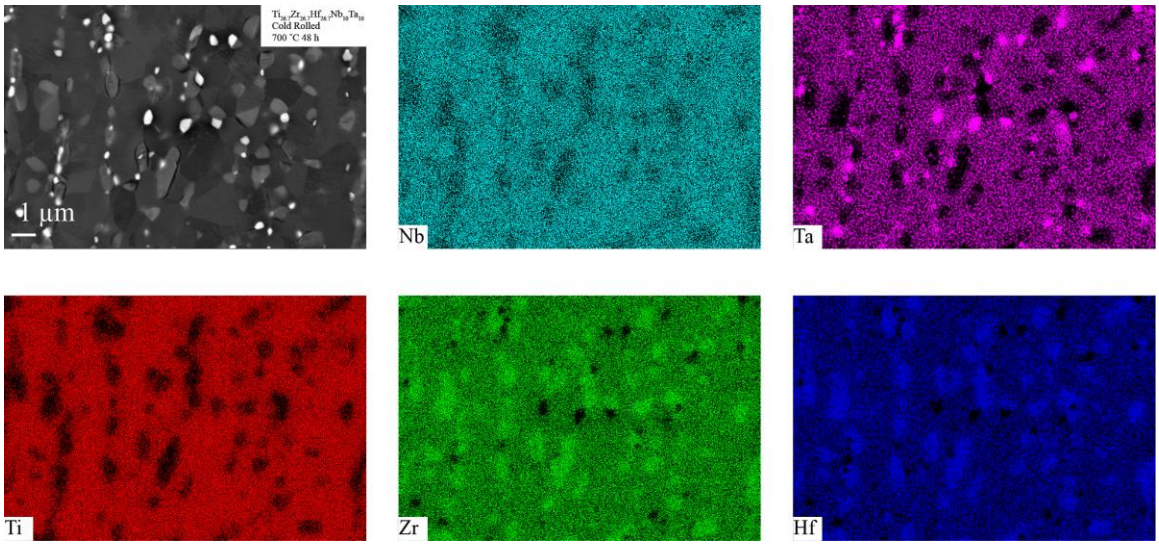

Figure 4.6: Microstructure of $Ti_{26.7}Zr_{26.7}Hf_{26.7}Nb_{10}Ta_{10}$ along with EDS results showing the Zr-Hf rich and Ta-rich phases.

Table 4.3: Area percentages of the different phases in the cold-rolled and recrystallized specimens of $Ti_{26.7}Zr_{26.7}Hf_{26.7}Nb_{10}Ta_{10}$ after annealing at for 700 °C for 4800 h.

Phase	Area % cold rolled 700 ˚C 4800 h	Area % in recrystallized 700 ˚C 4800 h
Ta rich phase	2.4 ± 1.0	4.0 ± 1.6
Hf-Zr rich phase	11.9 ± 2.5	18.5 ± 3.5

Interestingly, the Ta content in the Ta-rich phase is notably different between the recrystallized and cold conditions by nearly a factor of two, **Table 4.4**, suggesting that at least one condition was not at thermal equilibrium after 4800 h.

$Ti_5Zr_{20}Hf_{35}Nb_{20}Ta_{20}$ has a more drastic phase change compared to the other alloys. The microstructure is lamellar with Hf-Zr rich phase and Nb-Ta rich phase, see EDS maps in **Figure 4.7**, which are presumably HCP and BCC, respectively. With increasing time at 700 ˚C, the lamellar microstructure coarsens, **Figure 4.8a-c**. Hf-Ta binary does have a eutectoid point [114, 177]. However, while the lamellar structure is similar to eutectoid structures, it is most likely due to a miscibility gap between the BCC and HCP phases because there is no observed proeutectoid phase, **Figure 4.8**. In **Figure 4.9**, CALPHAD calculations on the simplified pseudobinary Hf_2Zr-NbTa, where $Ti_5Zr_{20}Hf_{35}Nb_{20}Ta_{20}$ would be approximately at 40% Nb + Ta content, also suggests that a eutectoid microstructure is not expected at 700 ˚C, but rather a decomposition from BCC to BCC and HCP. Compositions of the individual lamellae, shown in **Table 4.5**, are similar in both the cold rolled and recrystallized microstructures after 4800 h, where they are both roughly the same.

Hardness

The hardness of the alloys before and after 700 ˚C heat treatment is shown in **Figure 4.10**. $Ti_{20}Zr_{20}Hf_{20}Nb_{35}Ta_5$ and $Ti_{40}Zr_{20}Hf_{20}Nb_{10}Ta_{10}$, the two roughly single-phase alloys at 700 ˚C, do not show substantial hardening throughout heat treatment time, **Figure 4.10a-b**.

Table 4.4: Phase compositions of $Ti_{26.7}Zr_{26.7}Hf_{26.7}Nb_{10}Ta_{10}$ after 4800 h at 700 ˚C.

Condition	Phase	Ti (at%)	Zr (at%)	Hf (at%)	Nb (at%)	Ta (at%)
Cold Rolled	Hf-Zr rich	19.3 ± 3.9	31.3 ± 4.0	37.1 ± 4.6	5.0 ± 2.5	7.3 ± 4.1
4800h	Ta rich	24.1 ± 1.8	18.5 ± 3.5	22.4 ± 3.3	12.7 ± 2.1	22.3 ± 5.4
	Matrix	29.0 ± 0.2	22.8 ± 0.1	26.5 ± 0.1	10.7 ± 0.2	11.0 ± 0.2
Recrystallized	Hf-Zr rich	19.9 ± 1.2	33.9 ± 1.1	39.7 ± 1.2	3.1 ± 1.5	3.4 ± 0.8
4800 h	Ta rich	21.2 ± 2.5	8.2 ± 1.2	13.7 ± 1.8	17.9 ± 1.9	39.1 ± 4.9
	Matrix	29.9 ± 0.4	22.5 ± 0.2	26.5 ± 0.4	10.7 ± 0.3	10.5 ± 0.1

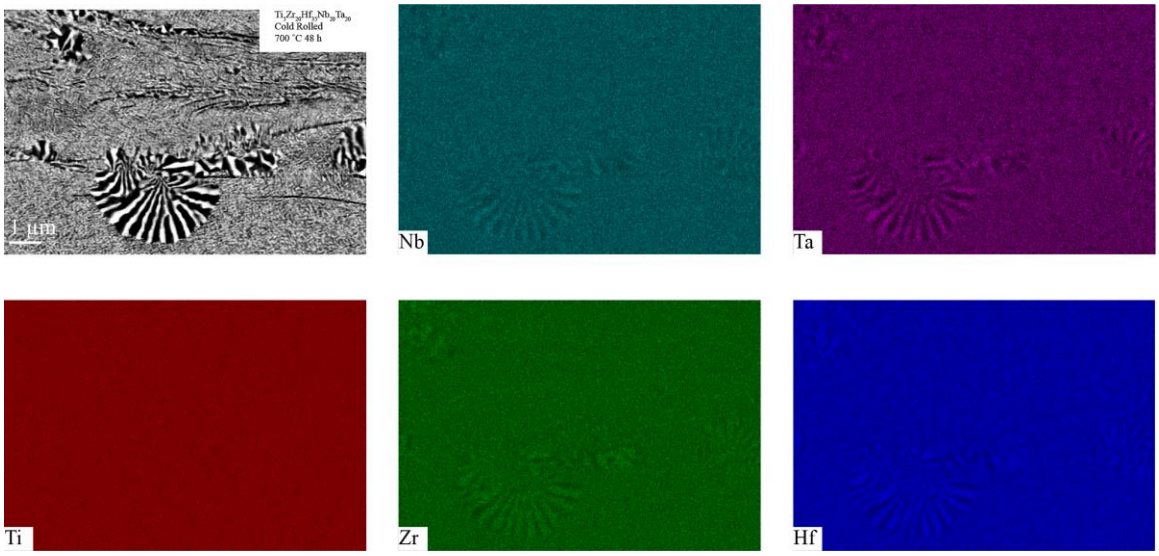

Figure 4.7: $Ti_5Zr_{20}Hf_{35}Nb_{20}Ta_{20}$ microstructure and EDS map showing separation of Zr-Hf and Nb-Ta.

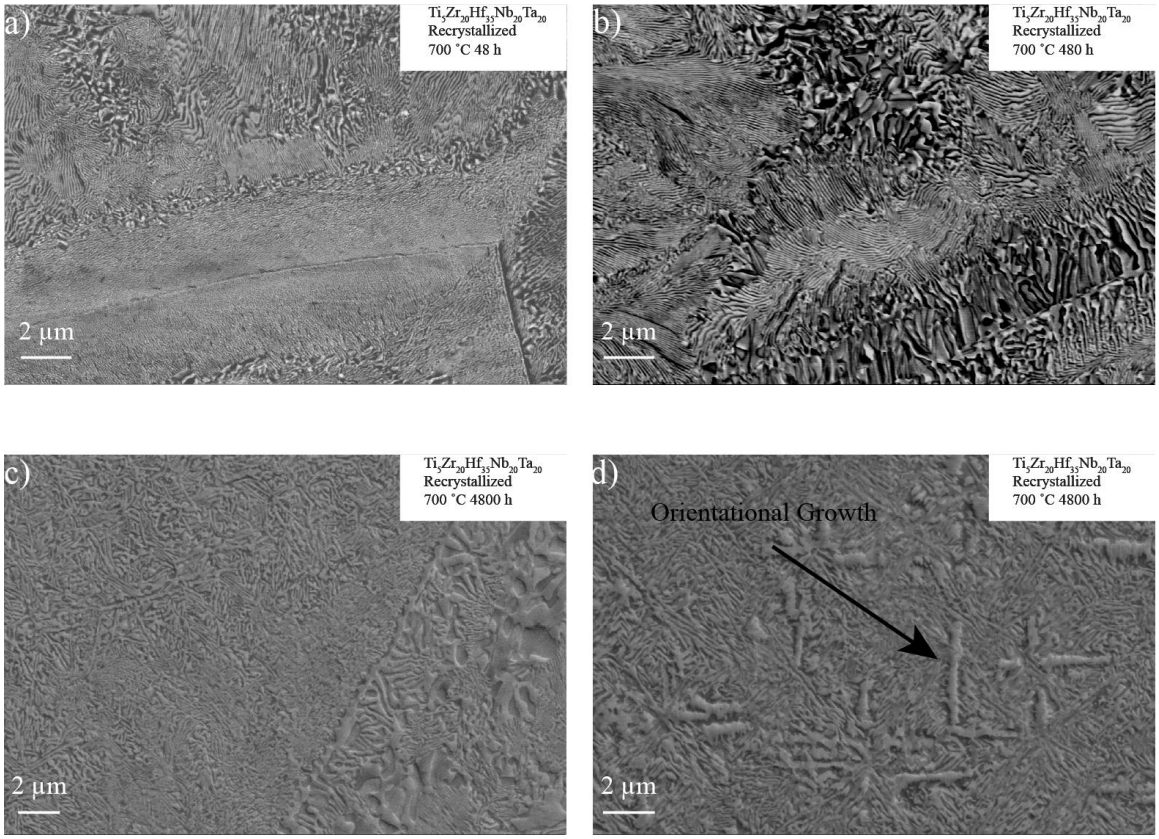

Figure 4.8: Coarsening of microstructure in $Ti_5Zr_{20}Hf_{35}Nb_{20}Ta_{20}$ at 700 °C after (a) 48 h, (b) 480 h, (c, d) 4800 h, (d) shows orientational growth.

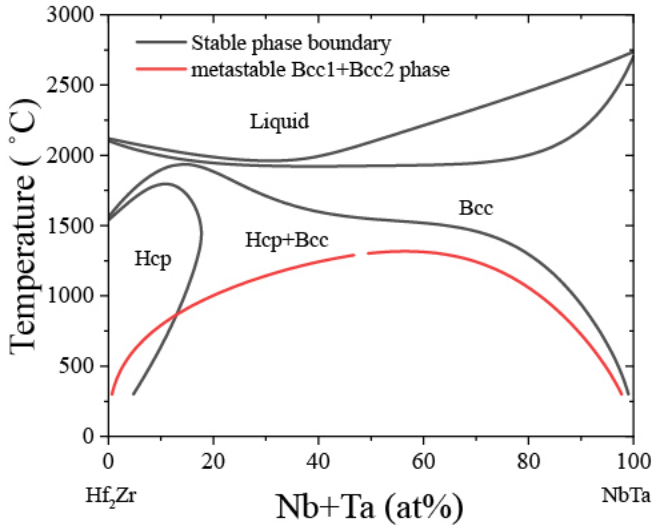

Figure 4.9: Psuedobinary of Hf_2Zr and NbTa showing phase decomposition rather than eutectoid transformation.

Table 4.5: Phase compositions of $Ti_5Zr_{20}Hf_{35}Nb_{20}Ta_{20}$ after 4800 h at 700 ˚C.

Condition	Phase	Ti (at%)	Zr (at%)	Hf (at%)	Nb (at%)	Ta (at%)
Cold Rolled	Hf-Zr rich	5.0 ± 0.5	23.8 ± 1.1	48.2 ± 1.7	11.6 ± 1.4	11.4 ± 1.6
4800h	Ta rich	5.6 ± 0.8	12.1 ± 2.2	27.0 ± 3.6	26.2 ± 2.5	29.1 ± 3.2
Recrystallized	Hf-Zr rich	4.7 ± 0.2	22.8 ± 1.3	47.6 ± 3.0	11.1 ± 1.3	13.7 ± 2.8
4800 h	Ta rich	5.3 ± 0.5	9.6 ± 2.3	23.5 ± 3.9	28.2 ± 2.6	33.5 ± 3.3

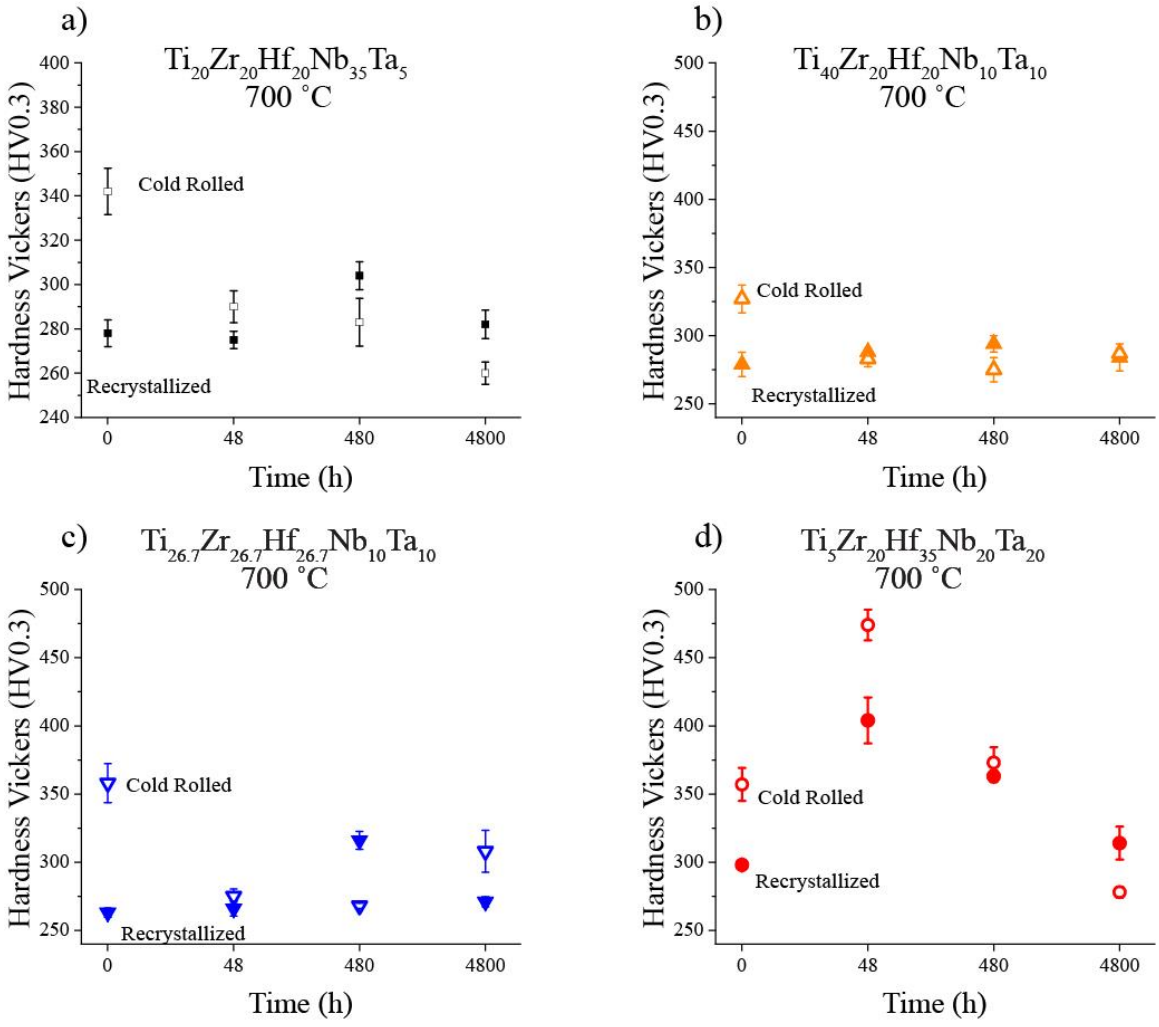

Figure 4.10: Hardness after 700 ˚C heat treatments: (a) $Ti_{20}Zr_{20}Hf_{20}Nb_{35}Ta_5$, (b) $Ti_{40}Zr_{20}Hf_{20}Nb_{10}Ta_{10}$, (c) $Ti_{26.7}Zr_{26.7}Hf_{26.7}Nb_{10}Ta_{10}$, and (d) $Ti_5Zr_{20}Hf_{35}Nb_{20}Ta_{20}$.

$Ti_{26.7}Zr_{26.7}Hf_{26.7}Nb_{10}Ta_{10}$ exhibits some minor hardening at 480 h for the recrystallized condition and 4800 h for the cold rolled condition, **Figure 4.10**. However, caution is needed in over-interpreting the hardness. The alloys in general have very large grains after heat treatment. Most indents, at ~45 μm diagonals, will likely be within one grain while one grain can take up a significant fraction of the sample area. Most BCC metals are known to have directionally dependent plasticity [178, 179] as also seen in RHEAs with hardness tests [180]. While minor increases in hardness could be attributed to the secondary phases, previous work on nanocrystalline [47] and bulk [29] TiZrHfNbTa show slight age softening with the introduction of secondary BCC phases. The convolution of BCC anisotropy and the possibility of secondary phase softening renders a full of judgement of the effect of secondary phase in $Ti_{26.7}Zr_{26.7}Hf_{26.7}Nb_{10}Ta_{10}$ difficult, but at first glance it is not a particularly effective hardener with only a modest increase from 263 HV0.3 in the recrystallized condition to 308 HV0.3 after 4800 h in the cold rolled sample. A clearer example of hardening by secondary phases is $Ti_5Zr_{20}Hf_{35}Nb_{20}Ta_{20}$, **Figure 4.10d**. Both the recrystallized and cold rolled condition show a peak in hardness at 48 h followed by softening with further annealing. The trend follows the coarsening of the microstructure seen in **Figure 4.8a-c**.

The effects of heat treatments at 1000 ˚C on phase stabilities require more skepticism. All the alloys expect for $Ti_5Zr_{20}Hf_{35}Nb_{20}Ta_{20}$ were indexed as single-phase BCC after prolonged heat treatment. However, $Ti_{26.7}Zr_{26.7}Hf_{26.7}Nb_{10}Ta_{10}$ and $Ti_{40}Zr_{20}Hf_{20}Nb_{10}Ta_{10}$ had poor XRD patterns at 4800 h that could not be improved with

diffractometer setup. A likely contributor to this issue is interstitial uptake from the residual gas in the quartz ampule. Seen in **Figure 4.11a-b**, hardness increases with time past 48 h in both the recrystallized and cold rolled starting conditions. Since most of the alloys were single-phase, albeit with some incidental grain boundary phases, contributors to strength from the microstructure are dislocation density and grain size, neither of which would increase strength over prolonged annealing time [175, 181]. Furthermore, the hardness at 4800 h exceeds that of the initial cold rolled condition, so strengthening must be arising from interstitial uptake, as has previously been seen in Nb alloys [182, 183] and Ta alloys [184].

O uptake at 1000 ˚C muddies the understanding of what is the thermally stable phase. O in the Ti-O, Zr-O, and Hf-O systems stabilizes the HCP phase at higher temperatures[114], and considering the Gibbs phase rule, the addition of O would promote another degree freedom for additional phases. By this reasoning, and because O is an HCP stabilizer, alloys that are predominately BCC despite the addition of O would likely remain predominately BCC without the O. However, the convolution cannot be fully removed when secondary phases are present, notably in $Ti_5Zr_{20}Hf_{35}Nb_{20}Ta_{20}$. EDS analysis of the secondary phases shows that it is rich in O compared to the base material, **Figure 4.12**. Similar behavior has been seen in β-Ti alloys where O promotes α and ω formation and embrittlement [185], and similar microstructures were seen in purposefully contaminated TiZrHfNbTa [50] where a secondary BCC phase and HCP formed.

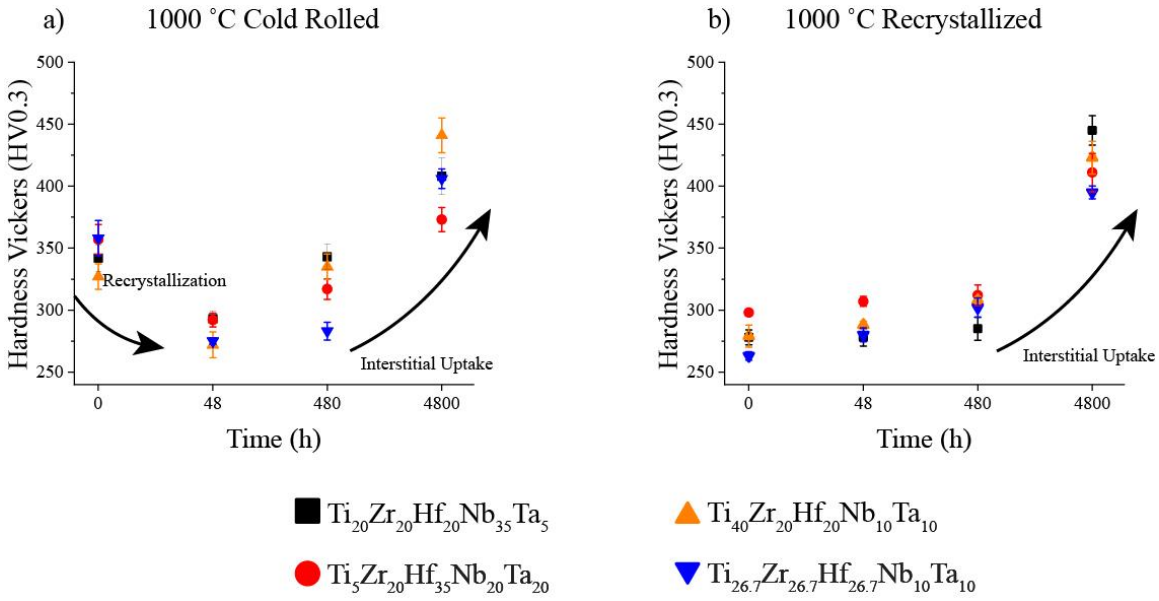

Figure 4.11: Hardness of the 1000˚C samples: (a) cold rolled specimens, and (b) recrystallized samples.

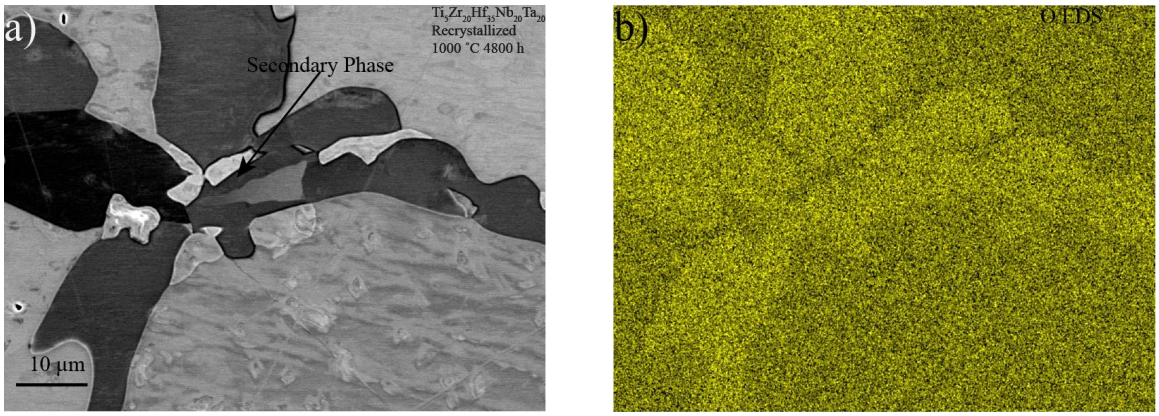

Figure 4.12: (a) BSE image of $Ti_5Zr_{20}Hf_{35}Nb_{20}Ta_{20}$ after 4800 h at 1000 ˚C, showing a secondary phase. (b) EDS shows that the secondary phase is enriched in O.

Conclusion

Derivatives of the TiZrHfNbTa were cast, homogenized, cold rolled, and some recrystallized to study thermal stability up to 4800 h at 700 ˚C and 1000 ˚C. At 700 ˚C three distinct microstructures were observed: (i) a mostly single-phase BCC microstructure with occasional secondary phases at the grain boundaries or left behind by the grain boundaries, (ii) a BCC microstructure with discretely precipitated HCP and BCC, (iii) eutectoid like lamellar structure. The first microstructure is seen in $Ti_{20}Zr_{20}Hf_{20}Nb_{35}Ta_5$ and $Ti_{40}Zr_{20}Hf_{20}Nb_{10}Ta_{10}$ while $Ti_{26.7}Zr_{26.7}Hf_{26.7}Nb_{10}Ta_{10}$ and $Ti_5Zr_{20}Hf_{35}Nb_{20}Ta_{20}$ fit into the second and third respectively. Of these structures, only the lamellar structure of $Ti_5Zr_{20}Hf_{35}Nb_{20}Ta_{20}$ showed consistent hardening, with a maximum hardness obtained at 48 h. The 1000 ˚C samples, generally, show single-phase microstructure with minor grain boundary phases excepting $Ti_5Zr_{20}Hf_{35}Nb_{20}Ta_{20}$ and $Ti_{40}Zr_{20}Hf_{20}Nb_{10}Ta_{10}$ in some heat treatments. However, these results are convoluted by interstitial uptake, inferred from high hardness values measured in the 4800 h 1000 ˚C specimens.

Appendix – Supplementary Material

Initial Condition XRD

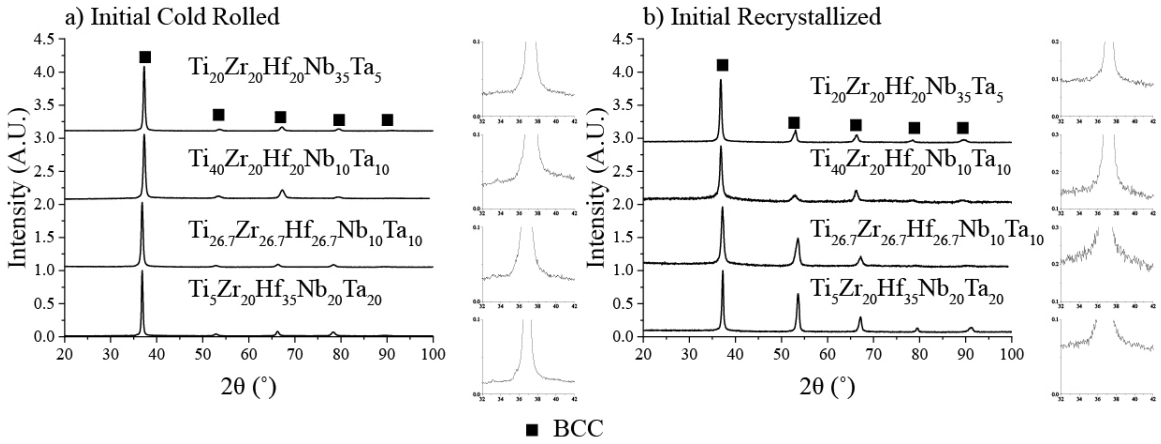

Supplementary Figure 4.1: XRD patterns from the initial (a) cold rolled and (b) recrystallized specimens.

Initial Condition SEM-EDS

$Ti_{20}Zr_{20}Hf_{20}Nb_{35}Ta_5$ - Cold Rolled
Initial Condition

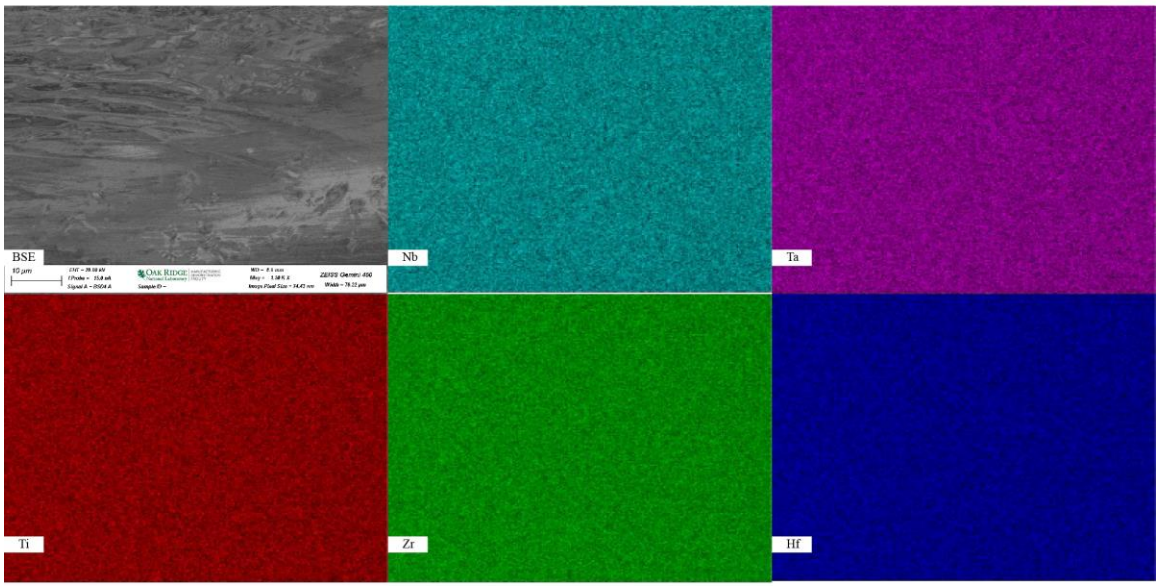

Supplementary Figure 4.2: $Ti_{20}Zr_{20}Hf_{20}Nb_{35}Ta_5$ in the initial condition after cold rolling.

$Ti_{40}Zr_{20}Hf_{20}Nb_{10}Ta_{10}$ - Cold Rolled
Initial Condition

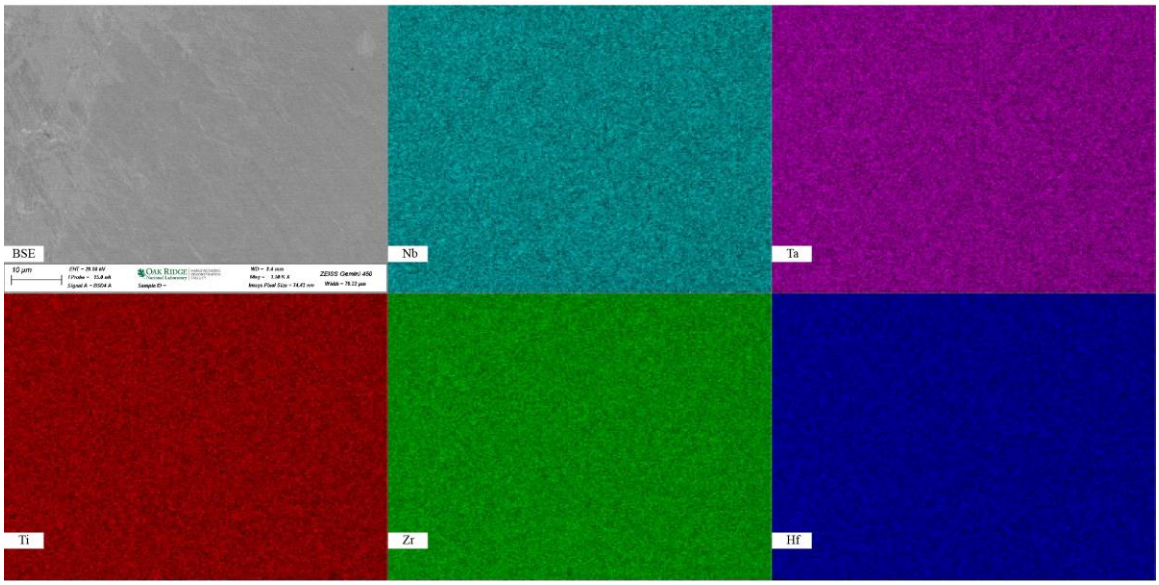

Supplementary Figure 4.3: $Ti_{40}Zr_{20}Hf_{20}Nb_{10}Ta_{10}$ in the initial condition after cold rolling.

$Ti_{26.7}Zr_{26.7}Hf_{26.7}Nb_{10}Ta_{10}$ - Cold Rolled
Initial Condition

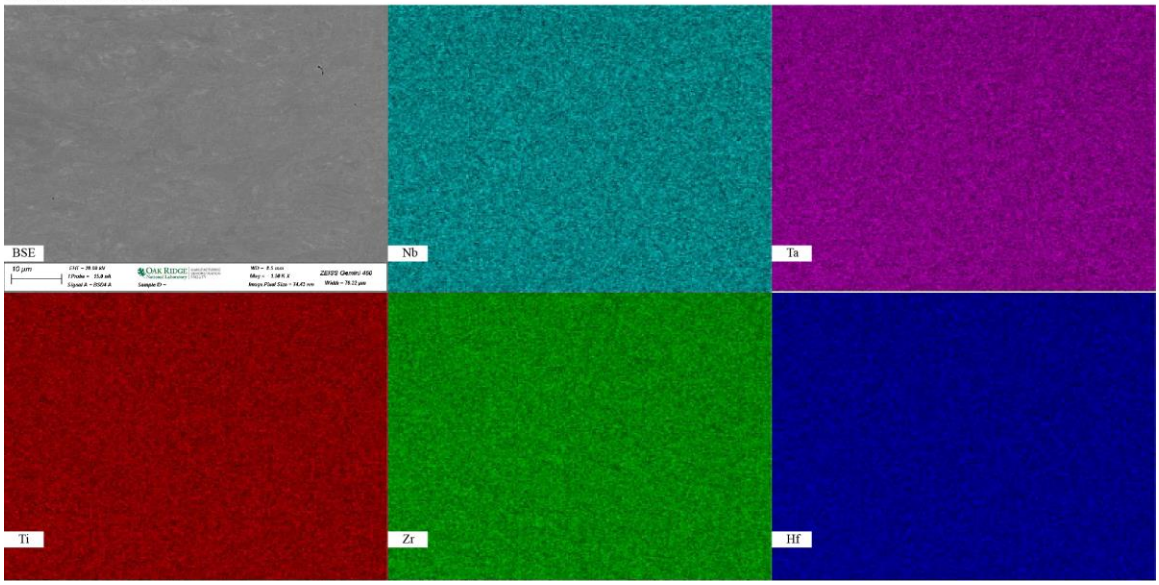

Supplementary Figure 4.4: $Ti_{26.7}Zr_{26.7}Hf_{26.7}Nb_{10}Ta_{10}$ in the initial condition after cold rolling.

$Ti_5Zr_{20}Hf_{35}Nb_{20}Ta_{20}$ - Cold Rolled
Initial Condition

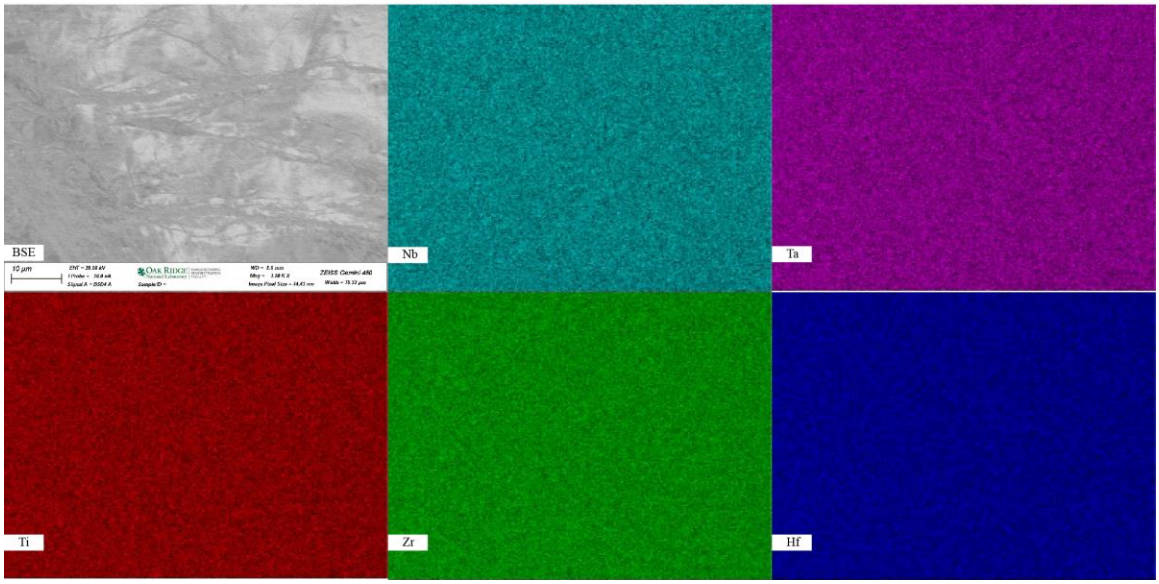

Supplementary Figure 4.5: $Ti_5Zr_{20}Hf_{35}Nb_{20}Ta_{20}$ in the initial condition after cold rolling.

$Ti_{20}Zr_{20}Hf_{20}Nb_{35}Ta_5$ - Recrystallized
Initial Condition

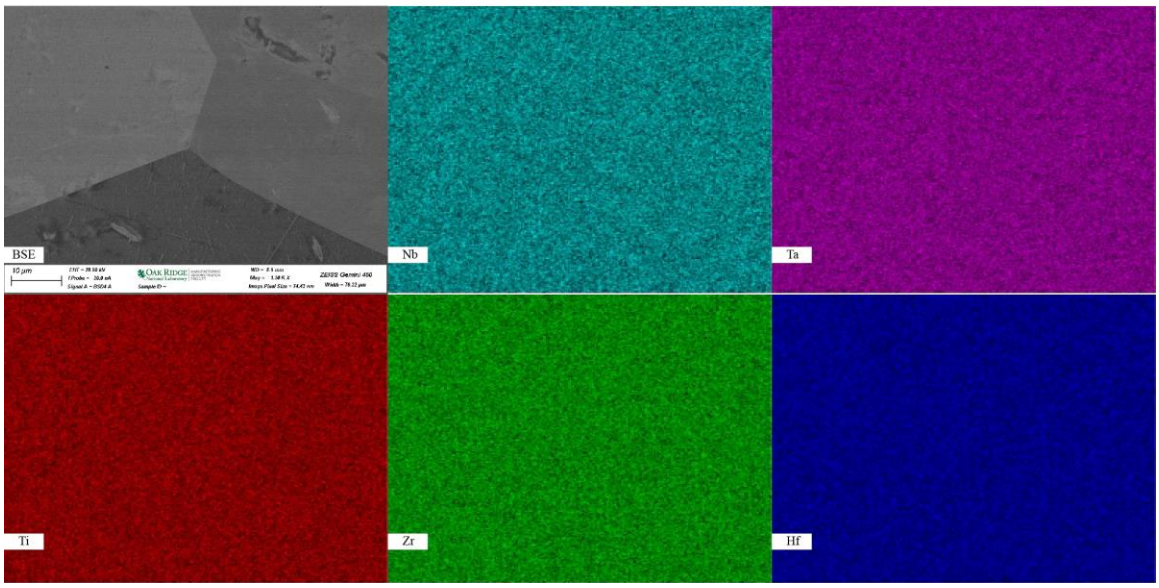

Supplementary Figure 4.6: $Ti_{20}Zr_{20}Hf_{20}Nb_{35}Ta_5$ in the initial condition after recrystallization.

$Ti_{40}Zr_{20}Hf_{20}Nb_{10}Ta_{10}$ - Cold Rolled
Initial Condition

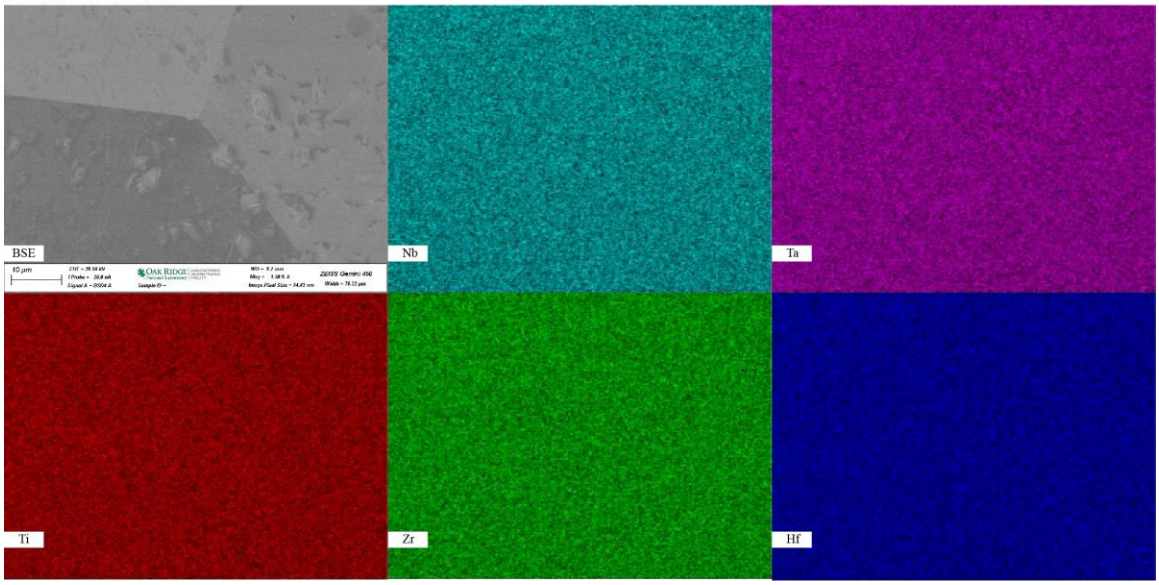

Supplementary Figure 4.7: $Ti_{40}Zr_{20}Hf_{20}Nb_{10}Ta_{10}$ in the initial condition after recrystallization.

$Ti_{26.7}Zr_{26.7}Hf_{26.7}Nb_{10}Ta_{10}$ - Recrystallized
Initial Condition

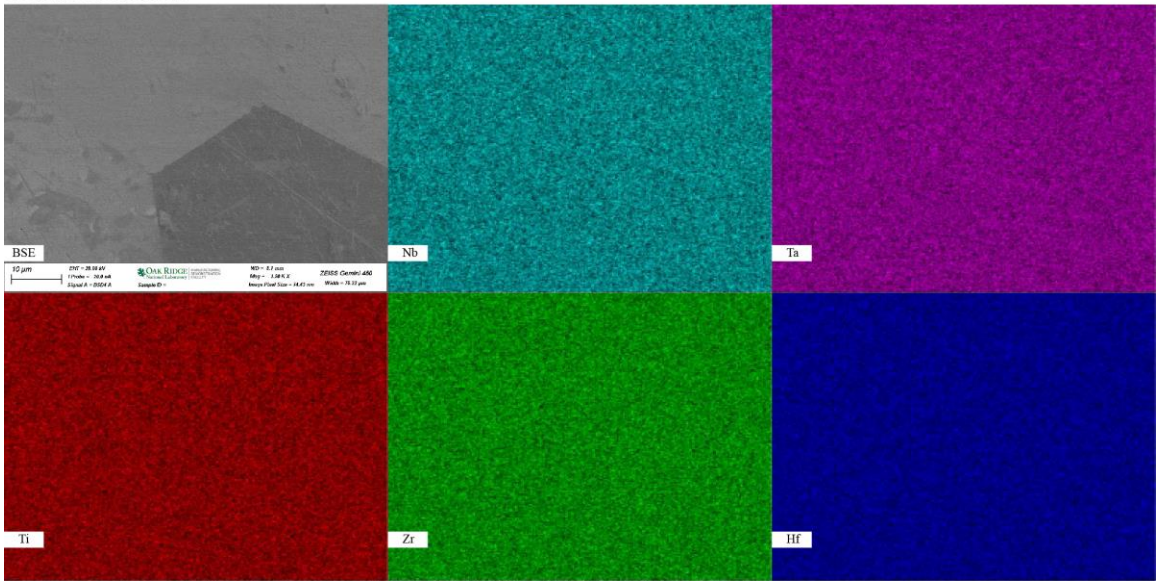

Supplementary Figure 4.8: $Ti_{26.7}Zr_{26.7}Hf_{26.7}Nb_{10}Ta_{10}$ in the initial condition after recrystallization.

$Ti_5Zr_{20}Hf_{35}Nb_{20}Ta_{20}$ - Recrystallized
Initial Condition

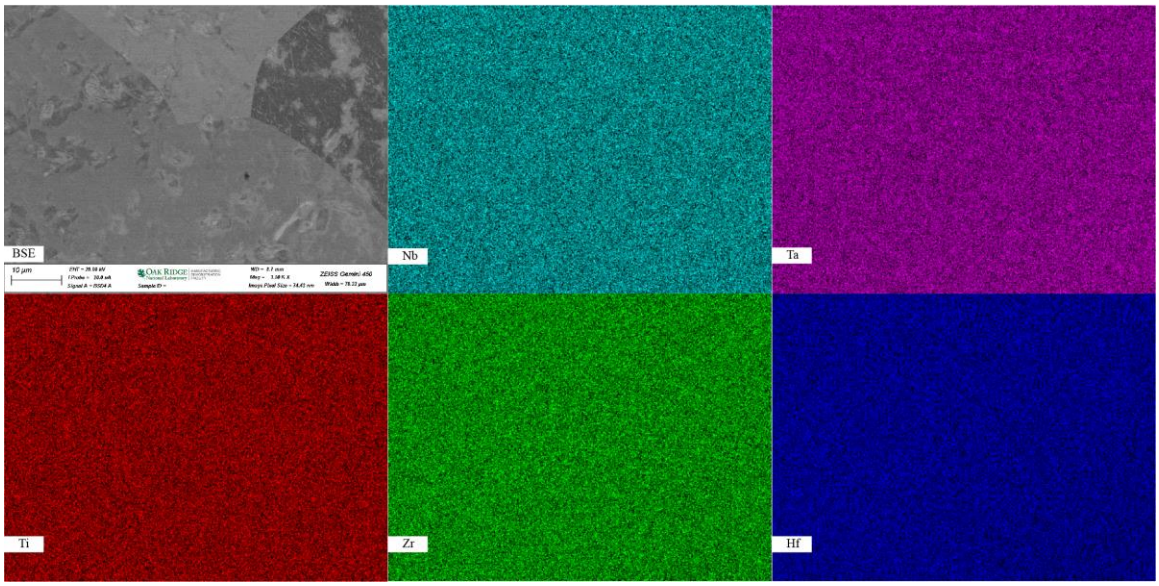

Supplementary Figure 4.9: $Ti_5Zr_{20}Hf_{35}Nb_{20}Ta_{20}$ in the initial condition after recrystallization.

700 ˚C and 1000 ˚C XRD

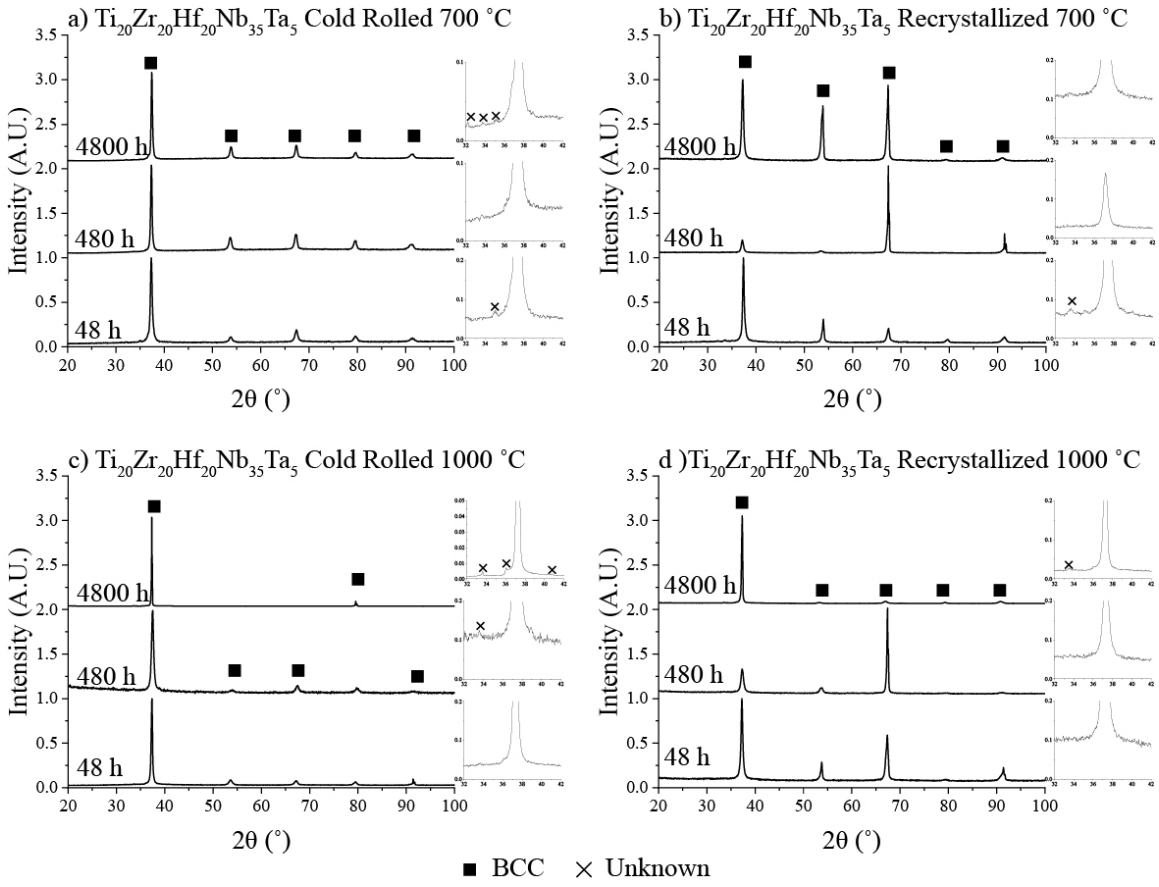

Supplementary Figure 4.10: XRD patterns for $Ti_{20}Zr_{20}Hf_{20}Nb_{35}Ta_5$ at 700 ˚C after (a) cold rolling, (b) recrystallization, and at 1000 ˚C after (c) cold rolling and (d) recrystallization.

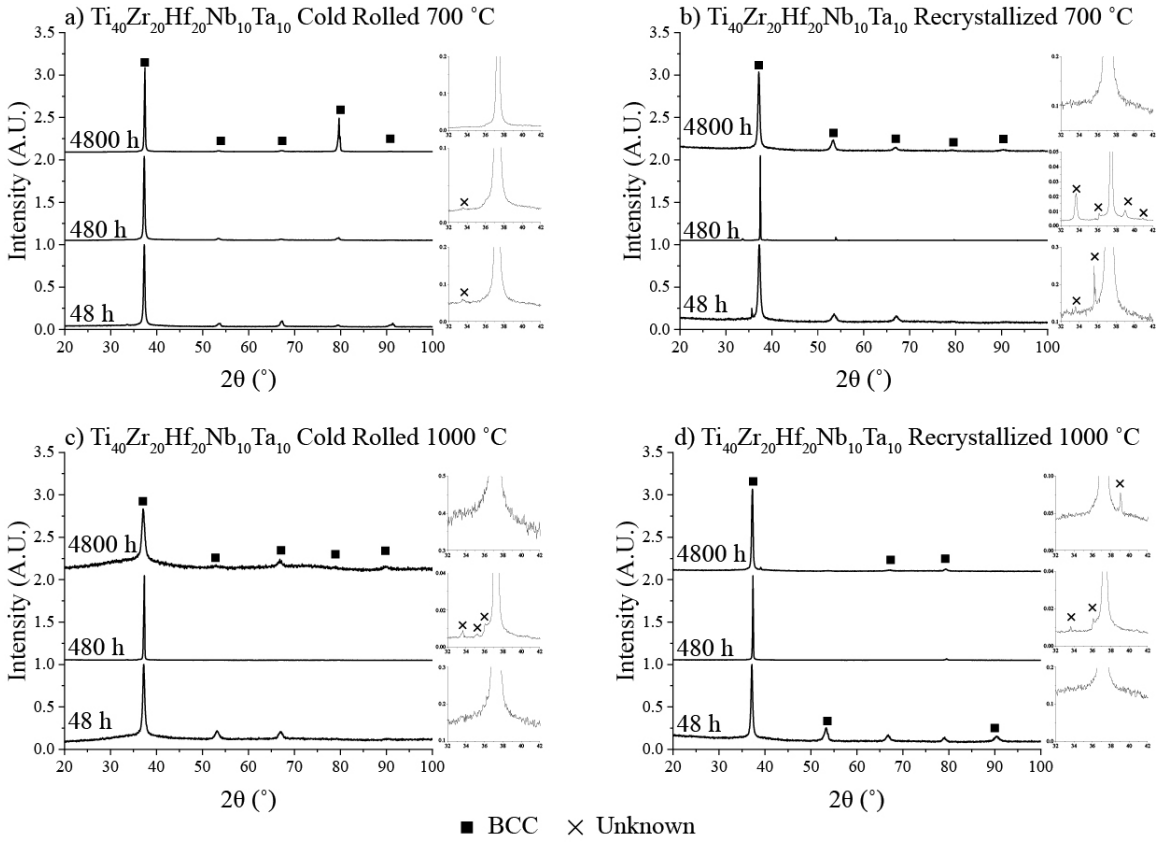

Supplementary Figure 4.11 XRD patterns for $Ti_{40}Zr_{20}Hf_{20}Nb_{10}Ta_{10}$ at 700 ˚C after (a) cold rolling, (b) recrystallization, and at 1000 ˚C after (c) cold rolling and (d) recrystallization.

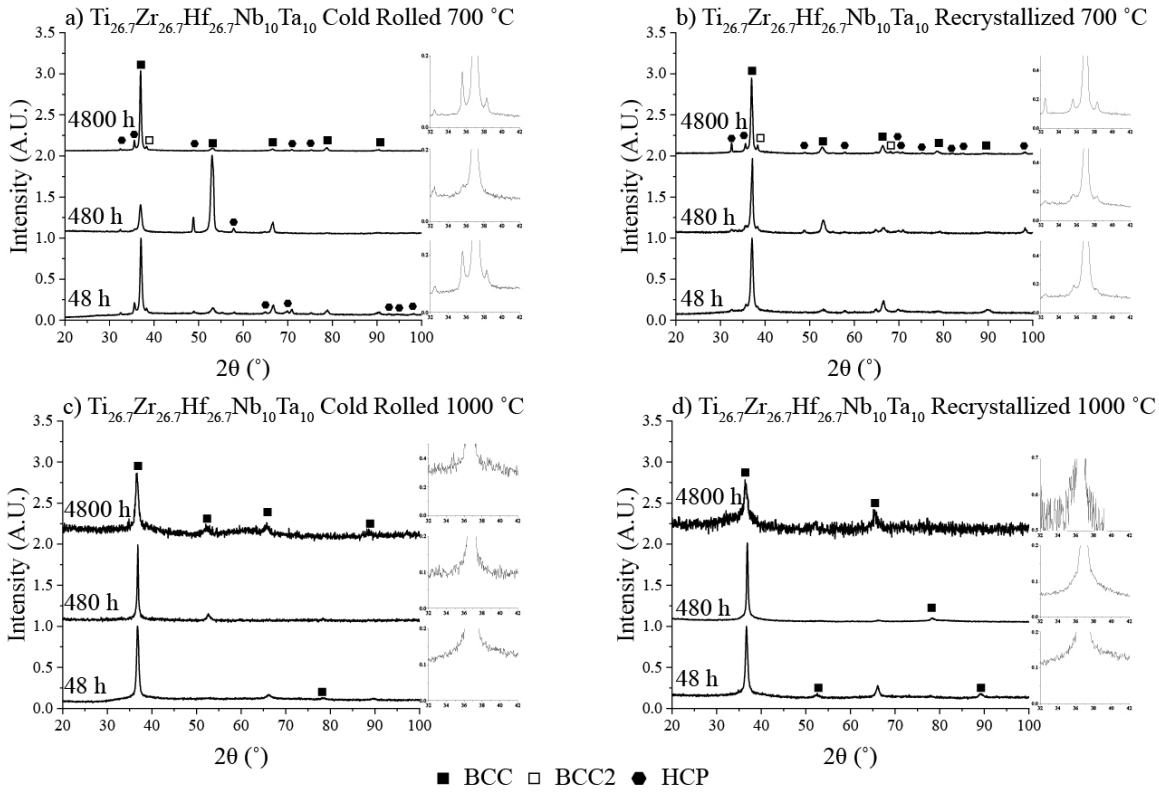

Supplementary Figure 4.12: XRD patterns for $Ti_{26.7}Zr_{26.7}Hf_{26.7}Nb_{10}Ta_{10}$ at 700 ˚C after (a) cold rolling, (b) recrystallization, and at 1000 ˚C after (c) cold rolling and (d) recrystallization.

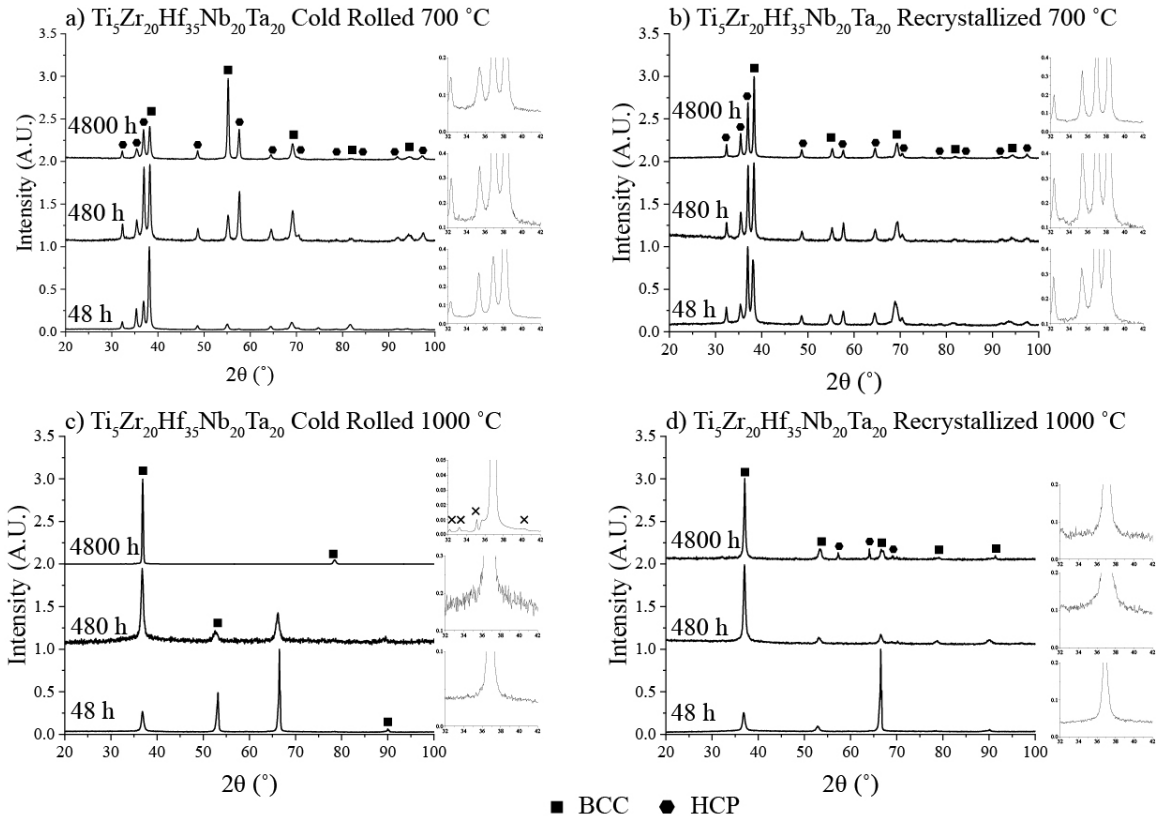

Supplementary Figure 4.13: XRD patterns for $Ti_5Zr_{20}Hf_{35}Nb_{20}Ta_{20}$ at 700 ˚C after (a) cold rolling, (b) recrystallization, and at 1000 ˚C after (c) cold rolling and (d) recrystallization.

<u>$Ti_{20}Zr_{20}Hf_{20}Nb_{35}Ta_5$ 700 ˚C and 1000 ˚C SEM-EDS</u>

$Ti_{20}Zr_{20}Hf_{20}Nb_{35}Ta_5$ - Cold Rolled
700 ˚C - 48 h

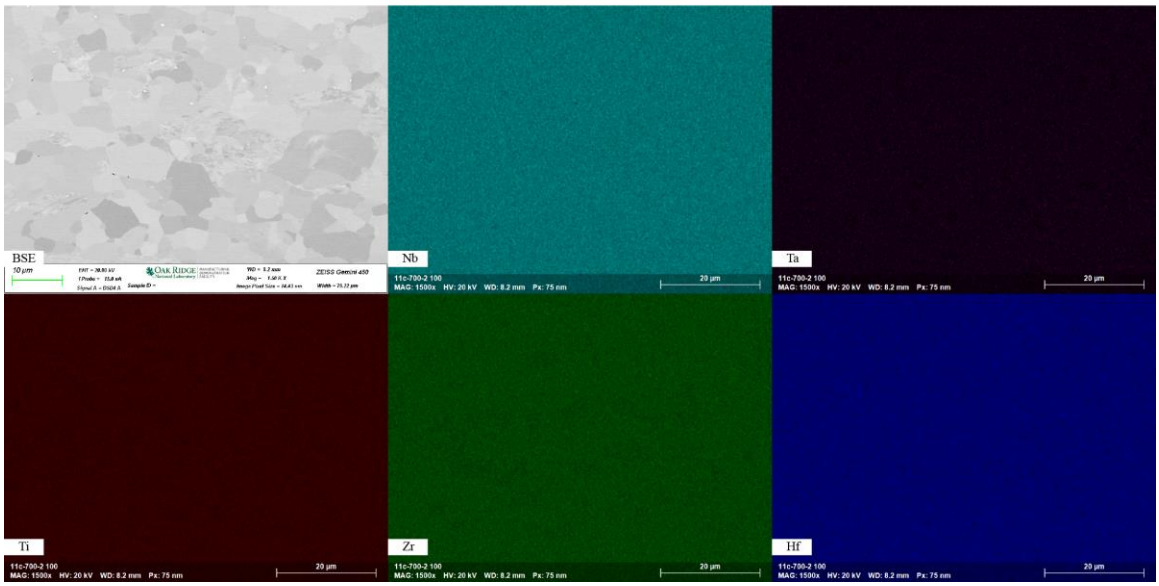

Supplementary Figure 4.14: $Ti_{20}Zr_{20}Hf_{20}Nb_{35}Ta_5$ after 48 h at 700 ˚C beginning in the cold rolled condition, with accompanying EDS maps.

$Ti_{20}Zr_{20}Hf_{20}Nb_{35}Ta_5$ - Cold Rolled
700 ˚C - 480 h

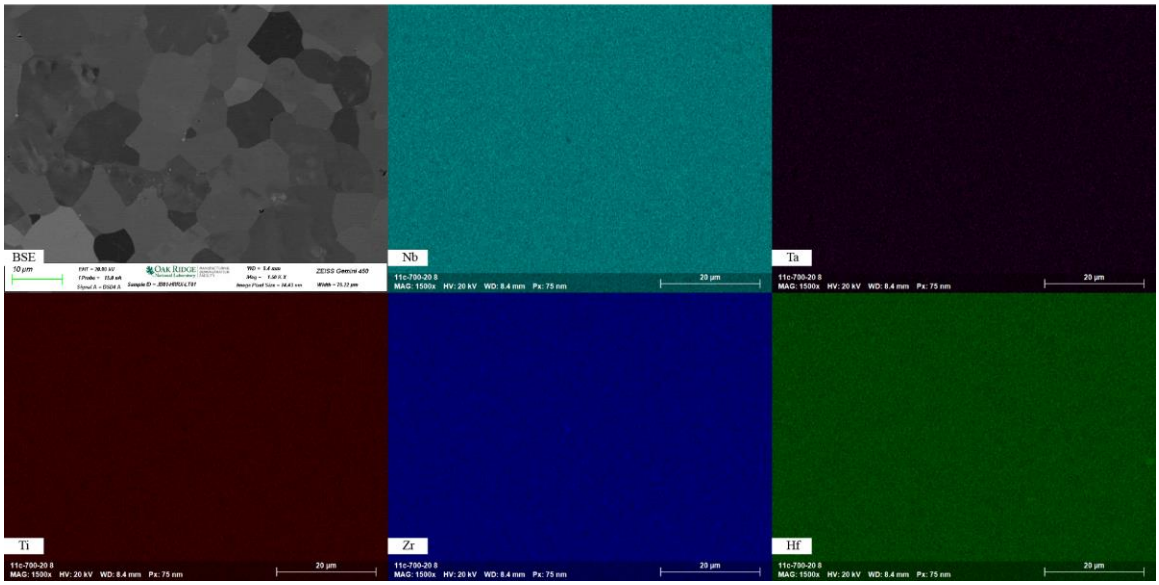

Supplementary Figure 4.15: $Ti_{20}Zr_{20}Hf_{20}Nb_{35}Ta_5$ after 480 h at 700 ˚C beginning in the cold rolled condition, with accompanying EDS maps.

$Ti_{20}Zr_{20}Hf_{20}Nb_{35}Ta_5$ - Cold Rolled
700 ˚C - 4800 h

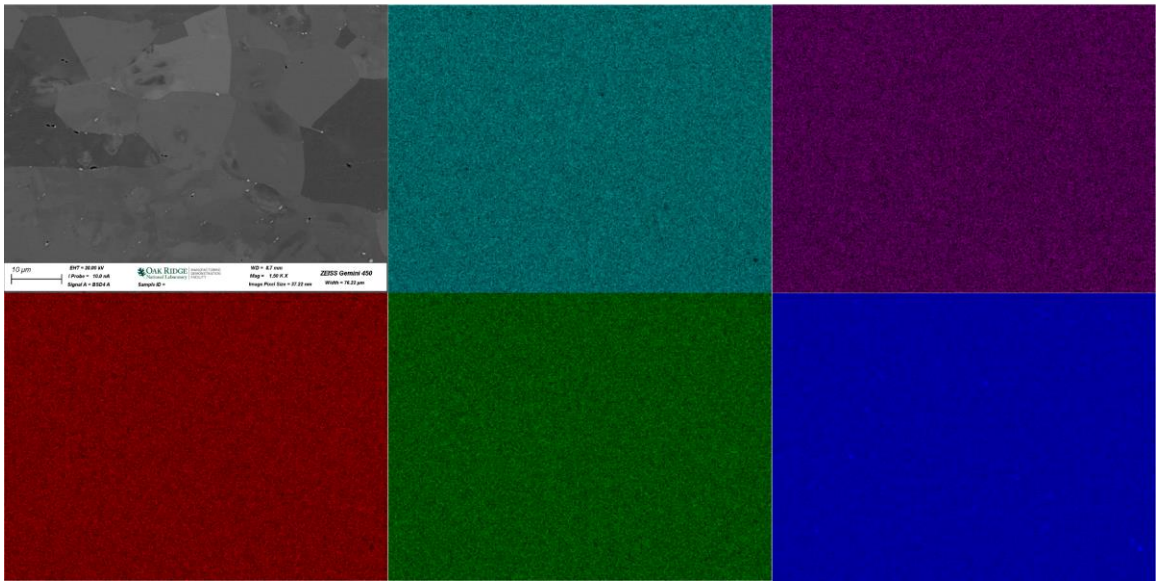

Supplementary Figure 4.16: $Ti_{20}Zr_{20}Hf_{20}Nb_{35}Ta_5$ after 4800 h at 700 ˚C beginning in the cold rolled condition, with accompanying EDS maps.

$Ti_{20}Zr_{20}Hf_{20}Nb_{35}Ta_5$ - Recrystallized
700 ˚C - 48 h

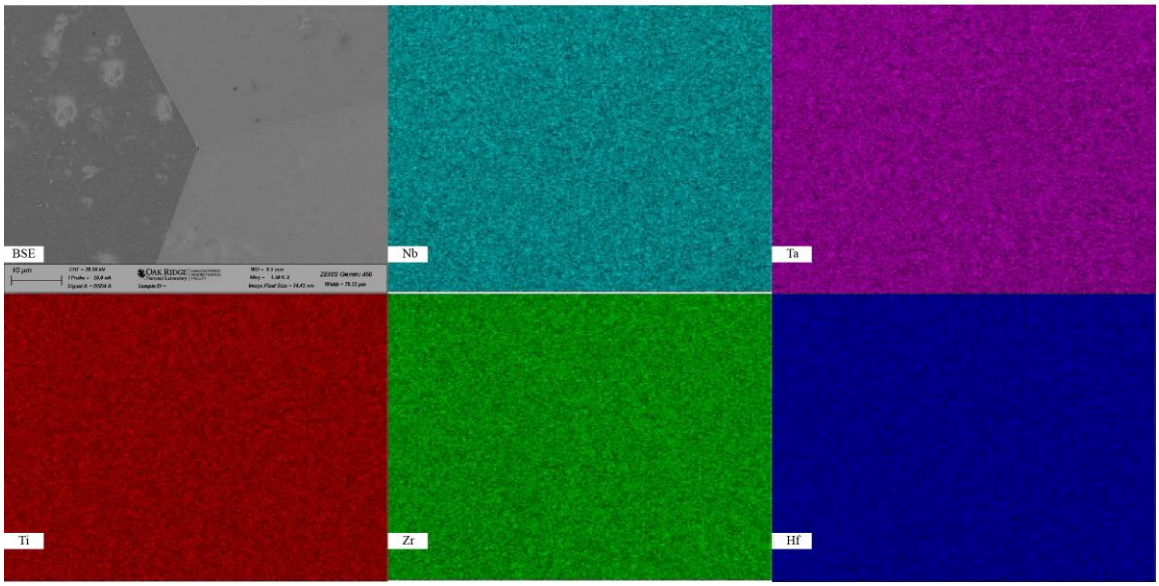

Supplementary Figure 4.17: $Ti_{20}Zr_{20}Hf_{20}Nb_{35}Ta_5$ after 48 h at 700 ˚C beginning in the recrystallized condition, with accompanying EDS maps.

$Ti_{20}Zr_{20}Hf_{20}Nb_{35}Ta_5$ - Recrystallized
700 ˚C - 480 h

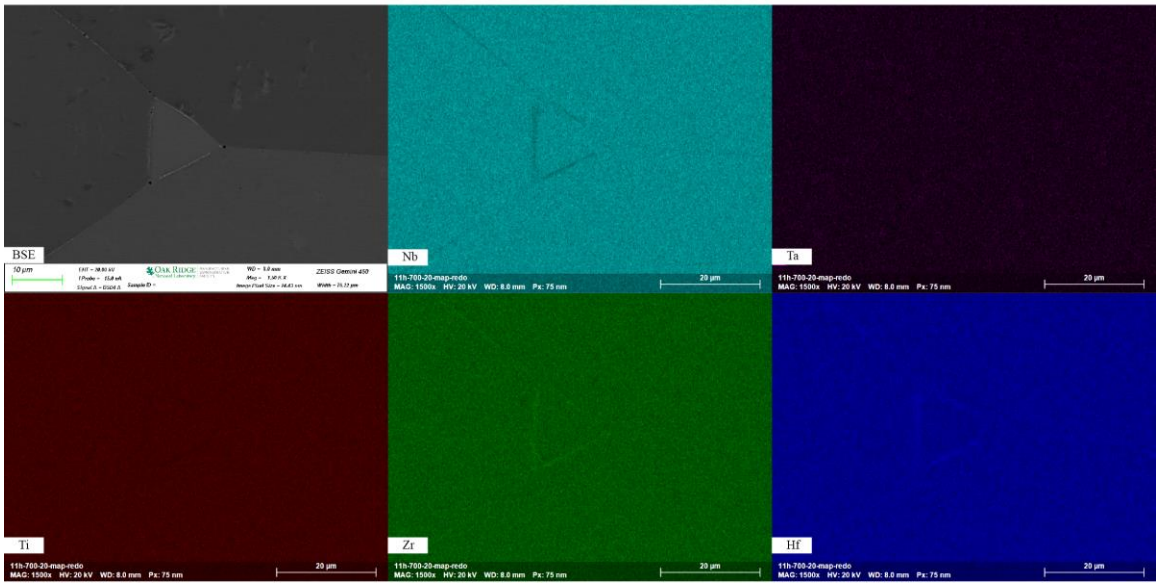

Supplementary Figure 4.18: $Ti_{20}Zr_{20}Hf_{20}Nb_{35}Ta_5$ after 480 h at 700 ˚C beginning in the recrystallized condition, with accompanying EDS maps.

$Ti_{20}Zr_{20}Hf_{20}Nb_{35}Ta_5$ - Recrystallized
700 ˚C - 4800 h

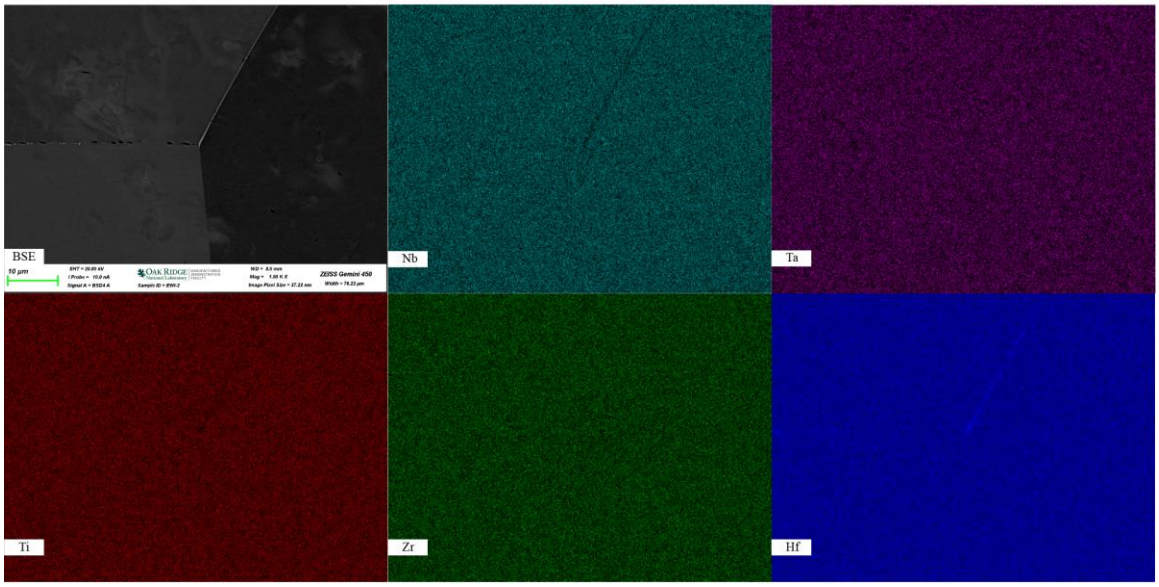

Supplementary Figure 4.19: $Ti_{20}Zr_{20}Hf_{20}Nb_{35}Ta_5$ after 4800 h at 700 ˚C beginning in the recrystallized condition, with accompanying EDS maps.

$Ti_{20}Zr_{20}Hf_{20}Nb_{35}Ta_5$ - Cold Rolled
1000 ˚C - 48 h

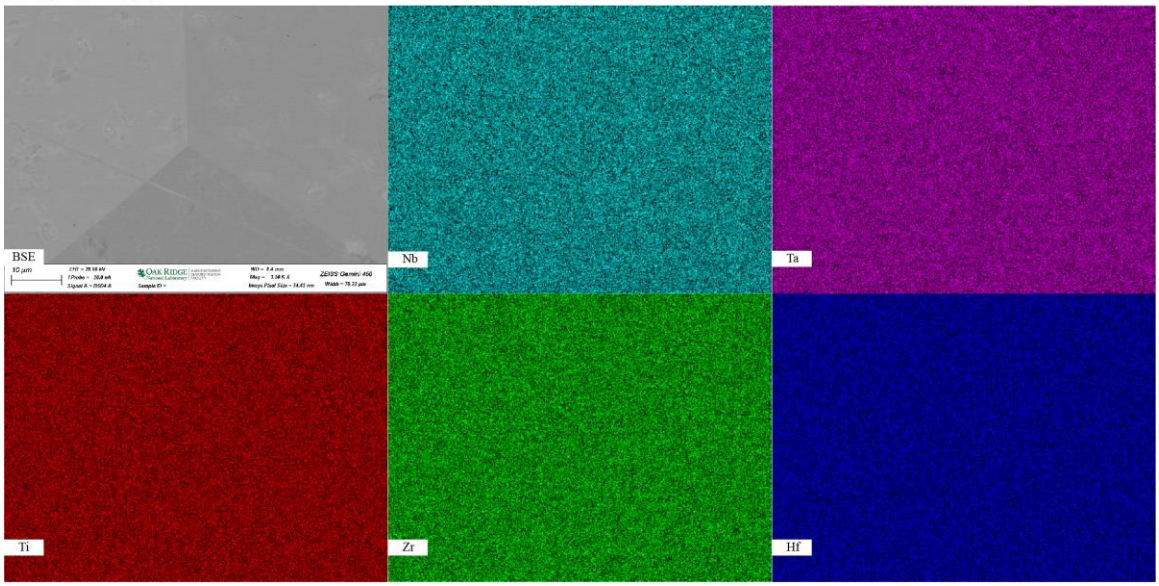

Supplementary Figure 4.20: $Ti_{20}Zr_{20}Hf_{20}Nb_{35}Ta_5$ after 48 h at 1000 ˚C beginning in the cold rolled condition, with accompanying EDS maps.

$Ti_{20}Zr_{20}Hf_{20}Nb_{35}Ta_5$ - Cold Rolled
1000 ˚C - 480 h

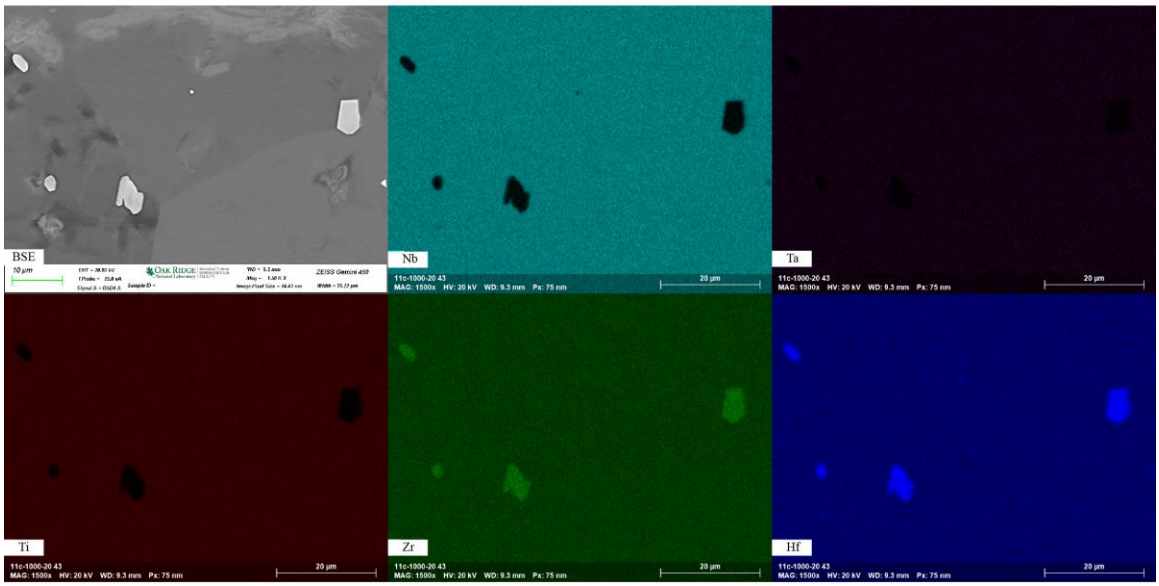

Supplementary Figure 4.21: $Ti_{20}Zr_{20}Hf_{20}Nb_{35}Ta_5$ after 480 h at 1000 ˚C beginning in the cold rolled condition, with accompanying EDS maps.

$Ti_{20}Zr_{20}Hf_{20}Nb_{35}Ta_5$ - Cold Rolled
1000 ˚C - 4800 h

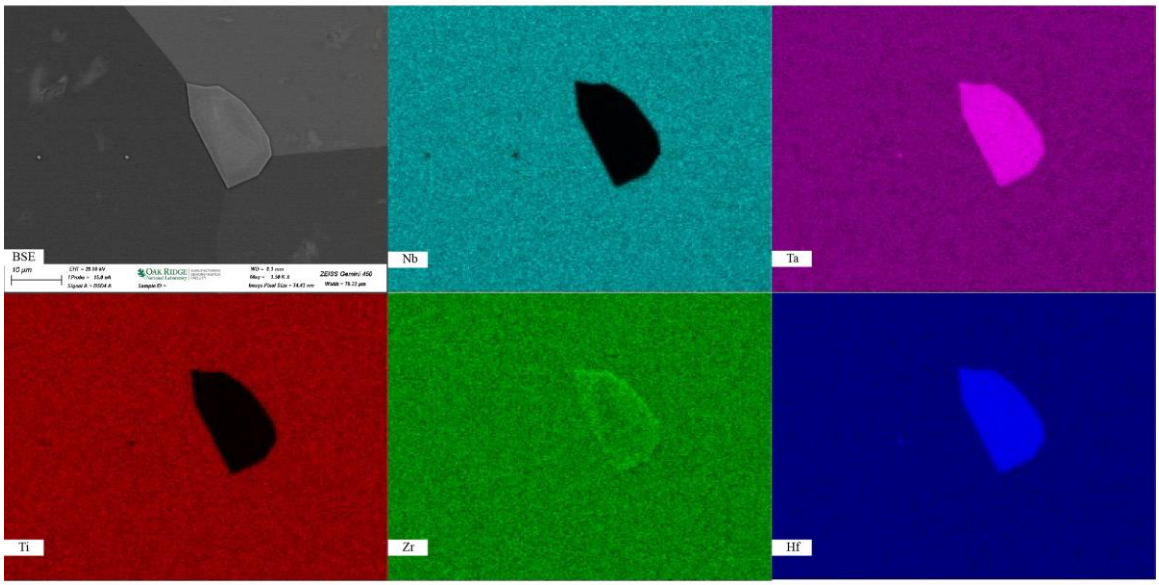

Supplementary Figure 4.22: $Ti_{20}Zr_{20}Hf_{20}Nb_{35}Ta_5$ after 4800 h at 1000 ˚C beginning in the cold rolled condition, with accompanying EDS maps.

$Ti_{20}Zr_{20}Hf_{20}Nb_{35}Ta_5$ - Recrystallized
1000 ˚C - 48 h

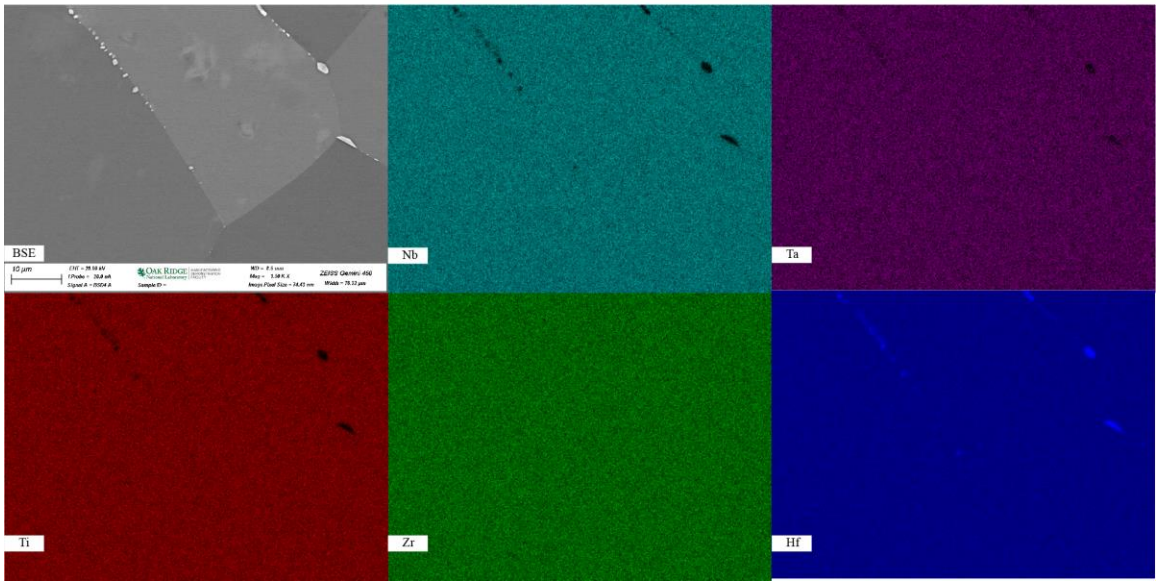

Supplementary Figure 4.23: $Ti_{20}Zr_{20}Hf_{20}Nb_{35}Ta_5$ after 48 h at 1000 ˚C beginning in the recrystallized condition, with accompanying EDS maps.

$Ti_{20}Zr_{20}Hf_{20}Nb_{35}Ta_5$ - Recrystallized
1000 ˚C - 480 h

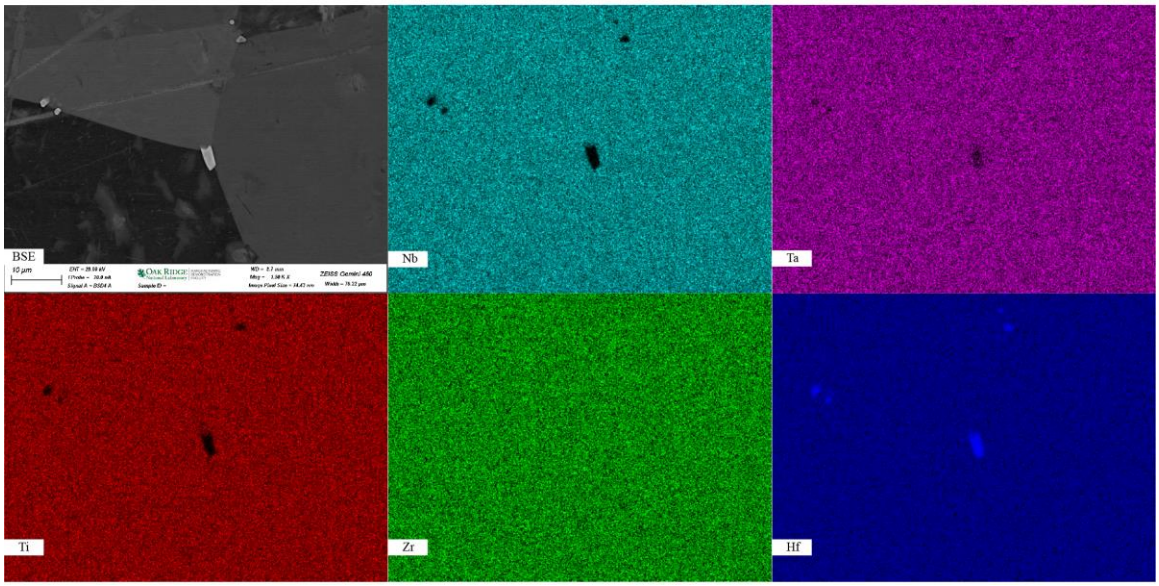

Supplementary Figure 4.24: $Ti_{20}Zr_{20}Hf_{20}Nb_{35}Ta_5$ after 480 h at 1000 ˚C beginning in the recrystallized condition, with accompanying EDS maps.

$Ti_{20}Zr_{20}Hf_{20}Nb_{35}Ta_5$ - Recrystallized
1000 ˚C - 4800 h

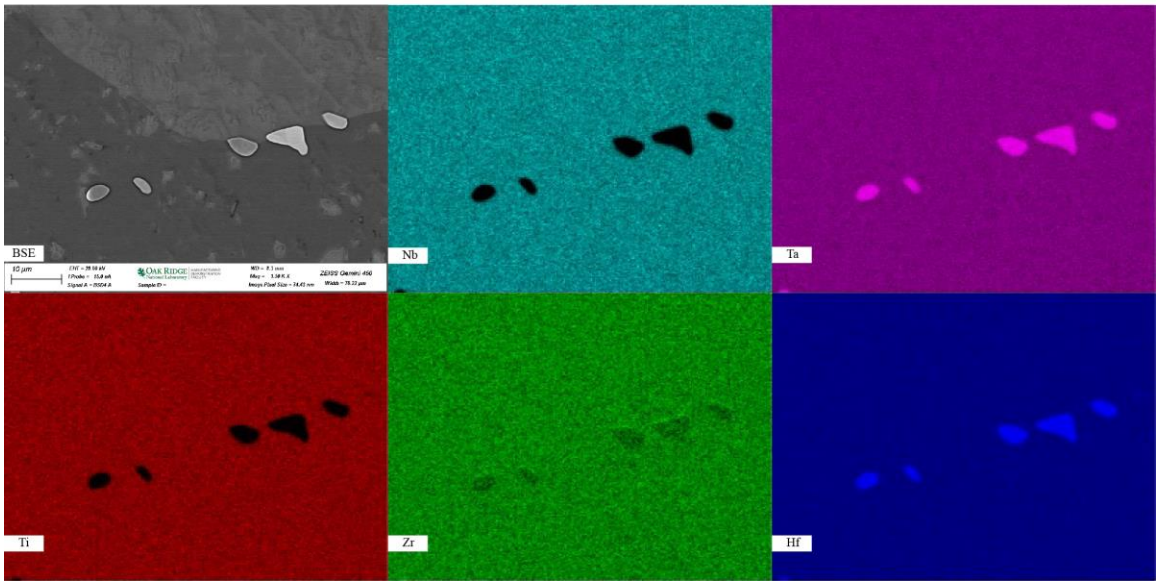

Supplementary Figure 4.25: $Ti_{20}Zr_{20}Hf_{20}Nb_{35}Ta_5$ after 4800 h at 1000 ˚C beginning in the recrystallized condition, with accompanying EDS maps.

<u>$Ti_{40}Zr_{20}Hf_{20}N_{10}Ta_{10}$ 700 ˚C and 1000 ˚C SEM-EDS</u>

$Ti_{40}Zr_{20}Hf_{20}Nb_{10}Ta_{10}$ - Cold Rolled
700 ˚C - 48 h

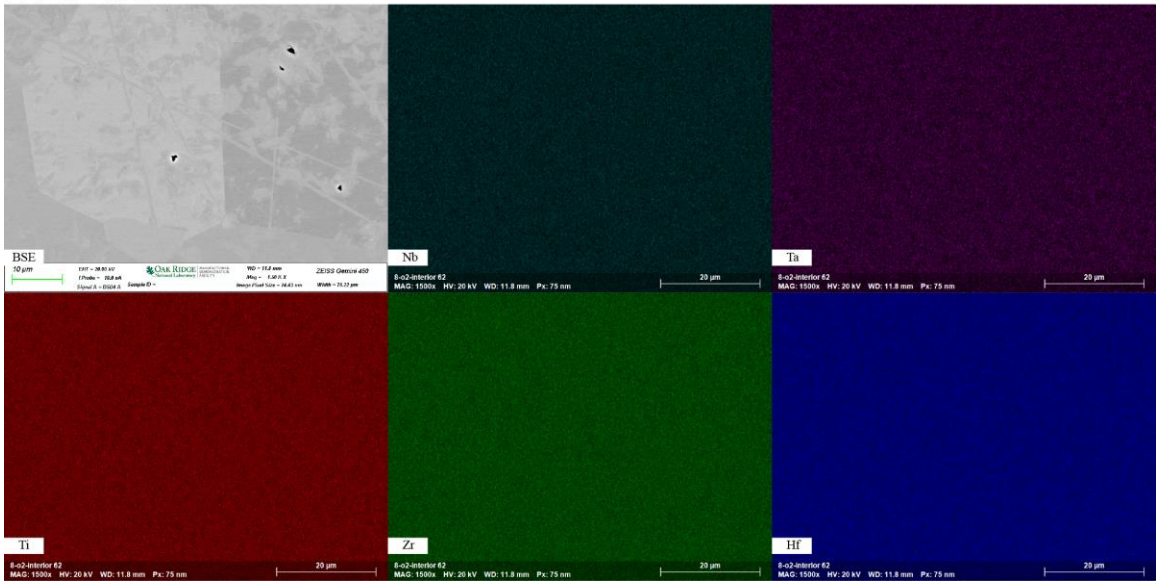

Supplementary Figure 4.26: $Ti_{40}Zr_{20}Hf_{20}N_{10}Ta_{10}$ after 48 h at 700 ˚C beginning in the cold rolled condition, with accompanying EDS maps.

$Ti_{40}Zr_{20}Hf_{20}Nb_{10}Ta_{10}$ - Cold Rolled
700 ˚C - 480 h

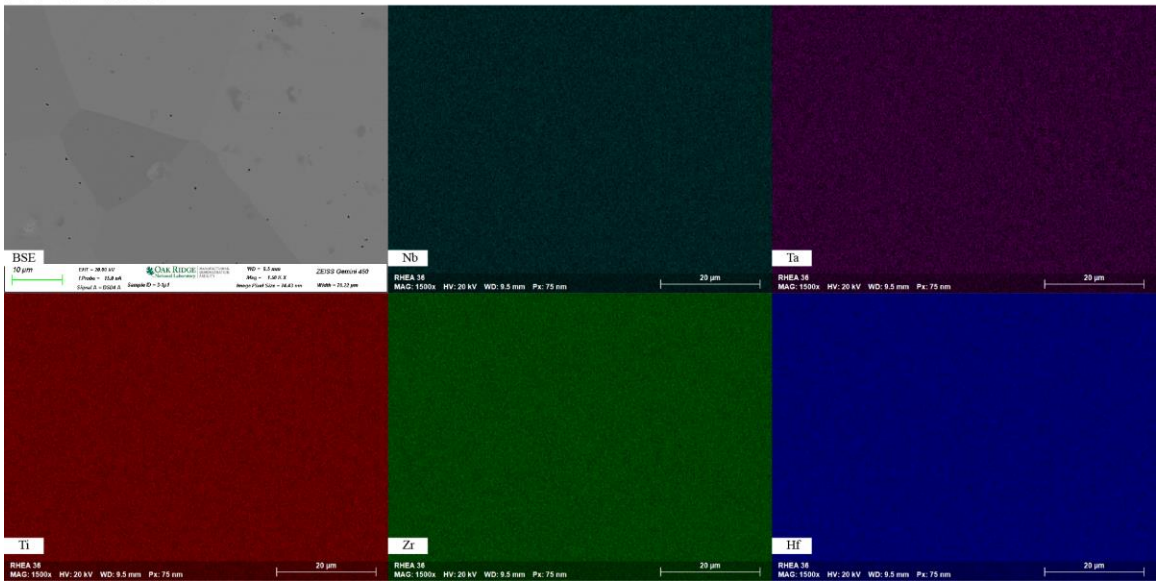

Supplementary Figure 4.27: $Ti_{40}Zr_{20}Hf_{20}N_{10}Ta_{10}$ after 480 h at 700 ˚C beginning in the cold rolled condition, with accompanying EDS maps.

$Ti_{40}Zr_{20}Hf_{20}Nb_{10}Ta_{10}$ - Cold Rolled
700 ˚C - 4800 h

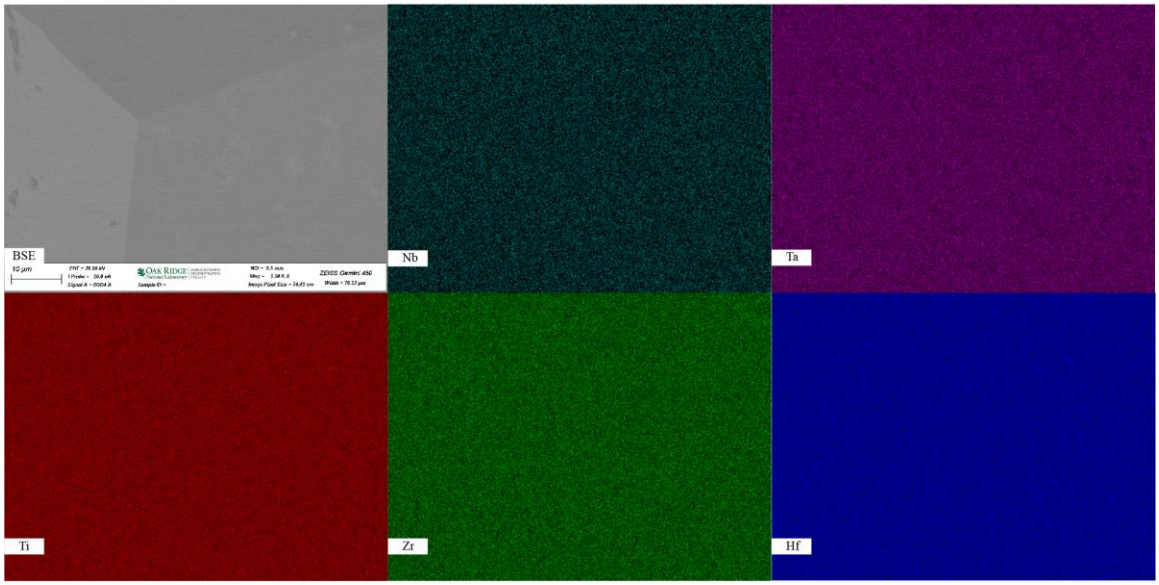

Supplementary Figure 4.28: $Ti_{40}Zr_{20}Hf_{20}N_{10}Ta_{10}$ after 4800 h at 700 ˚C beginning in the cold rolled condition, with accompanying EDS maps.

$Ti_{40}Zr_{20}Hf_{20}Nb_{10}Ta_{10}$ - Recrystallized
700 ˚C - 48 h

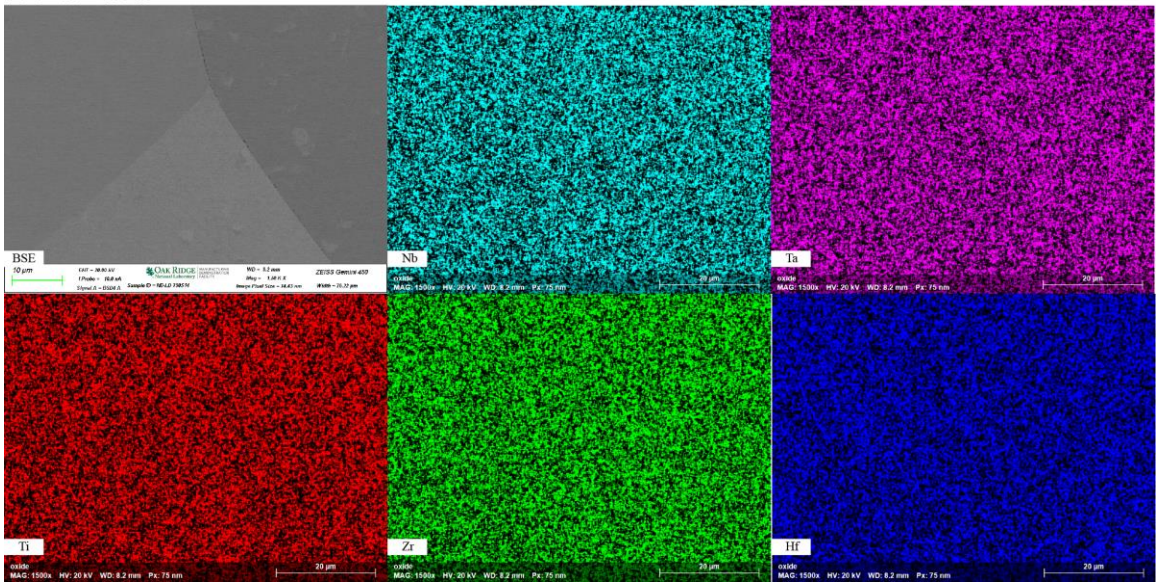

Supplementary Figure 4.29: $Ti_{40}Zr_{20}Hf_{20}N_{10}Ta_{10}$ after 48 h at 700 ˚C beginning in the recrystallized condition, with accompanying EDS maps.

$Ti_{40}Zr_{20}Hf_{20}Nb_{10}Ta_{10}$ - Recrystallized
700 ˚C - 480 h

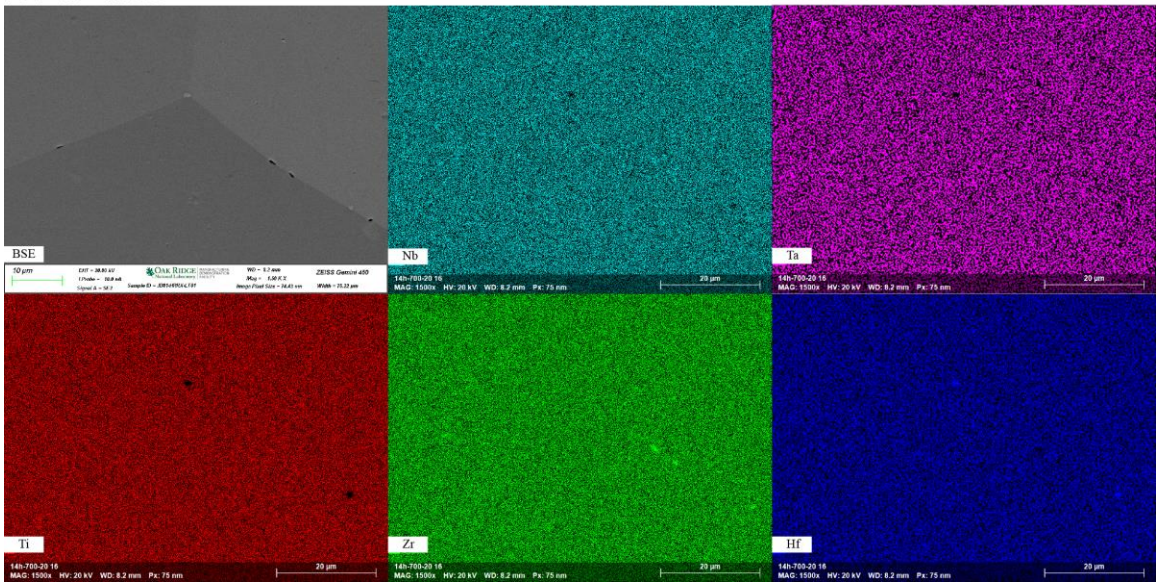

Supplementary Figure 4.30: $Ti_{40}Zr_{20}Hf_{20}N_{10}Ta_{10}$ after 480 h at 700 ˚C beginning in the recrystallized condition, with accompanying EDS maps.

$Ti_{40}Zr_{20}Hf_{20}Nb_{10}Ta_{10}$ - Recrystallized
700 ˚C - 4800 h

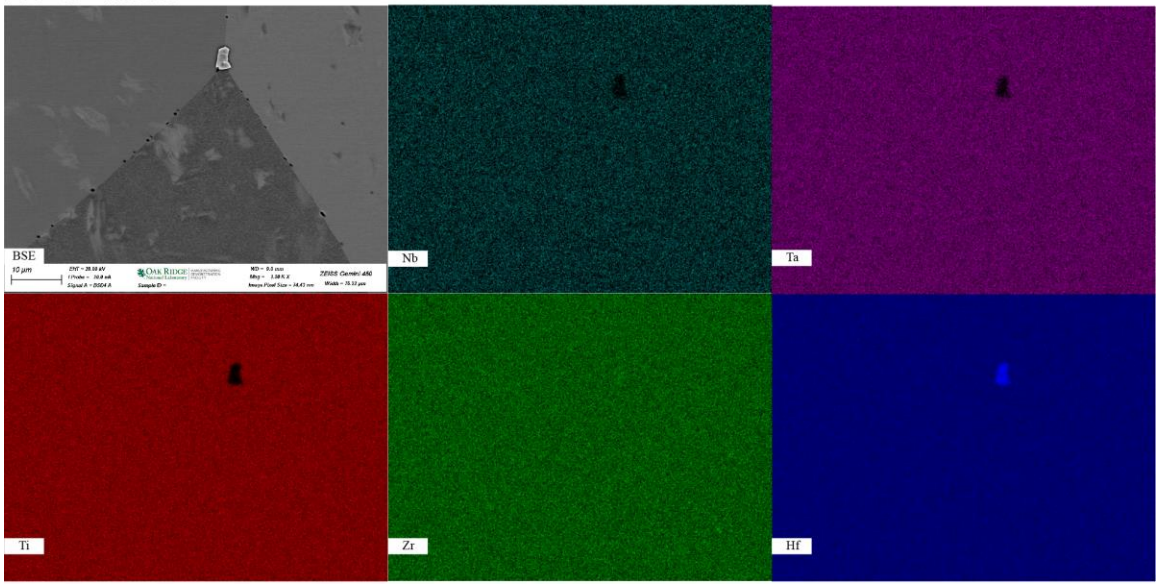

Supplementary Figure 4.31: $Ti_{40}Zr_{20}Hf_{20}N_{10}Ta_{10}$ after 4800 h at 700 ˚C beginning in the recrystallized condition, with accompanying EDS maps.

$Ti_{40}Zr_{20}Hf_{20}Nb_{10}Ta_{10}$ - Cold Rolled
1000 ˚C - 48 h

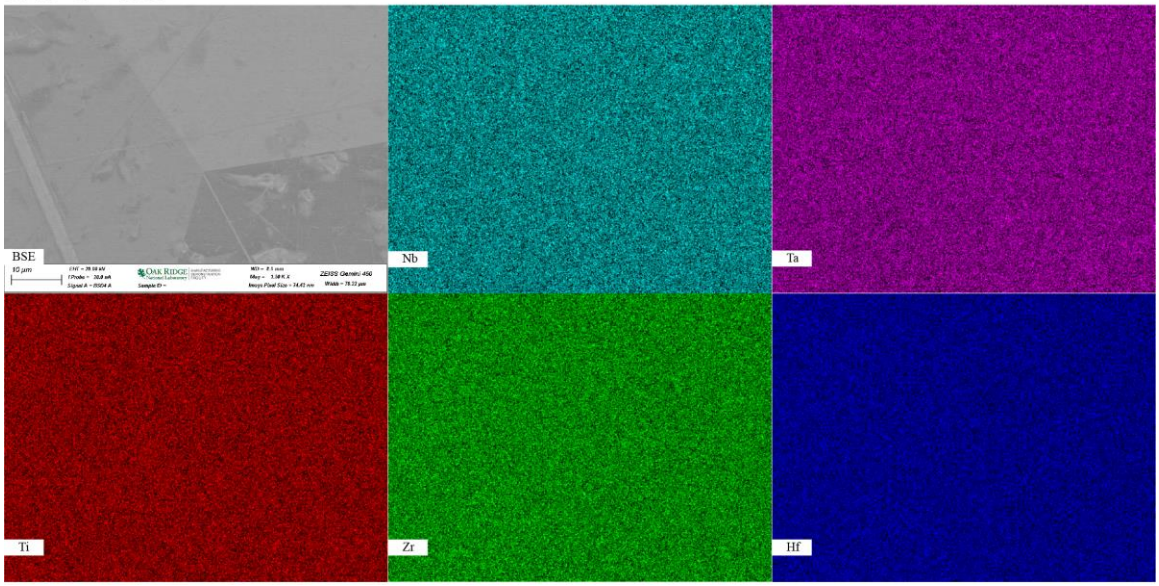

Supplementary Figure 4.32: $Ti_{40}Zr_{20}Hf_{20}N_{10}Ta_{10}$ after 48 h at 1000 ˚C beginning in the cold rolled condition, with accompanying EDS maps.

$Ti_{40}Zr_{20}Hf_{20}Nb_{10}Ta_{10}$ - Cold Rolled
1000 ˚C - 480 h

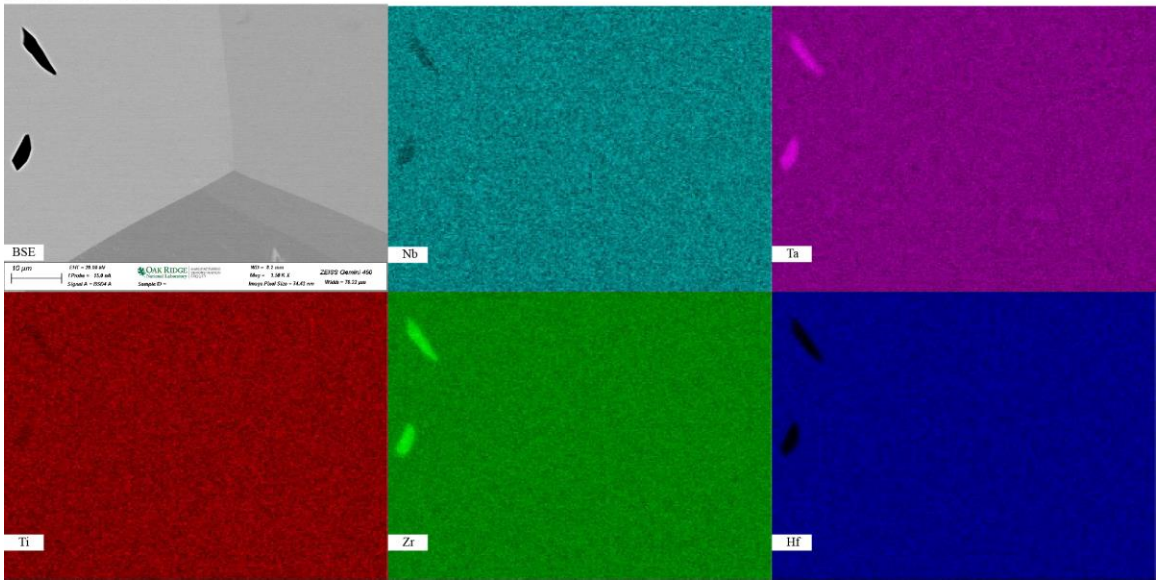

Supplementary Figure 4.33: $Ti_{40}Zr_{20}Hf_{20}N_{10}Ta_{10}$ after 480 h at 1000 ˚C beginning in the cold rolled condition, with accompanying EDS maps.

$Ti_{40}Zr_{20}Hf_{20}Nb_{10}Ta_{10}$ - Cold Rolled
1000 ˚C - 4800 h

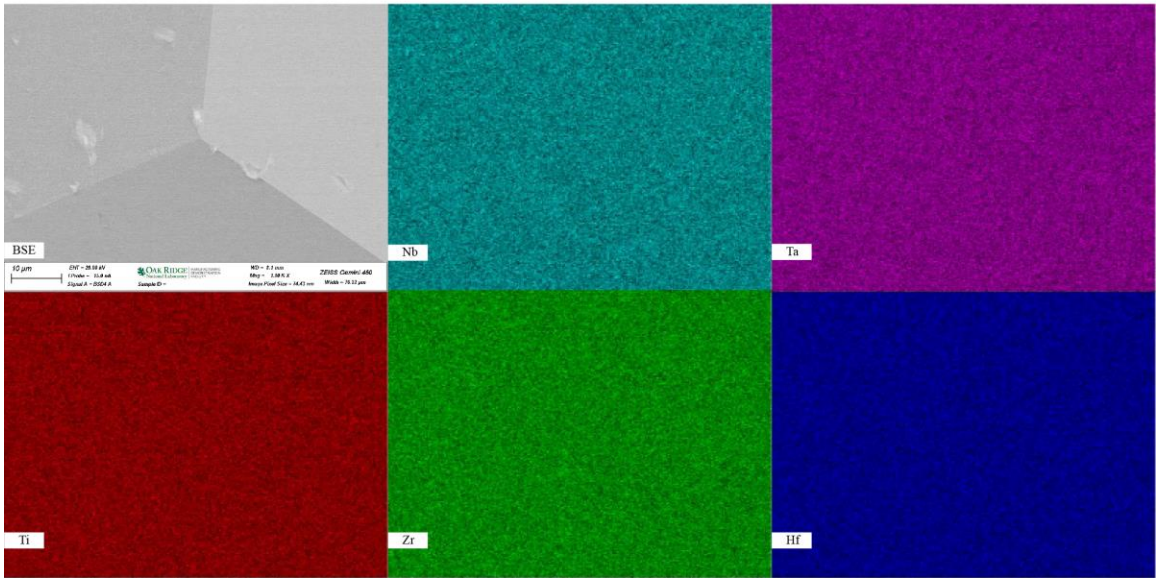

Supplementary Figure 4.34: $Ti_{40}Zr_{20}Hf_{20}N_{10}Ta_{10}$ after 4800 h at 1000 ˚C beginning in the cold rolled condition, with accompanying EDS maps.

$Ti_{40}Zr_{20}Hf_{20}Nb_{10}Ta_{10}$ - Recrystallized
1000 ˚C - 48 h

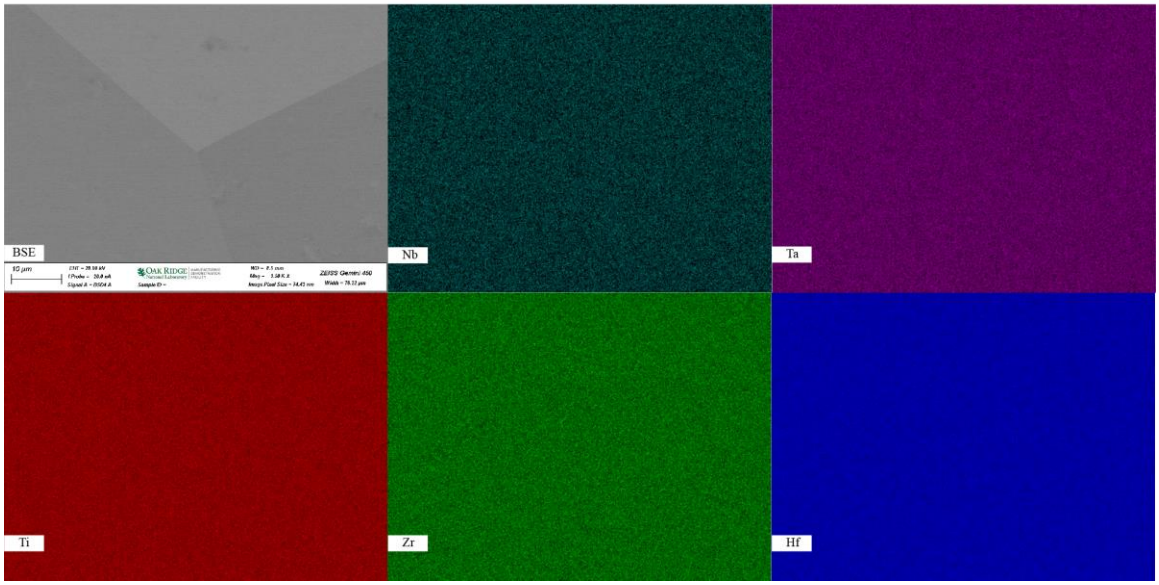

Supplementary Figure 4.35: $Ti_{40}Zr_{20}Hf_{20}N_{10}Ta_{10}$ after 48 h at 1000 ˚C beginning in the recrystallized condition, with accompanying EDS maps.

$Ti_{40}Zr_{20}Hf_{20}Nb_{10}Ta_{10}$ - Recrystallized
1000 ˚C - 480 h

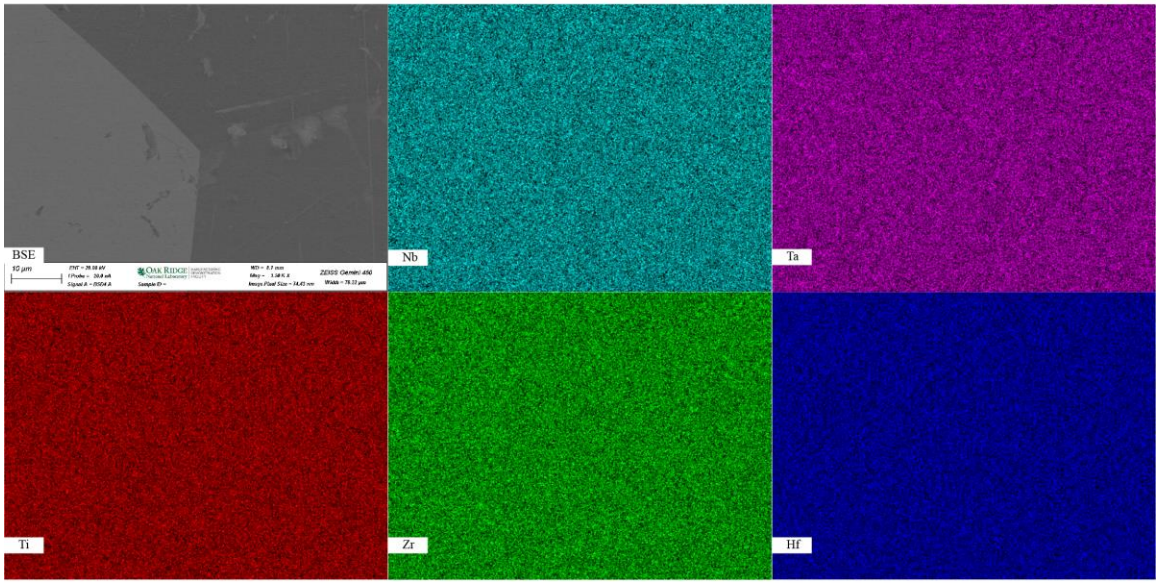

Supplementary Figure 4.36: $Ti_{40}Zr_{20}Hf_{20}N_{10}Ta_{10}$ after 480 h at 1000 ˚C beginning in the recrystallized condition, with accompanying EDS maps.

$Ti_{40}Zr_{20}Hf_{20}Nb_{10}Ta_{10}$ - Recrystallized
1000 ˚C - 4800 h

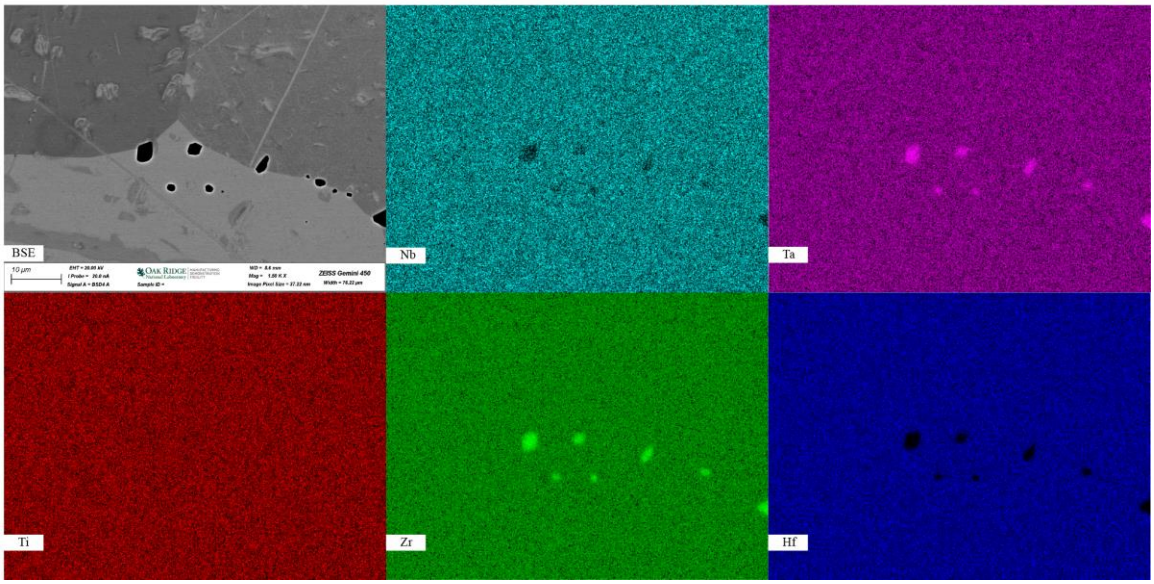

Supplementary Figure 4.37: $Ti_{40}Zr_{20}Hf_{20}N_{10}Ta_{10}$ after 4800 h at 1000 ˚C beginning in the recrystallized condition, with accompanying EDS maps.

<u>$Ti_{26.7}Zr_{26.7}Hf_{26.7}N_{10}Ta_{10}$ 700 ˚C and 1000 ˚C SEM-EDS</u>

$Ti_{26.7}Zr_{26.7}Hf_{26.7}Nb_{10}Ta_{10}$ - Cold Rolled
700 ˚C - 48 h

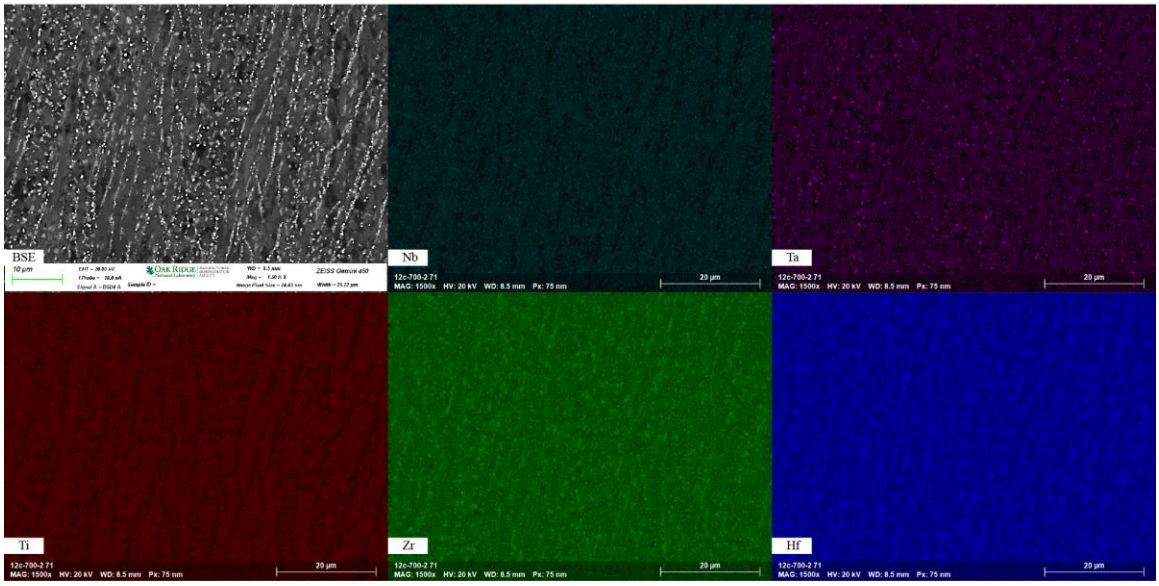

Supplementary Figure 4.38: $Ti_{26.7}Zr_{26.7}Hf_{26.7}N_{10}Ta_{10}$ after 48 h at 700 ˚C beginning in the cold rolled condition, with accompanying EDS maps.

$Ti_{26.7}Zr_{26.7}Hf_{26.7}Nb_{10}Ta_{10}$ - Cold Rolled
700 ˚C - 480 h

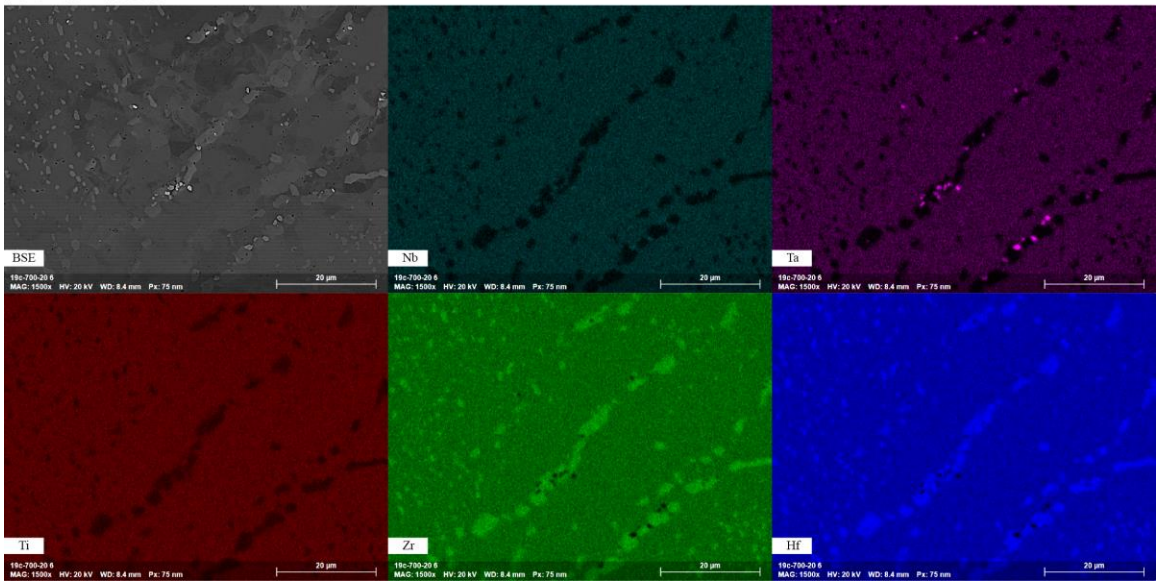

Supplementary Figure 4.39: $Ti_{26.7}Zr_{26.7}Hf_{26.7}N_{10}Ta_{10}$ after 480 h at 700 ˚C beginning in the cold rolled condition, with accompanying EDS maps.

$Ti_{26.7}Zr_{26.7}Hf_{26.7}Nb_{10}Ta_{10}$ - Cold Rolled
700 ˚C - 4800 h

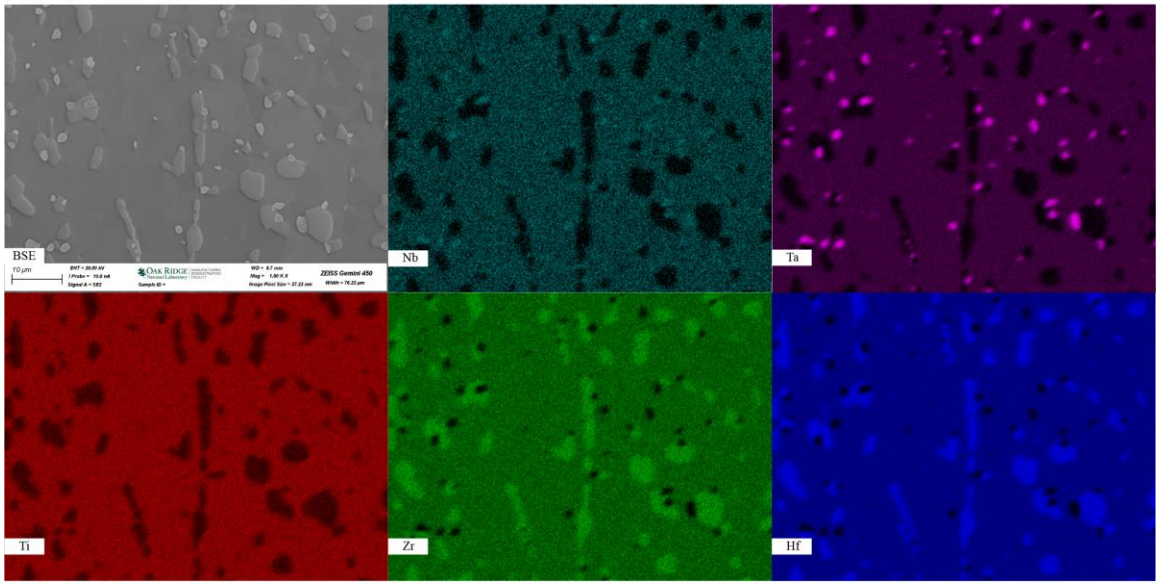

Supplementary Figure 4.40: $Ti_{26.7}Zr_{26.7}Hf_{26.7}N_{10}Ta_{10}$ after 4800 h at 700 ˚C beginning in the cold rolled condition, with accompanying EDS maps.

$Ti_{26.7}Zr_{26.7}Hf_{26.7}Nb_{10}Ta_{10}$ - Recrystallized
700 ˚C - 48 h

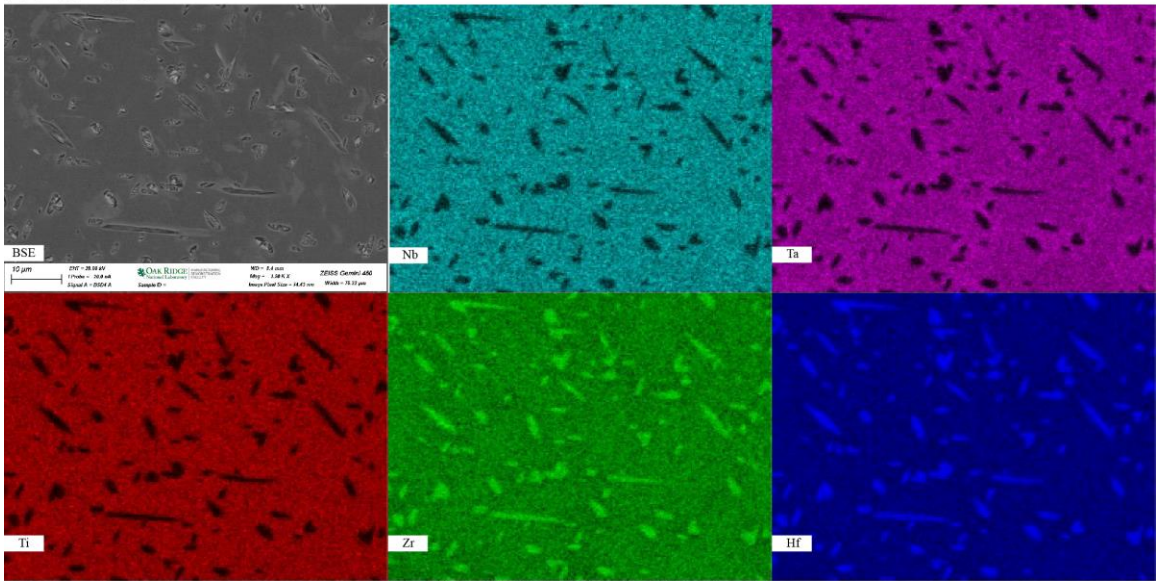

Supplementary Figure 4.41: $Ti_{26.7}Zr_{26.7}Hf_{26.7}N_{10}Ta_{10}$ after 48 h at 700 ˚C beginning in the recrystallized condition, with accompanying EDS maps.

$Ti_{26.7}Zr_{26.7}Hf_{26.7}Nb_{10}Ta_{10}$ - Recrystallized
700 ˚C - 480 h

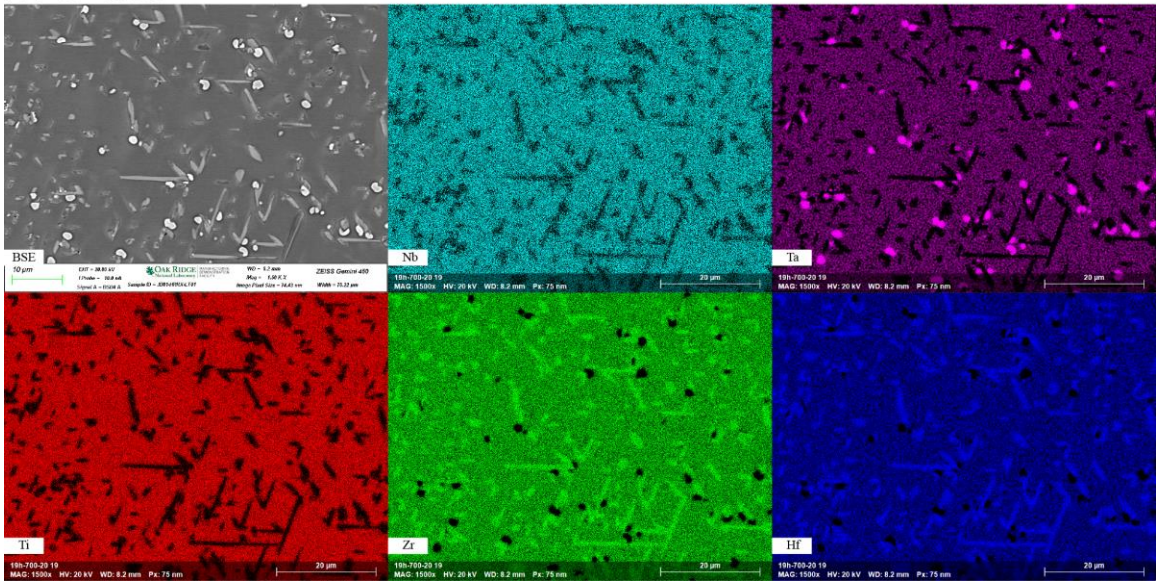

Supplementary Figure 4.42: $Ti_{26.7}Zr_{26.7}Hf_{26.7}N_{10}Ta_{10}$ after 480 h at 700 ˚C beginning in the recrystallized condition, with accompanying EDS maps.

$Ti_{26.7}Zr_{26.7}Hf_{26.7}Nb_{10}Ta_{10}$ - Recrystallized
700 ˚C - 4800 h

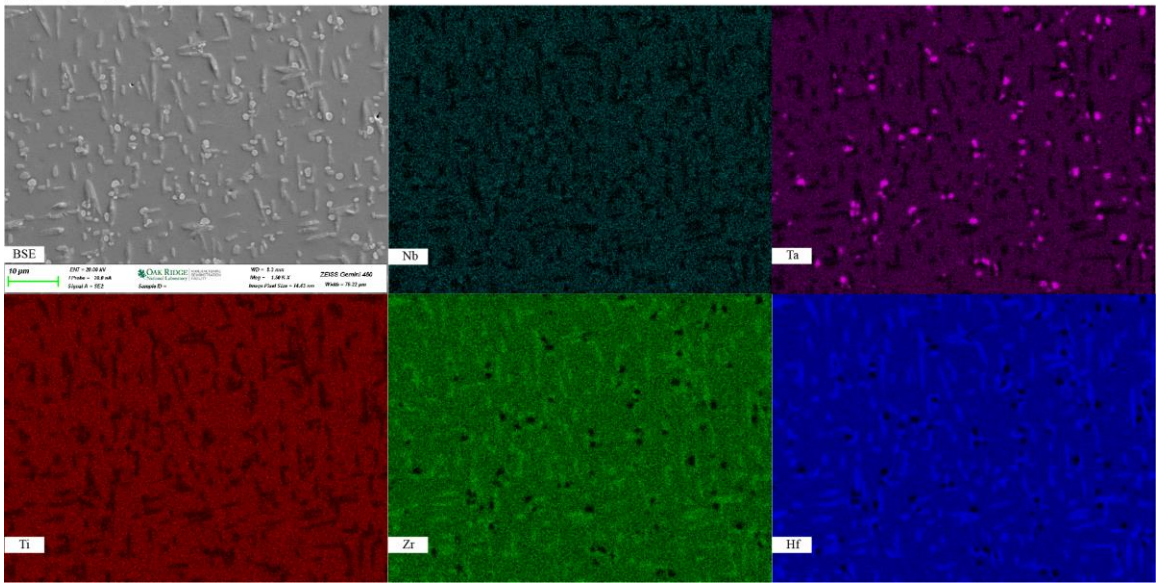

Supplementary Figure 4.43: $Ti_{26.7}Zr_{26.7}Hf_{26.7}N_{10}Ta_{10}$ after 4800 h at 700 ˚C beginning in the recrystallized condition, with accompanying EDS maps.

$Ti_{26.7}Zr_{26.7}Hf_{26.7}Nb_{10}Ta_{10}$ - Cold Rolled
1000 ˚C - 48 h

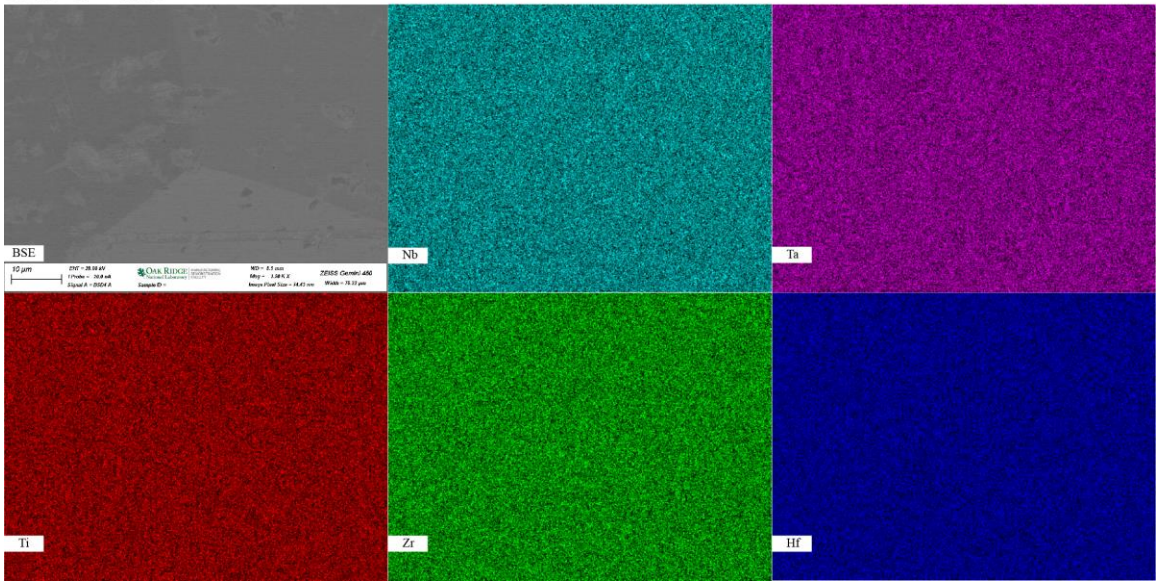

Supplementary Figure 4.44: $Ti_{26.7}Zr_{26.7}Hf_{26.7}N_{10}Ta_{10}$ after 48 h at 1000 ˚C beginning in the cold rolled condition, with accompanying EDS maps.

$Ti_{26.7}Zr_{26.7}Hf_{26.7}Nb_{10}Ta_{10}$ - Cold Rolled
1000 ˚C - 480 h

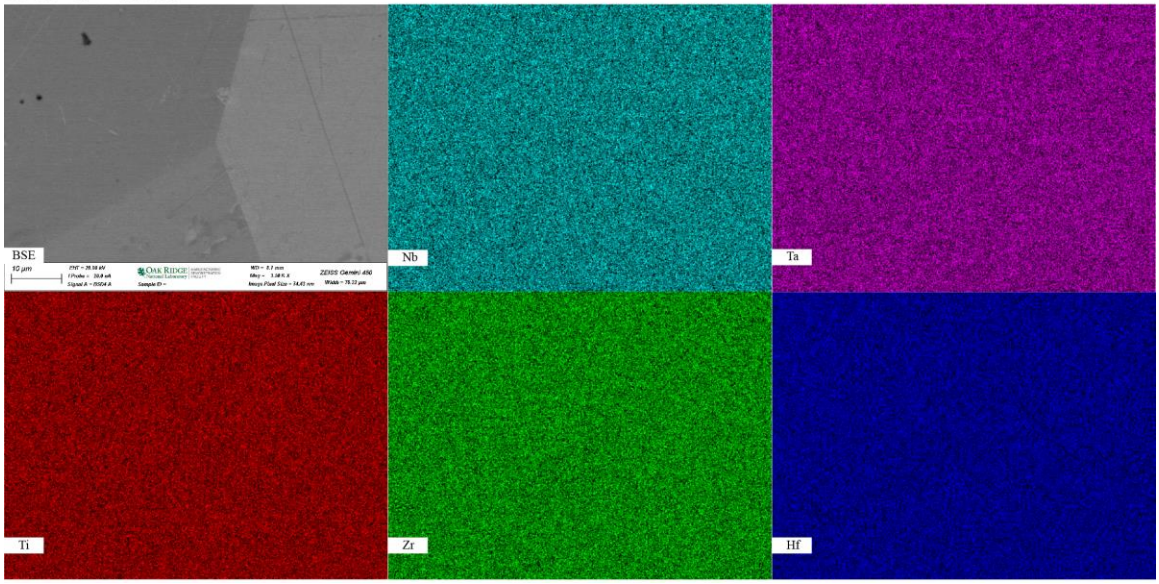

Supplementary Figure 4.45: $Ti_{26.7}Zr_{26.7}Hf_{26.7}N_{10}Ta_{10}$ after 480 h at 1000 ˚C beginning in the cold rolled condition, with accompanying EDS maps.

$Ti_{26.7}Zr_{26.7}Hf_{26.7}Nb_{10}Ta_{10}$ - Cold Rolled
1000 ˚C - 4800 h

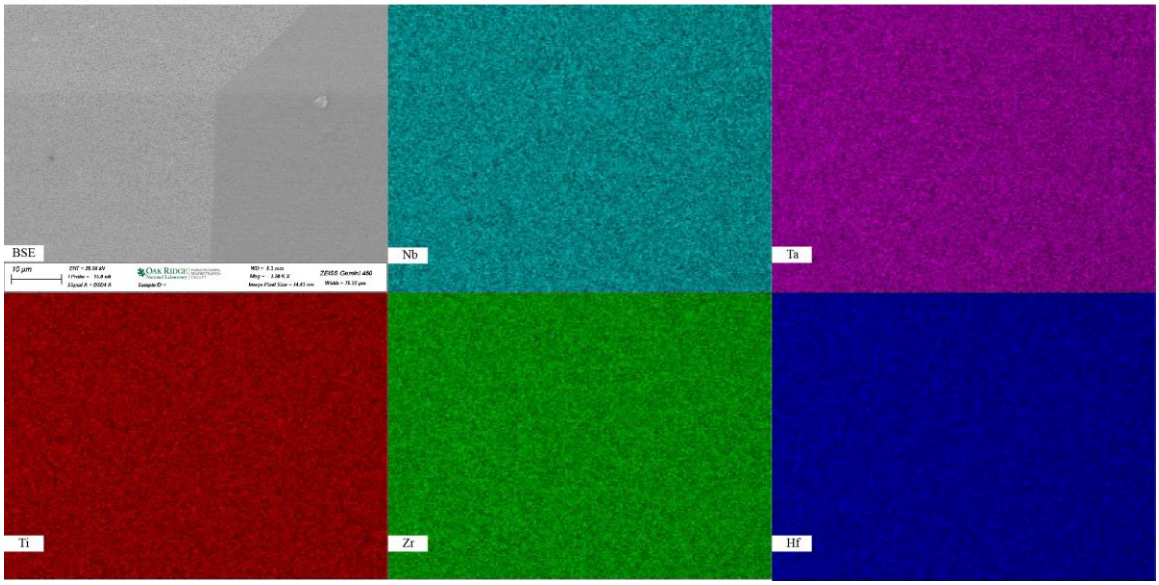

Supplementary Figure 4.46: $Ti_{26.7}Zr_{26.7}Hf_{26.7}N_{10}Ta_{10}$ after 4800 h at 1000 ˚C beginning in the cold rolled condition, with accompanying EDS maps.

$Ti_{26.7}Zr_{26.7}Hf_{26.7}Nb_{10}Ta_{10}$ - Recrystallized
1000 ˚C - 48 h

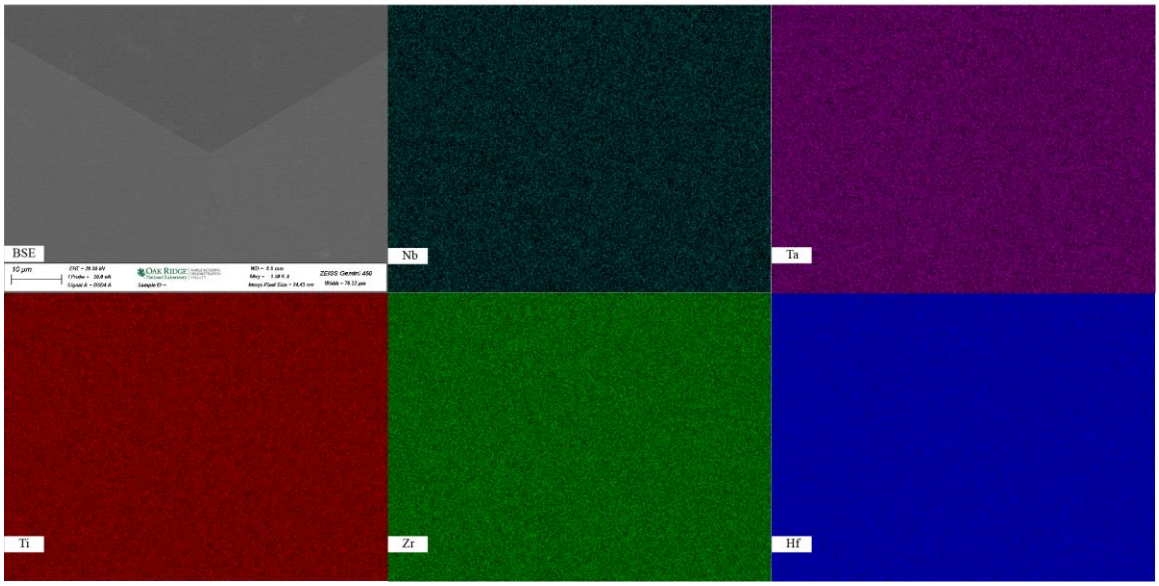

Supplementary Figure 4.47: $Ti_{26.7}Zr_{26.7}Hf_{26.7}N_{10}Ta_{10}$ after 48 h at 1000 ˚C beginning in the recrystallized condition, with accompanying EDS maps.

$Ti_{26.7}Zr_{26.7}Hf_{26.7}Nb_{10}Ta_{10}$ - Recrystallized
1000 ˚C - 480 h

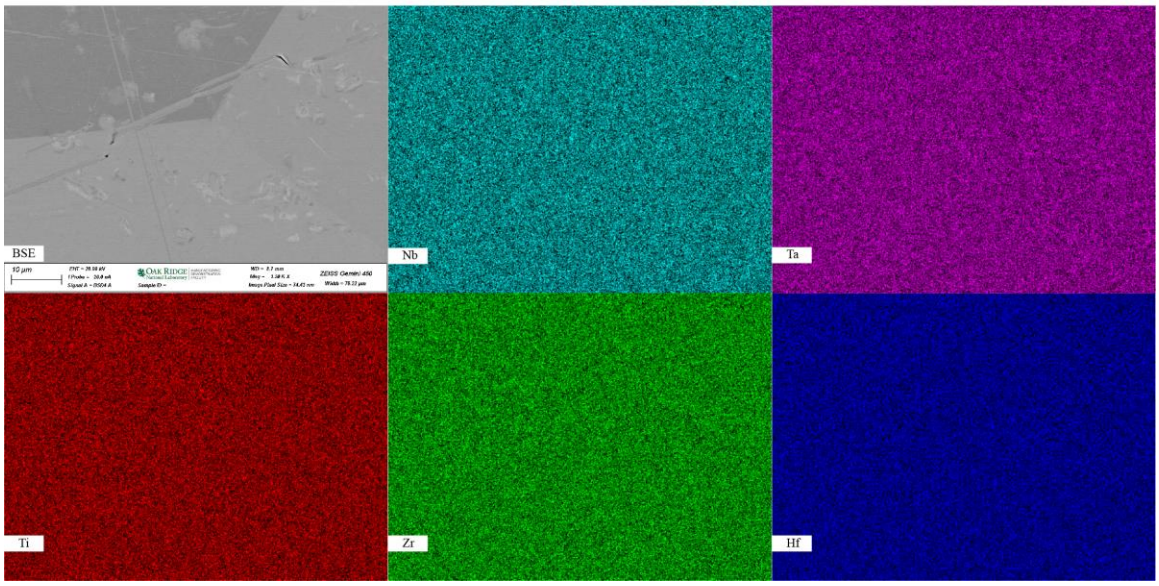

Supplementary Figure 4.48: $Ti_{26.7}Zr_{26.7}Hf_{26.7}N_{10}Ta_{10}$ after 480 h at 1000 ˚C beginning in the recrystallized condition, with accompanying EDS maps.

$Ti_{26.7}Zr_{26.7}Hf_{26.7}Nb_{10}Ta_{10}$ - Recrystallized
1000 ˚C - 4800 h

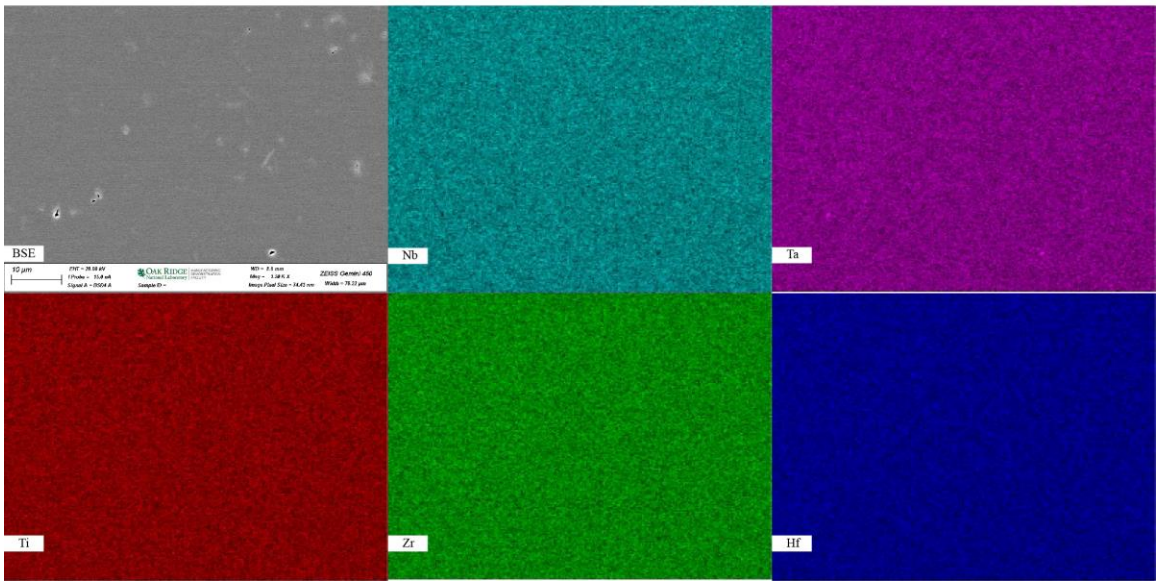

Supplementary Figure 4.49: $Ti_{26.7}Zr_{26.7}Hf_{26.7}N_{10}Ta_{10}$ after 4800 h at 1000 ˚C beginning in the recrystallized condition, with accompanying EDS maps.

<u>$Ti_5Zr_{20}Hf_{35}N_{20}Ta_{20}$ 700 ˚C and 1000 ˚C SEM-EDS</u>

$Ti_5Zr_{20}Hf_{35}Nb_{20}Ta_{20}$ - Cold Rolled
700 ˚C - 48 h

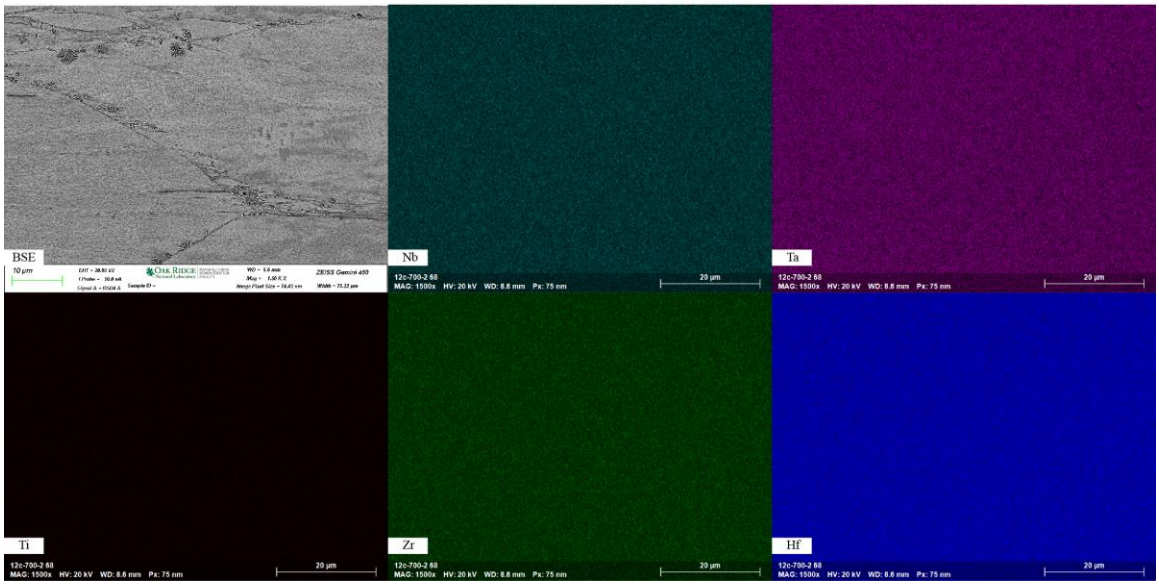

Supplementary Figure 4.50: $Ti_5Zr_{20}Hf_{35}N_{20}Ta_{20}$ after 48 h at 700 ˚C beginning in the cold rolled condition, with accompanying EDS maps.

$Ti_5Zr_{20}Hf_{35}Nb_{20}Ta_{20}$ - Cold Rolled
700 ˚C - 480 h

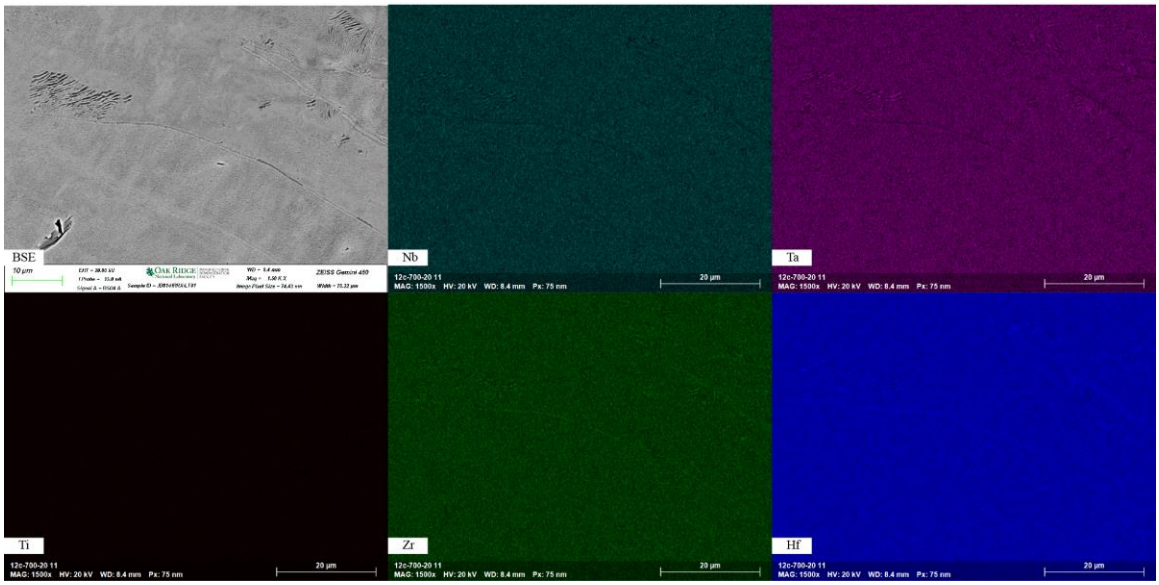

Supplementary Figure 4.51: $Ti_5Zr_{20}Hf_{35}N_{20}Ta_{20}$ after 480 h at 700 ˚C beginning in the cold rolled condition, with accompanying EDS maps.

$Ti_5Zr_{20}Hf_{35}Nb_{20}Ta_{20}$ - Cold Rolled
700 ˚C - 4800 h

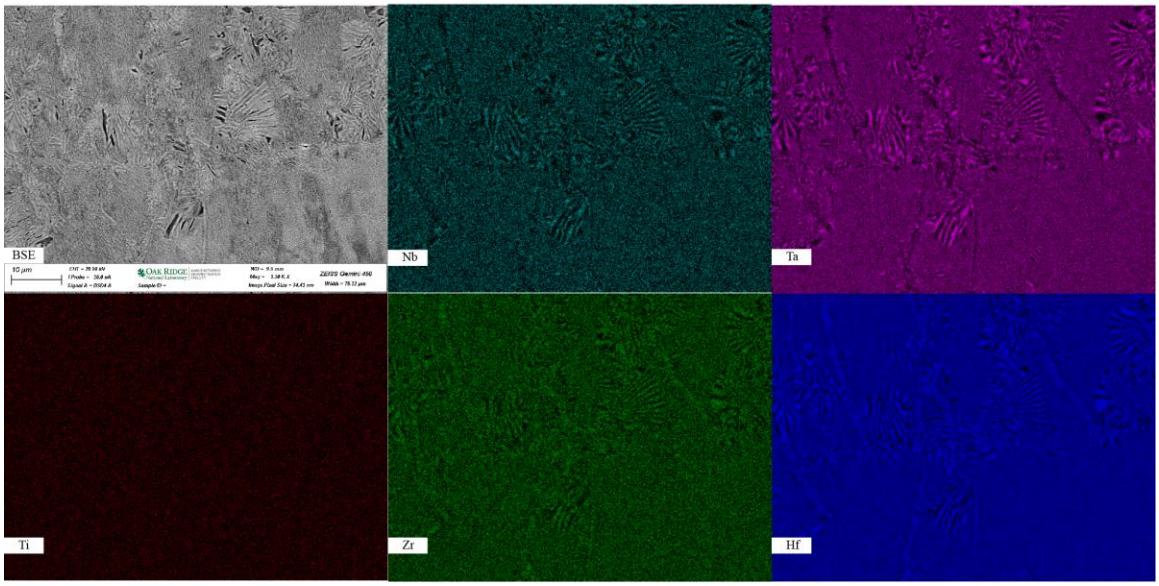

Supplementary Figure 4.52: $Ti_5Zr_{20}Hf_{35}N_{20}Ta_{20}$ after 4800 h at 700 ˚C beginning in the cold rolled condition, with accompanying EDS maps.

$Ti_5Zr_{20}Hf_{35}Nb_{20}Ta_{20}$ - Recrystallized
700 ˚C - 48 h

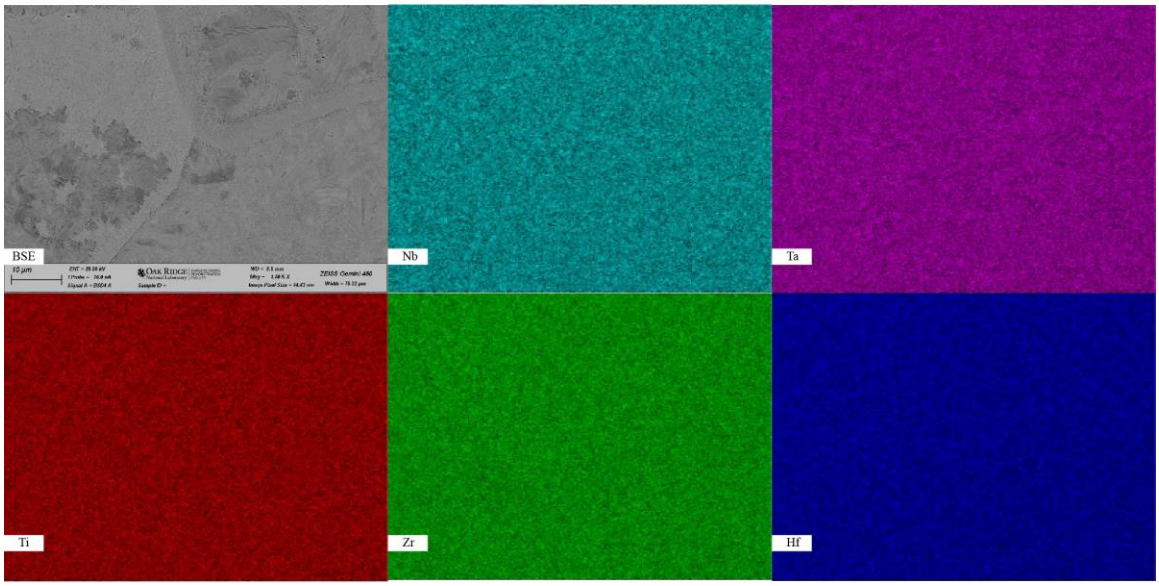

Supplementary Figure 4.53: $Ti_5Zr_{20}Hf_{35}N_{20}Ta_{20}$ after 48 h at 700 ˚C beginning in the recrystallized condition, with accompanying EDS maps.

$Ti_5Zr_{20}Hf_{35}Nb_{20}Ta_{20}$ - Recrystallized
700 ˚C - 480 h

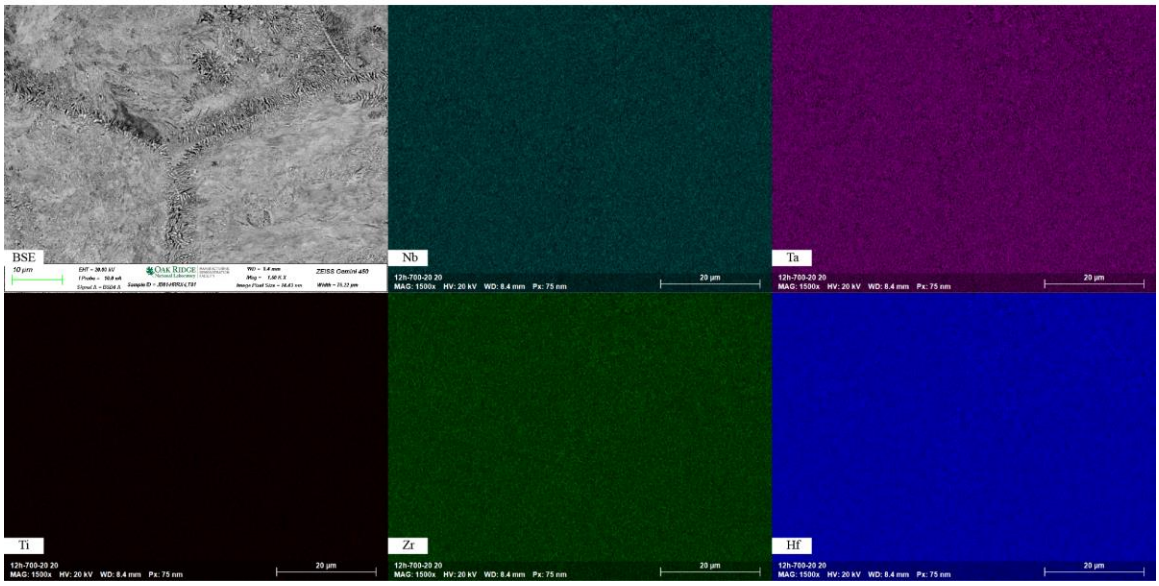

Supplementary Figure 4.54: $Ti_5Zr_{20}Hf_{35}N_{20}Ta_{20}$ after 480 h at 700 ˚C beginning in the recrystallized condition, with accompanying EDS maps.

$Ti_5Zr_{20}Hf_{35}Nb_{20}Ta_{20}$ - Recrystallized
700 ˚C - 4800 h

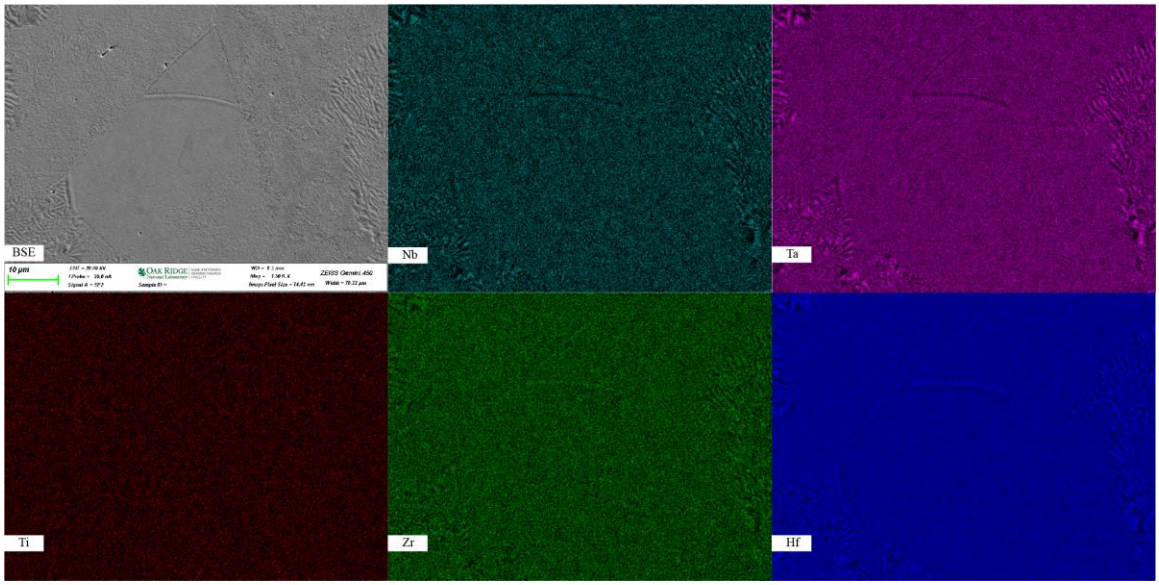

Supplementary Figure 4.55: $Ti_5Zr_{20}Hf_{35}N_{20}Ta_{20}$ after 4800 h at 700 ˚C beginning in the recrystallized condition, with accompanying EDS maps.

$Ti_5Zr_{20}Hf_{35}Nb_{20}Ta_{20}$ - Cold Rolled
1000 ˚C - 48 h

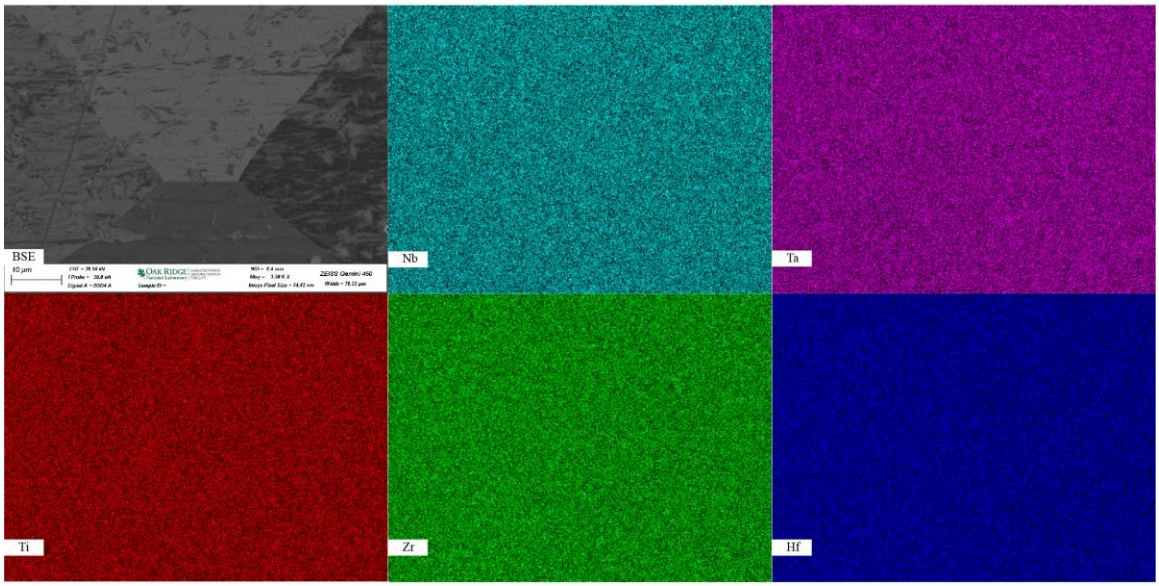

Supplementary Figure 4.56: $Ti_5Zr_{20}Hf_{35}N_{20}Ta_{20}$ after 48 h at 1000 ˚C beginning in the cold rolled condition, with accompanying EDS maps.

$Ti_5Zr_{20}Hf_{35}Nb_{20}Ta_{20}$ - Cold Rolled
1000 ˚C - 480 h

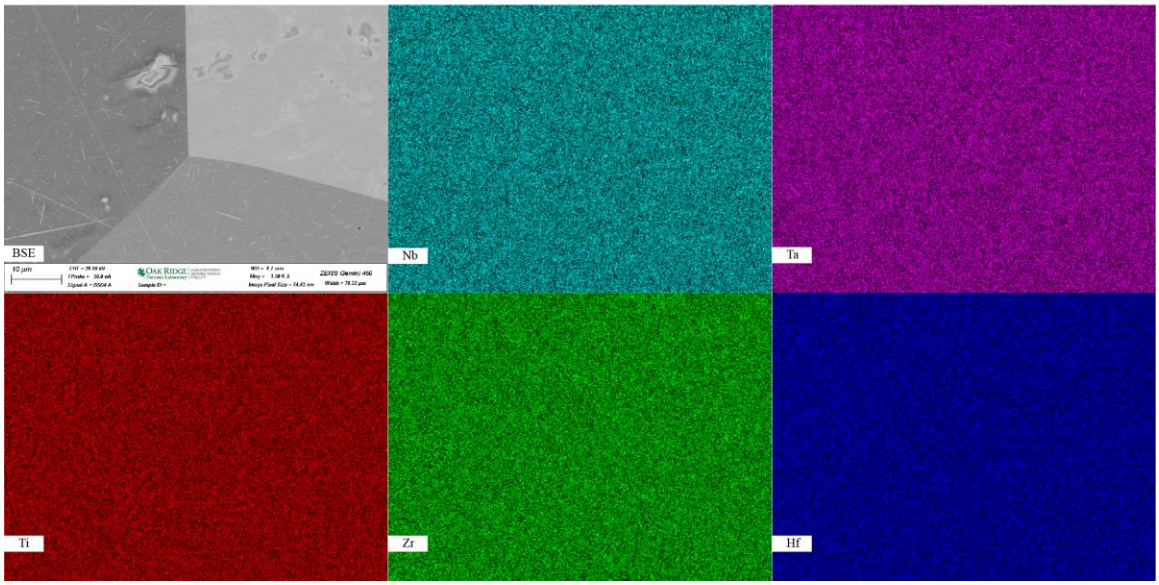

Supplementary Figure 4.57: $Ti_5Zr_{20}Hf_{35}N_{20}Ta_{20}$ after 480 h at 1000 ˚C beginning in the cold rolled condition, with accompanying EDS maps.

$Ti_5Zr_{20}Hf_{35}Nb_{20}Ta_{20}$ - Cold Rolled
1000 ˚C - 4800 h

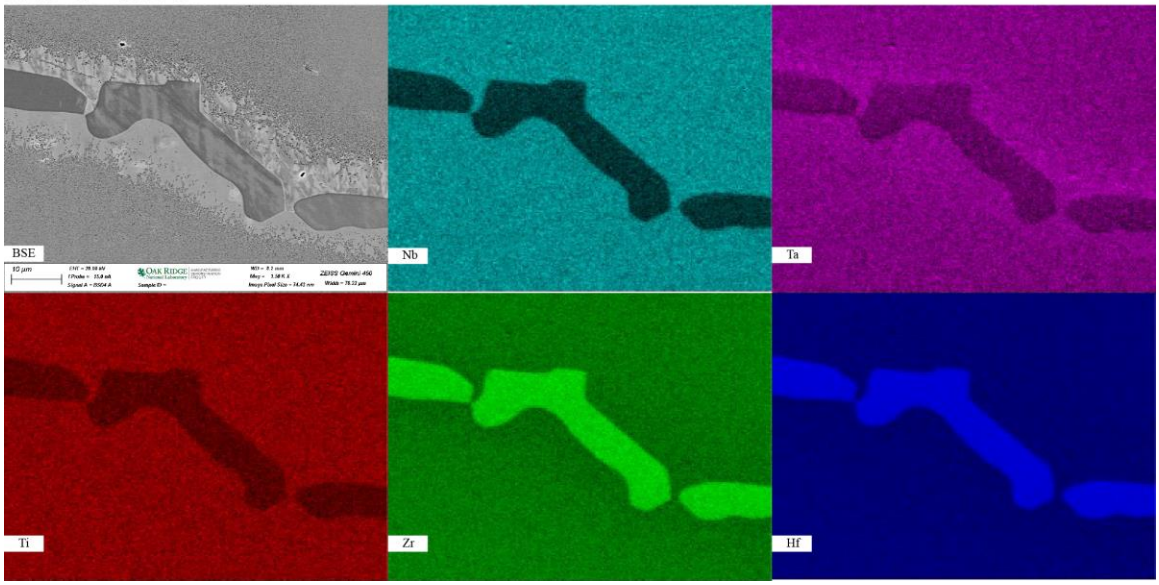

Supplementary Figure 4.58: $Ti_5Zr_{20}Hf_{35}N_{20}Ta_{20}$ after 4800 h at 1000 ˚C beginning in the cold rolled condition, with accompanying EDS maps.

$Ti_5Zr_{20}Hf_{35}Nb_{20}Ta_{20}$ - Recrystallized
1000 ˚C - 48 h

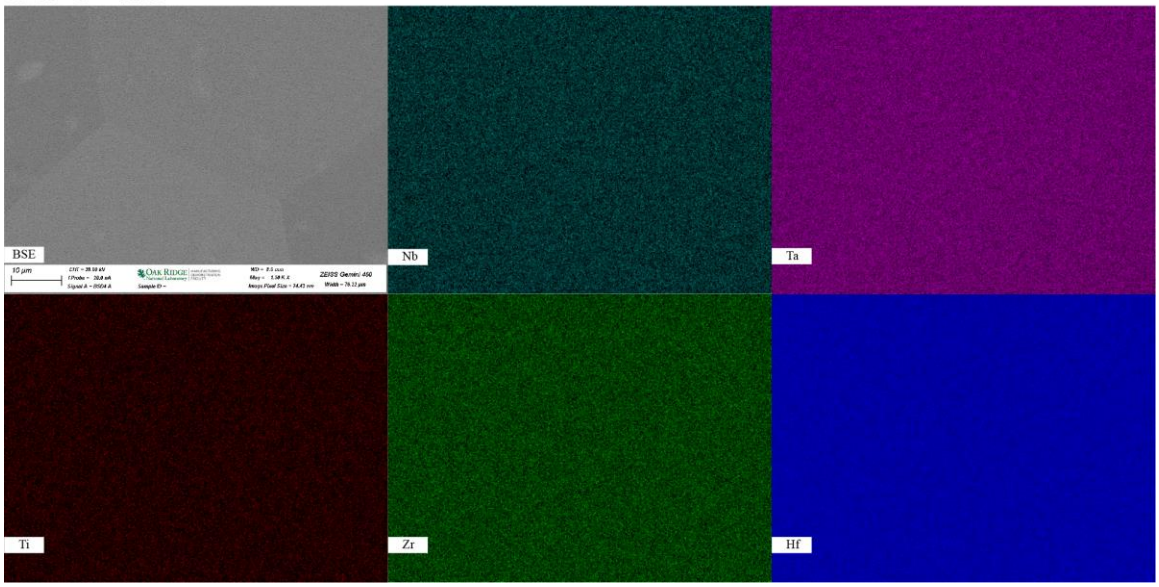

Supplementary Figure 4.59: $Ti_5Zr_{20}Hf_{35}N_{20}Ta_{20}$ after 48 h at 1000 ˚C beginning in the recrystallized condition, with accompanying EDS maps.

$Ti_5Zr_{20}Hf_{35}Nb_{20}Ta_{20}$ - Recrystallized
1000 ˚C - 480 h

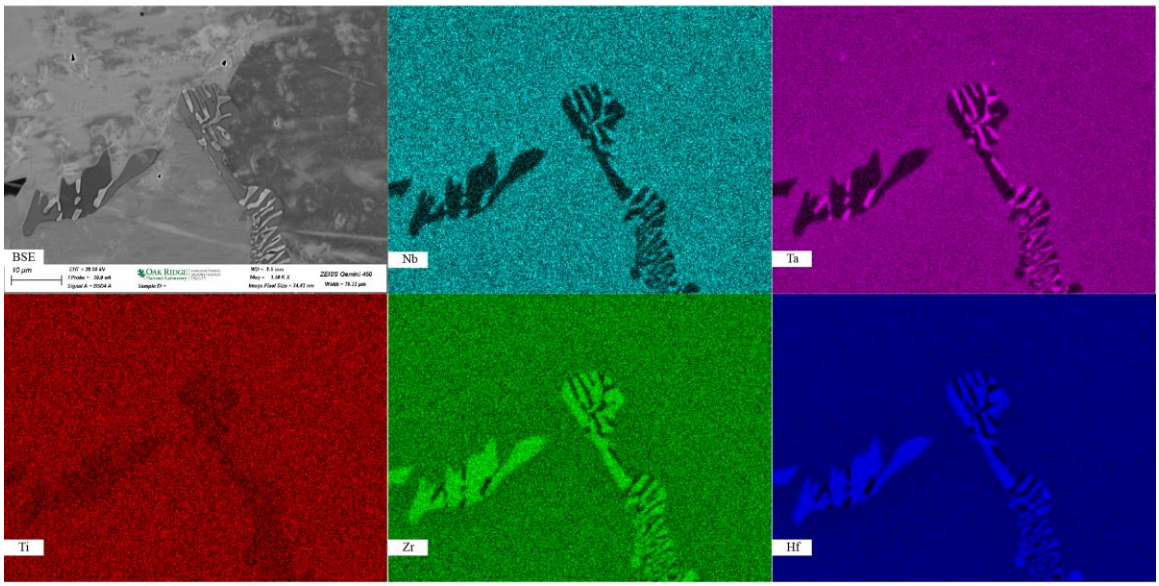

Supplementary Figure 4.60: $Ti_5Zr_{20}Hf_{35}N_{20}Ta_{20}$ after 480 h at 1000 ˚C beginning in the recrystallized condition, with accompanying EDS maps.

$Ti_5Zr_{20}Hf_{35}Nb_{20}Ta_{20}$ - Recrystallized
1000 ˚C - 4800 h

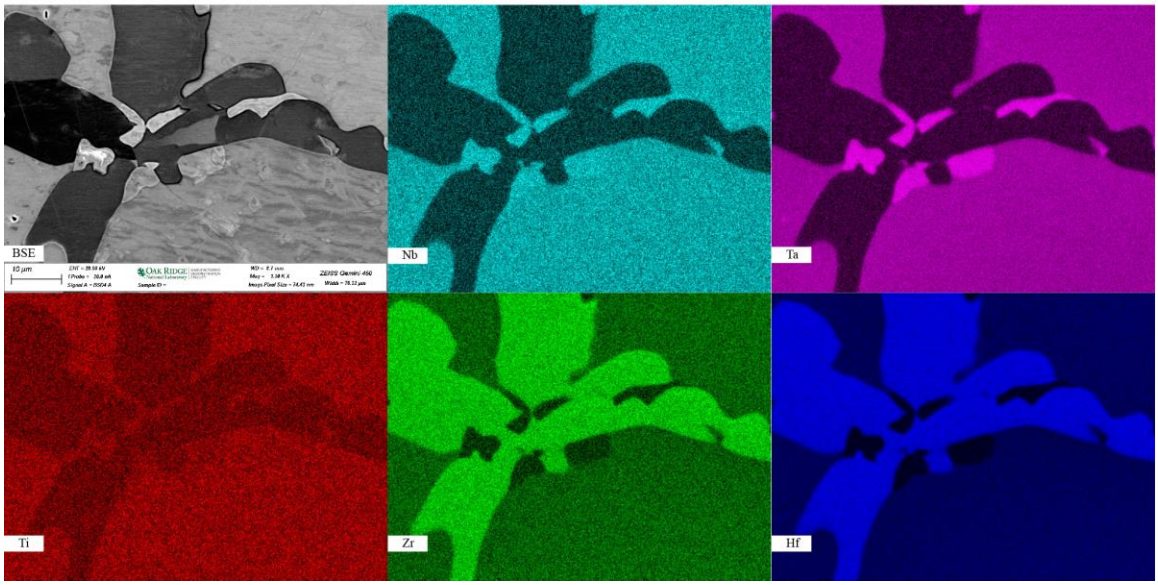

Supplementary Figure 4.61: $Ti_5Zr_{20}Hf_{35}N_{20}Ta_{20}$ after 4800 h at 1000 ˚C beginning in the recrystallized condition, with accompanying EDS maps.

Chapter 5 Final remarks and outlook

RHEAs are being considered as an alloy class with the potential to go beyond current Ni-based superalloys. To be useful engineering materials, they will require high temperature strength, oxidation resistance, room-temperature ductility, fabricability, and a stable microstructure at intermediate to high temperatures. TiZrHfNbTa meets the room-temperature ductility requirement, but it and its derivatives still suffer, in one form or another, from insufficient mechanical-properties data, including at elevated temperatures and at relevant strain rates.

This work has tackled a couple of these gaps by focusing on the room-temperature mechanical behavior and the intermediate-temperature thermal stability of Ti-Zr-Hf-Nb-Ta alloys. Although the results described in this thesis add significantly to the available literature, the field could benefit from additional characterization, especially TEM. Nevertheless, even with what we have learned so far, current limitations and future opportunities for RHEAs have been clearly identified as summarized below.

Given that the yield strengths of the investigated alloys agree well with predictions of dislocation theory, future studies can utilize this strength theory as a starting point for alloy design. CALPHAD results also suggests that alloy composition can be varied over wide ranges while keeping the melting point relatively constant. Therefore, in principle, drastic compositional changes are possible to tune other properties without sacrificing high-temperature strengths since the latter depend mainly on the melting temperature.

The alloys in the single-phase state have toughness values that fall within the range of other structural materials, but their absolute values should be regarded skeptically

because the generally low work hardening rates of RHEAs makes it difficult to conduct valid toughness tests even when the specimen geometry meets criteria specified in ASTM standards. Finally, the microstructures of most apparently single-phase RHEAs alternate between single-phase above about 1000 ˚C and multi-phase at lower temperatures making them most likely unsuitable for applications in which components cycle through these temperatures.

While TiZrHfNbTa and the studied derivatives are hard and ductile at room temperature, their lack of high-temperature strength [24] and poor thermal stability suggests that they will not be practical engineering materials in the single-phase state. Even if room-temperature applications are the target of RHEAs, they are not suitable replacements for materials like β-titanium alloys [186] or quenched and partitioned steels [187] both of which can achieve similar behavior as ductile RHEAs for a fraction of the cost. There may be an opportunity to replace alloys such as TZM molybdenum and Ta-111 [4] for quasi-static high temperature use, but additional data need to be generated before the potential of RHEAs in this temperature regime can be judged.

References

[1] R.C. Reed, Superalloys - Fundamentals and Applications, Cambridge University Press, (2006).

[2] B.A. Pint, J.R. DiStefano, I.G. Wright, Oxidation resistance: One barrier to moving beyond Ni-base superalloys, Materials Science and Engineering: A 415(1-2) (2006) 255-263.

[3] J.H. Schneibel, J.C.A. Carmichael, E.P. George, High Strain Rate Tensile Testing of DOP-26 Iridium, Oak Ridge National Laboratory, Oak Ridge, TN, United States, (2007), ORNL/TM-2007/081.

[4] T.G. Nieh, J. Wadsworth, Recent Advances and Developments in Refractory Alloys, MRS Proceedings 322 (1993) 315.

[5] R.H. Cooper, Jr., E.E. Hoffman (Eds.) Refractory alloy technology for space nuclear power applications, USDOE Technical Information Center, Oak Ridge, TN, United States, (1984), OSTI ID 7122878.

[6] J.B. Conway, P.N. Flagella, CREEP-RUPTURE DATA FOR THE REFRACTORY METALS TO HIGH TEMPERATURES, Nuclear Systems Programs General Electric Co., Cincinnati, OH, (1969) 1-977, https://doi.org/10.2172/4755006, OSTI ID 4755006.

[7] D. Hobson, EFFECT OF ALLOYING ELEMENTS ON THE STRENGTH, STABILITY, AND CORROSION AND OXIDATION RESISTANCE OF COLUMBIUM A LITERATURE SURVEY, Oak Ridge National Laboratory, Oak Ridge, TN, (1962), https://doi.org/10.2172/4515686, OSTI ID 4515686.

[8] J.W. Yeh, S.K. Chen, S.J. Lin, J.Y. Gan, T.S. Chin, T.T. Shun, C.H. Tsau, S.Y. Chang, Nanostructured high-entropy alloys with multiple principal elements: Novel alloy design concepts and outcomes, Advanced Engineering Materials 6(5) (2004) 299-303.
[9] O.N. Senkov, G.B. Wilks, D.B. Miracle, C.P. Chuang, P.K. Liaw, Refractory high-entropy alloys, Intermetallics 18(9) (2010) 1758-1765.
[10] D.B. Miracle, O.N. Senkov, A critical review of high entropy alloys and related concepts, Acta Materialia 122 (2017) 448-511.
[11] F. Otto, Y. Yang, H. Bei, E.P. George, Relative effects of enthalpy and entropy on the phase stability of equiatomic high-entropy alloys, Acta Materialia 61(7) (2013) 2628-2638.
[12] O.N. Senkov, D.B. Miracle, K.J. Chaput, J.-P. Couzinie, Development and exploration of refractory high entropy alloys—A review, Journal of Materials Research 33(19) (2018) 3092-3128.
[13] B. Chen, L. Zhuo, Latest progress on refractory high entropy alloys: Composition, fabrication, post processing, performance, simulation and prospect, Elsevier Ltd, 2023.
[14] C.K.H. Borg, C. Frey, J. Moh, T.M. Pollock, S. Gorsse, D.B. Miracle, O.N. Senkov, B. Meredig, J.E. Saal, Expanded dataset of mechanical properties and observed phases of multi-principal element alloys, Scientific Data 7(1) (2020) 430.
[15] L. Zhuo, Y. Xie, B. Chen, A review on recent progress of refractory high entropy alloys: From fundamental research to engineering applications, Journal of Materials Research and Technology 33 (2024) 1097-1129.

[16] D.B. Miracle, O.N. Senkov, C. Frey, S. Rao, T.M. Pollock, Strength vs temperature for refractory complex concentrated alloys (RCCAs): A critical comparison with refractory BCC elements and dilute alloys, Acta Materialia 266 (2024) 119692.
[17] O.N. Senkov, S. Gorsse, D.B. Miracle, S.I. Rao, T.M. Butler, Correlations to improve high-temperature strength and room temperature ductility of refractory complex concentrated alloys, Materials & Design 239 (2024) 112762.
[18] O.N. Senkov, D.B. Miracle, S.I. Rao, Correlations to improve room temperature ductility of refractory complex concentrated alloys, Materials Science and Engineering: A 820 (2021) 141512.
[19] O.N. Senkov, G.B. Wilks, J.M. Scott, D.B. Miracle, Mechanical properties of Nb25Mo25Ta25W25 and V20Nb20Mo 20Ta20W20 refractory high entropy alloys, Intermetallics 19(5) (2011) 698-706.
[20] P. Kumar, X. Gou, D.H. Cook, M.I. Payne, N.J. Morrison, W. Wang, M. Zhang, M. Asta, A.M. Minor, R. Cao, Y. Li, R.O. Ritchie, Degradation of the mechanical properties of NbMoTaW refractory high-entropy alloy in tension, Acta Materialia 279 (2024) 120297.
[21] O.N. Senkov, J.M. Scott, S.V. Senkova, F. Meisenkothen, D.B. Miracle, C.F. Woodward, Microstructure and elevated temperature properties of a refractory TaNbHfZrTi alloy, Journal of Materials Science 47(9) (2012) 4062-4074.

[22] H.Y. Yasuda, Y. Yamada, K. Cho, T. Nagase, Deformation behavior of HfNbTaTiZr high entropy alloy singe crystals and polycrystals, Materials Science and Engineering: A 809 (2021) 140983.

[23] L.H. Mills, M.G. Emigh, C.H. Frey, N.R. Philips, S.P. Murray, J. Shin, D.S. Gianola, T.M. Pollock, Temperature-dependent tensile behavior of the HfNbTaTiZr multi-principal element alloy, Acta Materialia 245 (2023) 118618.

[24] C. Gadelmeier, Y. Yang, U. Glatzel, E.P. George, Creep strength of refractory high-entropy alloy TiZrHfNbTa and comparison with Ni-base superalloy CMSX-4, Cell Reports Physical Science 3(8) (2022) 100991.

[25] C.J. Liu, C. Gadelmeier, S.L. Lu, J.W. Yeh, H.W. Yen, S. Gorsse, U. Glatzel, A.C. Yeh, Tensile creep behavior of HfNbTaTiZr refractory high entropy alloy at elevated temperatures, Acta Materialia 237 (2022) 118188.

[26] J. Zhang, C. Gadelmeier, S. Sen, R. Wang, X. Zhang, Y. Zhong, U. Glatzel, B. Grabowski, G. Wilde, S.V. Divinski, Zr diffusion in BCC refractory high entropy alloys: A case of 'non-sluggish' diffusion behavior, Acta Materialia 233 (2022) 117970.

[27] D.H. Cook, P. Kumar, M.I. Payne, C.H. Belcher, P. Borges, W. Wang, F. Walsh, Z. Li, A. Devaraj, M. Zhang, M. Asta, A.M. Minor, E.J. Lavernia, D. Apelian, R.O. Ritchie, Kink bands promote exceptional fracture resistance in a NbTaTiHf refractory medium-entropy alloy, Science (New York, N.Y.) 384(6692) (2024) 178-184.

[28] G. Sahragard-Monfared, C.H. Belcher, S. Bajpai, M. Wirth, A. Devaraj, D. Apelian, E.J. Lavernia, R.O. Ritchie, A.M. Minor, J.C. Gibeling, C. Zhang, M. Zhang, Tensile

creep behavior of the Nb45Ta25Ti15Hf15 refractory high entropy alloy, Acta Materialia 272 (2024) 119940.

[29] O.N. Senkov, A.L. Pilchak, S.L. Semiatin, Effect of Cold Deformation and Annealing on the Microstructure and Tensile Properties of a HfNbTaTiZr Refractory High Entropy Alloy, Metallurgical and Materials Transactions A: Physical Metallurgy and Materials Science 49(7) (2018) 2876-2892.

[30] B. Yin, F. Maresca, W.A. Curtin, Vanadium is an optimal element for strengthening in both fcc and bcc high-entropy alloys, Acta Materialia 188 (2020) 486-491.

[31] M. Fujiwara, K. Natesan, M. Satou, A. Hasegawa, K. Abe, T. Takahashi, T. Sugawara, T. Shishido, Effects of Doping Elements on Oxidation Properties of Low-Activation Vanadium Alloys, Materials Transactions 42(6) (2001) 1048-1051.

[32] O.N. Senkov, S.V. Senkova, D.M. Dimiduk, C. Woodward, D.B. Miracle, Oxidation behavior of a refractory NbCrMo0.5Ta0.5TiZr alloy, Journal of Materials Science 47(18) (2012) 6522-6534.

[33] S. Sheikh, M.K. Bijaksana, A. Motallebzadeh, S. Shafeie, A. Lozinko, L. Gan, T.-K. Tsao, U. Klement, D. Canadinc, H. Murakami, S. Guo, Accelerated oxidation in ductile refractory high-entropy alloys, Intermetallics 97 (2018) 58-66.

[34] B.P. Bewlay, M.R. Jackson, P.R. Subramanian, J.C. Zhao, A review of very-high-temperature Nb-silicide-based composites, Metallurgical and Materials Transactions A 34(10) (2003) 2043-2052.

[35] M. Todai, T. Nagase, T. Hori, A. Matsugaki, A. Sekita, T. Nakano, Novel TiNbTaZrMo high-entropy alloys for metallic biomaterials, Scripta Materialia 129 (2017) 65-68.

[36] Z.Q. Xu, Z.L. Ma, Y. Tan, X.W. Cheng, Designing TiVNbTaSi refractory high-entropy alloys with ambient tensile ductility, Scripta Materialia 206 (2022) 114230.

[37] C.-H. Chang, M.S. Titus, J.-W. Yeh, Oxidation Behavior between 700 and 1300 °C of Refractory TiZrNbHfTa High-Entropy Alloys Containing Aluminum, Advanced Engineering Materials 20(6) (2018) 1700948.

[38] C.-M. Lin, C.-C. Juan, C.-H. Chang, C.-W. Tsai, J.-W. Yeh, Effect of Al addition on mechanical properties and microstructure of refractory AlxHfNbTaTiZr alloys, Journal of Alloys and Compounds 624 (2015) 100-107.

[39] E.A. Anber, D. Beaudry, C. Brandenburg, S. Lech, L. Backman, D.L. Foley, E.L. Wang, M.J. Waters, L. Perriere, J.-P. Couzinie, J.M. Rondinelli, E. Opila, M.L. Taheri, Oxidation resistance of Al-containing refractory high-entropy alloys, Scripta Materialia 244 (2024) 115997.

[40] B. Gorr, F. Müller, M. Azim, H.-J. Christ, T. Müller, H. Chen, A. Kauffmann, M. Heilmaier, High-Temperature Oxidation Behavior of Refractory High-Entropy Alloys: Effect of Alloy Composition, Oxidation of Metals 88(3) (2017) 339-349.

[41] R. Su, H. Zhang, G. Ouyang, L. Liu, D.D. Johnson, J.H. Perepezko, Oxidation mechanism in a refractory multiple-principal-element alloy at high temperature, Acta Materialia 246 (2023) 118719.

[42] B. Gorr, S. Schellert, F. Müller, H.-J. Christ, A. Kauffmann, M. Heilmaier, Current Status of Research on the Oxidation Behavior of Refractory High Entropy Alloys, Advanced Engineering Materials 23(5) (2021) 2001047.
[43] K.-C. Lo, Y.-J. Chang, H. Murakami, J.-W. Yeh, A.-C. Yeh, An oxidation resistant refractory high entropy alloy protected by CrTaO4-based oxide, Scientific Reports 9(1) (2019) 7266.
[44] B. Gorr, F. Müller, S. Schellert, H.-J. Christ, H. Chen, A. Kauffmann, M. Heilmaier, A new strategy to intrinsically protect refractory metal based alloys at ultra high temperatures, Corrosion Science 166 (2020) 108475.
[45] R.K. Dehury, R. Kumar, Y.G. Joshi, V. Gupta, Elemental Influence on Oxidation Behaviour of Cantor-Based and Refractory High Entropy Alloys: A Critical Review, Advanced Engineering Materials 26(11) (2024) 2302124.
[46] O.N. Senkov, S.L. Semiatin, Microstructure and properties of a refractory high-entropy alloy after cold working, Journal of Alloys and Compounds 649 (2015) 1110-1123.
[47] B. Schuh, B. Völker, J. Todt, N. Schell, L. Perrière, J. Li, J.P. Couzinié, A. Hohenwarter, Thermodynamic instability of a nanocrystalline, single-phase TiZrNbHfTa alloy and its impact on the mechanical properties, Acta Materialia 142 (2018) 201-212.
[48] F.G. Coury, T. Butler, K. Chaput, A. Saville, J. Copley, J. Foltz, P. Mason, K. Clarke, M. Kaufman, A. Clarke, Phase equilibria, mechanical properties and design of quaternary refractory high entropy alloys, Materials & Design 155 (2018) 244-256.

[49] S. Maiti, W. Steurer, Structural-disorder and its effect on mechanical properties in single-phase TaNbHfZr high-entropy alloy, Acta Materialia 106 (2016) 87-97.
[50] R. Poulain, M. Rajkowski, Y. Zhao, P. Gemagami, B. Appolaire, S. Laube, A. Kauffmann, L. Perrière, J.-P. Couzinié, T. Li, G. Laplanche, Oxygen-induced decomposition of the body-centered cubic HfNbTaTiZr high-entropy alloy, Acta Materialia 280 (2024) 120295.
[51] O.N. Senkov, J.K. Jensen, A.L. Pilchak, D.B. Miracle, H.L. Fraser, Compositional variation effects on the microstructure and properties of a refractory high-entropy superalloy AlMo0.5NbTa0.5TiZr, Materials and Design 139 (2018) 498-511.
[52] V. Soni, O.N. Senkov, B. Gwalani, D.B. Miracle, R. Banerjee, Microstructural Design for Improving Ductility of An Initially Brittle Refractory High Entropy Alloy, Scientific Reports 8(1) (2018) 1-10.
[53] V. Soni, B. Gwalani, T. Alam, S. Dasari, Y. Zheng, O.N. Senkov, D. Miracle, R. Banerjee, Phase inversion in a two-phase, BCC+B2, refractory high entropy alloy, Acta Materialia 185 (2020) 89-97.
[54] O.N. Senkov, B. Crossman, S.I. Rao, J.P. Couzinie, D.B. Miracle, T.M. Butler, R. Banerjee, M. Mills, Mechanical properties of an Al10Nb20Ta15Ti30V5Zr20 A2/B2 refractory superalloy and its constituent phases, Acta Materialia 254 (2023) 119017.
[55] O.N. Senkov, S.A. Kube, J.W. Drazin, V. Soni, D.B. Miracle, T.M. Butler, T.M. Pollock, R. Banerjee, Thermal and Elastic Properties of an A2/B2 Refractory High

Entropy Superalloy and Its Constituent Phases, Metallurgical and Materials Transactions A 55(8) (2024) 2704-2717.

[56] A. Sharma, S. Dasari, V. Soni, Z. Kloenne, J.-P. Couzinié, O.N. Senkov, D.B. Miracle, S.G. Srinivasan, H. Fraser, R. Banerjee, B2 to ordered omega transformation during isothermal annealing of refractory high entropy alloys: Implications for high temperature phase stability, Journal of Alloys and Compounds 953 (2023) 170065.

[57] J. Brodie, J. Wang, J.-P. Couzinié, M. Heczko, V. Mazánová, M.J. Mills, M. Ghazisaeidi, Stability of the B2 phase in refractory high entropy alloys containing aluminum, Acta Materialia 268 (2024) 119745.

[58] V. Soni, A. Chesetti, A. Sharma, S. Dasari, J.-P. Couzinié, O.N. Senkov, D.B. Miracle, S.G. Srivilliputhur, H. Fraser, R. Banerjee, Some insights into the high temperature phase stability of the BCC + B2 microstructure in aluminum containing refractory high entropy alloys, Journal of Materials Science 60 (2024) 1675–1688.

[59] S.A. Kube, C. Frey, C. McMullin, B. Neuman, K.M. Mullin, T.M. Pollock, Navigating the BCC-B2 refractory alloy space: Stability and thermal processing with Ru-B2 precipitates, Acta Materialia 265 (2024) 119628.

[60] C. Frey, B. Neuman, K. Mullin, A. Botros, J. Lamb, C.S. Holgate, S.A. Kube, T.M. Pollock, On the stability of coherent HfRu- and ZrRu-B2 precipitates in Nb-based alloys, Materials & Design 247 (2024) 113385.

[61] C. Frey, B. Neuman, A. Botros, S.A. Kube, T.M. Pollock, Refractory multi-principal element alloys with solution and aged HfRu-B2 precipitates, Scripta Materialia 255 (2025) 116411.

[62] C. Frey, H. You, S. Kube, G.H. Balbus, K. Mullin, S. Oppenheimer, C.S. Holgate, T.M. Pollock, High Temperature B2 Precipitation in Ru-Containing Refractory Multi-principal Element Alloys, Metallurgical and Materials Transactions A: Physical Metallurgy and Materials Science 55(6) (2024) 1739-1764.

[63] L. Pionke, J.W. Davis, Technical assessment of niobium alloys data base for fusion reactor applications, McDonnell Douglas Astronautics Co., St. Louis, MO, (1979), https://doi.org/10.2172/5419637, OSTI ID 5419637.

[64] Y. Zou, H. Ma, R. Spolenak, Ultrastrong ductile and stable high-entropy alloys at small scales, Nature Communications 6(1) (2015) 7748.

[65] Y. Xiao, Y. Zou, H. Ma, A.S. Sologubenko, X. Maeder, R. Spolenak, J.M. Wheeler, Nanostructured NbMoTaW high entropy alloy thin films: High strength and enhanced fracture toughness, Scripta Materialia 168 (2019) 51-55.

[66] Y. Zou, P. Okle, H. Yu, T. Sumigawa, T. Kitamura, S. Maiti, W. Steurer, R. Spolenak, Fracture properties of a refractory high-entropy alloy: In situ micro-cantilever and atom probe tomography studies, Scripta Materialia 128 (2017) 95-99.

[67] Z. Wang, H. Wu, Y. Wu, H. Huang, X. Zhu, Y. Zhang, H. Zhu, X. Yuan, Q. Chen, S. Wang, X. Liu, H. Wang, S. Jiang, M.J. Kim, Z. Lu, Solving oxygen embrittlement of

refractory high-entropy alloy via grain boundary engineering, Materials Today 54 (2022) 83-89.

[68] J.P. Couzinié, L. Lilensten, Y. Champion, G. Dirras, L. Perrière, I. Guillot, On the room temperature deformation mechanisms of a TiZrHfNbTa refractory high-entropy alloy, Materials Science and Engineering A 645 (2015) 255-263.

[69] L. Lilensten, J.P. Couzinié, L. Perrière, A. Hocini, C. Keller, G. Dirras, I. Guillot, Study of a bcc multi-principal element alloy: Tensile and simple shear properties and underlying deformation mechanisms, Acta Materialia 142 (2018) 131-141.

[70] N.D. Stepanov, N.Y. Yurchenko, S.V. Zherebtsov, M.A. Tikhonovsky, G.A. Salishchev, Aging behavior of the HfNbTaTiZr high entropy alloy, Materials Letters 211 (2018) 87-90.

[71] C.C. Juan, M.H. Tsai, C.W. Tsai, W.L. Hsu, C.M. Lin, S.K. Chen, S.J. Lin, J.W. Yeh, Simultaneously increasing the strength and ductility of a refractory high-entropy alloy via grain refining, Materials Letters 184 (2016) 200-203.

[72] S. Chen, K.-K. Tseng, Y. Tong, W. Li, C.-W. Tsai, J.-W. Yeh, P.K. Liaw, Grain growth and Hall-Petch relationship in a refractory HfNbTaZrTi high-entropy alloy, Journal of Alloys and Compounds 795 (2019) 19-26.

[73] G. Dirras, J. Gubicza, A. Heczel, L. Lilensten, J.P. Couzinié, L. Perrière, I. Guillot, A. Hocini, Microstructural investigation of plastically deformed Ti20Zr20Hf20Nb20Ta20 high entropy alloy by X-ray diffraction and transmission electron microscopy, Materials Characterization 108 (2015) 1-7.

[74] M. Tanaka, S. Okajo, S. Yamasaki, T. Morikawa, Persistent slip observed in TiZrNbHfTa: A body-centered high-entropy cubic alloy, Scripta Materialia 200 (2021) 113895.

[75] M.A. Charpagne, J.C. Stinville, F. Wang, N. Philips, T.M. Pollock, Orientation dependent plastic localization in the refractory high entropy alloy HfNbTaTiZr at room temperature, Materials Science and Engineering A 848 (2022) 143291.

[76] C.-C. Juan, K.-K. Tseng, W.-L. Hsu, M.-H. Tsai, C.-W. Tsai, C.-M. Lin, S.-K. Chen, S.-J. Lin, J.-W. Yeh, Solution strengthening of ductile refractory HfMoxNbTaTiZr high-entropy alloys, Materials Letters 175 (2016) 284-287.

[77] O.N. Senkov, S. Rao, K.J. Chaput, C. Woodward, Compositional effect on microstructure and properties of NbTiZr-based complex concentrated alloys, Acta Materialia 151 (2018) 201-215.

[78] O.N. Senkov, S.I. Rao, T.M. Butler, K.J. Chaput, Ductile Nb alloys with reduced density and cost, Journal of Alloys and Compounds 808 (2019) 151685.

[79] F.G. Coury, M. Kaufman, A.J. Clarke, Solid-solution strengthening in refractory high entropy alloys, Acta Materialia 175 (2019) 66-81.

[80] L. Fang, J. Wang, X. Li, X. Tao, Y. Ouyang, Y. Du, Effect of Cr content on microstructure characteristics and mechanical properties of ZrNbTaHf0.2Crx refractory high entropy alloy, Journal of Alloys and Compounds 924 (2022) 166593.

[81] Y. Liu, Y. Zhang, H. Zhang, N. Wang, X. Chen, H. Zhang, Y. Li, Microstructure and mechanical properties of refractory HfMo0.5NbTiV0.5Six high-entropy composites, Journal of Alloys and Compounds 694 (2017) 869-876.

[82] Z. An, A. Li, S. Mao, T. Yang, L. Zhu, R. Wang, Z. Wu, B. Zhang, R. Shao, C. Jiang, B. Cao, C. Shi, Y. Ren, C. Liu, H. Long, J. Zhang, W. Li, F. He, L. Sun, J. Zhao, L. Yang, X. Zhou, X. Wei, Y. Chen, Z. Lu, F. Ren, C.-T. Liu, Z. Zhang, Han, Xiaodong, Negative mixing enthalpy solid solutions deliver high strength and ductility, Nature 2024 (2024) 1-6.

[83] Y.D. Wu, Y.H. Cai, T. Wang, J.J. Si, J. Zhu, Y.D. Wang, X.D. Hui, A refractory Hf25Nb25Ti25Zr25 high-entropy alloy with excellent structural stability and tensile properties, Materials Letters 130 (2014) 277-280.

[84] T. Li, S. Wang, W. Fan, Y. Lu, T. Wang, T. Li, P.K. Liaw, CALPHAD-aided design for superior thermal stability and mechanical behavior in a TiZrHfNb refractory high-entropy alloy, Acta Materialia (2023) 118728.

[85] C. Zhang, H. Wang, X. Wang, Y.T. Tang, Q. Yu, C. Zhu, M. Xu, S. Zhao, R. Kou, X. Wang, B.E. MacDonald, R.C. Reed, K.S. Vecchio, P. Cao, T.J. Rupert, E.J. Lavernia, Strong and ductile refractory high-entropy alloys with super formability, Acta Materialia 245 (2023) 118602.

[86] S.-P. Wang, E. Ma, J. Xu, New ternary equi-atomic refractory medium-entropy alloys with tensile ductility: Hafnium versus titanium into NbTa-based solution, Intermetallics 107 (2019) 15-23.

[87] Y. Huang, J. Gao, S. Wang, D. Guan, Y. Xu, X. Hu, W.M. Rainforth, Q. Zhu, I. Todd, Influence of tantalum composition on mechanical behavior and deformation mechanisms of TiZrHfTax high entropy alloys, Journal of Alloys and Compounds 903 (2022) 163796.

[88] H. Huang, Y. Wu, J. He, H. Wang, X. Liu, K. An, W. Wu, Z. Lu, Phase-Transformation Ductilization of Brittle High-Entropy Alloys via Metastability Engineering, Advanced Materials 29(30) (2017) 1701678.

[89] S. Wang, S. Lu, M. Wu, D. Wang, G. Zhu, C. Yang, D. Shu, B. Sun, L. Vitos, Decreasing Zr content to improve tensile properties of non-equiatomic TiZrHfNb medium entropy alloys with transformation-induced plasticity, Materials Science and Engineering A 832 (2022) 142476.

[90] G. Ji, Z. Zhou, F. Meng, X. Yang, R. Sheng, J. Qiao, P.K. Liaw, M. Li, L. Jiang, S. Chen, Y. Tong, Effect of Zr addition on the local structure and mechanical properties of Ti–Ta–Nb–Zr refractory high-entropy alloys, Journal of Materials Research and Technology 19 (2022) 4428-4438.

[91] Y. Yuan, Y. Wu, Z. Yang, X. Liang, Z. Lei, H. Huang, H. Wang, X. Liu, K. An, W. Wu, Z. Lu, Formation, structure and properties of biocompatible TiZrHfNbTa high-entropy alloys, Materials Research Letters 7(6) (2019) 225-231.

[92] Z. Han, L. Meng, J. Yang, G. Liu, J. Yang, R. Wei, G. Zhang, Novel BCC VNbTa refractory multi-element alloys with superior tensile properties, Materials Science and Engineering: A 825 (2021) 141908.

[93] W. Li, K. Xiong, L. Yang, S. Zhang, J. He, Y. Wang, Y. Mao, An ambient ductile TiHfVNbTa refractory high-entropy alloy: Cold rolling, mechanical properties, lattice distortion, and first-principles prediction, Materials Science and Engineering A 856 (2022) 144046.

[94] S. Wang, D. Shu, P. Shi, X. Zhang, B. Mao, D. Wang, P.K. Liaw, B. Sun, TiZrHfNb refractory high-entropy alloys with twinning-induced plasticity, Journal of Materials Science & Technology 187 (2024) 72-85.

[95] X. Zhang, W. Wang, J. Wu, S. Wang, J. Sun, J.Y. Chung, S.J. Pennycook, Deformation twinning in Ti48.9Zr32.0Nb12.6Ta6.5 medium entropy alloy, Materials Science and Engineering: A 809 (2021) 140931.

[96] X. Wen, Y. Wu, H. Huang, S. Jiang, H. Wang, X. Liu, Y. Zhang, X. Wang, Z. Lu, Effects of Nb on deformation-induced transformation and mechanical properties of HfNbxTa0.2TiZr high entropy alloys, Materials Science and Engineering: A 805 (2021) 140798.

[97] Y. Jung, K. Lee, S.J. Hong, J.K. Lee, J. Han, K.B. Kim, P.K. Liaw, C. Lee, G. Song, Investigation of phase-transformation path in TiZrHf(VNbTa)x refractory high-entropy alloys and its effect on mechanical property, Journal of Alloys and Compounds 886 (2021) 161187.

[98] L. Lilensten, J.P. Couzinié, J. Bourgon, L. Perrière, G. Dirras, F. Prima, I. Guillot, Design and tensile properties of a bcc Ti-rich high-entropy alloy with transformation-induced plasticity, Materials Research Letters 5(2) (2017) 110-116.

[99] M. Abdel-Hady, K. Hinoshita, M. Morinaga, General approach to phase stability and elastic properties of β-type Ti-alloys using electronic parameters, Scripta Materialia 55(5) (2006) 477-480.

[100] Z. Lei, X. Liu, Y. Wu, H. Wang, S. Jiang, S. Wang, X. Hui, Y. Wu, B. Gault, P. Kontis, D. Raabe, L. Gu, Q. Zhang, H. Chen, H. Wang, J. Liu, K. An, Q. Zeng, T.G. Nieh, Z. Lu, Enhanced strength and ductility in a high-entropy alloy via ordered oxygen complexes, Nature 563(7732) (2018) 546-550.

[101] S. Wang, Y. He, X. Zhang, J. Wang, M. Wu, D. Shu, H. Tang, B. Sun, The effects of interstitial oxygen on mechanical properties of TiZrNb medium-entropy alloy over a wide temperature range, Journal of Alloys and Compounds 989 (2024) 174394.

[102] L. Backman, E.J. Opila, Thermodynamic assessment of the group IV, V and VI oxides for the design of oxidation resistant multi-principal component materials, Journal of the European Ceramic Society 39(5) (2019) 1796-1802.

[103] H. Suzuki, Solid solution hardening in body-centred cubic alloys, in: Dislocations in solids 4, F.R.N. Nabarro (Eds.), (1980) 191-217.

[104] C. Lee, F. Maresca, R. Feng, Y. Chou, T. Ungar, M. Widom, K. An, J.D. Poplawsky, Y.C. Chou, P.K. Liaw, W.A. Curtin, Strength can be controlled by edge dislocations in refractory high-entropy alloys, Nature Communications 12(1) (2021) 6-13.

[105] Y.W. Wang, Q.F. He, Z.H. Ye, Y. Liao, C.W. Li, Q. Wang, J.F. Gu, Ductilization of single-phase refractory high-entropy alloys via activation of edge dislocation, Acta Materialia 284 (2025) 120614.

[106] C. Baruffi, F. Maresca, W.A. Curtin, Screw vs. edge dislocation strengthening in body-centered-cubic high entropy alloys and implications for guided alloy design, MRS Communications 12(6) (2022) 1111-1118.

[107] F. Maresca, W.A. Curtin, Theory of screw dislocation strengthening in random BCC alloys from dilute to “High-Entropy” alloys, Acta Materialia 182 (2020) 144-162.

[108] S.I. Rao, C. Woodward, B. Akdim, O.N. Senkov, D. Miracle, Theory of solid solution strengthening of BCC Chemically Complex Alloys, Acta Materialia 209 (2021) 116758.

[109] R.E. Kubilay, A. Ghafarollahi, F. Maresca, W.A. Curtin, High energy barriers for edge dislocation motion in body-centered cubic high entropy alloys, npj Computational Materials 7(1) (2021) 1-9.

[110] F. Maresca, W.A. Curtin, Mechanistic origin of high strength in refractory BCC high entropy alloys up to 1900K, Acta Materialia 182 (2020) 235-249.

[111] G. Laplanche, P. Gadaud, L. Perrière, I. Guillot, J.P. Couzinié, Temperature dependence of elastic moduli in a refractory HfNbTaTiZr high-entropy alloy, Journal of Alloys and Compounds 799 (2019) 538-545.

[112] Y.X. Ye, B.L. Musico, Z.Z. Lu, L.B. Xu, Z.F. Lei, V. Keppens, H.X. Xu, T.G. Nieh, Evaluating elastic properties of a body-centered cubic NbHfZrTi high-entropy

alloy – A direct comparison between experiments and ab initio calculations, Intermetallics 109 (2019) 167-173.

[113] C. Lee, G. Kim, Y. Chou, B.L. Musicó, M.C. Gao, K. An, G. Song, Y.C. Chou, V. Keppens, W. Chen, P.K. Liaw, Temperature dependence of elastic and plastic deformation behavior of a refractory high-entropy alloy, Science Advances 6(37) (2020) eaaz4748.

[114] ASM Handbook Volume 3: Alloy Phase Diagrams, Okamoto, M.E. Schlesinger, E.M. Mueller (Eds.), ASM International, Materials Park, OH, 2016.

[115] T. Tsuru, S. Han, S. Matsuura, Z. Chen, K. Kishida, I. Iobzenko, S.I. Rao, C. Woodward, E.P. George, H. Inui, Intrinsic factors responsible for brittle versus ductile nature of refractory high-entropy alloys, Nature Communications 15(1) (2024) 1-10.

[116] T.M. Pollock, S. Tin, Nickel-Based Superalloys for Advanced Turbine Engines Chemistry, Microstructure, and Properties, Journal of Propulsion and Power 22(2) (2006) 361-374.

[117] E.P. George, W.A. Curtin, C.C. Tasan, High entropy alloys: A focused review of mechanical properties and deformation mechanisms, Acta Materialia 188 (2020) 435-474.

[118] O.N. Senkov, J.M. Scott, S.V. Senkova, D.B. Miracle, C.F. Woodward, Microstructure and room temperature properties of a high-entropy TaNbHfZrTi alloy, Journal of Alloys and Compounds 509(20) (2011) 6043-6048.

[119] V.T. Nguyen, M. Qian, Z. Shi, T. Song, L. Huang, J. Zou, Compositional design of strong and ductile (tensile) Ti-Zr-Nb-Ta medium entropy alloys (MEAs) using the atomic mismatch approach, Materials Science and Engineering: A 742 (2019) 762-772.

[120] S.Y. Chen, Y. Tong, K.K. Tseng, J.W. Yeh, J.D. Poplawsky, J.G. Wen, M.C. Gao, G. Kim, W. Chen, Y. Ren, R. Feng, W.D. Li, P.K. Liaw, Phase transformations of HfNbTaTiZr high-entropy alloy at intermediate temperatures, Scripta Materialia 158 (2019) 50-56.

[121] S. Wang, M. Wu, D. Shu, G. Zhu, D. Wang, B. Sun, Mechanical instability and tensile properties of TiZrHfNbTa high entropy alloy at cryogenic temperatures, Acta Materialia 201 (2020) 517-527.

[122] S. Wang, M. Wu, D. Shu, B. Sun, Kinking in a refractory TiZrHfNb0.7 medium-entropy alloy, Materials Letters 264 (2020) 127369.

[123] H. Chen, T. Hanemann, S. Seils, D. Schliephake, A. Srinivasan Tirunilai, M. Heilmaier, K.-P. Weiss, A. Kauffmann, Influence of Temperature and Plastic Strain on Deformation Mechanisms and Kink Band Formation in Homogenized HfNbTaTiZr, Crystals 11(2) (2021) 81.

[124] K.M. Kim, H.Y. Kim, S. Miyazaki, Effect of Zr content on phase stability, deformation behavior, and young's modulus in Ti-Nb-Zr alloys, Materials 13(2) (2020) 476.

[125] Y.X. Ye, Z.P. Lu, T.G. Nieh, Dislocation nucleation during nanoindentation in a body-centered cubic TiZrHfNb high-entropy alloy, Scripta Materialia 130 (2017) 64-68.

[126] A. Motallebzadeh, N.S. Peighambardoust, S. Sheikh, H. Murakami, S. Guo, D. Canadinc, Microstructural, mechanical and electrochemical characterization of TiZrTaHfNb and Ti1.5ZrTa0.5Hf0.5Nb0.5 refractory high-entropy alloys for biomedical applications, Intermetallics 113 (2019) 106572.

[127] I.A. Su, K.K. Tseng, J.W. Yeh, B. El-Sayed, C.H. Liu, S.H. Wang, Strengthening mechanisms and microstructural evolution of ductile refractory medium-entropy alloy Hf20Nb10Ti35Zr35, Scripta Materialia 206 (2022) 114225.

[128] L. Qi, D.C. Chrzan, Tuning ideal tensile strengths and intrinsic ductility of bcc refractory alloys, Physical Review Letters 112(11) (2014) 115503.

[129] L. Kaufman, H. Bernstein, Computer calculation of phase diagrams with special reference to refractory metals, Academic Press Inc, United States, 1970.

[130] A.T. Dinsdale, SGTE data for pure elements, Calphad 15(4) (1991) 317-425.

[131] Y. Yang, B.P. Bewlay, Y.A. Chang, Liquid-Solid Phase Equilibria in Metal-Rich Nb-Ti-Hf-Si Alloys, Journal of Phase Equilibria and Diffusion 28(1) (2007) 107-114.

[132] W. Cao, S.L. Chen, F. Zhang, K. Wu, Y. Yang, Y.A. Chang, R. Schmid-Fetzer, W.A. Oates, PANDAT software with PanEngine, PanOptimizer and PanPrecipitation for multi-component phase diagram calculation and materials property simulation, Calphad 33(2) (2009) 328-342.

[133] Designation: E112 − 13 Standard Test Methods for Determining Average Grain Size 1, ASTM, 100 Barr Harbor Drive, PO Box C700, West Conshohocken, PA 19428-2959, (2021).

[134] Handbook of elastic properties of solids, liquids, and gases: Volume I, M. Levy, H. Bass, R. Stern (Eds.), Academic Press Inc, London UK, (2001).

[135] G. Winkens, A. Kauffmann, J. Herrmann, A.K. Czerny, S. Obert, S. Seils, T. Boll, C. Baruffi, Y. Rao, W.A. Curtin, R. Schwaiger, M. Heilmaier, The influence of lattice misfit on screw and edge dislocation-controlled solid solution strengthening in Mo-Ti alloys, Communications Materials 4(1) (2023) 26.

[136] S. Lampman, Wrought Titanium and Titanium Alloys, in: ASM Handbook Committee (Ed.), ASM Handbook, Volume 02 - Properties and Selection: Nonferrous Alloys and Special-Purpose Materials, ASTM International (1990), pp. 592-633.

[137] J.B. Nelson, D.P. Riley, An experimental investigation of extrapolation methods in the derivation of accurate unit-cell dimensions of crystals, Proceedings of the Physical Society 57(3) (1945) 160-160.

[138] B.D. Cullity, S.R. Stock, Elements of X-Ray Diffraction, Pearson Education Limited Edinburgh Gate, Harlow, Essex CM20 2JE, England, (2014).

[139] H.M. Rietveld, A profile refinement method for nuclear and magnetic structures, Journal of Applied Crystallography 2(2) (1969) 65-71.

[140] B. Gludovatz, A. Hohenwarter, D. Catoor, E.H. Chang, E.P. George, R.O. Ritchie, A fracture-resistant high-entropy alloy for cryogenic applications, Science 345(6201) (2014) 1153-1158.

[141] D. Raabe, K. Luecke, Rolling and annealing textures of bcc metals, Materials Science Forum 157-6(pt 1) (1994) 597-610.

[142] C. Varvenne, A. Luque, W.A. Curtin, Theory of strengthening in fcc high entropy alloys, Acta Materialia 118 (2016) 164-176.

[143] A. Ghafarollahi, W.A. Curtin, Screw-controlled strength of BCC non-dilute and high-entropy alloys, Acta Materialia 226 (2022) 117617.

[144] D. Nguyen-Manh, A.P. Horsfield, S.L. Dudarev, Self-interstitial atom defects in bcc transition metals: Group-specific trends, Physical Review B - Condensed Matter and Materials Physics 73(2) (2006) 4-7.

[145] T. Angsten, T. Mayeshiba, H. Wu, D. Morgan, Elemental vacancy diffusion database from high-throughput first-principles calculations for fcc and hcp structures, New Journal of Physics 16 (2014) 015018.

[146] P.J. Yang, Q.J. Li, T. Tsuru, S. Ogata, J.W. Zhang, H.W. Sheng, Z.W. Shan, G. Sha, W.Z. Han, J. Li, E. Ma, Mechanism of hardening and damage initiation in oxygen embrittlement of body-centred-cubic niobium, Acta Materialia 168 (2019) 331-342.

[147] E.P. George, D. Raabe, R.O. Ritchie, High entropy alloys, Nature Reviews Materials 4(7-8) (2019) 515-534.

[148] B. Gludovatz, A. Hohenwarter, K.V.S. Thurston, H. Bei, Z. Wu, E.P. George, R.O. Ritchie, Exceptional damage-tolerance of a medium-entropy alloy CrCoNi at cryogenic temperatures, Nature Communications 7(1) (2016) 10602.

[149] D. Liu, Q. Yu, S. Kabra, M. Jiang, P. Forna-Kreutzer, R. Zhang, M. Payne, F. Walsh, B. Gludovatz, M. Asta, A.M. Minor, E.P. George, R.O. Ritchie, Exceptional

fracture toughness of CrCoNi-based medium-and high-entropy alloys at 20 kelvin, Science 378(6623) (2022) 978-983.

[150] S.P. Wang, E. Ma, J. Xu, Notch fracture toughness of body-centered-cubic (TiZrNbTa)–Mo high-entropy alloys, Intermetallics 103 (2018) 78-87.

[151] X.J. Fan, R.T. Qu, Z.F. Zhang, Remarkably high fracture toughness of HfNbTaTiZr refractory high-entropy alloy, Journal of Materials Science and Technology 123 (2022) 70-77.

[152] M. Moschetti, A. Hohenwarter, M. Alfreider, J.P. Couzinié, T. Wei, J. Davis, A. Xu, D. Bhattacharyya, J.J. Kruzic, B. Gludovatz, Fracture Toughness Investigations of an Ion-Irradiated Nanocrystalline TiZrNbHfTa Refractory High-Entropy Alloy, Advanced Engineering Materials 26 (2024) 2400541.

[153] E1820-22 Standard Test Method for Measurement of Fracture Toughness, ASTM International (2022).

[154] C.F. Shih, Relationships between the J-integral and the crack opening displacement for stationary and extending cracks, J. Mech. Phys. Solids 29(4) (1981) 305-326.

[155] C.-S. Seok, Correction methods of an apparent negative crack growth phenomenon, International Journal of Fracture 102 (2000) 259-269.

[156] T.L. Anderson, Fracture Mechanics - Fundamentals and Applications, Third Edition ed., Taylor & Francis, Boca Raton, FL, 2005.

[157] S. Zherebtsov, N. Yurchenko, D. Shaysultanov, M. Tikhonovsky, G. Salishchev, N. Stepanov, Microstructure and Mechanical Properties Evolution in HfNbTaTiZr

Refractory High-Entropy Alloy During Cold Rolling, Advanced Engineering Materials 22 (2020) 2000105.

[158] X.K. Zhu, J.A. Joyce, Review of fracture toughness (G, K, J, CTOD, CTOA) testing and standardization, Engineering Fracture Mechanics 85 (2012) 1-46.

[159] J. Sumpter, An Experimental Investigation of the *T* Stress Approach, Constraint Effects in Fracture, E. Hackett, K. Schwalbe, R. Dodds Jr. (Eds.), 100 Barr Harbor Drive, PO Box C700, West Conshohocken, PA 19428-2959, ASTM International, (1993).

[160] R.L. Tregoning, J.A. Joyce, Application of T-stress based constraint correction to A533B steel fracture toughness data, Fatigue and fracture mechanics ASTM STP 1417 33 (2002) 307-327.

[161] A.H. Sherry, C.C. France, M.R. Goldthorpe, Compendium of T-Stress Solutions for Two and Three Dimensional Cracked Geometries, Fatigue of Fracture of Engineering Materials and Structures (1995) 141-155.

[162] N.P. O'Dowd, C.F. Shih, Two-Parameter Fracture Mechanics Theory and Applications, in: J.D. Landes, D.E. McCabe, J.A.M. Boulet (Eds.), Fracture Mechanics: Twenty-Fourth Volume., ASTM International, Bethesda, MD, 1992.

[163] S.-X. Wu, Y.-W. Mai, B. Cotterell, Q solutions for compact tension and single-edge cracked tension specimens, International Journal of Fracture 68 (1995) 97-103.

[164] J.H. Chen, R. Cao, Micromechanism of Cleavage Fracture of Metals, First ed., Butterworth-Heinemann (imprint of Elsevier), The Boulevard, Langford Lane, Kidlington, Oxford OX5 1 GB, UK, 2015.

[165] H.G. Pisarski, R. Hammond, K. Watt, Significance of splits and pop-ins observed during fracture toughness testing of line pipe steel, Proceedings of 7th International Pipeline Conference, ASME, Calgary, Alberta, Canada, 2008, pp. 473-482.

[166] S. Banerjee, U.P. Singh, On the origin of pop-in crack extension, Acta Metallurgical et Materialia 39(6) (1991) 1073-1084.

[167] M. Srinivas, G. Malakondaiah, P.R. Rao, On 'apparent pop-in' during ductile fracture toughness testing being related to the yield-point phenomenon in armco iron, Scripta Metallurgica 23(9) (1989) 1627-1632.

[168] R. Cao, Y.J. Yan, W.S. Du, Z.L. Tian, Y. Peng, J.H. Chen, Fracture behaviour of 8%Ni 980 MPa high strength steel at various temperatures Part 2 – COD tests, Materials Science and Technology 27(1) (2011) 145-155.

[169] E 813 Standard Test Method for JIc, A Measure of Fracture Toughness, ASTM International (1991), .

[170] J.D. Landes, Evaluation of the ISO J initiation procedure using the EURO fracture toughness data set, International Journal of Fracture 145 (2007) 285-297.

[171] K. Wallin, Specimen Size Limitations in J-R Curve Testing -- Standards Versus Reality, J. ASTM Int. 4(9) (2007) 1-12.

[172] B. Gludovatz, S.E. Naleway, R.O. Ritchie, J.J. Kruzic, Size-dependent fracture toughness of bulk metallic glasses, Acta Materialia 70 (2014) 198-207.

[173] P. Manikandan, K.N. Kumar, G.S. Rao, A.K. Jha, P.R. Narayanan, B. Pant, R.M. Cherian, Fracture Toughness of Ti–15V–3Cr–3Sn–3Al Titanium Alloy in Different Heat-

Treated Conditions, Transactions of the Indian Institute of Metals 72(6) (2019) 1507-1510.

[174] A. Bhattacharjee, V.K. Varma, S.V. Kamat, A.K. Gogia, S. Bhargava, Influence of b Grain Size on Tensile Behavior and Ductile Fracture Toughness of Titanium Alloy Ti-10V-2Fe-3Al, METALLURGICAL AND MATERIALS TRANSACTIONS 37A (2006) 1423-1433.

[175] D. Raabe, 23 - Recovery and Recrystallization: Phenomena, Physics, Models, Simulation, in: D.E. Laughlin, K. Hono (Eds.), Physical Metallurgy (Fifth Edition), Elsevier, Oxford, 2014, pp. 2291-2397.

[176] F. Otto, A. Dlouhý, K.G. Pradeep, M. Kuběnová, D. Raabe, G. Eggeler, E.P. George, Decomposition of the single-phase high-entropy alloy CrMnFeCoNi after prolonged anneals at intermediate temperatures, Acta Materialia 112 (2016) 40-52.

[177] O.N. Senkov, T.I. Daboiku, T.M. Butler, M.S. Titus, N.R. Philips, E.J. Payton, High-temperature mechanical properties and oxidation behavior of Hf-27Ta and Hf-21Ta-21X (X is Nb, Mo or W) alloys, International Journal of Refractory Metals and Hard Materials 96 (2021) 105467.

[178] M.S. Duesbery, V. Vitek, Plastic anisotropy in b.c.c. transition metals, Acta Materialia 46(5) (1998) 1481-1492.

[179] Z.Q. Wang, I.J. Beyerlein, An atomistically-informed dislocation dynamics model for the plastic anisotropy and tension–compression asymmetry of BCC metals, International Journal of Plasticity 27(10) (2011) 1471-1484.

[180] A. Raturi, K. Biswas, N.P. Gurao, Elastic and plastic anisotropy in a refractory high entropy alloy utilizing combinatorial instrumented indentation and electron backscatter diffraction, Journal of Alloys and Compounds 896 (2022) 162902.

[181] G. Dieter, Mechanical Metallurgy, McGraw-Hill, New York, New York (1986).

[182] K.V. Ravi, R. Gibala, The strength of niobium-oxygen solid solutions, Acta Metallurgica 18(6) (1970) 623-634.

[183] Z.C. Szkopiak, Hardness of niobium-nitrogen and niobium-oxygen alloys, Journal of the Less Common Metals 19(2) (1969) 93-103.

[184] H. Inouye, C.T. Liu, Low-pressure oxidation of T-111 and effect on tensile properties, Metals and Ceramics Division, Oak Ridge National Laboratory, Oak Ridge, TN, United States, (1974), ORNL Report TM-4621.

[185] Z. Liu, G. Welsch, Effects of oxygen and heat treatment on the mechanical properties of alpha and beta titanium alloys, Metallurgical Transactions A 19(3) (1988) 527-542.

[186] S. Bahl, S. Suwas, K. Chatterjee, Comprehensive review on alloy design, processing, and performance of β Titanium alloys as biomedical materials, International Materials Reviews 66(2) (2021) 114-139.

[187] L. Wang, J.G. Speer, Quenching and Partitioning Steel Heat Treatment, Metallography, Microstructure, and Analysis 2(4) (2013) 268-281.

Vita

William “Jack” Carpenter was born in Oregon and grew up in Wyoming. After receiving his B.S. in Metallurgical Engineering at the South Dakota School of Mines and Technology, he went to University of Tennessee, Knoxville to receive a Masters in 2021 and a PhD 2025. His dissertation focused, oddly enough, on the room temperature properties of high temperature materials with a focus on tension, fracture toughness, and thermal stability.